

The Pennsylvania State University
The Graduate School
Department of Materials Science and Engineering

MESOSCALE FABRICATION AND DESIGN

A Dissertation in
Materials Science and Engineering

by
Gregory R. Hayes

© 2011 Gregory R. Hayes

Submitted in Partial Fulfillment
of the Requirements
for the Degree of

Doctor of Philosophy

May 2011

The dissertation of Gregory R. Hayes was reviewed and approved* by the following:

James H. Adair
Professor of Materials Science and Engineering
Dissertation Co-Advisor
Co-Chair of Committee

Mary I. Frecker
Professor of Mechanical Engineering
Dissertation Co-Advisor
Co-Chair of Committee

Christopher L. Muhlstein
Associate Professor of Materials Science and Engineering

Eric M. Mockensturm
Associate Professor of Mechanical Engineering

Harriet B. Nembhard
Bashore Career Professor of Industrial and Manufacturing Engineering

Donald A. Koss
Professor Emeritus of Materials Science and Engineering

Gary L. Messing
Distinguished Professor Emeritus Materials Science and Engineering
Head of the Department of Materials Science and Engineering

*Signatures are on file in the Graduate School

ABSTRACT

A strong link between mechanical engineering design and materials science and engineering fabrication can facilitate an effective and adaptable prototyping process. In this dissertation, new developments in the lost mold-rapid infiltration forming (LM-RIF) process is presented which demonstrates the relationship between these two fields of engineering in the context of two device applications. Within the LM-RIF process, changes in materials processing and mechanical design are updated iteratively, often aided by statistical design of experiments (DOE). This approach allows fast and reliable prototyping of devices that are not readily manufacturable with tradition techniques.

The first of these device applications is a new surgical instrument designed for natural orifice transluminal endoscopic surgery procedures (NOTES). NOTES aims to eliminate external incisions during surgery by performing surgical procedures using an endoscope inserted into the body via a natural orifice (e.g., the mouth). Therefore, surgical instruments used in NOTES procedures must be used through the working channel of the endoscope; typically 2-6mm in diameter. The instrument designed and fabricated herein has length dimensions on the millimeter scale with small features on the micron scale making it ideally suited to be fabricated via the LM-RIF process.

The second device application explored is a high stiffness, large elastic deformation, cellular structure. These cellular contact aided compliant mechanisms (C3M), find application in aviation, as morphing technology in aircraft wings has been proven to increase flight efficiency as well as improve maneuverability. The high stiffness and high elastic strain of a material consisting of a large number of small C3M cells can facilitate morphing in aircraft structures. While large arrays of C3M devices can be meters in scale, single cells have length scales on the

millimeter scale and thickness and features on the micron scale making them suitable for fabrication with the LM-RIF process.

The LM-RIF process was originally developed by Antolino and Hayes et al to fabricate mesoscale components. In this dissertation the focus is on advancements in the process and underlying science. The presented advancements to the LM-RIF process include an augmented lithography procedure, the incorporation of engineered aqueous and non-aqueous colloidal suspensions, an assessment of constrained drying forces during LM-RIF processing, mechanical property evaluation, and finally prototype testing and validation. Specifically, the molding procedure within the LM-RIF process is capable of producing molds with thickness upwards of 1mm, as well as multi-layering to create three dimensional structures. Increasing the mold thickness leads to an increase in the smallest feature resolvable; however, the increase in mold thickness and three dimensional capability has expanded the mechanical design space.

Tetragonally stabilized zirconia (3Y-TZP) is an ideal material for mesoscale instruments, as it is biocompatible, exhibits high strength, and is chemically stable. In this work, aqueous colloidal suspensions were formulated with two new gel-binder systems, increasing final NOTES instrument yield from 0% to upwards of 40% in the best case scenario. The effects of the gel-binder system on the rheological behavior of the suspension along with the thermal characteristics of the gel-binder system were characterized. Finally, mechanical properties of ceramic specimens were obtained via 3-point bend testing.

One of the main yield limiting steps in mesoscale instrument fabrication via the LM-RIF process is cracking during drying. New one dimensional and three dimensional drying models were developed for the system. Within the analysis, drying time, drying stress, and constrained drying stress are calculated and a comparison is made between the geometric design and the state of constrained drying stress. NOTES instruments with a filleted connection between segments

show a higher final yield and a lower constrained drying stress than those with angular segment joints.

Another candidate material for NOTES devices as well as C3M devices is 300 series stainless steel (300 series stainless steel). 300 series stainless steel is a common biocompatible material; it is used in surgical applications, exhibits a high corrosion resistance, and has high strength to failure. New, high solids loading, non-aqueous colloidal suspensions of 300 series stainless steel were formulated and incorporated into the LM-RIF process. The rheological behavior and thermal characteristics of the non-aqueous colloidal suspensions were analyzed and engineered to operate within the LM-RIF process. Final part yield with the non-aqueous colloidal suspensions was higher than that of the aqueous ceramic suspensions. Mechanical properties of 300 series stainless steel specimens were determined via 3-point bend testing.

Furthermore, new composite non-aqueous colloidal suspensions of 3Y-TZP and 300 series stainless steel were formulated and incorporated into the LM-RIF process. The composite materials showed an increase in final part yield, and an increase in yield strength compared to pure 300 series stainless steel was determined by Vickers hardness testing. The successful incorporation of composite suspensions in the LM-RIF process was facilitated through an analysis of the rheological behavior as a function of solids loading and ceramic to metal ratio.

Optimized designs of NOTES instruments, as well as C3M devices were manufactured using the LM-RIF process with the non-aqueous 300 series stainless steel suspension. The performance of the prototype NOTES instruments was evaluated and compared against the theoretically predicted performance results, showing good agreement. Similarly, good agreement was seen between the stress-displacement behavior of prototype C3M devices when compared to the theoretically calculated stress-displacement results. Finally, in a comparison by endoscopic surgeons at Hershey Medical Center between an existing industry standard endoscopic device and

the mesoscale instrument prototypes fabricated via the LM-RIF process, the prototype design performed favorably in almost all categories.

In this dissertation, advancements to the LM-RIF process are presented outlining an improved meso-scale fabrication process capable of producing large arrays of millimeter scale parts with micron scale resolution. The formulation of new aqueous binder systems and non-aqueous binder systems was completed for the 3Y-TZP and 300 series stainless steel material systems, respectively. A theoretical analysis of constrained drying within the LM-RIF was completed with results influencing the topology of the devices being fabricated. Finally, prototype NOTES instruments and C3M devices were tested and showed good agreement when compared with theoretical performance calculations.

TABLE OF CONTENTS

List of Figures	x
List of Tables	xxiv
Acknowledgments.....	xxvi
Chapter 1 Overview	1
Natural Orifice Translumenal Endoscopic Surgical Instrument Tool Tip	2
Cellular Contact-Aided Compliant Mechanisms	3
Classification of Materials Incorporated into the LM-RIF	3
Thesis Objective.....	4
Chapter Summaries	5
Chapter 2. Background and Literature Review	5
Chapter 3. The Lost Mold-Rapid Infiltration Forming Process	6
Chapter 4. Constrained Drying for the LM-RIF Process	7
Chapter 5. Non-Aqueous Processing of Metal Materials via the LM-RIF Process.....	8
Chapter 6: Conclusions and Future Work	9
Appendices	10
(A) Aqueous Colloidal Processing for the LM-RIF Process.....	10
(B) Multilayer Topology Optimization for the LM-RIF Process.....	10
(C) Drying Model Programs	10
(D) Non-aqueous Zirconia and Stainless Steel Composite Colloidal Suspensions	10
(E) Nomenclature	10
References	11
Chapter 2 Background and Literature Review.....	13
Natural Orifice Translumenal Endoscopic Surgical Instrument Tool Tip	13
Cellular Contact-Aided Compliant Mechanisms	17
Mesoscale Fabrication Methods.....	21
Design of Experiments.....	28
Constrained Drying Theory of Aqueous Ceramics applied to the LM-RIF Process.....	28
References	31
Chapter 3 The Lost Mold-Rapid Infiltration Forming Process.....	38
Process Overview.....	38
Mask Design and Fabrication.....	44
Mold Fabrication in Two and Three Dimensions	45
Colloidal Suspension Preparation	51

Colloidal Processing of Yttria Tetragonal Polycrystalline Zirconia	53
316L Stainless Steel	55
Mold Infiltration and Sintering to Form Final Components	55
Yttria Partially-Stabilized Tetragonal Zirconia	55
316L Stainless Steel	57
Conclusion	60
References	61
Chapter 4 Constrained Drying for the LM-RIF Process	63
Introduction	63
One dimensional model	68
Three Dimensional Model	70
Model Calibration	75
Forceps Test Case	79
Conclusions	82
References	83
Chapter 5 Non-Aqueous Processing of Metal Materials via the LM-RIF Process	85
Introduction	85
Application 1: NOTES Surgical Forceps	87
Application 2: High Stiffness-High Elastic Strain C3M device	88
Colloidal Processing	89
Rheology	94
State of Dispersion	95
LM-RIF processing, casting and sintering parameters	100
Chemical Analysis	105
Mechanical Property Evaluation of 300 series stainless steel Specimens	108
Prototype Testing	110
Forceps Validation at Penn State's Hershey Medical Center	112
Conclusion	119
References	119
Chapter 6 Conclusions and Future Work	123
Conclusions	124
Future Work	127
Three dimensional part design	128
Curved segmented C3M devices	129
Incorporation of critical point drying into the LM-RIF process	132
Constrained Drying Modeling and Stresses	134
Multi-Material Components and Mechanical Testing	135
References	142
Appendix A Aqueous Colloidal Processing for the LM-RIF Process	143
LM-RIF Processing	152
Colloidal Suspension Properties	153

Rheology	157
Green strength	158
Thermal Analysis	159
Conclusion	165
References	165
Appendix B Multilayer Topology Optimization for the LM-RIF Process.....	169
Introduction.....	169
Problem Statement	171
3D Compliance Minimization.....	172
Formulation	172
Results and Validation	175
3D Compliant Mechanism Design	176
Objectives.....	176
Formulation	178
Design Space.....	179
Results and Validation	180
Application to Forceps Design and Results	180
Boundary Conditions.....	180
Results	181
Conclusions and Recommendations	183
References	184
Matlab Scripts	185
Mathematica® Code to Calculate Stiffness Matrix	189
Appendix C Drying Model Programs	192
1 Dimensional Drying Model in Matlab®	192
3 Dimensional Constrained Drying Model in Comsol Multiphysics® v3.5a	195
Appendix D Non-aqueous Zirconia and Stainless Steel Composite Colloidal Suspensions ...	240
Introduction.....	240
Rheological Properties of Composite Suspensions	243
State of Dispersion of Composite Suspensions.....	248
Conclusion	255
References	256
Appendix E Nomenclature.....	258
References	260
Appendix F Design of Experiments.....	261
References	265

LIST OF FIGURES

- Figure 2.1. Overview of NOTES technique, where surgeries are performed without external incisions. The tool tip designed and fabricated herein would be inserted through the endoscope and remotely manipulated by the surgeon through the handle of the endoscope[5]. 14
- Figure 2.2. Left, two endoscopes are shown side by side, an endoscopic instrument is inserted near the handle of one of the endoscopes. Center, the working end of an endoscope, showing one working channel with an example endoscopic instrument inserted through the channel. Right, an internal surgery is depicted utilizing an endoscope with inserted instrument. The endoscope has perforated the stomach and is inside the internal body cavity permitting access to organs such as the appendix, long and short intestine, gall bladder, liver, spleen, and pancreas [7-9]. 15
- Figure 2.3. Mesoscale forceps designed by Aguirre et al. that was fabricated with the LM-RIF process described herein [10]. The forceps arms are actuated in a grasping motion controlled by the sliding of the outer sheath over the arms to close or open the forceps tip with sheath extension or retraction, respectively. 16
- Figure 2.4. The tradeoff between high stiffness and high elastic strain materials is shown. The region of interest for high stiffness - high strength materials is highlighted in yellow. Cellular structures are one method to achieve materials that occupy the relatively unexplored yellow region of interest [12]. We aim to create a new class of materials and devices in the yellow region through a combination of material processing science and material design..... 18
- Figure 2.5. Top, A three by four cellular array C3M device with contact aided deformation mechanisms is presented., Bottom, the designed undeformed cellular shape of the unit cell vs. the deformed shape, with the contact mechanism active, is shown. These C3M devices are designed to maximize global strain; which is noted as strain in the x-direction [14]. 20
- Figure 2.6. Hierarchy of fabrication techniques used in large array meso-scale manufacturing. Only the LM-RIF process is capable of large array fabrication of 3D parts with high aspect ratios and small feature resolution, using multiple materials. 27
- Figure 2.7. The three stages of drying are shown, the point of maximum drying induced stress is highlighted at the end of the constant drying rate period and is the critical drying point. Stage 1 is the constant rate drying period, where evaporation is taking place from the surface. In Stage 2, the falling rate period, drying stress is reducing, but there may be residual stress and deformation from Stage 1. In stage 3, the end of the falling rate period, where equilibrium is reached with the surrounding atmosphere. 29
- Figure 3.1. The feature size versus part size comparison are presented for various types of fabrication approaches; focused ion beam and fast atom beam (FIB and FAB), wire electrical discharge machining (Wire EDM), and computer numerical control ultra

precision machining (CNC UPM). The lost mold-rapid infiltration forming (LM-RIF) process fills a gap in manufacturing size regime above semiconductor fabrication sizes in the sub-10 micron range, and below traditional bulk machining near 300 micron features while adding the ability to simultaneously manufacture large arrays of parts. Furthermore, LM-RIF can be integrated with novel design approaches to create innovative structural components for a variety of applications including surgical instruments.40

Figure 3.2. The LM-RIF chart. The process starts with a theoretically optimized mechanical design based on initial determination of mechanical properties, followed by mold fabrication, colloidal processing, and final part fabrication. Final parts are tested and characterized, with the mechanical properties used to design changes in the design and fabrication for future generations of materials and/or design components. Changes in the design geometry of the part are completed through the Design Feedback loop, while changes to the manufacturing process and material system are completed through the Fabrication Feedback loop.42

Figure 3.3. The fabrication, design and testing relationships are shown for manufacturing surgical instrument prototypes. In each of the sections, metal 300 series powder and prototypes are shown on the left, with 3YTZP prototypes shown on the right. In FEA Design, optimized instruments are designed with known strength values from mechanical testing. In the Fabrication Process, the LM-RIF process is employed and colloidal chemistry is used to concentrate and disperse particulates of 300 series steel and 3YTZP. The concentrated suspensions are cast into lithography based molds and sintered. Once sintered, free-standing parts are ready for mechanical testing. At this stage, characterization of the prototypes takes place, and changes to the colloidal suspensions can be made through the fabrication feedback loop. Testing of the as fabricated material takes place using appropriate mechanical tests (ceramics in 3-point bending and metallic parts with tensile tests). As this process is iterative, processing improvements that lead to strength variations are fed back into the design, where new topologies can be generated.....43

Figure 3.4. Two examples of photolithographic mask layouts are shown: Left, surgical forceps, and bend bars; Right, other geometric shapes and C3M devices are depicted. On the left hand side there are about 600 parts. On the right hand side there are almost 50 C3M parts. Ceramic, metal or particulate composites for LM-RIF can be used to make components from masks such as those illustrated.45

Figure 3.5. A summary of innovations for LM-RIF in the mold fabrication. (A) lithography stack, with mold fabrication directly on the refractory substrate. Without the UV filter, trapezoidal cross-sections (i.e., non-orthogonal side walls, are present in the mold cavity. (B) the mold fabrication process is shown, starting with the computer aided design (CAD) that dictates the mask layout, and finally being patterned as the mold shown in the optical photomicrographs. (C) A mold cross section is shown in the SEM photomicrograph highlighting the various channel widths possible for the 250 μm resist thickness.....47

Figure 3.6. The minimum feature resolution increases with increasing photoresist thickness, as calculated by Yang et al. [9]. The UV light source has a wavelength of

- 400 nm, and the contact gap between the photoresist and the mask is assumed to be $5\mu\text{m}$ for our process. The minimum feature resolution is then calculated with the inset equation.47
- Figure 3.7. Top: Three methods to create 3D multilayer components by the LM-RIF process are shown based on the recent discussion by del Campo [8]. In Method A, molds are laminated before infiltration. Method B, molds are infiltrated prior to filling. Method C, the mold is infiltration as the layers are added. Bottom: An SEM photomicrograph of two laminated layers of photoresist molds using Method A is shown from the top view. The layer of photoresist patterned with square cavities was laminated over an array of triangular molds patterned into the bottom layer of photoresist. Negligible distortion is present in the photoresist patterns for the top and bottom layers and uniform adhesion was observed across the two layers laminated on the substrate.50
- Figure 3.8. Powder processing steps are related to every aspect in the LM-RIF process, including mechanical design, mechanical properties, processing parameters, and particulate properties. While working to improve the LM-RIF process, all powder processing attributes must be considered as part of the overall system, and not separately. Arrows indicate the dependence of each processing step on one another. ...53
- Figure 3.9. Uniform top surfaces for LM-RIF parts are produced by a planarization process. Top: Molds are infiltrated via a screen printer squeegee. Once infiltrated, parts are allowed to gel in a 100% humidity environment, and then dried in ambient conditions. Alternately, we have recently explored critical point drying with part yields exceeding 90 percent. Bottom: After sintering in ambient, air atmosphere, the final part is left free standing on the original substrate [3, 4].57
- Figure 3.10. Similar to ceramic fabrication, all processing takes place on the refractory substrate. Top (from left), SU-8 molds are infiltrated with the metal slurry leaving a thin layer on top of the molds. The thin overburden layer is removed via the planarization process following drying in ambient conditions. Bottom (from left), the molded parts are subjected to two furnace treatments, an initial processing step in air removes organic additives including the binder system and mold material. Part sintering takes place in a reducing atmosphere of 5 mol percent hydrogen in nitrogen known as forming gas. Final parts are free standing on the original substrate.58
- Figure 3.11. Example forceps parts are shown as fabricated with the LM-RIF process. The mesoscale parts have a size scale on the order of mm and critical dimensions on the order of microns. Top: An SEM image of a ceramic forceps is shown, while Bottom: an optical image of metallic forceps is shown.60
- Figure 4.1. The mold used in the LM-RIF process is shown in yellow, while the green ceramic body is shown in white. A: The standard method of drying ceramics is to first demold the part, afterwards allowing the part to dry, where it can shrink freely in all dimensions. B: Within the LM-RIF process, forceps parts are required to dry while still in the mold, leading to constrained drying, where the part cannot freely shrink. In this case, stresses arise not only from drying, but also from the interaction

of the part with the mold during shrinking. The aspect ratio of the forceps is defined as L/W65

Figure 4.2. An optical image of a sintered, cracked forceps made with the LM-RIF process. In this case, the forceps developed cracks during drying, and was therefore broken upon sintering. Quantifying the stresses experienced by the part during drying will allow engineers to minimize drying forces. Arrows highlight a few of the fracture sites due to drying stresses.....65

Figure 4.3. Top: The yield of fired parts is given as a function of forceps shape and forceps aspect ratio. As the aspect ratio increases from left right, going from 1:10 to 1:40, the yield of parts that have survived through the drying stage and the sintering stage significantly decreases. Constrained drying stresses in the LM-RIF process lead to drying cracks. Bottom: the shrinkage of dried forceps arms is shown for two different forceps shapes. The straight walled forceps with gripping teeth is the most constrained geometrically, and therefore shows the smallest shrinkage during drying. The smaller the drying shrinkage for a given part leads to increased internal constrained drying stresses, thus decreasing the yield.67

Figure 4.4. Normalized moisture mass versus time is shown, as calculated from the 1D model applied to the forceps drying problem for a thickness of $400\mu\text{m}$. The transition from the constant drying rate period to the decreasing drying rate period takes place at approximately 0.1 hours (360s), indicating the time at which the maximum drying stress will occur. Furthermore, equilibrium with the surrounding atmosphere occurs at approximately 0.6 hours (2200s).70

Figure 4.5. The system of partial differential equations is applied, within COMSOL, to a specific domain, such as the one shown. By defining internal moisture potential (μ_n), temperature (T), external moisture potential (μ_a), and boundary conditions, accurate predictions of drying processes can be made through the determination of the μ^1 , as it ranges from initial to external moisture potential.75

Figure 4.6. A schematic diagram of cylindrical samples used to verify the one dimensional and three dimensional drying models. Only the top face was exposed to external drying conditions, rendering both one and three dimensional drying models relevant.....76

Figure 4.7. The normalized moisture mass as a function of time is plotted for the experimental cylindrical sample. In addition, the one dimensional and three dimensional drying models were used to describe the one sided drying process of the cylindrical test sample. Good agreement can be seen between the drying trends of both models and the experimental data. In the case of the three dimensional model, the internal and external moisture potential parameters were varied in order to get the fit shown above. These parameters were then carried forward in the predictions of stresses within forceps domain geometries.....78

Figure 4.8. Internal moisture potential is plotted at four separate times during the drying process. The moisture potential decreases from the initial value of 160, to the external moisture potential of 15. At $t=300$ seconds, the first stage of drying is

- apparent, as the moisture potential has no gradient through the thickness of the part, and drying is occurring at the surface. As drying continues, the drying front moves into the sample, and finally, equilibrium with the surrounding atmosphere occurs after 15 hours.79
- Figure 4.9. The drying stress is depicted for the curved and straight forceps designs. The order of magnitude of the drying stress is similar for both designs. Additionally, the large drying stress located at the base of the forceps is artificial, and stems from the mechanical boundary conditions defined within COMSOL. The stress is shown for a time of 360 seconds, corresponding to the end of the constant drying rate period (see Figure 4.7), and also the maximum state of drying stress. The curved forceps arms experience an order of magnitude less constrained drying stress than the straight forceps arms.80
- Figure 4.10. The constrained drying stress is depicted for the curved and straight forceps designs. The state of stress experienced by the curved forceps shape is an order of magnitude less than that of the straight forceps. Therefore, the shape of the part being manufactured with the LM-RIF process greatly affects the constrained drying stress, thereby affecting the final part yield. Also, the large drying stress located at the base of the forceps is artificial, and stems from the mechanical boundary conditions defined within COMSOL. The stress is shown for a time of 360 seconds, corresponding to the end of the constant drying rate period, and also the maximum state of drying stress.....82
- Figure 5.1. The design of the NOTES forceps/cutting surgical instrument to be fabricated with the LM-RIF process is shown. A description of the forceps is given in Chapter 1. The forceps is shown in the closed state with the sheath fully extended to close the distal end of the surgical forceps instrument.....88
- Figure 5.2. There is a region of interest for new materials properties with high stiffness and large elastic strain shown in grey. New material designs aim to shift the current maximum elastic strains to higher values, as indicated by red arrow. A C3M unit cell is shown on the right hand side, for Left: the undeformed unit cell, and Right: the fully elastically deformed cell. The Young's modulus for stainless steel and YTZP (containing 3 mole percent yttria) is 200 GPa. The predicted C3M device strains are 12 to 15%. In contrast, typical pure elastic strain in high stiffness materials is approximately 0.2%. Thus, high elastic strain devices can be produced by optimized design of relatively inelastic materials [12, 13].89
- Figure 5.3. The formulation flow chart of non-aqueous colloidal suspensions is shown. The order of addition is shown in the upper left corner of the component boxes. The attrition mill is kept at 10°C and sealed to limit evaporation of any solvent during milling. A typical formulation sheet is shown in Figure 5.4.....90
- Figure 5.4. A typical formulation sheet is shown, calculating the constituent amounts of a final 300 series stainless steel colloidal suspension in Microsoft Excel©. The desired final suspension volume, as well as the solids loading in vol% and dispersant/binder in wt% of the dry powder are input into the blue cells. Using Excel©, calculations of the relative amount of solvent, dispersant, and powder are

carried out. Confirmation of the performed calculation is shown in green. This tracking sheet serves as an easy way to vary and document suspension parameters.92

Figure 5.5. Top: particle size, measured using the sedimentation approach with a commercial particle size analyzer (Horiba CAPA 700, Irvine, CA), is shown for the as received powder, and the milled powder after 1 and 20 hours of milling. A decrease in the recorded size is evident; however, this is expected due to the change in particle shape from spherical to platelet-like. Bottom: Scanning electron micrographs of the as received and milled powder for 1 hour and 20 hours is shown. The change in particle shape from spherical to platelet-like is evident. No major agglomeration, or cold welding occurred during the milling process. Furthermore, the oleic acid dispersant is bound to the surface of the particles, and does appear to have formed segregated agglomerates of organic material.93

Figure 5.6. The viscosity and shear stress vs shear rate is shown for a 60 vol% 300 series stainless steel suspension in ethanol with oleic acid at 5wt% of the powder as the dispersant. At high shear, the viscosity of 2.1 Pa.s is able to be cast into the molds, while the Bingham yield point of 117 Pa is also able to be overcome in the LM-RIF processing. The method for determining Bingham yield point, and high shear viscosity is indicated by the black dashed arrows.95

Figure 5.7. Oleic acid, depicted here by ACDLabs Chems sketch, is approximately 2nm long, bonding to the surface of the metal particle via the carboxylic acid head group shown on the right hand side. The bond angle of the oleic acid with the particle surface is assumed to be 45°, yielding a final steric barrier of 1.4nm.99

Figure 5.8. The calculated interaction energy for two 300 series stainless steel particles in ethanol is shown. There is a very large minimum energy well at 50 nm separation distance, due to the low dielectric constant of ethanol and large particle size. There is also a steric barrier of 1.4 nm at 50 of separation distance due to the surface roughness of the particles and the steric repulsion of the oleic acid on the surface of the particles. Table 5.3 lists the parameters used in the calculation. 100

Figure 5.9. Left: Scanning electron micrograph of a cross sectional sample of the sintered 300 series stainless steel material. While minor porosity is present, no major bubbles can be found. Right: An optical micrograph of the same sample is shown. While there is an interconnected metallic phase, there is also a secondary material present at the original particle boundaries. 102

Figure 5.10. Using ImageJ [30] area analysis, there is 5.5% porosity in the sample after the sintering process. The remaining 94.5% is not fully 300 series stainless steel due to inclusions of another phase located at the original particle boundaries prior to sintering. Left: The second phase material can be seen as small light gray particles, as opposed to the larger dark pores. Right: ImageJ area analysis shows the locations of the large porosity in the cross section sample. 102

Figure 5.11. AES count rate vs kinetic energy scans are shown for the polished cross sectional sample. The bulk metal material consists of iron, chromium, and nickel, which is consistent with stainless steel, while the secondary phase inclusions are of

- two types. Type one, includes oxygen, manganese, carbon, and silicon, indicative of the polished preparation, while type two consists of chromium, oxygen, and manganese, indicative of a chromium rich second phase. Although there is chromium rich second phase, there is still chromium present in the main metal matrix. 105
- Figure 5.12. A full chemical analysis of the metallic parts was completed for all four stages of processing including the as received powder, post attrition milling, post organic burnout, and post sintering. Top: The full spectrum of elements investigated are shown, including high chromium and nickel content, indicative of 300 series stainless steel. Bottom: a restricted view is shown up to 2.5 at% to more clearly illustrate the lower at% elements. 107
- Figure 5.13. An optical image of a sample 3-point bend specimen (300x400x5000 μ m) is shown undergoing ductile fracture. The test specimens were fabricated using the LM-RIF process. Mechanical testing was carried out in collaboration with Professor Muhlstein, at The Pennsylvania State University. 109
- Figure 5.14. A fabricated forceps with the LM-RIF process is depicted using optical microscopy. See also Figure 3.1 for a schematic of the forceps instrument. Top: an optical image of as fabricated forceps with aspect ratio of 1:40. Bottom left: assembled forceps device in the open position, showing a total jaw opening of 1.3mm. The retracting and extending sheath composed of glass, for demonstration, can be seen in the bottom right in the optical image. Bottom right: the assembled forceps in the closed position, showing the grasping function and the fully extended sheath closing the instrument tips. 111
- Figure 5.15. The tip location of an actuated forceps is plotted as a function of sheath location. Good agreement is seen between the Finite Element Analysis (FEA) theoretically calculated tip location, and experimentally (EXP) observed tip location. The observed tip location was measured in real time via photos captured with a digital camera (Pixelink, Inc.). A larger tip location corresponds to the forceps closing. Figure courtesy of Aguirre et al. [33]. 112
- Figure 5.16. Prototype forceps assembled into a NOTES device for hospital testing. An inset is shown highlighting that the microstructure of the prototype device is similar to the previously analyzed microstructure. The forceps device, after being spot welded to an actuation cable, is connected to a handle, shown in blue. With this handle, surgeons are able to actuate the sheath, opening and closing the forceps. The entire forceps and actuation wire are meant to work within an endoscope, as described in Chapter 2 [33]. 113
- Figure 5.17. The prototype forceps was tested against an industry standard instrument in a variety of real-life simulations shown in both the Top and Bottom comparisons. Endoscopic surgeons ranked the performance of the prototype forceps against the standard instrument for all tests completed. The forceps instrument performed as well as, or better than, the standard instrument in almost all of the tasks at hand. This validates the LM-RIF process as an important step in designing and fabricating devices on size scales that were previously unattainable [34]. The ability of the LM-

- RIF to allow design engineers to re-engineer the opening and closing mechanism of the forceps, allowing more precise gripping control, facilitated the preference of the prototype instrument over the standard instrument..... 115
- Figure 5.18. Prototype C3M arrays consisting of 9 unit cells each are shown in the optical image. A U.S. dime is included for perspective. These devices, fabricated with the LM-RIF process are over 2 centimeters in width, 400 μ m in thickness, and have features as small as 50 microns in the contact mechanism [13, 35]. The contact mechanism can be seen in the right hand figure, where the dash pot mechanism contacts itself in as the cell deforms. 116
- Figure 5.19. A specialized test rig, shown from the top view and side view was developed to mechanically evaluate the C3M devices. The rig consists of a force gauge to monitor the force as a function of deformation. The deformation is controlled using a micrometer. Right: the sample mounting rig is able to support the C3M device, apply a load, and comply with the auxetic deformation of the cellular array [35]..... 117
- Figure 5.20. Experimentally determined force displacement data is compared to theoretically calculated data for assumed elastic moduli of 100, 110, and 150GPa. Relatively good agreement is obtained for the experimentally measured data and the theoretical data calculated with E=150GPa. The experimental data is from the digital micrometer read out, while the image processed specimen displacement data is measured through an external camera system above the test rig [35]. 118
- Figure 6.1. A computer aided design drawing of a three layer biopsy needle device is shown. This device is an ideal candidate to evaluate the mold multi-layering scenarios described in Chapter 2. In this test case, three layers are stacked on top of one another, with additional layers offset along the length of the needle, giving rise to the sequence of barbs along the side of the needle [1]..... 129
- Figure 6.2. The next generation curved wall C3M devices are compared to the original straight walled designs. The curve walled design topology shows an increase in the performance of the device in terms of global strain, and should show a decrease in the constrained drying stress experienced by the part during LM-RIF processing [2]. ... 130
- Figure 6.3. The photolithography mask layout for the curved C3M devices is depicted. More than 75 arrays of C3M devices, consisting of the curved and straight C3M designs are present on the mask. Once LM-RIF processing is carried out, mechanical testing, and evaluation of the devices will be performed..... 131
- Figure 6.4. Optical microscopy images of curved C3M unit cells are shown. In (A) and (B) the contact mechanism shows good edge resolution, along with minimal distortion. In (C) a complete unit cell is shown with a US dime for scale reference. By fabricating curved C3M devices, the adaptability of the LM-RIF process has been demonstrated. Future work includes the mechanical testing and validation of the curved designs. 132

Figure 6.5. A pressure-temperature phase diagram, reproduced from Matson et al. [6] is shown, along with the description of the critical point drying process (A-D). In critical point drying, the transition from liquid to gas takes place at a temperature and pressure above the critical point of the fluid, eliminating capillary forces during drying. The process starts at point A, and with an increase in pressure and temperature moves to point B and C. In the CO₂ system, the temperature and pressure must be above 31°C and 72.8atm in order to transition into the supercritical fluid regime. Once above the critical point, the pressure is reduced (point D), and the dry part can be removed from the pressure vessel. 134

Figure 6.6. The schematic representation of a hybrid material forceps instrument is shown. In this device, in a single lithography layer, a flexible material would be located on one side of the instrument, while a stiff material would be bonded to that material in plane, and located on the other side of the device. This hybrid design requires that the two materials are able to successfully bonded together, as well as additional lithography and casting processes to successfully fill a mold cavity with two different colloidal suspensions [11]. 136

Figure 6.7. Starting from the top left, and proceeding row by row, the process presented to fabricate hybrid devices is as follows. 1) Fabricate SU8 mold on refractory substrate utilizing mask A, as described in Chapter 2. 2) Fill the entire mold cavity with the positive photoresist place holder. 3) Expose desired regions of positive photoresist through mask B. 4) Develop away the treated positive photoresist. At this point, an SU8 mold is partially empty and partially filled with positive photoresist. 5) Cast material 1 into the empty cavities in the SU8 mold. 6) Dissolve the positive photoresist, opening the rest of the original SU8 mold cavity. 7) Cast material 2 into the open areas in the SU8 mold. 8) A burnout process will be needed to remove the mold and any binder present. 9) The final hybrid material device will be left on the refractory substrate. 138

Figure 6.8. (A) The designed photomask for fabricating hybrid material components as well as mechanical property test structures within the LM-RIF process is shown. The top half of the photomask is dedicated to the fabrication of hybrid forceps designs, while the bottom half of the mask is dedicated to mechanical test specimens for standard tensile testing, as well as theta geometry tensile test specimens. Details of the mechanical testing structures are given in Figure 6.9. In (B) and (C) the photomask layout is shown in detail for the hybrid material instruments. The first lithography step is performed with the entire design (mask A, shown in black), while the second lithography step is performed with the partial design (mask B, shown in red). The final hybrid design is shown in (C), where the intersection between the black and red designs corresponds to the intersection between the two materials in the hybrid forceps. The mask layout was developed in collaboration with Brian Babcox. 140

Figure 6.9. Tensile and theta mechanical test specimen to be used for evaluation of the material properties. The specimen are indicated in black. Top, a tensile test specimen is shown. Prior to testing, the four corners of the test specimen will be cut, leaving just the tensile specimen present in the test rig. The reason for having the surrounding material prior to testing is to provide support for the small and then

sample, during sample loading. Bottom, theta tensile test specimens are utilized to test tensile strength while using a compressive force. This geometry facilitates tensile testing of small, delicate samples. Multiple theta specimens can be tested in succession.....	141
Figure A.1. To successfully fabricate intricate parts using the LM-RIF process, such as the forceps arm shown here, green bodies have to be formed that do not undergo a dimensional change during processing. Therefore, new binder systems were developed to work within the LM-RIF process.	144
Figure A.2. The magnitude of the scale up process is demonstrated, as previously fabricated bend bars were 300 μ m in length, the forceps designs were 300 μ m in cross sectional width. This scale up led to many challenges, including mold fabrication, and green body formation.	145
Figure A.3. Unlike traditional forming techniques, where the cast green part can be removed from the mold prior to drying (left), the LM-RIF process requires that the green part stay molded throughout the drying process (right), leading to stresses that occur when the part starts to shrink.....	146
Figure A.4. A: Catastrophic failure of forceps due to drying cracking is shown as the starting point, and the need for improved processing, B: Fractured forceps due to drying cracking but with additional binder and gel present, C: Intact forceps fabricated with ideal binder and gel levels as per DOE experimentation, and D: microstructure of the forceps shown in C.	148
Figure A.5. The process flow diagram is shown for Binder system 1. The order of addition of components is given by the numbers in the top left corner of the gray boxes, noting that polymer binder is the final addition.....	151
Figure A.6. The process flow diagram is shown for Binder system 2. The order of addition of components is given by the numbers in the top left corner of the gray boxes, noting that polymer binder is the final addition.....	152
Figure A.7. The electric interaction of a particle with an ionic solvent is shown for a electro-positive particle. Positive and negative ions in solution are represented with a (+) and (-), respectively. The measured ζ -potential, or electric potential at the intersection of the Stern layer and diffuse layer, is labeled in the bottom right. ζ -potential is a key parameter in calculating the interaction energy barriers between particles in suspension. This figure was re-created from Adair et al. [30].....	154
Figure A.8. The total interaction energy curve for the 3Y-TZP particles is shown as a function of distance. Electrosteric dispersion creates a high barrier energy to agglomeration around 6nm separation distance, while a steric barrier prevents the particles from approaching the primary minimum at a separation distance of zero. This theoretical curve is determined using the parameters appropriate to the LM-RIF process.....	156

- Figure A.9. The shear stress and viscosity is plotted against shear rate for both Binder system 1 and Binder system 2. For Binder system 1, the high shear viscosity and Bingham yield point are 15Pa.s and 600 Pa, respectively. For Binder system 2, the high shear viscosity and Bingham yield point are 4.3 Pa.s and 186 Pa, respectively. 158
- Figure A.10. Thermogravimetric analysis of Binder systems 1 and 2 and the mold material SU8 are compared. All show complete removal by 600°C, however, the binder systems undergo combustion prior to the mold material, indicating that the binder systems only provide support to the green part during the drying process. 160
- Figure A.11. Differential scanning calorimetry indicates that there is no real glass transition temperature in Binder systems 1 and 2 in the temperature range of interest. As these binder systems are in the presence of chemically initiated gelled matrix, it is not expected that there would be a glass transition temperature. 161
- Figure A.12. Final sintered parts using Binder system 1 with complex geometries that underwent constrained drying during processing. A: a splined forceps design with aspect ratio 1:40. B: a splined forceps design with aspect ratio of 1:20. C: closed porosity exists in the microstructure, limiting strength and decreasing reliability. D and E show an annulus and a gear to demonstrate the range of geometries possible with the LM-RIF process. 162
- Figure A.13. Left: three forceps designs are shown with an aspect ratio of 1:20. Right: the differences of the three forceps designs are highlighted: straight linkage with gripping teeth, straight linkage without gripping teeth, and splined linkage without gripping teeth. 163
- Figure A.14. Sintered part yield is shown as a function of aspect ratio (1:10, 20, 30, 40) for the various forceps designs; straight linkage with gripping teeth, straight linkage without gripping teeth, and splined (curved) linkage without gripping teeth. 163
- Figure B.1. One arm of a forceps design is shown with parameters length (L), width (w), instrument opening (δ_{hop}), arm separation (δ_{hs}) and angled tip distance (H3) labeled. This arm is made from a monolithic material, currently having a constant thickness throughout. 170
- Figure B.2. An example of a 3 layer cantilever beam is shown, with each layer having a thickness of t and the loads P1 and P2, for demonstration are placed at the right end of the beam. While the thickness of each of the layers is constant within each layer, the width and length of the layers are allowed to vary. 171
- Figure B.3. The updating scheme for the stiffness matrix is depicted along with node numbering, from 2D to 3D, with details shown in the accompanying Matlab code. 173
- Figure B.4. The problem statement is given for the 3D compliance minimization formulation. Where x is the vector of design variables with x_{min} being the minimum relative density, U, F, and K are the global displacement, force, and stiffness matrices, V(x) and V0 are the material volume and design domain volume, and f is the allowed volume fraction. 175

- Figure B.5. Top: Design space for the 3D cantilever beam problem; the left side of the design space is fixed (clamped), and loads P1 and P2 are applied downward on the right side. Additionally, the design space is discretized into 3 layers with the layer 1 comprising the front shaded face of the design space, layer 2 being in the center of the design space, and layer 3 at the far side, comprising load P2. Middle: Resulting topologies of each individual layer are shown. As load P1 and P2 are applied to layer 1 and layer 3 respectively, layer 2 does not directly interact with the applied loads. Therefore some areas of layer 2 can be excluded from the final design through the density filter. Bottom: the assembled 3D final truss structure with 3 layers is shown. 176
- Figure B.6. An example of a design space used for compliant mechanism topology optimization is shown. Within the design space, input forces, output forces, boundary conditions, and number of elements in each direction can be prescribed. 177
- Figure B.7. The design space used in the validation of the final code using the inverter problem is shown. This test problem works well, as the solution to the inverter problem is well understood [5]. 179
- Figure B.8. Optimization results for the topology of a force inverter are shown as function of 3 layers. These results match the well known results for the force inverter problem. 180
- Figure B.9. Design space of one of a forceps arms is shown. Input forces, shown in red, were applied at the top of the space, and could be in one of two directions. Output forces, shown in green, were the desired responses of the input forces. The output forces and directions were required for appropriate forceps articulation. 181
- Figure B.10. Final convergence occurred after roughly 45 iterations, and 9 hours. 182
- Figure B.11. Final forceps design is shown as a function of the 3 layers. Layer 1 corresponds to the front shaded face of the design space. Layer 2 comprises the input and output forces, and layer 3 corresponds to the face opposite the gray shaded face of the design space. Stacking layer 1, 2, and 3 to form the final complete topology would create one forceps arm. 183
- Figure D.1. The formulation process for homogeneous composites of 300 series stainless steel and 3Y-TZP is shown. Both material systems are in the same solvent, while having different dispersants present. The final composition of the composite suspension can be tailored through controlling the volume of 3Y-TZP suspension added to the 300 series stainless steel suspension. The order of addition of components is labeled in the upper left corner of each component. 243
- Figure D.2. Left: Top: Composite mixtures of 1:1 volume ratio of stainless steel to zirconia in a suspension of ethanol and xylenes, at a ratio of 1:1, show an exponential increase in the average apparent viscosity as a function of volume % solid, and fit by the Dougherty-Krieger relationship. The maximum packing vol% is 0.72, almost the theoretical limit of hard sphere packing. The platelet like shape of the 300 series stainless steel particles in the system, as well as the addition of

smaller 3Y-TZP particles is the reason for this high maximum packing fraction. Bottom: A spherical comparison was carried out by fixing the maximum packing fraction at 0.65 and plotting in comparison to the Top best fit curve, the deviation of the measured viscosity increase from the spherical Dougherty-Krieger model can be seen as the shift between the red black curves. Error bars given are for 95% confidence interval, while standard error is used for the parameters in the best fit line. Right. The relative orientation of the platelet particles leads to a higher packing density than that possible with spherical particles [12]......246

Figure D.3. Top: The apparent viscosity of a composite suspension with 40 volume % solids loading and varying volume ratios of stainless steel to zirconia particles is shown. As the zirconia content increases (moving from right to left in the figure) in the composite suspension, the average apparent viscosity also increases. It is expected that viscosity will decrease with the addition of a second particle size distribution in the system, as smaller particles are seen as an additional “fluid” to the larger particles [11] , with a minimum occurring around 65vol% large particles, and constant total solids loading [11]. Error bars given are for 95% confidence interval. Bottom: the data is fit with a trend line that highlights the affects of adding large particles to the small particle suspension. Further rheological experimentation can provide the information needed to model the system, as described by Farris et al. [11]......247

Figure D.4. The interaction energy curves as a function of particle separation distance are given for the three possible interactions in the composite system. Green: a 300 series stainless steel particle interaction with another stainless steel particle. In this case, the separation distance is large due to the surface roughness of the 300 series stainless steel powder, as well as the fact that there is an assumed 3Y-TZP powder between the attracting particles, due to the fact that this is a composite. If not such particle were there, then the curve would look like the interaction energy curve in Chapter 5. Red: a 3Y-TZP to 3Y-TZP interaction shows the smallest separation distance, as well as the deepest secondary minimum energy well. Blue: a 300 series stainless steel particle interaction with a 3Y-TZP particle. The large separation distance comes from the assumed roughness of the 300 series stainless steel particle, as well as a smallest secondary minimum energy well.251

Figure D.5. Cross sectional optical microscopy images are shown for sintered composites ranging from 55.7 to 63 vol% 300 series stainless steel. As the vol% of 300 series stainless steel increases, the composite changes from having almost no interconnected metallic phase, to almost completely interconnected metallic phase. The image analysis of volume percent 300 series stainless steel measured versus calculated is shown in Table 3.8.253

Figure D.6. A polished cross sectional image of a sintered composite material with 60.6 vol% 300 series stainless steel is shown in A. In B, ImageJ software was used to identify the porosity in the sample, and quantify it at 4.5%.....254

Figure D.7. Vickers hardness results numbers are shown as a function of indentation number for composite suspensions of 100, 63, 60.5, and 56 vol% 300 series stainless steel. The composite parts have HV values very close together, at 324 ± 18 , 306 ± 15 ,

and 344 ± 13 HV for 56 vol%, 60.5vol%, and 63vol% 300 series stainless steel, however, the 100vol% 300 series stainless steel has significantly lower hardness of 208 ± 6 . An increase in hardness performance could lead to new device designs. The \pm values given are for the 95% confidence interval.255

Figure F.1. The design space of interest in the DOE study is shown as a function of binder vol% gel wt% and solids loading. Each point in the design space represents an executed experimental trial with green part yield as the output metric. The arrows indicate the initial results of the DOE trials with increasing green part yield following the directions indicated by the arrows.262

Figure F.2. The main effects of mold surface coating, immersion chemical and experiemental replication are given. Results indicate that a non wetting surface treatment should be utilized, along with an ethanol immersion drying scheme. Furthermore, operator influence on part yield is notably high with the difference between operator 1 and 2 shown in the experiment replication [1].265

LIST OF TABLES

<p>Table 2.1. Manufacturing methods for micro components are summarized in terms of smallest feature resolution, aspect ratio, multi-material system capability, and array manufacturing capability. Furthermore, the basis for the technique is used to classify the various methods in terms of lithography, injection molding, machining, printing, and laser forming. The developed LM-RIF process is listed under lithography techniques and outlined in black.....</p>	24
<p>Table 4.1. The scalar parameters are given for the 1D model used to evaluate the normalized moisture content during drying as a function of time, t</p> <p>To calculate drying stresses and shrinkage effects of complex geometries, a more realistic model was implemented, based on the initial work of Kowalski et al. [15]. In this model, drying stresses and dimensional changes are calculated as a function of time and initial conditions, yielding a more complete description of the drying system being investigated for the LM-RIF processed devices. For a comprehensive review, readers are referred to Kowalski et al. [15] to gain a complete description of the drying system equations. However, the fundamental system of partial differential equations, describing the drying body for the three dimensional model is given in Equations (4.2) to (4.5). The boundary conditions used to solve the system of equations, and the initial condition parameters are given in Equations (4.6) to (4.8) and.....</p>	69
<p>Table 4.2. The scalar parameters are given for the 3D model used to evaluate the normalized moisture content, in addition to the constrained drying stresses during drying as a function of time, t</p>	72
<p>Table 5.1. The nominal elemental composition of 316L stainless steel powder is listed in at% [2].....</p>	86
<p>Table 5.2. The parameters used in equations (5.1) to (5.3) are provided.....</p>	96
<p>Table 5.3. The parameters used to theoretically calculate the interaction energy between two 300 series stainless steel particles in suspension. The program Hamaker 2.1 was used to carry out the calculation [26].....</p>	98
<p>Table 5.4. After fired parts are mounted in an epoxy (Epoxy Bond110, Allied High Tech Products, CA), cross sectional samples were prepared with the processing steps shown below. All polishing products were provided by Allied High Tech Products and polishing was performed on a MetPrep 4 Polishing Machine (Allied High Tech Products, CA).....</p>	101
<p>Table 5.5. The parameters of the AES system are listed. A 10 minute Argon ion sputter was used to remove any oxidation to the surface of a cross sectional sample of part of a forceps device prepared via the polishing scheme described above.</p>	103

Table 5.6. The atomic percentages of the elements found in the steel parts are given as a function of the process stage. The as received store bought powder, after milling with oleic acid dispersant, after organic removal at 600°C in ambient atmosphere, and finally, after sintering at 1300°C in 5% H ₂ /N ₂	108
Table 5.7. The yield stress and ultimate tensile stress are given for four samples tested in 3-point bend. In sample 4, the test was stopped before the ultimate tensile strength could be measured due to the upper loading point pinching the test bar against the lower loading point. This problem was fixed, and the other tests were successfully completed [33]. The 95% confidence interval is given for both the yield stress and ultimate tensile stress.	110
Table 5.8. The endoscopic tool evaluation tests are listed along with their description, and the intended feature/ability tested. Data was collected via a survey given to participating surgeons after the tests were completed [34].	114
Table 6.1. The main research contributions of this dissertation are given as they correspond to the LM-RIF process. Each contribution helped to further advance the capabilities of the LM-RIF process.	126
Table A.1. The parameters used to theoretically calculate the interaction energy between two 3Y-TZP particles in solution. The program Hamaker 2.1 was used to carry out the calculation [34].	155
Table A.2. Diametral compression testing of dry green disks.	159
Table A.3. Three Point bend test strength results for Binder systems 1 and 2.	164
Table B.1. Comparison table showing which items were changed when modifying the 99 line code into 3 dimensions.	173
Table D.6.2. The parameters used to calculate the interactions energy as a function particle to particle separation distance are listed. The three cases of particle interaction are metal to metal, ceramic to ceramic, and metal to ceramic are listed.	249
Table D.6.3. The theoretically calculated volume fraction of 300 series stainless steel in the composites is compared with the measured volume percent using ImageJ [15] software. Measured volume percent of 300 series stainless steel is consistently less than the calculated target goals. One reason for this may be inherent porosity, not accounted for the in the calculated vol%.	253
Table E.6.4. The parameters and variables utilized throughout this dissertation are defined in terms of units, and the value assigned.	258
Table F.1. The results of MSFFSP are given in terms of green part yield for two replications. The largest impact on part yield is seen in the additional experimental replication. Replication 1 and 2 were completed by two different experimentalists, showing that human variation is still present within the LM-RIF.	263

ACKNOWLEDGEMENTS

First and foremost I thank Dr. James H. Adair for his confidence in me, his advice, and his support of my research and my personal progress throughout my entire dissertation. Thank you.

Secondly, I thank Dr. Mary I. Frecker. Her confidence in me, along with her advice and understanding, helped me progress into the researcher that I am today. Thank you.

Thirdly, I thank Nick Antolino for his contribution to the project, his teamwork, and his friendship. Without Nick, this project would not have been possible. Thank you.

I would also like to thank the NIH Nanoparticulate Enabled Surgical Instrument Group, and the C3M Cellular Contact-aided Compliant Mechanism Group: Drs. Adair, Frecker, Mockensturm, Muhlstein, Nembhard, and Lesieutre, and students: Milton Aguirre, Sam Cirone, Vipul Mehta, Roi Meïrom, Chumpol Yuangyai, and others. Furthermore, I would like to thank the Research Computing and Cyberinfrastructure (RCC) group, specifically Dr. Abdul Aziz and Anand Singh, for their help with modeling.

I would like to acknowledge the members of my Committee, Drs. Adair, Frecker, Mockensturm, Muhlstein, Nembhard, and Koss; each one has helped me along the way.

In addition, my friends at PSU, including Trevor Goff, Nick Antolino, Nick Dellas, Russell Maier, and Milton Aguirre have been instrumental in keeping me grounded through this process. I would also like to acknowledge the Cheese Shoppe, for supplying me with friendship and the greatest coffee. I would like to thank my parents, Joe and Leslie Hayes for giving me the support needed, self respect, and confidence to try my best and be proud of my accomplishments.

My brother and friend Doug requires acknowledgment, whose role in my life goes without comparison. Finally, I thank Lisa Hüther, for her friendship, her support, and her devotion.

The work in this manuscript is partially funded under NSF STTR 0637850, NSF 0900368, and NSF 0437214, the NSF I/UCRC Ceramic and Composite Materials Center. This work was also supported by the Pennsylvania State University Materials Research Institute Nano Fabrication Network and the National Science Foundation Cooperative Agreement No. 0335765, National Nanotechnology Infrastructure Network, with Cornell University. Any opinions, findings, and conclusions or recommendations expressed in this publication are those of the author(s) and do not necessarily reflect the views of Cornell University nor those of the National Science Foundation. The authors also gratefully acknowledge the partial support provided by grant number R21EB006488 from the National Institute of Biomedical Imaging And Bioengineering. The content in this paper is solely the responsibility of the authors and does not necessarily represent the official views of the National Institute of Biomedical Imaging And Bioengineering or the National Institutes of Health.

Chapter 1

Overview

Throughout history, the boundaries of mechanical design have been constrained by the limits of material properties. Just as the discovery of new materials propelled human innovation during the Stone, Bronze, and Steel Ages, the recent progress made in materials science likewise extends the fields of medicine and science [1]. To this end, materials' properties continue to guide design in the same fundamental way they always have. As contemporary advances in materials science broaden their applications, mechanical design engineers can dictate the desired material properties for a specific application. Now, more than ever, materials scientists and mechanical engineers must work together to design new devices from engineered materials.

As engineering applications become increasingly complex, the need for collaboration between mechanical engineering design and materials science engineering becomes increasingly apparent. Just as advance in mechanical design have motivated materials scientists to develop new materials with tailored properties, breakthroughs in materials science have, in turn, motivated mechanical engineers to design new and improve existing devices. This exchange of engineering knowledge can be found in the development of almost every present day device and component, ranging from large scale applications such as composite materials used in the automotive and aerospace industries, to small scale applications such as microelectromechanical systems (MEMS).

In this dissertation, a collaborative effort between mechanical engineering and materials science engineering is utilized to further the development of two devices: (1) a minimally invasive surgical instrument tool tip, and (2) a contact-aided compliant cellular mechanism. Throughout this work, mechanical design will influence the formulation of colloidal suspensions

and processing parameters in the materials fabrication areas, while measured material properties, along with processing yield results, and processing constraints will influence the mechanical design.

This dissertation presents a novel fabrication technique, the lost mold-rapid infiltration forming (LM-RIF) process. This development is based on the initial work of Antolino et al. [2, 3], to manufacture large arrays of meso-scale forceps (designed by Aguirre et al. [4]) and contact-aided cellular mechanisms (designed by Mehta et al. [5, 6]) by combining colloidal science with ultra thick photoresist molding methods.

Natural Orifice Translumenal Endoscopic Surgical Instrument Tool Tip

Natural orifice translumenal endoscopic surgery (NOTES) is the next revolution in surgical procedures [7, 8]. These procedures have decreased risk of infection, facilitated shorter hospital stays, and decreased cosmetic scarring when compared to their traditional surgical procedure counterparts [9]. With current NOTES procedures, instruments are manipulated and actuated via long guide wires through endoscopes inserted into the body. Due to small working channels in current endoscopes, NOTES instruments must be small, articulate, and versatile. As NOTES procedures become more complex, new instruments must be developed to expand the capabilities of surgeons. These new surgical instrument requirements are compatible with the dimensions and material capabilities of the mesoscale fabrication process developed in this dissertation.

Cellular Contact-Aided Compliant Mechanisms

Current research in aviation technology has shown that morphing technology in aircraft wings can increase flight efficiency, as well as improve maneuverability [10]. Morphing skins must be designed to have high stiffness and high elasticity. Some current morphing skin designs consist of large arrays of intricate cellular structures [5, 6]. The ability of these skins to have high stiffness as well as high elastic strain is dependent on ability to produce intricate parts out of materials with high stiffness. The meso-scale fabrication process developed in this thesis satisfies the fabrication demands for cellular structures with potential application to morphing skins.

Classification of Materials Incorporated into the LM-RIF

Within the LM-RIF process, material systems have been introduced that comply with the design requirements of surgical instruments for NOTES procedures and morphing skin designs. Stainless steel, by definition, is a steel alloy with a minimum of 10.5% chromium by mass. This biocompatible steel does not corrode or oxidize as easily as regular steel, while offering comparable mechanical properties [11]. Stainless steels are minimally affected by both air and water at ambient temperatures, especially when the chromium content is increased to 13-26%. Stainless steel resists corrosion by forming a thin layer of chromium(III) oxide on the surface that quickly forms and re-forms if the surface is scratched or damaged [11]. There are over 150 variations of stainless steel, categorized by their crystal structure. Austenitic stainless steels comprise over 70% of all stainless steels. Austenitic stainless steels have a maximum of 0.15 at% carbon and a minimum of 16 at% chromium. The low carbon content allows the material to be more ductile and easily formed [11]. Ferritic stainless steels are generally the best structurally, but are also more prone to corrosion due to the decreased chromium and nickel contents. Ferritic

steels contain other elements such as molybdenum, aluminum, or titanium. Martensitic stainless steels are strong and able to be machined, and also able to be hardened through heat treatment. Martensitic steels are magnetic, and are also more susceptible to corrosion than the other types.

Stainless steels are also classified by the American Iron and Steel Institute (AISI) grades. The 300-series by this classification contains all of the austenitic chromium-nickel alloys. Type 300 series, used in this work, is an extra-low carbon grade of type 316, which is commonly used in surgical applications. “L” grade steels denote low carbon content, with a maximum of 0.03 at% [12]. The molybdenum prevents specific kinds of corrosion that could be caused from contact with parts of the human body. The L grades can also be welded without significant loss of the corrosion resistant chromium by the precipitation of chromium carbides in the microstructure [12].

Zirconium oxide (ZrO_2) is a widely used biocompatible ceramic. Pure zirconia is in a monoclinic crystal structure and occurs regularly in nature as baddeleyite. At increasing temperatures, ZrO_2 transforms to first a tetragonal phase (~ 1275 °C) and subsequently a cubic crystal structure at ~ 1500 °C. When zirconia undergoes the phase transitions as a function of temperature, the phase transformations induce high stresses, causing cracking upon cooling. To alleviate this problem, ZrO_2 is often stabilized in its tetragonal structure with other oxides as solid solution dopants such as yttrium oxide (Y_2O_3). Zirconia, like many other ceramics, has a very high strength and toughness, but shows catastrophic failure through brittle crack propagation rather than graceful failure due to ductile mechanisms.

Thesis Objective

The objective of this dissertation is to develop a new meso-scale fabrication process that is compatible with particulate material suspensions, and is applicable to both surgical instruments

and C3M devices. Secondly, the manufacturing technique will create large arrays of free standing parts, have the desired large aspect ratios, maintain good resolution, and have 3-dimensional capabilities. Furthermore, the fabrication approach must be adaptable and integrated with the mechanical design and prototype testing procedures in order to simultaneously improve materials properties, processing, and final prototype performance.

It is hypothesized that a combination of lithography molding techniques, colloidal science, and mechanical design and mechanical testing, will lead to a new fabrication process for particulate material systems to manufacture meso-scale devices. Additionally, incorporating an analysis of the predicted stresses due to drying into the original device design can be used to improve the final design, and increase the yield and properties of future instruments. Lastly, it will be demonstrated that a broad range of particulate material systems can be incorporated into the fabrication process, including ceramic and metal materials, as well as stacking of photoresist molds to create 3-dimensional shapes.

Chapter Summaries

Chapter 2. Background and Literature Review

In Chapter 2, an introduction to two of the device applications for the LM-RIF process is given. First, endoscopic surgery is explained, highlighting the need for new surgical instruments. The new surgical instrument designs fall within the processing regime of the LM-RIF process. Secondly, C3M devices for the aerospace industry are introduced. The large array like structures of C3M devices are comprised of intricate individual unit cells, which are ideally manufactured via the LM-RIF process.

Next, an introduction to the design and fabrication of mesoscale devices is given. A detailed literature review of mesoscale device fabrication is presented, highlighting the most successful methods to date. Furthermore, within the context of fabricating the prototype devices in this thesis, a hierarchy was developed to provide a decision path to select the best mesoscale fabrication method for a given application. In this way, the LM-RIF process is shown to be superior to other manufacturing techniques on the mesoscale.

Following the discussion of fabrication techniques, a design of experiments methodology is introduced. Design of experiments was utilized in Appendix A to identify the most influential variables affecting part yield during fabrication.

Finally, an introduction to the drying of particulate based bodies is given. Initially, drying theory in general is introduced, highlighting the drying mechanisms responsible for drying, drying stress, and drying shrinkage. The constrained drying problem is then introduced, setting the stage for the modeling discussion presented in Chapter 4.

Chapter 3. The Lost Mold-Rapid Infiltration Forming Process

The objective of Chapter 3 is to outline the development of the lost mold-rapid infiltration forming (LM-RIF) process used to fabricate prototype parts and test specimens. The capabilities of the LM-RIF process are described in relation to feature size and part size of devices. Furthermore, the scope of the LM-RIF process is described, highlighting the relation between materials science processing, mechanical properties, and mechanical design. Advancements of the LM-RIF process in this thesis are highlighted relative to the initial development reported by Antolino et al. [2, 3], Aguirre et al. [13, 14], and Mehta et al. [5].

Within the description of the LM-RIF process, the procedures used to create lithography based molds on polycrystalline substrates are outlined. Furthermore, examples of

photolithographic masks used to fabricate the prototype designs are included. A description of the loss of feature size, as a function of mold thickness is shown, followed by a procedure to stack molds to create three dimensional molds.

Finally, details on the steps used within the LM-RIF process are explained. First, aqueous colloidal processing of nanoscale zirconia is presented including an overview of the formulation of new gel-binder systems used to fabricate ceramic parts. Also shown is a new non-aqueous process for the 300 series stainless steel. Following colloidal suspension formulation, other process steps including mold infiltration, drying, mold removal, and sintering steps are explained. Examples of prototype parts from aqueous ceramic suspensions and non-aqueous metallic suspensions are presented.

Chapter 4. Constrained Drying for the LM-RIF Process

The objectives of Chapter 4 include developing a model for the drying process and mechanical strain induced in the ceramic green bodies. Chapter 4 details the part yield of ceramic devices produced with the LM-RIF process. The main mechanism of part failure is cracking during the drying process. In the LM-RIF process, not only does stress arise due purely to drying, but shrinkage during drying can cause an interaction of the drying part with the mold wall, creating a constrained drying stress. Therefore, two theoretical models were developed to assess the drying rate, drying stress and constrained drying stress experienced by the part during processing. A limited one dimensional model developed in Matlab provides fast analysis, while a detailed three dimensional model written in Comsol Multiphysics[®] provides a constrained drying stress analysis. The limitation of the one dimensional program is that it does not take into consideration strains in three dimensions nor internal drying stresses. Conversely, the three dimensional program has those capabilities, but is slightly more cumbersome to program, and

assumptions must be made in determining the proper coefficients needed for the system of equations. Initially, the drying of disks cast with the same colloidal suspensions used in the LM-RIF process is investigated. Sample weight as a function of time was measured and compared against the model predictions to validate the boundary conditions and the models. Following model validation, the drying time and drying stress of forceps devices was investigated. Drying stress and constrained drying stress were compared, followed by the effect of forceps shape on total drying stress. The effect of forceps shape on drying stress was utilized in device redesign for both new forceps and new C3M designs.

Chapter 5. Non-Aqueous Processing of Metal Materials via the LM-RIF Process

The objective of Chapter 5 is to utilize processing science to successfully incorporate non-aqueous colloidal suspensions into the LM-RIF. In this way, the scope of particulate materials accessible with the LM-RIF process is broadened to include 300 series stainless steel. Furthermore, the mechanical properties and performance of prototyped devices are evaluated. To this end, the particle size, rheological properties, and colloidal stability of suspensions is discussed. Following colloidal suspension formulation, cross-sectional samples of fabricated parts are examined, including porosity, and chemical analysis utilizing Auger electron spectroscopy. Three-point bend testing was completed for a strength analysis of the metallic devices. Once mechanical strength was obtained, final device prototypes were fabricated and tested for device performance. In the case of the surgical forceps, a study was completed at Hershey Medical Center comparing the fabricated forceps instrument to the forceps device currently in use by surgeons. In the case of the forceps instrument and the C3M device, the prototype designs showed good agreement with theoretical predictions.

Chapter 6: Conclusions and Future Work

In Chapter 6, conclusions are summarized, and future work suggested. The future work in the development of processing procedures and scientific investigation within the LM-RIF process is presented. Initially, conclusions are drawn from each chapter, highlighting the important findings. Following conclusions, future work on stacking lithography molds to create three dimensional devices is discussed, and a simple test design is presented. Next, preliminary LM-RIF processing results of C3M devices with curved walls are discussed. The curved walled design is an attempt to lower drying stress during fabrication, while simultaneously increasing device performance. Additionally, a new drying process is described, critical point drying, which may be able to increase part yield dramatically by eliminating surface tension effects during processing. The future design and processing of surgical instruments is discussed. Future designs include a hybrid material system, to take advantage of materials with vastly different stiffness. The lithographic processing steps required to create hybrid material parts are described, along with a depiction of a photolithographic mask that can be used to carry out the processing. Finally, future mechanical testing procedures are outlined to fully characterize the strength of mesoscale parts fabricated with the LM-RIF process.

Appendices

(A) Aqueous Colloidal Processing for the LM-RIF Process

(B) Multilayer Topology Optimization for the LM-RIF Process

(C) Drying Model Programs

(D) Non-aqueous Zirconia and Stainless Steel Composite Colloidal Suspensions

(E) Nomenclature

(F) Design of Experiments

Appendix A provides the formulation and characterization of two new gel-binders systems utilized with the aqueous processing of nanoparticulate zirconia within the LM-RIF process. The state of dispersion, colloidal stability, and rheological properties of the suspensions are quantified. Green strength, as well as final sintered part strength is investigated. Finally, prototyped ceramic parts are shown.

Appendix B provides a synopsis of a design project used to topologically determine a forceps instrument that can be manufactured using the LM-RIF process in 3 layers. A method to develop device topologies that may not be intuitively obvious is described using a topology optimization routine written in MatlabTM. The optimization code is tested, and the topology of a sample forceps-like device is determined for a three layer LM-RIF process.

Appendix C comprises the Comsol[®] Multiphysics 3.5a code and MatlabTM codes used to model the constrained drying stresses discussed in Chapter 5.

Appendix D describes the metal and ceramic particulate composites that were formulated and incorporated into the LM-RIF process using the new non-aqueous process. Colloidal stability and rheological properties of the composite materials were investigated. Specifically, the change

in viscosity at constant solids loading, with varying ratio of metal to ceramic particulates and the change in viscosity at constant particulate ratio and varying solids content was measured.

Interestingly, the flattened metal platelet colloidal dispersion was aided by the presence of the nanoscale zirconia particles. Finally, sintered part hardness was determined via Vickers indentation testing.

Appendix E provides a description of the nomenclature used throughout this dissertation.

Appendix F provides details on the design of experiments (DOE) work utilized to determine the most influential parameters on part yield within the LM-RIF. The incorporation of DOE provided a systematic experimental approach to minimize experimental time as well as provide insight into LM-RIF parameters.

References

1. Hummel, R.E., *Understanding materials science: history, properties, applications*. 2004: Springer.
2. Antolino, N.E., G. Hayes, R. Kirkpatrick, C.L. Muhlstein, M.I. Frecker, E.M. Mockensturm, and J.H. Adair, *Lost Mold Rapid Infiltration Forming of Mesoscale Ceramics: Part 1, Fabrication*. *Journal of the American Ceramic Society*, 2009. 92(1): p. S63-S69.
3. Antolino, N.E., G. Hayes, R. Kirkpatrick, C.L. Muhlstein, M.I. Frecker, E.M. Mockensturm, and J.H. Adair, *Lost Mold-Rapid Infiltration Forming of Mesoscale Ceramics: Part 2, Geometry and Strength Improvements*. *Journal of the American Ceramic Society*, 2009. 92(1): p. S70-S78.
4. Aguirre, M.E., G. Hayes, M. Frecker, N. Antolino, and J. Adair. *Fabrication and Design of a Nanoparticulate Enabled Micro Forceps*. in *32nd Annual Mechanisms and Robotics Conference (MR) Topic: MR-8 Medical Devices and their Applications*. 2008.
5. Mehta, V., Hayes, G.H., Frecker, M.I., Adair, J.H., *Design, Fabrication, and Testing of Meso-scaled Cellular Contact-aided Compliant Mechanisms*, in *ASME 2010 Conference on Smart Materials, Adaptive Structures and Intelligent Systems, SMASIS2010*. 2010: Philadelphia, Pennsylvania, USA.

6. Mehta, V., M. Frecker, and G.A. Lesieutre, *Stress Relief in Contact-aided Compliant Cellular Mechanisms*. ASME Journal of Mechanical Design, 2009. 31(9): p. 1-11.
7. Rattner, D. and A. Kalloo, *ASGE/SAGES working group on natural orifice transluminal endoscopic surgery - October 2005*. Surgical Endoscopy and Other Interventional Techniques, 2006. 20(2): p. 329-333.
8. Rattner, D.W., *NOTES: 'where have we been and where are we going' (2008:22(5)1143-1145) and 'transvaginal endoscopic appendectomy in humans: a unique approach to NOTES 'world's first' (2008:22(5)1343-1347)*. Surgical Endoscopy and Other Interventional Techniques, 2008. 22(10): p. 2327-2327.
9. Miedema, B., E. Sporn, J. Astudillo, and K. Thaler, *Epilogue: the future of notes*. Eur J Vasc Endovasc Surg., 2008. 40(3): p. 117-119.
10. Thill, C., J. Etches, I. Bond, K. Potter, and P. Weaver, *Morphing skins*. Aeronautical Journal, 2008. 112(1129): p. 117-139.
11. Garcia, C., F. Martin, Y. Blanco, M.P. de Tiedra, and M.L. Aparicio, *Corrosion behaviour of duplex stainless steels sintered in nitrogen*. Corrosion Science, 2009. 51(1): p. 76-86.
12. Erhard, K. and P.K. Samal, *Powder Metallurgy Stainless Steels: Processing, Microstructures, and Properties*. 2007: ASM International.
13. Aguirre, M., G. Hayes, M. Frecker, J. Adair, and N. Antolino. *Fabrication and Design of a Nanoparticulate Enabled Micro Forceps*. in *ASME 2008 International Design Engineering Technical Conferences & Computers and Information in Engineering Conference*. 2008. New York, NY.
14. Aguirre, M., G. Hayes, C. Yuangyai, M. Frecker, J. Adair, and N. Antolino. *Fabrication and Strength-Based Design of a Meso-Forceps*. in *ASME 2009 International Design Engineering Technical Conferences*. 2009. San Diego, CA.

Chapter 2

Background and Literature Review

In this Chapter, a detailed introduction to two device applications of the LM-RIF is presented, followed by a thorough overview of the microfabrication literature to date, along with a simplified way to explain the importance of the LM-RIF processing method, and finally, background is provided on drying particulate materials, as a supplement to the introduction given in Chapter 4.

Natural Orifice Translumenal Endoscopic Surgical Instrument Tool Tip

NOTES, or natural orifice translumenal endoscopic surgery, is being viewed as the next revolution in surgical procedures [1, 2]. NOTES procedures have decreased risk of infection, facilitate shorter hospital stays, and decrease cosmetic scarring when compared to traditional open surgery procedure counterparts [3]. In minimally invasive surgery developed to date, surgical procedures are performed using long slender instruments inserted through small incisions in the body. NOTES aims to eliminate the small external incisions by performing surgical procedures using an endoscope inserted into the body via a natural orifice (e.g., the mouth) [4]. Surgical instruments used in NOTES procedures must be used through the working channel of the endoscope; typically 2-6 mm in diameter, as shown in Figure 2.1.

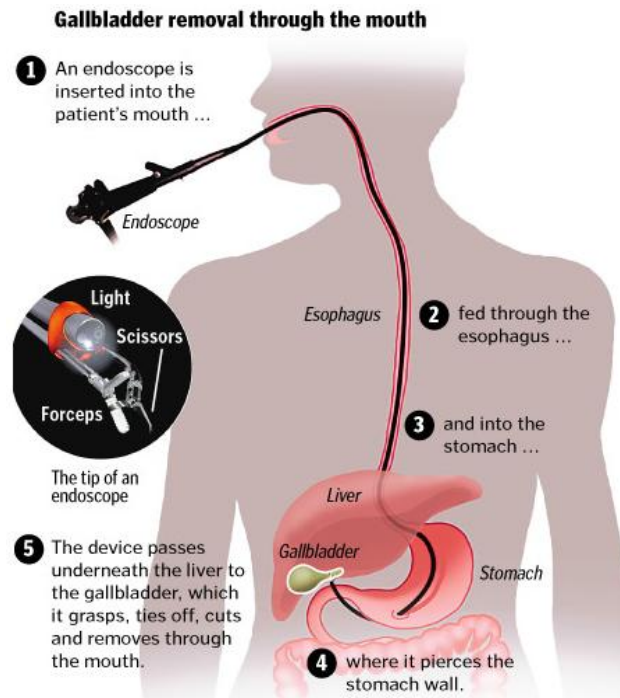


Figure 2.1. Overview of NOTES technique, where surgeries are performed without external incisions. The tool tip designed and fabricated herein would be inserted through the endoscope and remotely manipulated by the surgeon through the handle of the endoscope[5].

As endoscopes become increasingly complex with 2 or more working channels, there is a need to create smaller instruments to fit inside working channels that are 2 mm or smaller in diameter [6]. As shown in Figure 2.2, endoscopes need to be flexible and articulate to gain access to the internal body cavity. Secondly, surgical instruments, used with the flexible endoscopes, need to be functional throughout the range of motion of the endoscope, as well as small enough to fit within the size constraints of the endoscope working channel. While many NOTES surgical instrument designs are adapted from minimally invasive surgery instruments, new instruments are being designed to better meet the needs of surgeons and, in turn, patients.



Figure 2.2. Left, two endoscopes are shown side by side, an endoscopic instrument is inserted near the handle of one of the endoscopes. Center, the working end of an endoscope, showing one working channel with an example endoscopic instrument inserted through the channel. Right, an internal surgery is depicted utilizing an endoscope with inserted instrument. The endoscope has perforated the stomach and is inside the internal body cavity permitting access to organs such as the appendix, long and short intestine, gall bladder, liver, spleen, and pancreas [7-9].

The fabrication process developed in this research study will address the mesoscale forceps instrument developed by Aguirre et al. [10], see Figure 2.3. The forceps is intended to be a tissue grasping device, and to fit into an endoscope used in NOTES procedures. The topology of the forceps is shown in Figure 2.3. There is a line of symmetry through the center of the forceps, between the arms. Grasping motion control is actuated via the extension and retraction of an outer sheath over the forceps arms, pinching the arms closed for grasping or allowing the arms to open, respectively. The unique design of the forceps includes a contact point between the arms as the grasping ends are forced closer together. When contact occurs between the compliant arms during the extension of the outer sheath for elastic deformation of the arms, mechanical stress is redistributed throughout the entire forceps, decreasing the maximum stress the forceps experiences, and allowing further actuation. With this contact aided deformation topology, the forceps can be precisely designed for maximum deformation, and thus maximum opening between the arms, a property that endoscopic surgeons have emphasized as important in NOTES procedures. Furthermore, the forceps designs can be tailored to work with a specific set of mechanical properties, allowing the fabrication of forceps to be carried out with a variety of materials. While these forceps are designed to be monolithic, they have orders of magnitude

variation in their dimensions. For example, the gap between the forceps arms is on the order of 10's of microns, the width of the arms is 100's of microns and the length of the forceps is 1000's of microns. These properties make it an ideal case for microfabrication, specifically, the LM-RIF process.

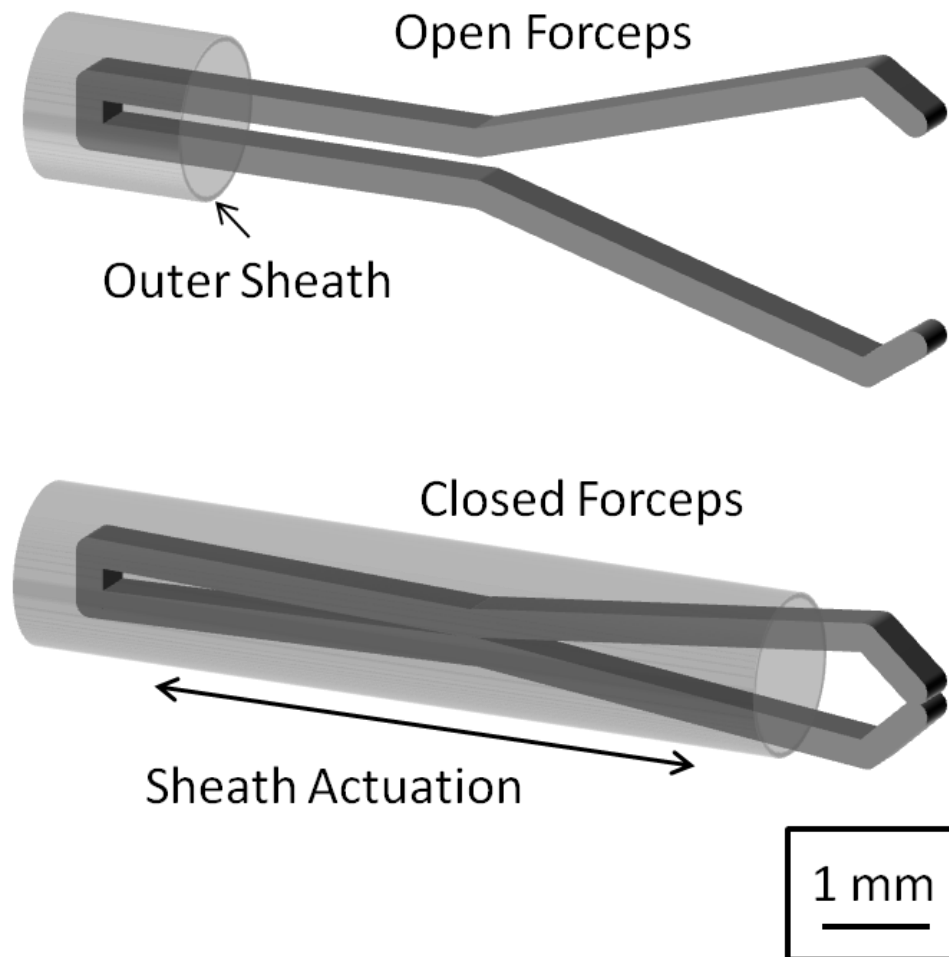


Figure 2.3. Mesoscale forceps designed by Aguirre et al. that was fabricated with the LM-RIF process described herein [10]. The forceps arms are actuated in a grasping motion controlled by the sliding of the outer sheath over the arms to close or open the forceps tip with sheath extension or retraction, respectively.

Cellular Contact-Aided Compliant Mechanisms

Current work in aviation has shown that morphing technology in aircraft wings can increase flight efficiency, as well as improve maneuverability. For a comprehensive overview of the morphing skin literature, see Thill et al. [11]. To account for large shape change in aircraft wings, flexible, morphing skins must be developed that have both the required stiffness and elasticity. Inherently, as shown in Figure 2.4, there is a tradeoff between high elastic modulus materials and high elastic strain materials [12], with the desired materials property region of interest highlighted in yellow. However, the work of Olympio et al. [13], shows that cellular structures can be used to achieve high stiffness, high elastic strain materials using honeycomb based cells.

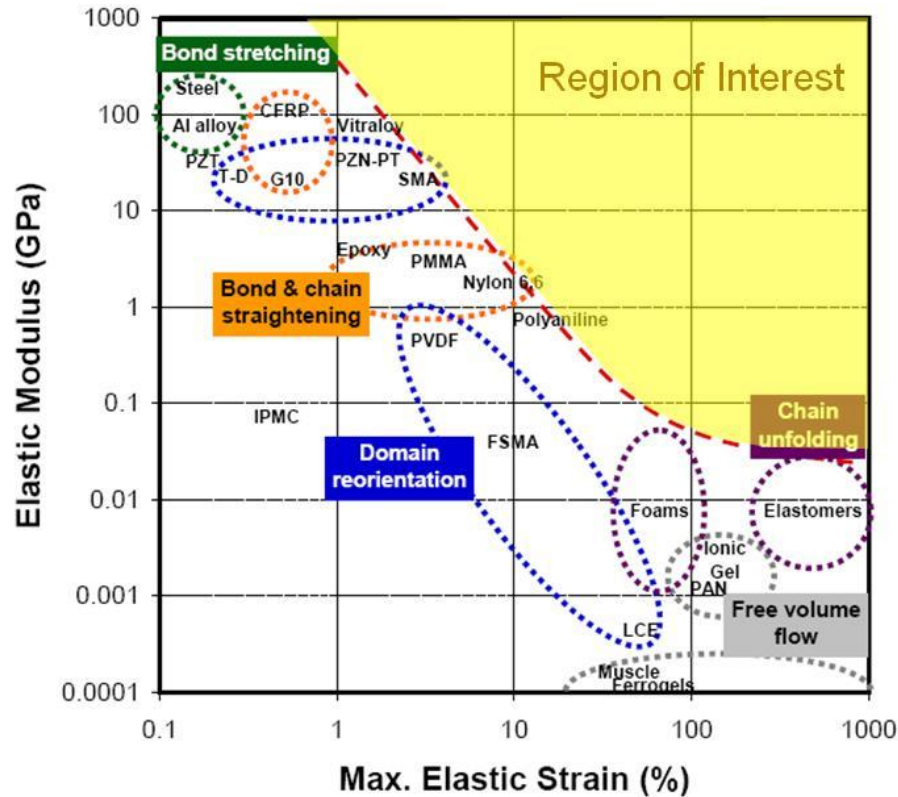


Figure 2.4. The tradeoff between high stiffness and high elastic strain materials is shown. The region of interest for high stiffness - high strength materials is highlighted in yellow. Cellular structures are one method to achieve materials that occupy the relatively unexplored yellow region of interest [12]. We aim to create a new class of materials and devices in the yellow region through a combination of material processing science and material design.

The concept of cellular contact aided compliant mechanisms (C3M) is shown in Figure 2.5. The C3M device in the figure is designed to be monolithic (i.e., a single component material), while maximizing the deformation in the horizontal (x) direction. Within each cell structure is a contact mechanism. Just as in the mechanical deformation of the forceps, as a cell deforms, the contact mechanism becomes active, and the walls of the device experience stress redistribution, permitting additional deformation without reaching the maximum allowable stress. The C3M cells are amenable to the LM-RIF process due to the large variation in dimension. The

height and width of an individual cell is approximately 1-2 cm, the width of the walls of the cell are on the order of 100's of microns, while the gap within the contact mechanism is on the order of 10's of microns. Furthermore, the number of cells in the array can vary greatly, making the total length and width of a device a few centimeters. Just as with the forceps design, these large variations in dimension make this device an ideal case to be fabricated with the LM-RIF process.

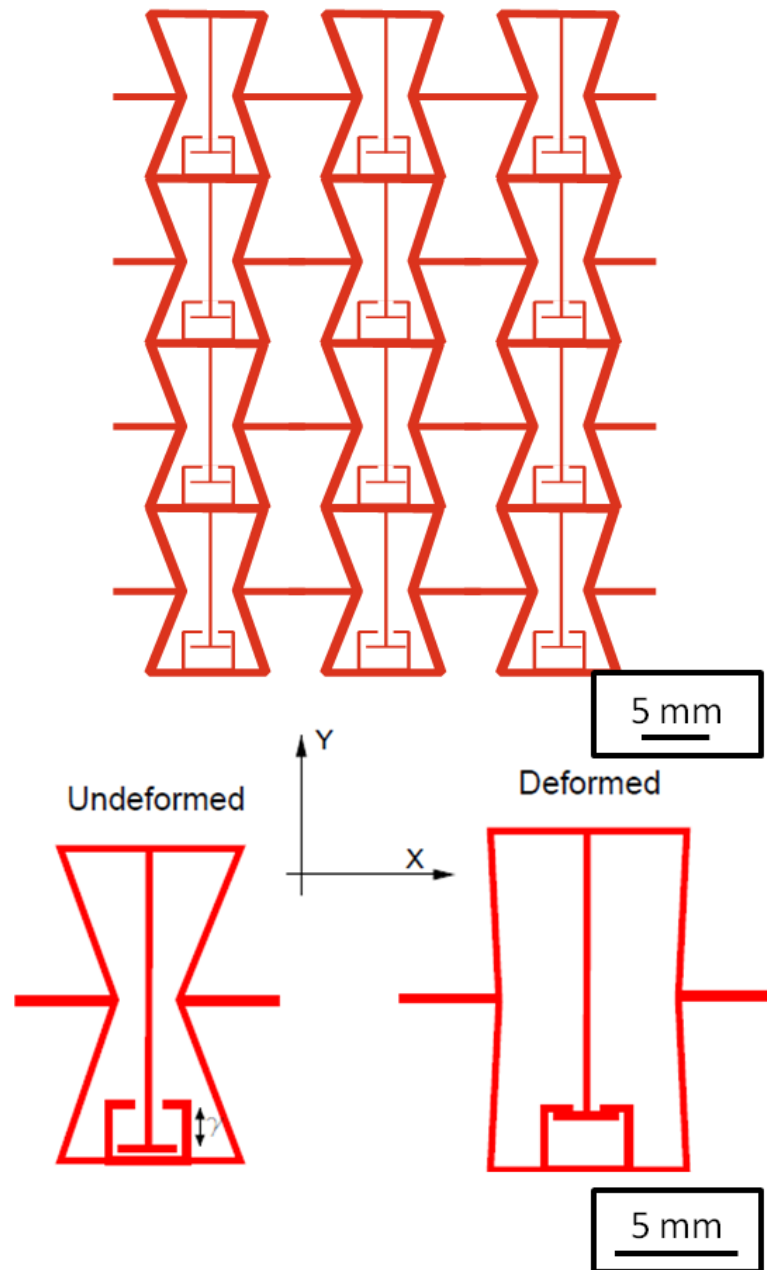


Figure 2.5. Top, A three by four cellular array C3M device with contact aided deformation mechanisms is presented., Bottom, the designed undeformed cellular shape of the unit cell vs. the deformed shape, with the contact mechanism active, is shown. These C3M devices are designed to maximize global strain; which is noted as strain in the x-direction [14].

Mesoscale Fabrication Methods

Dimensional constraints on both the surgical instrument tool tip, as well as the C3M device require fabrication of millimeter scale components with micron scale resolution. To manufacture these devices, a novel microfabrication process, the LM-RIF, has been developed based on a directed assembly, lost mold method. To date, many microfabrication techniques have been explored to create free standing parts, consisting of top down, and bottom up approaches [15]. Top-down approaches consist of processes typical to semi-conductor processing in which, for example, a film is deposited via vapor deposition techniques followed by chemical or reactive ion etching. Additionally, small scale machining technologies, such as direct ceramic machining, wire electrical discharge machining (EDM) [16], and low-temperature-co-fired-ceramics machining can cut and grind devices from bulk materials, but can only produce a few parts at a time, generally have significant surface flaws due to the mechanical approach, and yield large quantities of particulate debris [15]. Machining technologies are also limited by the cutting tool size used to shape the part [17].

Bottom-up techniques consist of the assembly of particulate elements via directed assembly or self-assembly. The additive processes provided by bottom-up approaches are attractive because of a more efficient use of materials and resources, while minimizing manufacturing debris, and avoiding size restrictions due to tool size. Self assembly [18] can be used to create arrays of small building blocks, which assemble due to specifically functionalized surfaces, and without the need for external intervention. Alternatively, directed assembly of particulates, via a molding [19, 20], printing [15], stereolithography [15], or selective laser sintering [21] process can be easily implemented to manufacture devices from a variety of materials available in particulate form. For example, the lost mold process that enabled the bronze age was developed over 6 thousand years ago. As shown by Bowden and Whitesides [22-

24], elegant and interesting shapes can be produced with self assembly strategies. The drawbacks of self assembly include arbitrary shape fabrication and the formation of shapes with a substantial thickness [25]. Therefore, in the current research, directed assembly methods are utilized to form complex particulate bodies with thicknesses of 20 to 300 microns with the LM-RIF process [26-28].

For directed assembly approaches, there are two main areas of research and development: direct writing methods, and lithography mold-based methods. Direct writing methods, such as direct ink writing [29] of ceramic slurries, do not have the edge control and subsequent edge resolution required for surgical instrumentation, and normally can only fabricate one structure at a time, making these processes relatively inefficient and time consuming. Lost mold processes, such as injection molding of polymer molds [30] and filling of photoresist molds [31] offer the ability to create free standing parts large enough, with the desired edge resolution, to be viable options for microfabrication. Furthermore, mold fabrication via lithography is one of the least expensive microfabrication techniques [32]. New advances in ultra thick photoresist techniques permit the fabrication of single layer lithographic molds up to 1mm thick, while maintaining good edge resolution [33]. Additionally, aqueous gel-casting [34, 35], aqueous tape-casting [36], and non-aqueous colloidal suspension formulation [37], has shown the capability to produce uniform green bodies via colloidal slurries that can be cast into the lithographic molds. Finally, filling photoresist molds with a particulate-based suspension opens the possibilities of processing a wide range of materials including metals, ceramics, composite materials, and multilayer laminated materials. Manufacturing methods for micro components are summarized by Table 2.1 in terms of smallest feature resolution, aspect ratio, multi-material system capability, and array manufacturing capability. Furthermore, the basis for the technique in terms of lithography, injection molding, machining, printing, and laser forming is used to classify the

manufacturing method. The LM-RIF process is listed under lithography techniques and outlined in black.

Table 2.1. Manufacturing methods for micro components are summarized in terms of smallest feature resolution, aspect ratio, multi-material system capability, and array manufacturing capability. Furthermore, the basis for the technique is used to classify the various methods in terms of lithography, injection molding, machining, printing, and laser forming. The developed LM-RIF process is listed under lithography techniques and outlined in black.

Technique Basis	Micro-Fabrication Method	Smallest Feature Resolution (μm)	Aspect Ratio	2D or 3D	Multi-Material Systems	Array Manufacturing	Ref.
Lithography Based Techniques	Microfabrica MEMS EFAB	10	high	2D/3D	No	Yes	[38]
	Casting suspensions into photolithographic masks on silicon	1-5	1-2	2D	Yes	Yes	[15]
	LM-RIF	1-10	1-40	2D/3D	Yes	Yes	[39, 40]
	Soft lithography	1-5	1-3	2D/3D	Yes	Yes	[24]
	Laminated object manufacturing	100	Vari-able	3D	Yes	No	[41]
	Low-temperature co-fired ceramic multilayer	25-100	Vari-able	3D	No	No	[15]
	LIGA	10-20	10	2D	Yes	Yes	[15]
Injection Molding/Extrusion	Micro injection molding	20-100	High	3D	Yes	No	[19]
	Co-extrusion	5-16	High	3D	Yes	No	[15]
	Metal embossing	50	high	2D	No	No	[15]
Machining	Direct ceramic machining of pre-sintered bodies	50	Vari-able	3D	No	No	[15]
	Microwire EDM	70	high	3D	No	No	[16]
	STM-tip electrochemical etching	0.01	-	2D	No	No	[15]
	Precision grinding	50	high	3D	Yes	No	[15]
	Diamond machining (lathe)	25	5	3D	Yes	No	[17]

	Surface micromachining	25	Vari-able	2D	Yes	No	[17]
Printing	Screen printing	100	low	2D	Yes	Yes	[15]
	Ink-jet printing of suspensions	70	low	2D	Yes	No	[15]
	Freeform ink-jet printing of suspensions	170	high	3D	Yes	No	[15]
	3DP process (printing ceramic binders)	200	Vari-able	3D	Yes	No	[15]
	Micropen writing	250	1	3D	Yes	No	[15]
Laser Forming	Laser chemical vapor deposition	10	500	3D	Yes	No	[42]
	Pulsed laser ablation	30-200	high	2D	Yes	No	[15]
	Microstereo-lithography	2	high	3D	Yes	No	[15]
	Selective laser sintering	500	high	3D	Yes	No	[21]
	Maple direct write	10-20	low	2D	No	No	[15]

As shown in Figure 2.6, multiple fabrication techniques were evaluated relevant to our objective of manufacturing large numbers of meso-scale components given in Table 2.1. The applied criteria include: the capability for large array fabrication, high aspect ratio in a free standing part, smallest feature resolution, potential for 3D manufacturing, and capability for multiple material manufacturing. Meso-scale surgical instruments require components that are 1mm or less in the largest dimension while resolution needs to be at the micron or even sub-micron scale. This requirement eliminates all of the possible microfabrication approaches except the EFAB and LMRIF processes. The EFAB process invented by Cohen [43] uses electrochemical deposition of metals combined with lithographic techniques to produce 3D structures. There is little material data or material testing data available for the EFAB parts. However, a typical issue with multilayer electrochemical films and other types of multilayer materials produced at low temperatures, fabricated without the high temperature diffusion bonding used for ceramic-metal multilayer materials, is delamination [44]. Microfabrica, Inc., the company that practices the EFAB process taught by the Cohen patent [43], indicates that high strengths are achievable (1.2GPa) with some special alloys based on documents on their website [38], but pull off tests for delamination have failure stresses approximately one-half of the ultimate tensile strength. This may indicate an underlying limitation of the EFAB process. In any case, EFAB is limited to metallic systems that can be electrochemically deposited. In contrast, the LM-RIF process utilizes nanometer scale ceramic particulates that in some cases are combined with metal particulates or ceramic-metal multilayers, permitting a wide range of novel and innovative design strategies. Furthermore, two materials can be combined in a hierarchical fashion, at the particulate scale, in multilayers, and in hybrid material parts in the LM-RIF process.

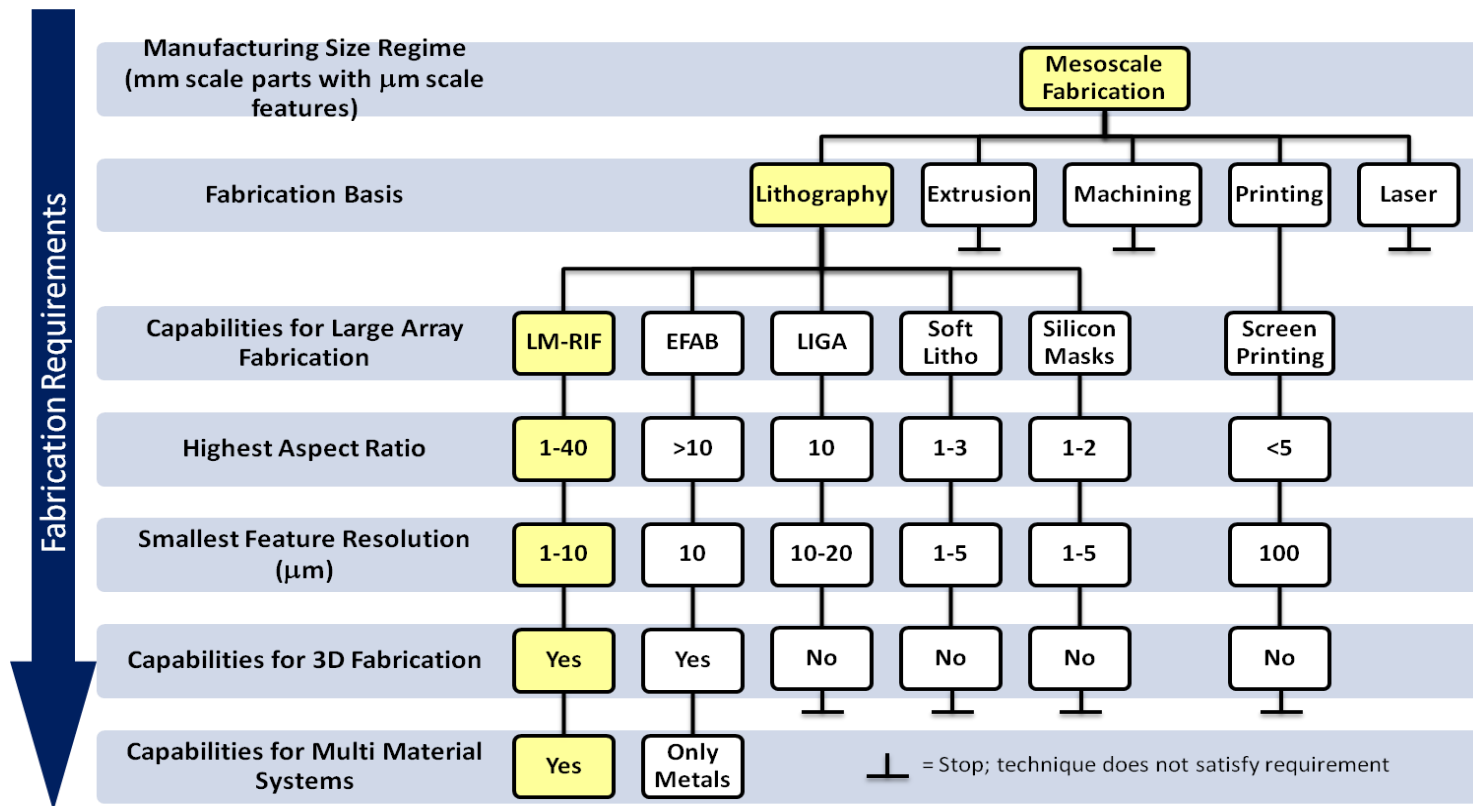


Figure 2.6. Hierarchy of fabrication techniques used in large array meso-scale manufacturing. Only the LM-RIF process is capable of large array fabrication of 3D parts with high aspect ratios and small feature resolution, using multiple materials.

Design of Experiments

The experimental design approach most commonly used in science, engineering, and manufacturing is overwhelmingly that of changing one factor at a time (OFAT) while attempting to maintain other variables constant [45]. While methodical, this approach is not time efficient and neglects the interaction among variables [46-48]. In cases where randomization is impractical, for example experiments dealing with hard to change factors, a split-plot (SP) design or some of its variants can be implemented. The multi stage split plot (MSSP) is an extension of the split plot design, and can significantly reduce the number of settings in each stage. The combination of split-plot arrangement with fractional factorial (FF) design, the multi stage fractional factorial split plot (MSFFSP) design, will here prove to be the most efficient and effective design because it provides the smallest number of settings as well as the smallest number of experimental trials. In a concurrent study by Yuangyai et al. [45], the MSFFSP design has been employed to gain insight into parameters that have a significant impact on final part properties. Further details can be found in Appendix F.

Constrained Drying Theory of Aqueous Ceramics applied to the LM-RIF Process

Drying theory of particulate bodies has been investigated for over 50 years; however, exact modeling of drying stress for arbitrary shapes has not been thoroughly described [49]. A typical drying curve for a particulate body is shown below in Figure 2.7. During the constant drying rate period (stage 1), free water is removed from the surface, while the surface of the material remains wet, drying shrinkage and stress increase to a maximum, denoted in the figure, as the critical drying point. After the critical point, stage 2 begins. Stage 2 is characterized by a retreating of the drying front from the surface to within the body, along with a decrease of the

drying rate. Stage 3 is the end of the decreasing drying rate, where moisture content, temperature, and relative humidity come to equilibrium with the surrounding atmosphere.

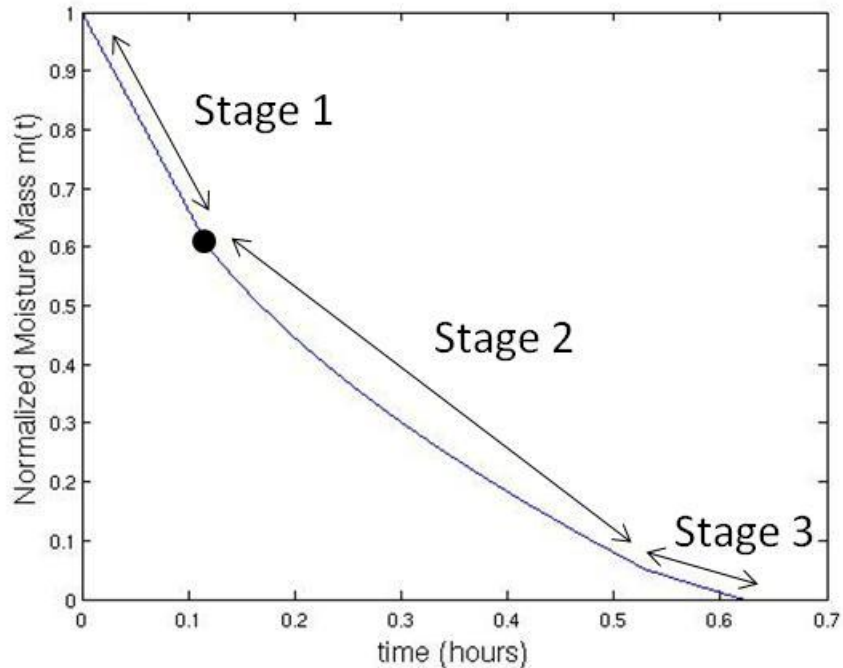


Figure 2.7. The three stages of drying are shown, the point of maximum drying induced stress is highlighted at the end of the constant drying rate period and is the critical drying point. Stage 1 is the constant rate drying period, where evaporation is taking place from the surface. In Stage 2, the falling rate period, drying stress is reducing, but there may be residual stress and deformation from Stage 1. In stage 3, the end of the falling rate period, where equilibrium is reached with the surrounding atmosphere.

Many scientists have studied the phenomena surrounding drying of particle based systems [50-68], while others still have tried to incorporate drying stress approximations into the models [69-77]. Throughout the literature, there are many mechanisms attributed to moisture mass transfer in a particulate body, which are summarized below [53]:

- **Liquid movement due to capillary forces:** first period of drying, due to capillary potential gradient.
- **Liquid movement due to concentration gradients:** concentration gradients of moisture throughout the body cause liquid diffusion.

- **Liquid and vapor movement due to pressure gradients:** Similar to the Darcy model, external pressure and shrinking cause liquid and vapor movement in the first stage of drying.
- **Vapor diffusion due to concentration gradients:** occurs in stage 2, when vapor created inside the body causes a change in pressure.
- **Osmotic pressure:** in colloidal bodies, portions can be soluble and non-soluble, creating an osmotic effect on moisture movement.
- **Effusion of vapor:** the mean free path of vapor molecules is on the order of size of the internal pores. Occurs during stage 2.
- **Thermodiffusion:** temperature gradients in the body cause additional moisture flux.
- **Evaporation condensation mechanism:** during the second stage of drying, differences in capillary pressure lead to condensation and necking in small capillaries, with evaporation from large pores.

Drying stresses can occur both internally, through capillary forces driven by surface tension and the pore size distribution in the particulate bed, and externally, due to mechanical interactions of the drying body with the mold walls as shrinkage occurs. During the LM-RIF fabrication process, parts tend to crack at the drying stage prior to firing. While drying stresses have long been studied, an analysis of mold geometries and stresses that arise due to complicated geometry has not been addressed in the literature. This analysis is needed to improve the yield, and therefore improve the surgical instrument design. In this analysis, the mechanical drying stresses arising from the green body shrinking in the mold were modeled and evaluated compared to mechanical design. Finite element analysis is used for the solution of differential equations over arbitrary domains, lending itself to the problem at hand.

References

1. Rattner, D. and A. Kalloo, *ASGE/SAGES working group on natural orifice transluminal endoscopic surgery - October 2005*. *Surgical Endoscopy and Other Interventional Techniques*, 2006. 20(2): p. 329-333.
2. Rattner, D.W., *NOTES: 'where have we been and where are we going' (2008:22(5)1143-1145) and 'transvaginal endoscopic appendectomy in humans: a unique approach to NOTES 'world's first' (2008:22(5)1343-1347)*. *Surgical Endoscopy and Other Interventional Techniques*, 2008. 22(10): p. 2327-2327.
3. Miedema, B., E. Sporn, J. Astudillo, and K. Thaler, *Epilogue: the future of notes*. *Eur J Vasc Endovasc Surg.*, 2008. 40(3): p. 117-119.
4. Hussain, A. and H. Mahmood. *NOTES: current status and expectations*. 2008: Springer Wien.
5. *Gallbladder removal through the mouth*. [cited 2010]; Available from: <http://mediligence.com/blog/2009/11/03/notes-procedures-offer-benefits-some-challenge/>.
6. Bardaro, S.J. and L. Swanstrom, *Development of advanced endoscopes for natural orifice transluminal endoscopic surgery (NOTES)*. *Minimally Invasive Therapy & Allied Technologies*, 2006. 15(6): p. 378-383.
7. Pro-Scope-Systems. *Flexible Endoscope*. 2011 [cited 2011]; Available from: <http://www.websites.medmatrix.com/proscopesystems/index.cfm>.
8. Loria, K. *Endoscopy: A new beginning for endoscopy*. 2010 [cited 2011]; Available from: <http://www.dotmed.com/legal/print/story.html?nid=13007>.
9. Columbia-Surgery. 2011 [cited 2011]; Available from: http://www.columbiasurgery.org/news/si/2007_endoscopic.html.
10. Aguirre, M.E., G. Hayes, M. Frecker, N. Antolino, and J. Adair. *Fabrication and Design of a Nanoparticulate Enabled Micro Forceps*. in *32nd Annual Mechanisms and Robotics Conference (MR) Topic: MR-8 Medical Devices and their Applications*. 2008.
11. Thill, C., J. Etches, I. Bond, K. Potter, and P. Weaver, *Morphing skins*. *Aeronautical Journal*, 2008. 112(1129): p. 117-139.

12. Henry, C. and G. McKnight. *Cellular variable stiffness materials for ultra-large reversible deformations in reconfigurable structures*. in *Smart Structures and Materials: Active Materials: Behavior and Mechanics*. 2006.
13. Olympio, K.R. and F. Gandhi, *Flexible Skins for Morphing Aircraft Using Cellular Honeycomb Cores*. *Journal of Intelligent Material Systems and Structures*, 2009.
14. Mehta, V., Hayes, G.H., Frecker, M.I., Adair, J.H., *Design, Fabrication, and Testing of Meso-scaled Cellular Contact-aided Compliant Mechanisms*, in *ASME 2010 Conference on Smart Materials, Adaptive Structures and Intelligent Systems, SMASIS2010*. 2010: Philadelphia, Pennsylvania, USA.
15. Heule, M., S. Vuillemin, and L.J. Gauckler, *Powder-based ceramic meso- and microscale fabrication processes*. *Advanced Materials*, 2003. 15(15): p. 1237-1245.
16. Yan, M.T., C.W. Huang, C.C. Fang, and C.X. Chang, *Development of a prototype Micro-Wire-EDM machine*. *Journal of Materials Processing Technology*, 2004. 149(1-3): p. 99-105.
17. Frazier, A.B., R.O. Warrington, and C. Friedrich, *The Miniaturization Technologies - Past, Present, and Future*. *Ieee Transactions on Industrial Electronics*, 1995. 42(5): p. 423-430.
18. Clark, T.D., J. Tien, D.C. Duffy, K.E. Paul, and G.M. Whitesides, *Self-assembly of 10- μ m-sized objects into ordered three-dimensional arrays*. *Journal of the American Chemical Society*, 2001. 123(31): p. 7677-7682.
19. Muller, T., V. Piottter, K. Plewa, M. Guttman, H.J. Ritzhaupt-Kleissl, and J. Hausselt, *Ceramic micro parts produced by micro injection molding: latest developments*. *Microsystem Technologies-Micro-and Nanosystems-Information Storage and Processing Systems*, 2009. 16(8-9): p. 1419-1423.
20. Fu, G., N.H. Loh, S.B. Tor, B.Y. Tay, Y. Murakoshi, and R. Maeda, *Injection molding, debinding and sintering of 300 series stainless steel microstructures*. *Applied Physics a-Materials Science & Processing*, 2005. 81(3): p. 495-500.
21. Nelson, J.C., N.K. Vail, J.W. Barlow, J.J. Beaman, D.L. Bourell, and H.L. Marcus, *Selective Laser Sintering of Polymer-Coated Silicon-Carbide Powders*. *Industrial & Engineering Chemistry Research*, 1995. 34(5): p. 1641-1651.
22. Bowden, N., A. Terfort, J. Carbeck, and G.M. Whitesides, *Self-assembly of mesoscale objects into ordered two-dimensional arrays*. *Science*, 1997. 276(5310): p. 233-235.

23. Terfort, A., N. Bowden, and G.M. Whitesides, *Three-dimensional self-assembly of millimetre-scale components*. Nature, 1997. 386(6621): p. 162-164.
24. Xia, Y.N. and G.M. Whitesides, *Soft lithography*. Annual Review of Materials Science, 1998. 28: p. 153-184.
25. Klajn, R., K.J.M. Bishop, M. Fialkowski, M. Paszewski, C.J. Campbell, T.P. Gray, and B.A. Grzybowski, *Plastic and moldable metals by self-assembly of sticky nanoparticle aggregates*. Science, 2007. 316(5822): p. 261-264.
26. Antolino, N.E., *Lost Mold-Rapid Infiltration Forming: Strength Control in Mesoscale 3Y-TZP Ceramics*, Doctor of Philosophy, dissertation in Materials Science and Engineering, The Pennsylvania State University, University Park, 2010.
27. Antolino, N.E., G. Hayes, R. Kirkpatrick, C.L. Muhlstein, M.I. Frecker, E.M. Mockensturm, and J.H. Adair, *Lost Mold Rapid Infiltration Forming of Mesoscale Ceramics: Part 1, Fabrication*. Journal of the American Ceramic Society, 2009. 92(1): p. S63-S69.
28. Antolino, N.E., G. Hayes, R. Kirkpatrick, C.L. Muhlstein, M.I. Frecker, E.M. Mockensturm, and J.H. Adair, *Lost Mold-Rapid Infiltration Forming of Mesoscale Ceramics: Part 2, Geometry and Strength Improvements*. Journal of the American Ceramic Society, 2009. 92(1): p. S70-S78.
29. Lewis, J.A., J.E. Smay, J. Stuecker, and J. Cesarano, *Direct ink writing of three-dimensional ceramic structures*. Journal of the American Ceramic Society, 2006. 89(12): p. 3599-3609.
30. Knitter, R., D. Gohring, P. Risthaus, and J. Hausselt, *Microfabrication of ceramic microreactors*. Microsystem Technologies, 2001. 7(3): p. 85-90.
31. Schonholzer, U.P., R. Hummel, and L.J. Gauckler, *Microfabrication of ceramics by filling of photoresist molds*. Advanced Materials, 2000. 12(17): p. 1261-+.
32. Lawes, R.A., *Manufacturing costs for microsystems/MEMS using high aspect ratio microfabrication techniques*. Microsystem Technologies-Micro-and Nanosystems-Information Storage and Processing Systems, 2007. 13(1): p. 85-95.
33. Lin, C.H., G.B. Lee, B.W. Chang, and G.L. Chang, *A new fabrication process for ultra-thick microfluidic microstructures utilizing SU-8 photoresist*. Journal of Micromechanics and Microengineering, 2002. 12(5): p. 590-597.

34. Janney, M.A., O.O. Omatete, C.A. Walls, S.D. Nunn, R.J. Ogle, and G. Westmoreland, *Development of low-toxicity gelcasting systems*. Journal of the American Ceramic Society, 1998. 81(3): p. 581-591.
35. Christian and P.J.A. Kenis, *Fabrication of ceramic microscale structures*. Journal of the American Ceramic Society, 2007. 90(9): p. 2779-2783.
36. Hotza, D. and P. Greil, *AQUEOUS TAPE CASTING OF CERAMIC POWDERS*. Materials Science and Engineering a-Structural Materials Properties Microstructure and Processing, 1995. 202(1-2): p. 206-217.
37. Imbaby, M.F. and K. Jiang, *Stainless steel-titania composite micro gear fabricated by soft moulding and dispersing technique*. Microelectronic Engineering. 87(5-8): p. 1650-1654.
38. Microfabrica. 2010 [cited 2010]; Available from: <http://www.microfabrica.com/>.
39. Antolino, N., G. Hayes, R. Kirkpatrick, C.L. Muhlstein, M. Frecker, and J. Adair, *Lost Mold Rapid Infiltration Forming of Mesoscale Ceramics: Part 1, Fabrication*. Journal of the American Ceramic Society, 2009. 92(s1): p. S63-S69.
40. Antolino, N., G. Hayes, R. Kirkpatrick, C.L. Muhlstein, M. Frecker, E. Mockensturm, and J. Adair, *Lost Mold Rapid Infiltration Forming of Mesoscale Ceramics: Part 2, Geometry and Strength Improvements*. Journal of the American Ceramic Society, 2009. 92(s1): p. S70-S78.
41. Tay, B.Y., J.R.G. Evans, and M.J. Edirisinghe, *Solid freeform fabrication of ceramics*. International Materials Reviews, 2003. 48(6): p. 341-370.
42. Wanke, M.C., O. Lehmann, K. Muller, Q.Z. Wen, and M. Stuke, *Laser rapid prototyping of photonic band-gap microstructures*. Science, 1997. 275(5304): p. 1284-1286.
43. USA Patent, U.S. 6,475,369 B1, Cohen, A.L. *Method for Electrochemical Fabrication*, 2002.
44. Adair, J.H., D.A. Anderson, G.O. Dayton, and T.R. ShROUT, *A Review of the Processing on Electronic Ceramics with Emphasis on Multilayer Ceramic Capacitor Fabrication*. Journal of Materials Education, 1987. 9(1&2): p. 71-118.
45. Yuangyai, C., Hayes, G., Antolino, N., Nembhard, H. B., and Adair, J. H. , *Yield Improvement for Lost Mold Rapid Infiltration Forming Process by a Multi-Stage Fractional Factorial Split Plot Design*. International Journal of Nanomanufacturing, 2009. 3(4): p. 351-367.

46. Giesbrecht, F.G. and M.L. Gumpertz, *Planning, Construction, and Statistical Analysis of Comparative Experiments*. 2004: John Wiley Sons.
47. Montgomery, D.C., *Design and Analysis of Experiments*. 5th ed. 2005: John Wiley
48. Ryan, T.P., *Modern Experimental Design*. 2007, New Jersey: John Wiley
49. Keum, Y.T. and J.W. Oh, *Finite element simulation of a ceramic drying process considering pore shape and porosity*. *Modelling and Simulation in Materials Science and Engineering*, 2005. 13(2): p. 225-237.
50. Banaszak, J. and S.J. Kowalski, *Theoretical and experimental analysis of stresses and fractures in clay like materials during drying*. *Chemical Engineering and Processing*, 2005. 44(4): p. 497-503.
51. Kowalski, S.J., *Thermomechanics of Constant Drying Rate Period*. *Archives of Mechanics*, 1987. 39(3): p. 157-176.
52. Kowalski, S.J., *Toward a thermodynamics and mechanics of drying processes*. *Chemical Engineering Science*, 2000. 55(7): p. 1289-1304.
53. Kowalski, S.J., *Thermomechanics of Drying Processes*. *Lecture Notes in Applied and Computational Mechanics*, ed. W. Pfeiffer. Vol. 8. 2003, New York: Springer.
54. Kowalski, S.J., *Thermomechanical approach to drying processes*. *Inzynieria Chemiczna I Procesowa*, 2004. 25(3): p. 1953-1962.
55. Kowalski, S.J., *Potentials of mass and heat transfer in drying of capillary-porous materials*. *Inzynieria Chemiczna I Procesowa*, 2004. 25(1): p. 87-97.
56. Kowalski, S.J. and K. Rajewska, *The effectiveness of ceramic drying by surface and volumetric heat supply*. *Inzynieria Chemiczna I Procesowa*, 2004. 25(3): p. 1151-1156.
57. Kowalski, S.J. and A. Rybicki, *Drying stress formation by inhomogeneous moisture and temperature distribution*. *Transport in Porous Media*, 1996. 24(2): p. 139-156.
58. Kowalski, S.J. and A. Rybicki, *Rate of drying and stresses in the first period of drying*. *Drying Technology*, 2000. 18(3): p. 583-600.
59. Scherer, G.W., *Drying Gels .I. General-Theory*. *Journal of Non-Crystalline Solids*, 1986. 87(1-2): p. 199-225.

60. Scherer, G.W., *Correction of Drying Gels .1. General-Theory*. Journal of Non-Crystalline Solids, 1987. 92(2-3): p. 375-382.
61. Scherer, G.W., *Drying Gels .5. Rigid Gels*. Journal of Non-Crystalline Solids, 1987. 92(1): p. 122-144.
62. Scherer, G.W., *Drying Gels .3. Warping Plate*. Journal of Non-Crystalline Solids, 1987. 91(1): p. 83-100.
63. Scherer, G.W., *Drying Gels .4. Cylinder and Sphere*. Journal of Non-Crystalline Solids, 1987. 91(1): p. 101-121.
64. Scherer, G.W., *Drying Gels .2. Film and Flat-Plate*. Journal of Non-Crystalline Solids, 1987. 89(1-2): p. 217-238.
65. Scherer, G.W., *Drying Gels .6. Viscoelastic Plate*. Journal of Non-Crystalline Solids, 1988. 99(2-3): p. 324-358.
66. Scherer, G.W., *Drying Gels .8. Revision and Review*. Journal of Non-Crystalline Solids, 1989. 109(2-3): p. 171-182.
67. Scherer, G.W., *Drying Gels .7. Diffusion During Drying*. Journal of Non-Crystalline Solids, 1989. 107(2-3): p. 135-148.
68. Scherer, G.W., *Theory of Drying*. Journal of the American Ceramic Society, 1990. 73(1): p. 3-14.
69. Banaszak, J. and S.J. Kowalski, *Stresses in viscoelastic plate dried convectively*. Drying Technology, 1999. 17(1-2): p. 97-117.
70. Banaszak, J. and S.J. Kowalski, *Drying induced stresses estimated on the base of elastic and viscoelastic models*. Chemical Engineering Journal, 2002. 86(1-2): p. 139-143.
71. Kowalski, S.J., *Thermomechanical approach to shrinking and cracking phenomena in drying*. Drying Technology, 2001. 19(5): p. 731-765.
72. Kowalski, S.J. and K. Rajewska, *Drying-induced stresses in elastic and viscoelastic saturated materials*. Chemical Engineering Science, 2002. 57(18): p. 3883-3892.
73. Kowalski, S.J., K. Rajewska, and A. Rybicki, *Destruction of wet materials by drying*. Chemical Engineering Science, 2000. 55(23): p. 5755-5762.

74. Scherer, G.W., *Stress and Fracture During Drying of Gels*. Journal of Non-Crystalline Solids, 1990. 121(1-3): p. 104-109.
75. Scherer, G.W., *Stress Development During Supercritical Drying*. Journal of Non-Crystalline Solids, 1992. 145(1-3): p. 33-40.
76. Smith, D.M., G.W. Scherer, and J.M. Anderson, *Shrinkage During Drying of Silica-Gel*. Journal of Non-Crystalline Solids, 1995. 188(3): p. 191-206.
77. Tirumkudulu, M.S. and W.B. Russel, *Cracking in drying latex films*. Langmuir, 2005. 21(11): p. 4938-4948.

Chapter 3

The Lost Mold-Rapid Infiltration Forming Process

Process Overview

As structural material applications require smaller and more precise components [1, 2], standard fabrication techniques such as CNCUPM (computer numerical controlled ultra precision machining) and precision wire EDM (electrical discharge machining) are no longer viable methods for production. Furthermore, the total part size, which can range from millimeters to centimeters, is not capable of being manufactured with small scale processes such as focused ion beam (FIB) or fast atom beam (FAB). Additionally, traditional machining techniques do not have the ability to simultaneously produce large numbers of parts, and are often limited with regard to the types of materials that can be used. Shown in Figure 3.1, the gap in feature size from sub-10 microns to about 300 microns, as a function of part size is shown for traditional manufacturing techniques. Therefore, there is a need for new fabrication approaches to create free standing parts at the millimeter size scale with micron scale feature resolution, defined herein as the meso-scale regime. The work involving the invention of the LM-RIF has been published in peer reviewed journals and is currently patent pending[†].

In this research, a new fabrication process, the lost mold-rapid infiltration forming (LM-RIF) process is presented, based on the initial work of Antolino and Hayes et al. [3, 4], to manufacture large arrays of meso-scale devices by coupling modern lithography methods with

[†]Published work includes:

- U.S. Patent, Patent Pending 61/150,568, J. H. Adair, M.F., C. Muhlstein, E. Mockenstrum, H. B. Nembhard, R. S. Haluck, A. Mathew, N. Antolino, G. Hayes, M. Aguirre, R. Kirkpatrick, and C. Yuangai. *Polycrystalline Complex-Shaped Meso-scale Components*, 2009.
- Antolino, N., G. Hayes, R. Kirkpatrick, C.L. Muhlstein, M. Frecker, and J. Adair, *Lost Mold Rapid Infiltration Forming of Mesoscale Ceramics: Part 1, Fabrication*. Journal of the American Ceramic Society, 2009. 92(s1): p. S63-S69.
- Antolino, N., G. Hayes, R. Kirkpatrick, C.L. Muhlstein, M. Frecker, E. Mockensturm, and J. Adair, *Lost Mold Rapid Infiltration Forming of Mesoscale Ceramics: Part 2, Geometry and Strength Improvements*. Journal of the American Ceramic Society, 2009. 92(s1): p. S70-S78.

advanced colloidal processing. The LM-RIF process is based on top-down design principles as discussed by Aguirre et al. [2], and Mehta et al. [1] and bottom-up manufacturing approaches using particulate processing science.

Furthermore, as discussed in Chapter 2, design of experiments (DOE) was utilized to determine the most influential parameters affecting part yield within the LM-RIF. Due to the complexity of the LM-RIF process, it was not feasible to investigate all of the factors affecting part yield in a standard experimental approach, such as changing one factor at a time. The intent of the incorporation of DOE into the LM-RIF process was to save experimental time while simultaneously determining the most influential parameters on part yield. The final results of the DOE investigation are utilized in Appendix A to successfully incorporate aqueous ceramic suspensions into the LM-RIF.

The ability to manipulate particulate based materials within the LM-RIF, ranging from metals to ceramics as well as composite particulates, allows the processing of high strength and biocompatible materials with applications ranging from advanced surgical instruments to novel cellular components. In this work, two material systems were chosen, yttria partially-stabilized tetragonal zirconia, and 300 series stainless steel. As shown in Figure 3.1, the LM-RIF process fills the need for a manufacturing process to span the gap in manufacturing processes by fabricating meso-scale parts. In addition to spanning the gap in manufacturing capability, the LM-RIF is compatible with a wide range of particulate based materials, and can produce large arrays of parts.

In this chapter an overview of the developed process will be given, highlighting each of the process steps and underlying science, with specific attention paid to the manufacturing of molds on the meso-scale. Further aspects about the formulation of colloidal suspensions, sintering, and final properties will be given in subsequent chapters.

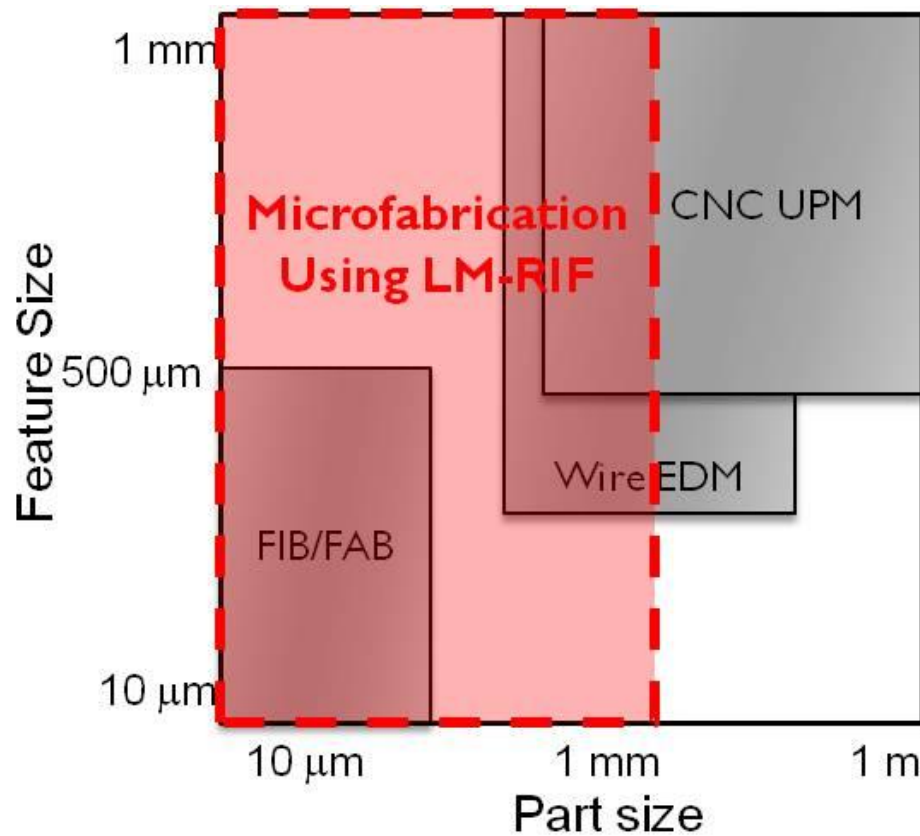


Figure 3.1. The feature size versus part size comparison are presented for various types of fabrication approaches; focused ion beam and fast atom beam (FIB and FAB), wire electrical discharge machining (Wire EDM), and computer numerical control ultra precision machining (CNC UPM). The lost mold-rapid infiltration forming (LM-RIF) process fills a gap in manufacturing size regime above semiconductor fabrication sizes in the sub-10 micron range, and below traditional bulk machining near 300 micron features while adding the ability to simultaneously manufacture large arrays of parts. Furthermore, LM-RIF can be integrated with novel design approaches to create innovative structural components for a variety of applications including surgical instruments.

The LM-RIF process, illustrated in Figure 3.2, is part of an integrated, iterative approach to both improve the mechanical design of the part being manufactured; via the design feedback loop, as well as improve the fabrication process itself; via the fabrication feedback loop that optimizes material mechanical properties. The LM-RIF process and manufacturing approach have been developed over multiple generations of parts to improve both the basic material properties and component geometry. Antolino et al. describes the basic approach to improve

material properties based on the manufacture of three mole percent yttria zirconia polycrystalline (3YTZP) mesoscale bend bars that are 15 x 20 x 370 microns in dimension [3, 4]. However, in these preliminary reports, neither larger parts that can completely bridge the manufacturing gap in Figure 2.1 into the 1 mm regime while maintaining micron scale features nor additional materials that expand the design space were reported. The innovations required to meet these challenges will be highlighted in this process overview chapter.

As illustrated in Figure 3.2 and Figure 3.3, the basic process begins with an initial mechanical design based on both size and shape optimization techniques [5]. Once the first generation design is finalized, a lithography-based mold fabrication step is used to translate the computer aided design (CAD) into a two or three dimensional mold. After molds are fabricated, a concentrated colloidal suspension (i.e., 40 to 50 volume percent solids) is formulated using the precursor particulate materials. The colloidal suspension is then cast into the mold via a screen printing squeegee, and solvent is removed by evaporation under carefully controlled conditions to minimize capillary forces to prevent part cracking. Final parts are obtained after a combined mold removal and sintering step. The finished parts are characterized, and appropriate changes can be made to the mechanical design, colloidal suspension parameters, or both to optimize components in subsequent generations. Through this process development, the ability to produce large arrays of parts from both metals and ceramics, as well as parts ranging in thickness from 10 to 400 microns has been demonstrated [6].

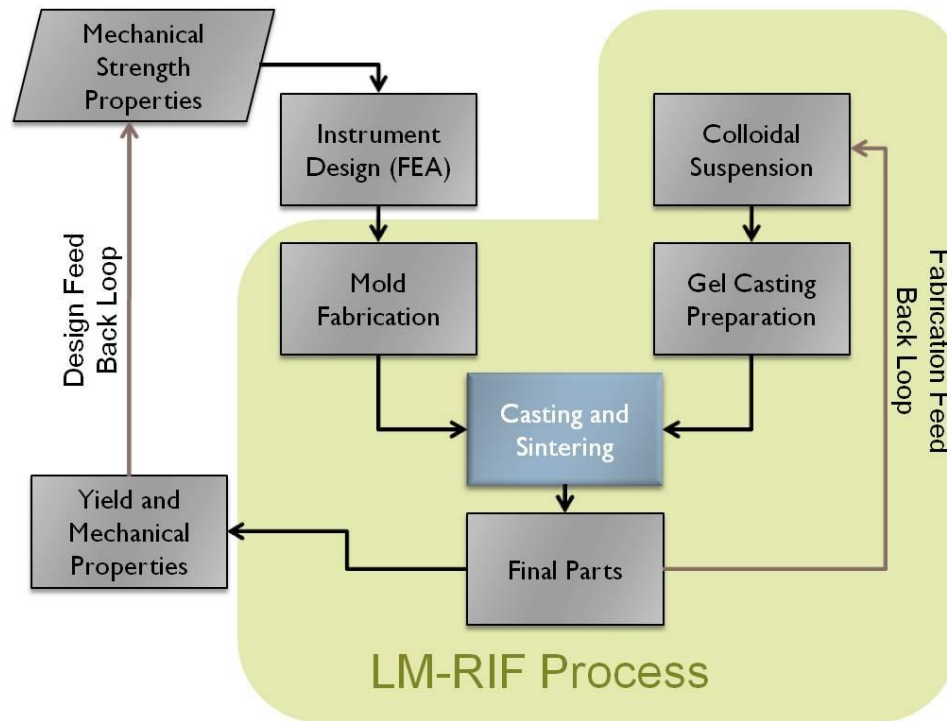


Figure 3.2. The LM-RIF chart. The process starts with a theoretically optimized mechanical design based on initial determination of mechanical properties, followed by mold fabrication, colloidal processing, and final part fabrication. Final parts are tested and characterized, with the mechanical properties used to design changes in the design and fabrication for future generations of materials and/or design components. Changes in the design geometry of the part are completed through the Design Feedback loop, while changes to the manufacturing process and material system are completed through the Fabrication Feedback loop.

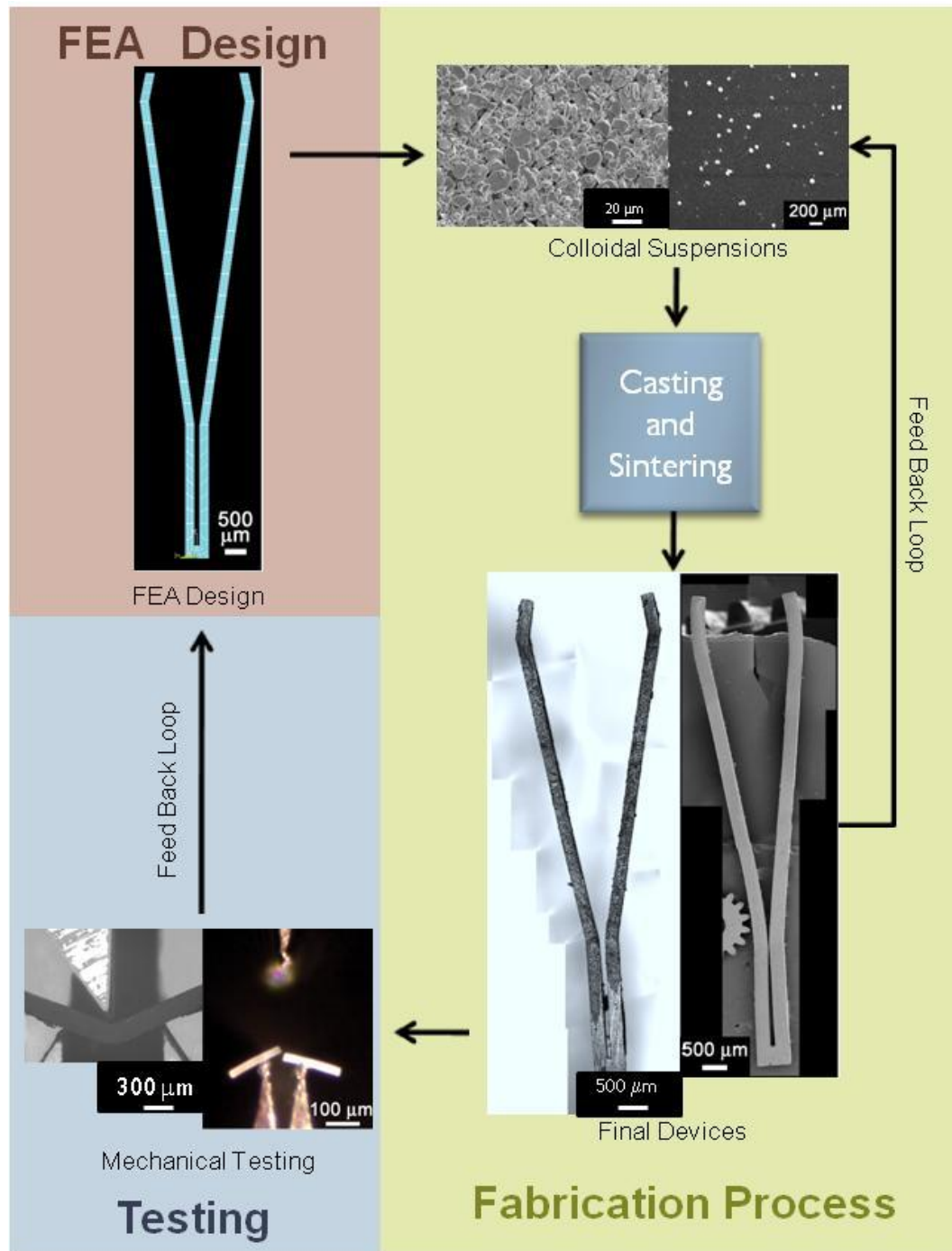


Figure 3.3. The fabrication, design and testing relationships are shown for manufacturing surgical instrument prototypes. In each of the sections, metal 300 series powder and prototypes are shown on the left, with 3YTZP prototypes shown on the right. In FEA Design, optimized instruments are designed with known strength values from mechanical testing. In the Fabrication Process, the LM-RIF process is employed and colloidal chemistry is used to concentrate and disperse particulates of 300 series steel and 3YTZP. The concentrated suspensions are cast into

lithography based molds and sintered. Once sintered, free-standing parts are ready for mechanical testing. At this stage, characterization of the prototypes takes place, and changes to the colloidal suspensions can be made through the fabrication feedback loop. Testing of the as fabricated material takes place using appropriate mechanical tests (ceramics in 3-point bending and metallic parts with tensile tests). As this process is iterative, processing improvements that lead to strength variations are fed back into the design, where new topologies can be generated.

Mask Design and Fabrication

The optimized design approach, developed by Frecker and co-workers [1, 5], is used to generate a photomask. In this process, the prototype parts are arranged in a layout to facilitate a high volume of parts fabricated per unit area, while satisfying part proximity constraints. Successful part spacing was determined to be a function of the mold thickness with the inter-part spacing at half of the mold thickness. In Figure 3.4, two examples of photolithographic mask layouts are shown. Both the surgical forceps and the C3M device masks are designed for 400 micron thick molds and patterned as standard negative-type photolithography masks with chrome on soda-lime-silica glass. The separation distances among parts, also known as the proximity of parts, on the mask layout is determined via the designed mold thickness, with a 1:1 ratio of mold thickness to inter-part spacing. While each patterned part on the photomask is designed for a particular mold thickness, it is possible to have single photomasks with multiple sections designed for various part thickness.

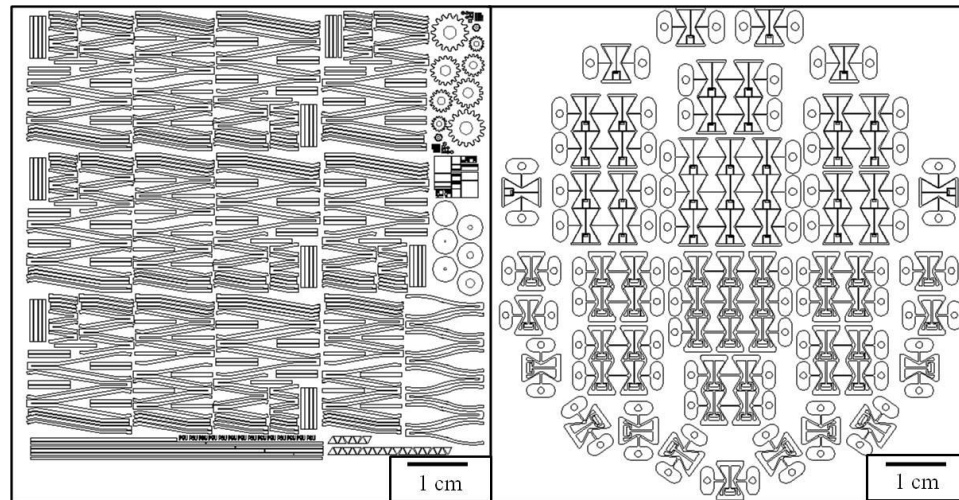


Figure 3.4. Two examples of photolithographic mask layouts are shown: Left, surgical forceps, and bend bars; Right, other geometric shapes and C3M devices are depicted. On the left hand side there are about 600 parts. On the right hand side there are almost 50 C3M parts. Ceramic, metal or particulate composites for LM-RIF can be used to make components from masks such as those illustrated.

Mold Fabrication in Two and Three Dimensions

In the mold fabrication process, polished polycrystalline, high purity (greater than 99.5 weight per cent) alumina substrates (courtesy of Kyocera Corporation or Coorstek) are used to avoid handling components between processing steps. SU8 (Microchem Corp.) photoresist molds are fabricated on the substrates using a modified UV lithography process. Initially, an antireflective coating of AZ-Barli-II 90 is spin coated onto the substrate to eliminate mold defects created by light scattering from the substrate surface. Secondly, a 10 μ m under layer of SU-8 photoresist is spin coated to form the bottom layer of the mold. This under layer assures part separation from the substrate before sintering and acts as a smooth, flat bottom surface for the mold. Finally, a SU-8 layer with the targeted thickness is deposited using a calculated volume technique adapted from Lin et al. [7] In this process, a known volume of SU-8 photoresist is deposited at 80°C onto a substrate of specific surface area. The photoresist is prebaked at 120°C

for 4 hours, with a temperature ramp of 2°C per minute, during which the solvent is evaporated from the resist, and self leveling takes place. Next, an initial optical exposure of 3 mJ/cm²/micron (thickness) is performed. The photoresist then undergoes a post exposure bake at 55°C for 30 minutes with a temperature ramp of 2°C per minute, and finally the resist is developed for 30 minutes with slight agitation. The mold layer is developed in propyleneglycol monomethyletheracetate (PGMEA, SU-8 Developer, Microchem Corp.). Following development, one of two additional mold manufacturing paths can be taken. For a single layer (i.e., two dimensional molds and subsequent components), a second flood exposure of approximately 4200 mJ/cm² in concert with an additional heat treatment at 180°C for 20 minutes fully crosslinks the resist. Alternatively following development, two or more mold layers can be laminated at 100°C with slight pressure (0.01 MPa). The process of stacking and laminating multiple mold layers is used to create three dimensional mold cavities and, as a consequence, more complex, three dimensional components. During the exposure steps, a UV light filter (Omega Optical, PL-360-LP) ensures vertical side walls in the final mold [8]. Figure 3.5 shows the UV lithography layering sequence, as well as the steps going from CAD design, to mask, to final mold cavity. In Figure 3.5 B, a cross sectional view of mold cavities is shown with varying length and width. It is noted that as mold thickness increases, minimum feature size increases. The minimum, stand alone, single CAD feature size for the parts fabricated herein was taken to be approximately 1/15 of the mold thickness, while inherent features of larger part geometries can be as small as 2-3 micrometers as shown in Figure 3.6 [9]. In Figure 3.6, the theoretical calculation of feature size as a function of mold thickness, developed by Yang et al. assumes a constant UV light source wavelength, a worst case scenario of a 5 micron contact gap between the photoresist surface and the photomask, and a photoresist thickness range of 25 to 1500 microns.

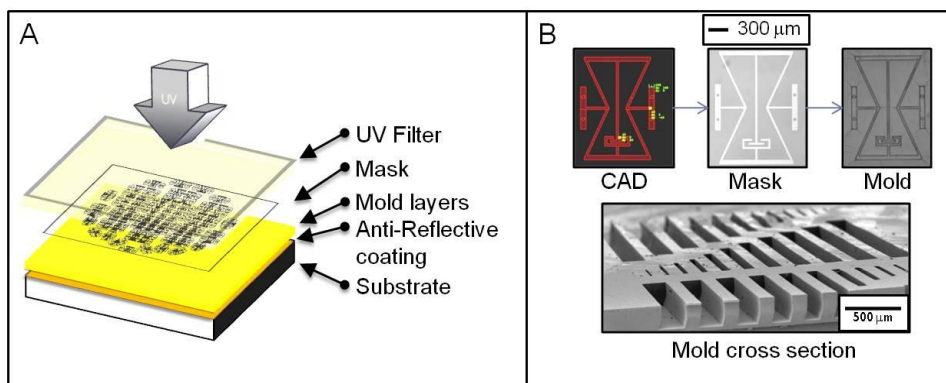


Figure 3.5. A summary of innovations for LM-RIF in the mold fabrication. (A) lithography stack, with mold fabrication directly on the refractory substrate. Without the UV filter, trapezoidal cross-sections (i.e., non-orthogonal side walls, are present in the mold cavity. (B) the mold fabrication process is shown, starting with the computer aided design (CAD) that dictates the mask layout, and finally being patterned as the mold shown in the optical photomicrographs. (C) A mold cross section is shown in the SEM photomicrograph highlighting the various channel widths possible for the 250 μm resist thickness.

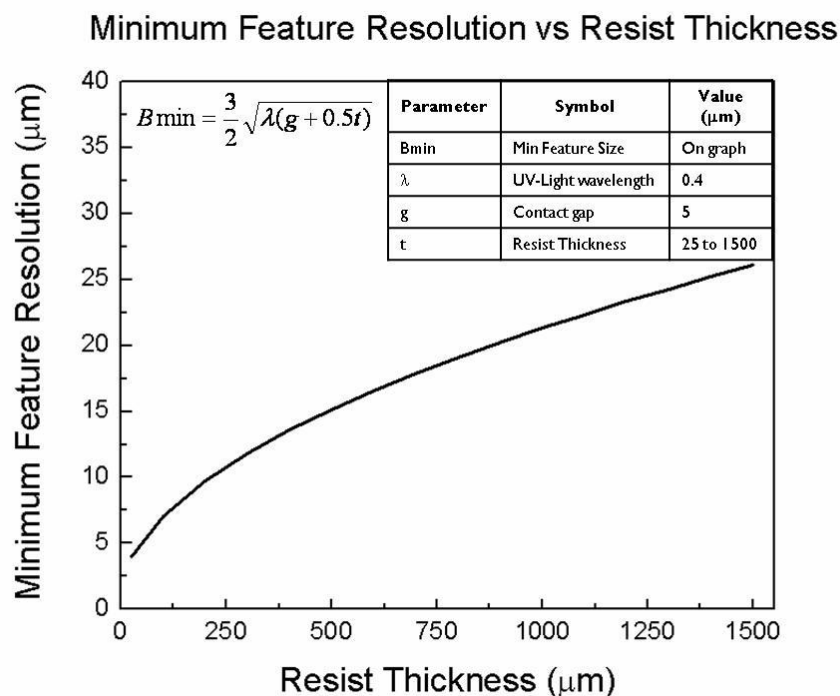


Figure 3.6. The minimum feature resolution increases with increasing photoresist thickness, as calculated by Yang et al. [9]. The UV light source has a wavelength of 400 nm, and the contact gap between the photoresist and the mask is assumed to be 5 μm for our process. The minimum feature resolution is then calculated with the inset equation.

The ability to extend the LM-RIF process to three dimensions is needed to facilitate new and better instrument designs, as well as to broaden the scope of applications for the LM-RIF fabrication method. While 2D lithography methods utilizing SU-8 have been established for almost 15 years [10], new 3D SU-8 techniques are only beginning to be developed. A brief overview of the three most promising techniques, as outlined by del Campo et al. [8], presents the advantages and disadvantages of each technique, and permits the most compatible 3D molding technique to be chosen for the LM-RIF process. These techniques as applied to the LM-RIF process are described next.

Three-dimensional molds can be produced using a layer by layer stacking sequence in one of three options shown in Figure 3.7. In option A for the LM-RIF process, a base mold is fabricated onto an alumina substrate, and subsequent layers are added on top of the base mold prior to mold infiltration. The subsequent layers are fabricated on top of polyimide film, which is then flipped upside down and laminated on top of the base mold. After adhesion of the additional layer to the base layer, the polyimide film is peeled from the top of the layer stack leaving a layered mold on the alumina substrate. This mold will then be infiltrated with the particulate slurry, followed by mold removal and sintering. In option B, molds are once again fabricated on both the base alumina substrate, as well as on top of a polyimide film. However, in this case, the mold layers are infiltrated with the particulate slurry prior to the lamination step. Once the filled layers are laminated, mold removal and sintering can be performed. In option C for LM-RIF, a base mold is fabricated on an alumina substrate and directly filled and planarized, just as in the 2D case. Following infiltration, a new layer of photoresist is deposited on top of the filled base mold and patterned using the lithography process described previously. After the new layer is patterned, it too can be infiltrated and the process repeated for the desired number of layers.

The most straight forward attempt for 3D fabrication for the LM-RIF process is option A. In this process, molds are filled in one step to eliminate lamination defects between layers.

However, filling under overhanging mold sections could prove difficult, as entrapped air and deforming molds could cause defects in final parts. Another potential limitation with process A is that aligning the mold layers during mold fabrication could prove difficult. In Process B, molds are filled prior to lamination in order to fill under overhanging mold sections. However, in this process, layers will be difficult to align, and laminating dry gelled green bodies could lead to various defects [11]. To avoid pressing two dry gelled layers together, process C fabricates subsequent mold layers on top of previously filled molds. In this way, complex overhanging shapes can be fabricated without the problem of laminating dry gelled green bodies. Problems may arise in process C as it could prove difficult to spin coat SU-8 on top of an irregular, particulate bed. Additionally, resist incorporation into a green body could cause poor lamination as well as defects during organic removal. Finally, the green body will be subjected to the entire lithography process, including heating and the resist developing solvent. In Figure 3.7 top, method A was chosen for initial trials to demonstrate the fabrication of three dimensional molds. In Figure 3.7, bottom, method A was used to laminate two molds layers. The lamination method showed good adhesion across the substrate between the top and bottom layers, along with minimal distortion of the patterned layers that may occur as the layers are pressed together. In this initial lamination trial, sample photoresist layers of a triangle pattern and a square pattern were used to test the lamination process. These patterns were chosen based on their simplicity, uniform patterning that would not require large overhanging mold sections.

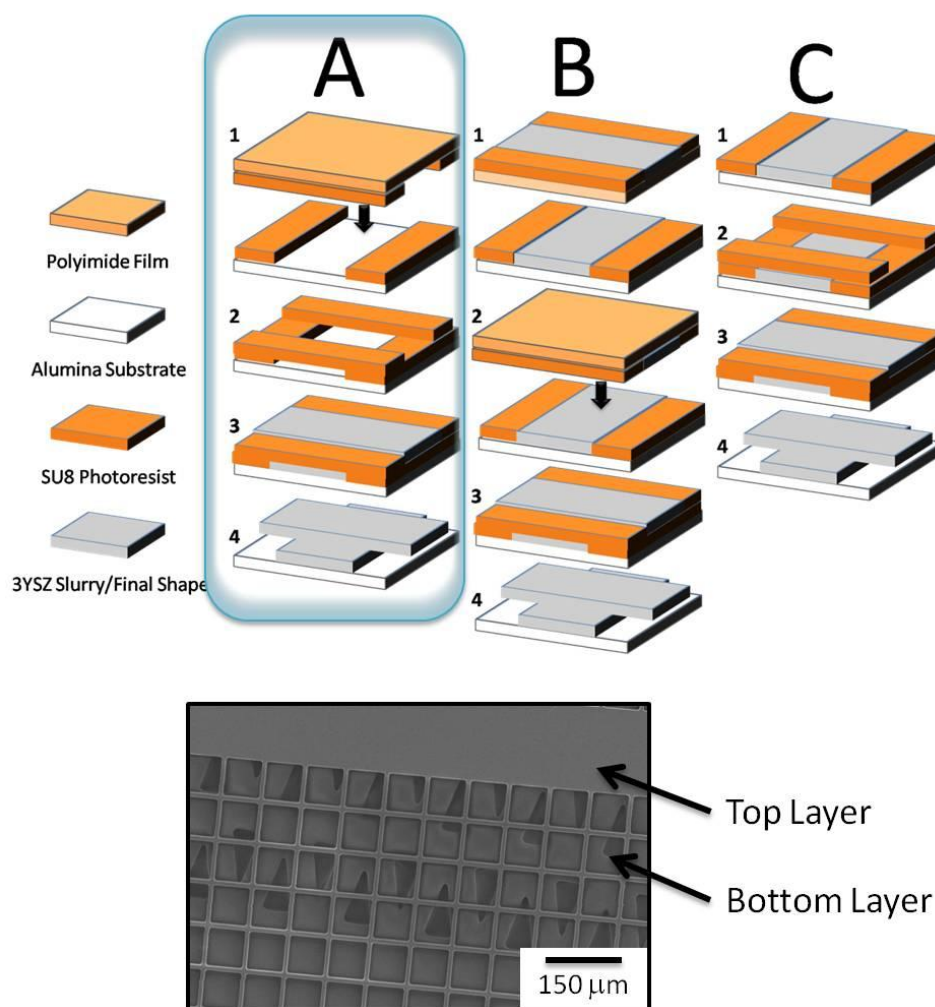


Figure 3.7. Top: Three methods to create 3D multilayer components by the LM-RIF process are shown based on the recent discussion by del Campo [8]. In Method A, molds are laminated before infiltration. Method B, molds are infiltrated prior to filling. Method C, the mold is infiltration as the layers are added. Bottom: An SEM photomicrograph of two laminated layers of photoresist molds using Method A is shown from the top view. The layer of photoresist patterned with square cavities was laminated over an array of triangular molds patterned into the bottom layer of photoresist. Negligible distortion is present in the photoresist patterns for the top and bottom layers and uniform adhesion was observed across the two layers laminated on the substrate.

Colloidal Suspension Preparation

Well dispersed, high solid loading suspensions are required during particulate processing to fabricate dense parts with desired mechanical integrity. The properties of the particulate that is being processed, including particle size distribution, shape, and chemistry, can affect the processing parameters used to create a colloidal suspension [11]. In particular, the high density from uniform particle packing of well-dispersed particulate has a positive influence on the sintering of the particulate body [12]. Likewise, poorly packed particulates from poorly dispersed, agglomerated particulates results in poorly sintered materials with trapped porosity, grain growth and other characteristics that compromise mechanical properties. [12] Thus, the particulate processing characteristics ultimately influence the final mechanical properties of components. If the processing parameters create colloidal suspensions with solids content too low, agglomerated particulates or other particulate created defects, the packing density in green state is compromised, and sintering to high density, to achieve mechanically strong parts, will not take place. Grain growth also takes place. Conversely, desired mechanical properties dictate processing parameters used to create suitable colloidal suspensions from particulates. If the desired mechanical strength is relatively low, and/or a porous final body is required for a particular application, the processing parameters can be modified to fit these requirements. The size and shape topology of the mechanical design also affect the processing parameters, as intricate designs may require special processing parameters. Finally, whether mechanical properties are dictated through design, or measured through experimentation, the mechanical design will need to be modified to fit within the given manufacturing system. Principally, as well as in the context of the LM-RIF process, powder processing parameters, mechanical properties, mechanical design, and initial powder properties are interrelated aspects of powder processing. As shown in Figure 3.8, variation in each of these attributes directly influences the others, and

thus, when working to improve the system as a whole, the impact of changes in one attribute must be evaluated for all other aspects. For example, properties of the particulate material being incorporated into the LM-RIF process, such as particle size, particle shape, agglomeration characteristics, density, and chemical stability, play a direct role in the processing parameters utilized, such as solvent environment, colloidal dispersion scheme, drying method, binder removal, and sintering. Furthermore, the properties of particulates, both alone, and in conjunction with the processing parameters have direct impacts on mechanical properties and mechanical design of fabricated devices. Additionally, mechanical design can dictate a specific material property, such as biocompatibility, high elastic modulus, or even desired feature size. These specifications influence the starting material powder material type and particle size, as well as desired mechanical properties, and can even constrain processing parameters. The interaction of some processing parameters, such as sintering temperature, on mechanical properties, has been described by Antolino [13]. Therefore, it is clear that the system of interactive particle processing must be considered as a whole, without neglecting the impact of one area on another. The colloidal processing for both an aqueous suspension of yttria partially-stabilized zirconia particles and a non-aqueous suspension for the 300 series stainless steel particulates will be described.

Interactive Particulate Processing

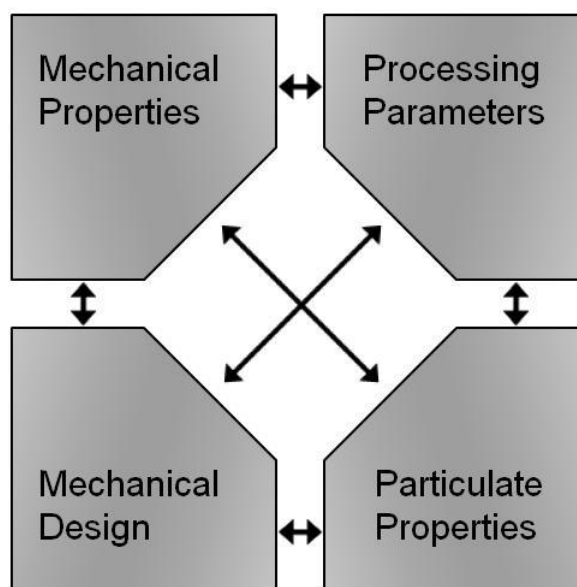


Figure 3.8. Powder processing steps are related to every aspect in the LM-RIF process, including mechanical design, mechanical properties, processing parameters, and particulate properties. While working to improve the LM-RIF process, all powder processing attributes must be considered as part of the overall system, and not separately. Arrows indicate the dependence of each processing step on one another.

Colloidal Processing of Yttria Tetragonal Polycrystalline Zirconia

Yttria tetragonal polycrystalline zirconia, YTZP, (Tosoh Corp. TZ-3Y) was dispersed and concentrated by chemically-aided attrition milling (CAAM) [14] to form a colloidal suspension. The aqueous dispersion scheme was developed in previous work by Antolino and Hayes et al. [3] and will not be described herein. After well dispersed, high solids loading suspensions are obtained (40 to 50 volume percent YTZP), gel-casting monomers and crosslinker, as well as binder and plasticizer are added to the system to strengthen the green part during further processing. A binary monomer system of methacrylamide and 1-vinyl-2-pyrrolidone along with the crosslinking agent N,N' -methylenebisacrylamide, are used in a 1.5:1.5:1 ratio. Preliminary experiments showed that this ratio had high solubility, as well as high strength, allowing a greater

volume percentage of high strength gel in the particulate matrix. Separately, a mixture of polyvinyl alcohol and polyethylene glycol in a 1:1 ratio as well as a mixture of polyvinyl pyrrolidone and triethylene glycol in a 2:1 ratio were added as a binder/plasticizer system. To optimize the yield of parts obtained from the LM-RIF, various amounts of gel-casting precursors, and binder/plasticizer were added to the system. As shown in Figure 3.8, the relationship among the attributes of powder processing is complicated. However, establishing the complex interrelationships among processing variables can reveal the critical variables and provide guidance for additional scientific study. Therefore, a design of experiments (DOE) was utilized to determine the most influential parameters [15]. The primary metric for the DOE was green part and sintered part yield as a function of the range of process parameters.

Initial results of the DOE work indicate that the addition of gel, binder, and a tailored solids loading significantly increases part yield from no part yield to 20-40% depending on aspect ratio and design of devices [15]. The DOE focused on both optimizing the part yield via changing the levels of gel content, solids loading, and binder content, plus assessing the part yield as a function of aspect ratio and device design. DOE results show that green part yield increases with higher binder content, lower gel content, lower solids loading and smaller device aspect ratio. Higher green part yield with increasing organic content was expected, but these results also show that the system favors the less rigid (crosslinked) binder to the more rigid (high crosslinked density) gelled monomer. Of course, the downside to higher organic content is that the parts poorly sinter because of low particle packing density with significant residual porosity present in the sintered components. We have found that the solids loading needs to be higher than 35 vol% to obtain dense ceramics parts after sintering. Additionally, the binder content is limited to 10 vol% due to solubility restrictions and the gel content must be at least 5 vol%, otherwise yield significantly decreases. At the lower limit of solids loading, set to the 40 vol% based on porosity considerations, the DOE results indicate that the gel content should be set to 15 wt% of water in

the system, with binder content set at 8 vol%. Further details of the DOE studies can be found in Yuangyai et al. [15].

316L Stainless Steel

Stainless steel, in particular 316L series, has been used previously as a surgical instrument material, and is available in powder form, permitting its incorporation into the fabrication scheme. Details for the metal formulations are given in Chapter 5 and will only be briefly described herein. Non-aqueous metal suspensions were developed using 316L series stainless steel powder (Carpenter Steel) to minimize oxidation of the powder during the process. The stainless steel suspension consists of an ethanol solvent, with oleic acid serving as dispersant by establishing a steric barrier to agglomeration among the particulates. The final, high solid loading, non-aqueous suspensions were then cast into the molds as described below.

Mold Infiltration and Sintering to Form Final Components

Yttria Partially-Stabilized Tetragonal Zirconia

Prior to mold infiltration, the gelation reaction was initiated, permitting a working time of approximately 25 min before the onset of irreversible cross-linking by the gel cast system. During the infiltration process, an excess of ceramic slurry was placed on top of the mold and worked into the mold cavities with a squeegee while simultaneously removing any bubbles. Following gelation, the samples were placed into an ethanol bath, to displace the water in the green gelled body with ethanol. The addition of the ethanol drying step limits cracking in the

green body by reducing the capillary drying forces. Capillary forces in the pore structure of green bodies are related to surface tension via Equation 2.1, given by Kowalski [16],

$$P^{cap} = \frac{-2\gamma}{r_c} \quad (2.1)$$

In equation 2.1, pore structures are assumed to be cylindrical, P^{cap} is the capillary pressure, γ is surface tension of the solvent, and r_c is the characteristic radius of curvature of the cylinder. For a wetting fluid, the fluid is in tension, giving rise to a negative value of P^{cap} . At 25°C, water with a surface tension at 72 mN/m creates significantly higher capillary forces than ethanol with a surface tension at 22 mN/m [17]. For example, assuming a characteristic radius of 10nm the P^{cap} is negative, attracting the particles, and -14 MPa and -4.5 MPa for water and Ethanol, respectively.

Alternatively, the ethanol can be removed via critical point drying [18]. Recently, we established that final part yield is increased to over 90 percent when critical point drying employed. The excess slurry on top of the mold is removed via planarization with 2400 grit polishing paper, again using ethanol as the planarizing liquid. The planarization step minimizes the top surface defects known as ‘dishing’ observed and corrected by Antolino et al. [3, 4].

Mold removal and sintering take place in a single furnace cycle in ambient atmosphere. First, the mold is removed via combustion at 400-600°C, followed by a sintering cycle to 1400°C for 2 hours. A typical furnace cycle is 1°C/min to 400°C with a 1hr hold, 1°C/min to 600°C with a 1hr hold, 5°C/min to 1400°C with a 2hr hold, followed by a furnace cool. Figure 3.9 A; shows the mold infiltration, and B; drying, and, finally, demolding and sintering processes for the ceramic material.

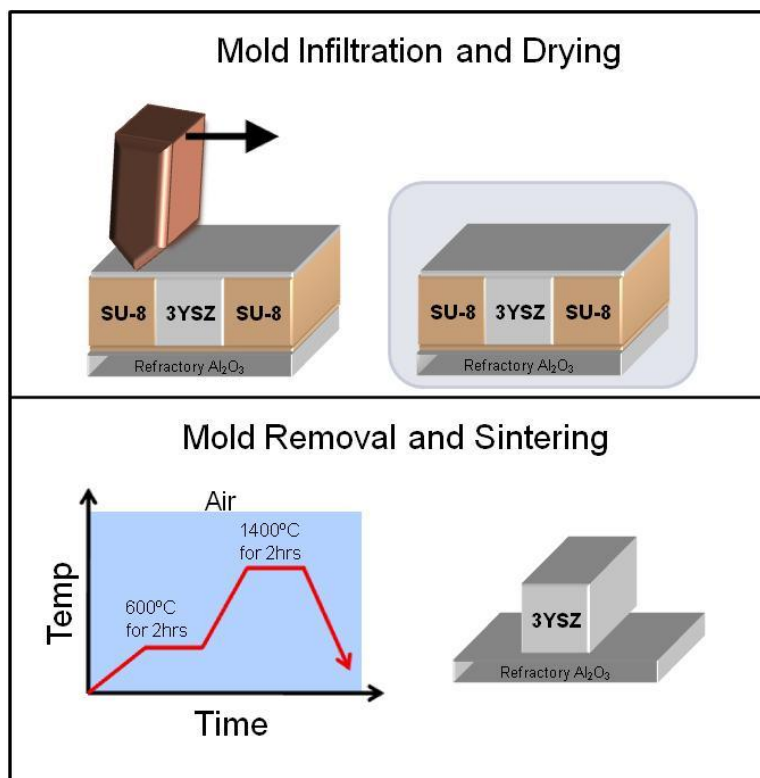


Figure 3.9. Uniform top surfaces for LM-RIF parts are produced by a planarization process. Top: Molds are infiltrated via a screen printer squeegee. Once infiltrated, parts are allowed to gel in a 100% humidity environment, and then dried in ambient conditions. Alternately, we have recently explored critical point drying with part yields exceeding 90 percent. Bottom: After sintering in ambient, air atmosphere, the final part is left free standing on the original substrate [3, 4].

316L Stainless Steel

In the present work, novel formulations based on 316L series stainless steel were developed. The stainless steel suspensions were cast into the SU-8 molds using the same squeegee technique described for the ceramic suspension. A thin layer of excess slurry was left on top of the mold to ensure complete mold filling prior to drying. Cast molds were dried in ambient atmosphere, followed by the removal of the excess slurry via a polishing cloth with ethanol as the polishing solvent. Figure 3.10 (top) shows the mold infiltration and drying process for the metal suspensions. In contrast to the finer YTZP particulates at nominally 65 nm, the

capillary pressure for the nominally 10 micron diameter stainless steel particles is estimated at -0.144 MPa and -0.045 MPa for water and ethanol, based on equation 2.1 with a characteristic radius of 1 micron, respectively. The increase in particle size from the ceramic to the metal system results in a decrease in the capillary pressure by two orders of magnitude. Thus, the coarser stainless steel green parts do not experience the larger capillary forces and green part yields are inherently higher than those obtained with the YTZP parts except when extra measures such as critical point drying are used.

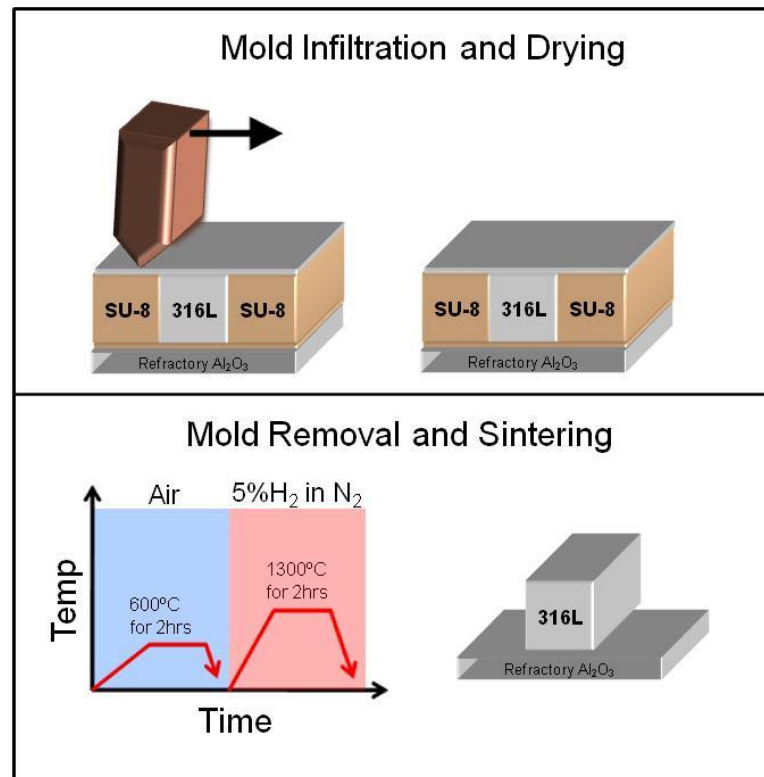


Figure 3.10. Similar to ceramic fabrication, all processing takes place on the refractory substrate. Top (from left), SU-8 molds are infiltrated with the metal slurry leaving a thin layer on top of the molds. The thin overburden layer is removed via the planarization process following drying in ambient conditions. Bottom (from left), the molded parts are subjected to two furnace treatments, an initial processing step in air removes organic additives including the binder system and mold material. Part sintering takes place in a reducing atmosphere of 5 mol percent hydrogen in nitrogen known as forming gas. Final parts are free standing on the original substrate.

Following infiltration and drying, the stainless steel parts are sintered in a two stage process. Initially, the mold is removed by thermolysis in the ambient, air atmosphere at 600°C. After demolding takes place, the free standing metal parts are sintered in forming gas (5% H₂ in N₂) at 1300°C for 2 hours. Figure 3.10 (bottom) summarizes the organic removal and sintering processes for the metal suspensions.

Following fabrication, free standing parts are evaluated for mechanical properties, as well as device functionality. As shown in Figure 3.2, changes to the mechanical design, as well as changes to the colloidal processing formulations can be made through the appropriate feedback loops, permitting fine tuning of the LM-RIF process.

Example prototype parts are shown below in Figure 3.11. Truly meso-scale parts can be fabricated using the LM-RIF process. Additionally, while just one example of a metallic and ceramic part is shown, these parts were manufactured in a large array of similar parts.

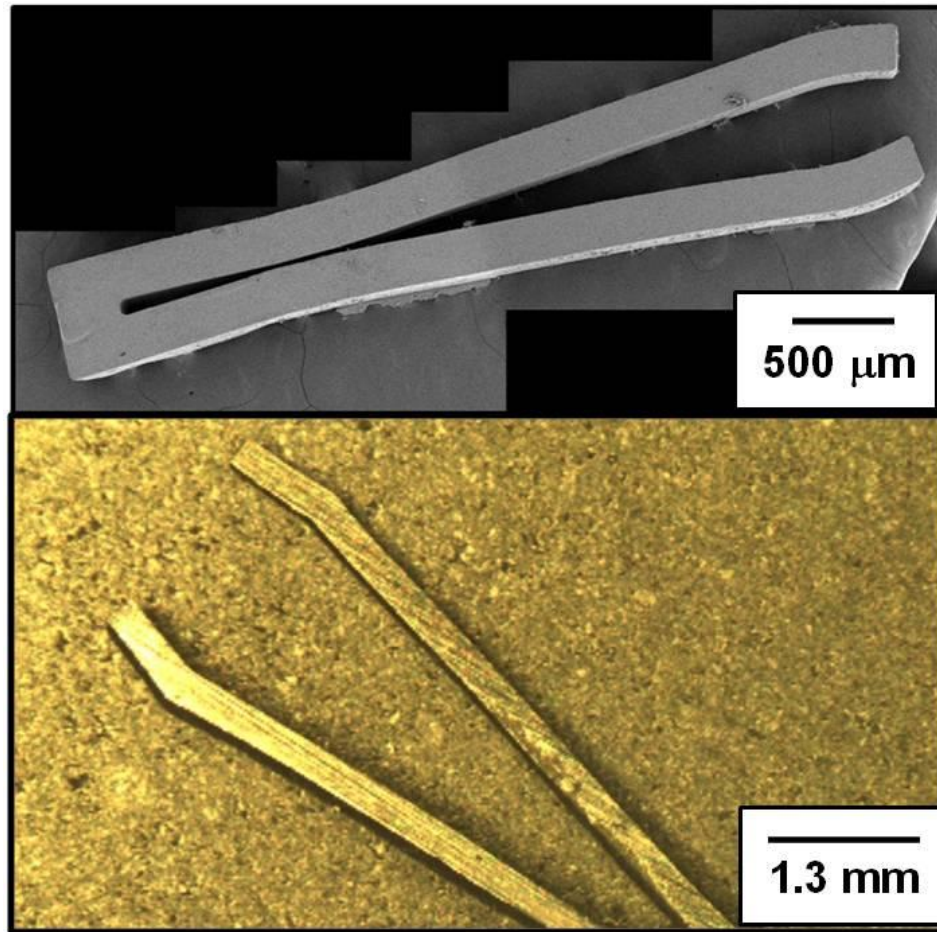


Figure 3.11. Example forceps parts are shown as fabricated with the LM-RIF process. The mesoscale parts have a size scale on the order of mm and critical dimensions on the order of microns. Top: An SEM image of a ceramic forceps is shown, while Bottom: an optical image of metallic forceps is shown.

Conclusion

In conclusion, a fabrication process on the meso-scale has been developed that can; (1) fabricate large arrays of surgical instruments; (2) be complementary to particulate based material systems; and, (3) have 3 dimensional capabilities. Furthermore, using this manufacturing technique for both surgical instrument and C3M device design is attractive because free standing parts are fabricated with the desired large aspect ratios while retaining good resolution on the

micron scale stemming from the lithographic based molds and colloidal infiltration processes.

Both YTZP and stainless steel components have been manufactured with the LM-RIF process to emphasize the range of materials possible with the fabrication approach.

References

1. Mehta, V., Hayes, G.H., Frecker, M.I., Adair, J.H., *Design, Fabrication, and Testing of Meso-scaled Cellular Contact-aided Compliant Mechanisms*, in *ASME 2010 Conference on Smart Materials, Adaptive Structures and Intelligent Systems, SMASIS2010*. 2010: Philadelphia, Pennsylvania, USA.
2. Aguirre, M.E., G. Hayes, M. Frecker, N. Antolino, and J. Adair. *Fabrication and Design of a Nanoparticulate Enabled Micro Forceps*. in *32nd Annual Mechanisms and Robotics Conference (MR) Topic: MR-8 Medical Devices and their Applications*. 2008.
3. Antolino, N.E., G. Hayes, R. Kirkpatrick, C.L. Muhlstein, M.I. Frecker, E.M. Mockensturm, and J.H. Adair, *Lost Mold Rapid Infiltration Forming of Mesoscale Ceramics: Part 1, Fabrication*. *Journal of the American Ceramic Society*, 2009. 92(1): p. S63-S69.
4. Antolino, N.E., G. Hayes, R. Kirkpatrick, C.L. Muhlstein, M.I. Frecker, E.M. Mockensturm, and J.H. Adair, *Lost Mold-Rapid Infiltration Forming of Mesoscale Ceramics: Part 2, Geometry and Strength Improvements*. *Journal of the American Ceramic Society*, 2009. 92(1): p. S70-S78.
5. Aguirre, M. and M. Frecker, *Size and Shape Optimization of a 1.0 mm Multifunctional Forceps-Scissors Surgical Instrument*. *ASME Journal of Medical Devices*, 2007. 2(1): p. 015001-1-015001-7.
6. Aguirre, M.E., G. Hayes, R. Meirom, M. Frecker, C. Muhlstein, J.H. Adair, and J.A. Kerr, *The Design and Fabrication of Narrow-Gauge (1 mm Diameter) Surgical Instruments for Natural Orifice Translumenal Endoscopic Surgery*. Under review in *The Journal of Mechanical Design*, 2011.
7. Lin, C.H., G.B. Lee, B.W. Chang, and G.L. Chang, *A new fabrication process for ultra-thick microfluidic microstructures utilizing SU-8 photoresist*. *Journal of Micromechanics and Microengineering*, 2002. 12(5): p. 590-597.
8. del Campo, A. and C. Greiner, *SU-8: a photoresist for high-aspect-ratio and 3D submicron lithography*. *Journal of Micromechanics and Microengineering*, 2007. 17(6): p. R81-R95.

9. Yang, R. and W.J. Wang, *A numerical and experimental study on gap compensation and wavelength selection in UV-lithography of ultra-high aspect ratio SU-8 microstructures*. Sensors and Actuators B-Chemical, 2005. 110(2): p. 279-288.
10. Lee, K.Y., N. LaBianca, S.A. Rishton, S. Zolgharnain, J.D. Gelorme, J. Shaw, and T.H.P. Chang. *Micromachining applications of a high resolution ultrathick photoresist*. 1995: Amer Inst Physics.
11. Adair, J.H., D.A. Anderson, G.O. Dayton, and T.R. Shroud, *A Review of the Processing on Electronic Ceramics with Emphasis on Multilayer Ceramic Capacitor Fabrication*. Journal of Materials Education, 1987. 9(1&2): p. 71-118.
12. Reed, J.S., *Principles of ceramics processing*. 1995: Wiley & Sons.
13. Antolino, N.E., *Lost Mold-Rapid Infiltration Forming: Strength Control in Mesoscale 3Y-TZP Ceramics*, Doctor of Philosophy, dissertation in Materials Science and Engineering, The Pennsylvania State University, University Park, 2010.
14. United States of America Patent, Adair, J.H., T.R. Shroud, G.L. Messing, T.H. Pecora, and M.M. Mandanas. *Dynamic Control and Enhanced Chemical Milling of Ceramics to Submicron Particle Sizes*, 2002.
15. Yuangyai, C., Hayes, G., Antolino, N., Nembhard, H. B., and Adair, J. H. , *Yield Improvement for Lost Mold Rapid Infiltration Forming Process by a Multi-Stage Fractional Factorial Split Plot Design*. International Journal of Nanomanufacturing, 2009. 3(4): p. 351-367.
16. Kowalski, S.J., *Thermomechanics of Drying Processes*. Lecture Notes in Applied and Computational Mechanics, ed. W. Pfeiffer. Vol. 8. 2003, New York: Springer.
17. *CRC Handbook of Chemistry and Physics*. 87 ed. 2006-2007, Boca Raton, FL: CRC Press.
18. Scherer, G.W., *Stress Development During Supercritical Drying*. Journal of Non-Crystalline Solids, 1992. 145(1-3): p. 33-40.

Chapter 4

Constrained Drying for the LM-RIF Process

Introduction

Drying stresses occurring during the colloidal processing of ceramic parts can lead to cracks and warping, both of which are undesirable in the final part [1]. As first presented in Chapter 1, drying stresses can occur both internally, through capillary forces driven by surface tension and the pore size distribution in the particulate bed, and externally, due to mechanical interactions of the drying body with the mold walls as shrinkage occurs.

Within the LM-RIF process, drying stress depends not only on the mold shape, but also the particulate suspension that is drying within the mold. As shown by Equation (2.1) the internal capillary forces due to drying are dependent on the surface tension of the solvent, as well as the particle size within the suspension. In comparison, the aqueous based 3Y-TZP suspension, with particle size of 114nm, experiences two orders of magnitude higher capillary pressure during drying than the ethanol based stainless steel suspension, with particle size of 10 μ m. This is not only due to the particle size, but also a difference in surface tension of the solvent, with the aqueous ceramic suspension having a surface tension of 72mN/m and ethanol based suspensions having 22mN/m. Furthermore, the larger particle size of the stainless steel suspensions allow a higher maximum solids loading of 60vol% particles in suspension compared to that of the ceramic suspensions at 40vol%. A higher solids loading dictates a lower porosity in the drying body, as well as decreases the amount of solvent leaving the green part. For these reasons, the drying process has been identified as the yield limiting process step of the ceramic parts, while in comparison, stainless steel parts easily survive the drying process following casting. In this

chapter, the drying stresses of ceramic 3Y-TZP suspensions after being cast into the mold are investigated.

During the LM-RIF fabrication process, parts tend to crack at the drying stage prior to firing. Drying stresses have long been studied, but an analysis of effect of mold geometry and stresses that arise due to complicated geometry has not previously been developed. This analysis is needed to improve the yield, and therefore improve the surgical instrument design for the complex shapes manufactured with the LM-RIF process. In this chapter, a new model of the mechanical drying stresses arising from the green body shrinking in the complex mold is described.

Throughout the drying literature, there have two main approaches to developing drying models. The first is mechanical modeling of drying, based on pore size and strength of materials [2-11]. The second approach based on thermomechanical models for drying considers drying forces based on chemical potentials in the surrounding atmosphere, as well as within the drying part [12-17]. Katekawa et al. [18] and Metzger et al. [19] have provided detailed overviews of the various drying models, the assumptions, and governing equations.

As shown in Figure 4.1, drying within the boundary conditions imposed by the LM-RIF process takes place while the parts are still contained in the mold. This constrained geometry leads to complicated stress states in the material during drying processes due to capillary effects, mold interactions during shrinkage, and large moisture gradients within the part during drying, as only the top surface of the part is exposed to atmosphere. Additionally, in Figure 4.2, a final part is shown, having multiple cracks that arose during the drying stage of fabrication.

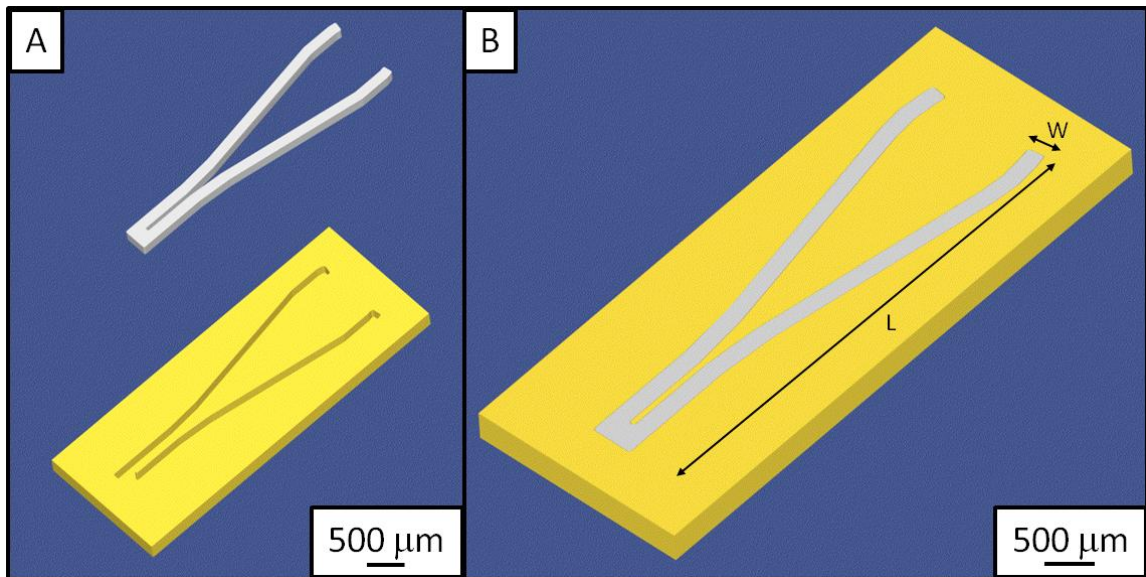


Figure 4.1. The mold used in the LM-RIF process is shown in yellow, while the green ceramic body is shown in white. A: The standard method of drying ceramics is to first demold the part, afterwards allowing the part to dry, where it can shrink freely in all dimensions. B: Within the LM-RIF process, forceps parts are required to dry while still in the mold, leading to constrained drying, where the part cannot freely shrink. In this case, stresses arise not only from drying, but also from the interaction of the part with the mold during shrinking. The aspect ratio of the forceps is defined as L/W .

A few of the drying induced fractures

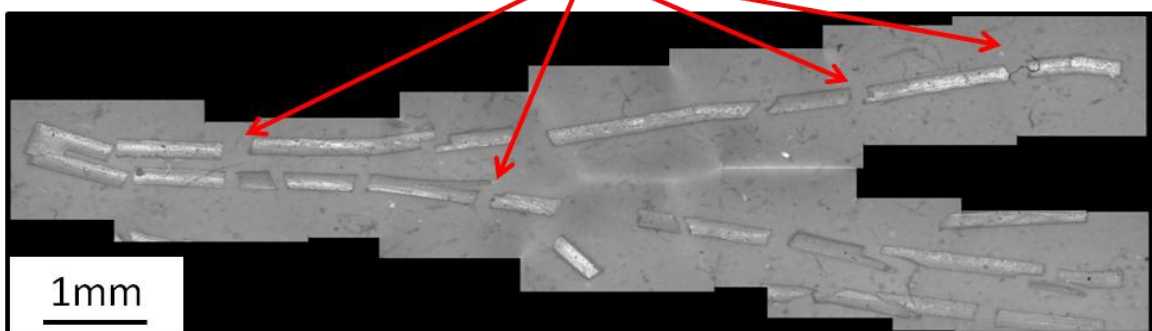


Figure 4.2. An optical image of a sintered, cracked forceps made with the LM-RIF process. In this case, the forceps developed cracks during drying, and was therefore broken upon sintering. Quantifying the stresses experienced by the part during drying will allow engineers to minimize drying forces. Arrows highlight a few of the fracture sites due to drying stresses.

The constrained drying stresses are a function of the geometry of the fabricated part. The aspect ratio of the part, defined as $AR=L/W$ in Figure 4.1 as the forceps arm width to the total length, has a dramatic effect on the magnitude of stress that part experiences during drying. The shape of the forceps arms also plays a role in determining the magnitude of constrained drying stress. For example as shown in Figure 4.3, as the aspect ratio of the forceps increases, sintered part yield decreases due to drying cracks. A series of experiments were carried out to quantify sintered part yield as a function of forceps shape and aspect ratio. Ceramic parts were fabricated via the protocol outlined in Chapter 3 with the suspension formulation given in Figure A.5. Following fabrication, intact parts were counted and a sintered part yield was determined for each of the forceps geometries. Furthermore in Figure 4.3, three variations in forceps shape were analyzed; a straight segmented forceps without gripping teeth, a straight segmented forceps with gripping teeth, and a curved segmented forceps without gripping teeth. The overall magnitude of the constrained drying forces is a function of the amount of shrinkage that the forceps underwent while still in the mold. Features such as teeth and sharp corners in the straight segmented versions of the forceps lead to increased constrained drying stresses.

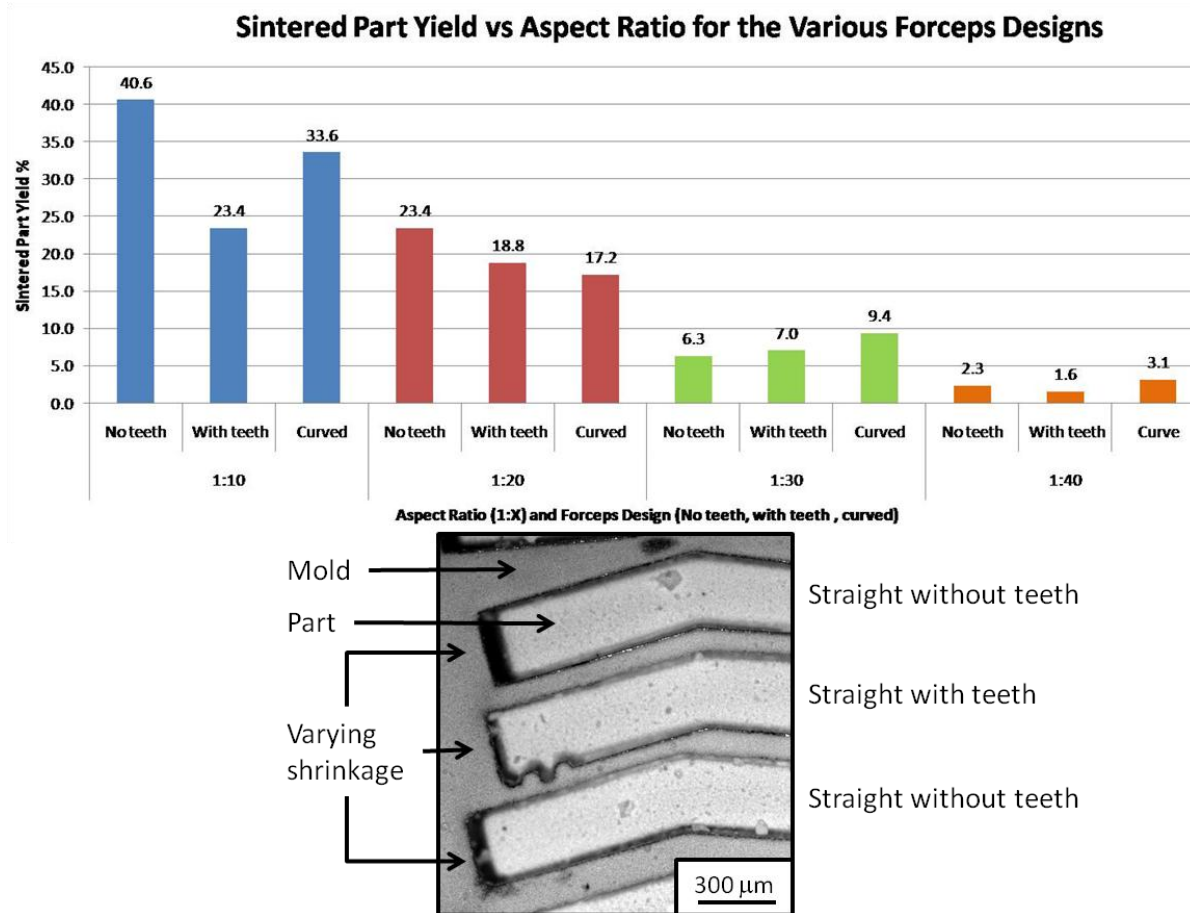


Figure 4.3. Top: The yield of fired parts is given as a function of forceps shape and forceps aspect ratio. As the aspect ratio increases from left right, going from 1:10 to 1:40, the yield of parts that have survived through the drying stage and the sintering stage significantly decreases. Constrained drying stresses in the LM-RIF process lead to drying cracks. Bottom: the shrinkage of dried forceps arms is shown for two different forceps shapes. The straight walled forceps with gripping teeth is the most constrained geometrically, and therefore shows the smallest shrinkage during drying. The smaller the drying shrinkage for a given part leads to increased internal constrained drying stresses, thus decreasing the yield.

In this work, a 1D model and 3D model have been developed to quantify the drying time of forceps parts made with the LM-RIF process. Both models have been experimentally verified. In addition, the 3D model has also been extrapolated to calculate constrained drying stresses during processing. The mechanical properties of the drying materials were measured via diametral compression testing and are discussed in Appendix A. For example, the ultimate tensile strength was determined to be $\sigma_{ult} = 4.06 \pm 0.44$ MPa with elastic modulus $E = 7.9 \pm 1.6$ MPa measured by diametral compression testing. In the three dimensional model, the internal and external moisture potentials were determined by fitting the model to an experimental test. The resulting values were then used in future predictions.

One dimensional model

A one dimensional model originally developed by Ghosal et al. [20] has been adapted and used to evaluate the drying of forceps inside the mold, as well as a the drying of a cylindrical sample. The drying parameters for the ceramic system were tailored to the Ghosal model. This one dimensional model makes the following assumptions about the sample and drying system:

- 1) One dimensional drying is taking place: the sample dries in the mold with from one face with known surface area, and known sample thickness, resulting in unidirectional moisture movement.
- 2) No drying stress, or drying shrinkage is accounted for.
- 3) The moisture gradient is in the vertical direction.
- 4) Constant and known temperature.
- 5) Gravitational effects are negligible.

Within the one dimensional model, the parameters listed in Table 4.1 were used to calculate the normalized moisture mass as a function of drying time. These scalar parameters are adjustable, and can be set to describe a wide variety of particulate systems. For the aqueous based ceramic system, all parameter values were known, with the exception of temperature and relative humidity, which were measured.

Table 4.1. The scalar parameters are given for the 1D model used to evaluate the normalized moisture content during drying as a function of time, t .

<i>Parameter</i>	<i>Value</i>
Temperature	298 °K
Relative Humidity	0.64 %
Drying Part Thickness	400 μm
Volume Percent Solids	40 vol%
Particle Radius	55 nm

In Figure 4.4, the characteristic drying curve is plotted as calculated from the one dimensional drying model, using the above scalar parameters. Calculations were carried out in Matlab (Mathworks, 2007a). A sample program can be found in Appendix C. The constant drying rate period (Stage 1) ends at approximately 0.1 hours (360 s), indicating the time at which the maximum drying stress will occur. Furthermore, equilibrium with the surrounding atmosphere occurs at approximately 0.6 hours (2200s). (Stage 3).

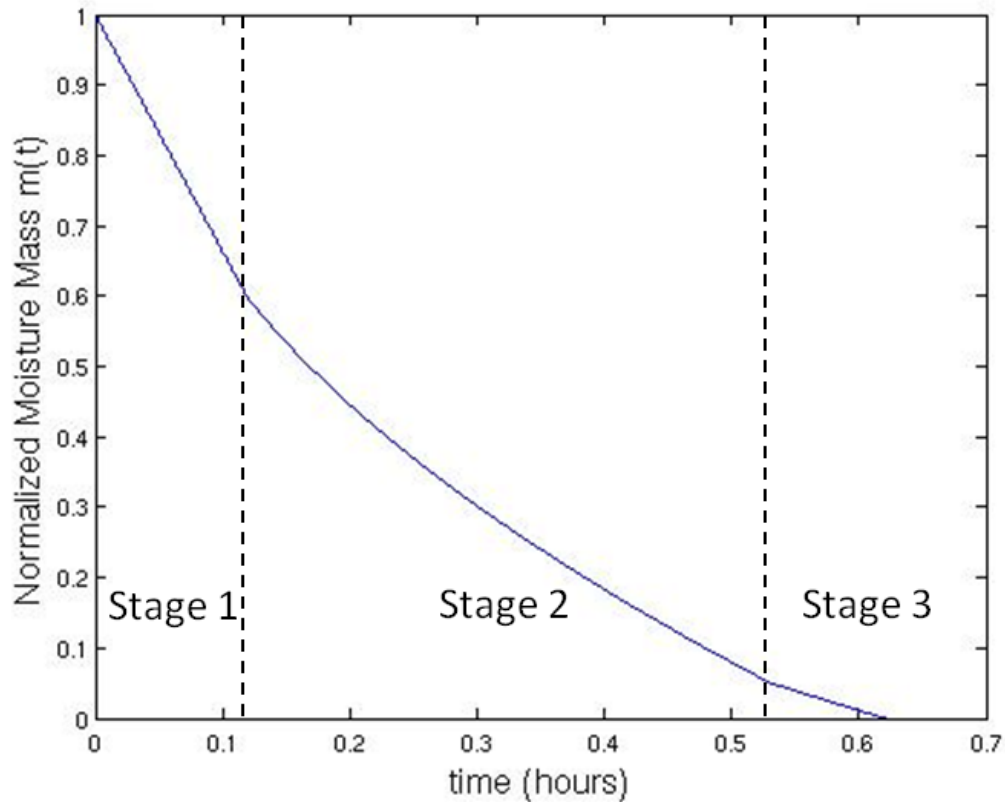


Figure 4.4. Normalized moisture mass versus time is shown, as calculated from the 1D model applied to the forceps drying problem for a thickness of $400\mu\text{m}$. The transition from the constant drying rate period to the decreasing drying rate period takes place at approximately 0.1 hours (360s), indicating the time at which the maximum drying stress will occur. Furthermore, equilibrium with the surrounding atmosphere occurs at approximately 0.6 hours (2200s).

Three Dimensional Model

To calculate drying stresses and shrinkage effects of complex geometries, a more realistic model was implemented, based on the initial work of Kowalski et al. [15]. In this model, drying stresses and dimensional changes are calculated as a function of time and initial conditions, yielding a more complete description of the drying system being investigated for the LM-RIF processed devices. For a comprehensive review, readers are referred to Kowalski et al. [15] to gain a complete description of the drying system equations. However, the fundamental system of partial differential equations, describing the drying body for the three dimensional model is given in Equations (4.2) to (4.5). The boundary conditions used to solve the system of equations, and the initial condition parameters are given in Equations (4.6) to (4.8) and

Table 4.2, respectively. The variables for all equations are defined in glossary in Appendix E. This three dimensional model operates under the following assumptions about the system:

- 1) Gravitational effects are negligible.
- 2) The morphology of the green part is uniform throughout the body.
 - a. This assumption is necessary to easily apply finite element theory and the continuum based modeling approach. In theory, a more complicated model taking into account variation within the green part as a function of part thickness could be developed as an improvement to the model presented here.
- 3) Temperature is constant throughout the entire period of drying.
- 4) Moisture movement is controlled through the moisture potential gradient, as prescribed by the boundary conditions within the system.
- 5) The parts are large enough to be analyzed with a continuum approach.
 - a. The minimum cross sectional dimension of a drying part is 400 μ m. With a particle size of 114nm in diameter, there are $(400\text{E}-6)/(114\text{E}-9) = 3500$ particles along the smallest linear dimension of a drying part.
- 6) There is a linear relationship between the moisture potential and moisture content in the system in the form:

$$\mu^l = -\frac{\gamma^{(x)}}{\rho^s} \varepsilon + C^{l(x)} \theta^l \quad (4.1)$$

The system of partial differential equations describing a drying body:

Dimensional change in the x-direction:

$$M \left(\frac{\partial^2 u_x}{\partial x^2} + \frac{\partial^2 u_x}{\partial y^2} + \frac{\partial^2 u_x}{\partial z^2} \right) + \mathbf{M} + A^* \left(\frac{\partial^2 u_x}{\partial x^2} + \frac{\partial^2 u_y}{\partial x \partial y} + \frac{\partial^2 u_z}{\partial x \partial z} \right) = \frac{\gamma^{(x)}}{C^{l(x)}} \frac{\partial \mu^l}{\partial x} \quad (4.2)$$

Dimensional change in the y-direction:

$$M \left(\frac{\partial^2 u_y}{\partial x^2} + \frac{\partial^2 u_y}{\partial y^2} + \frac{\partial^2 u_y}{\partial z^2} \right) + \mathbf{M} + A^* \left(\frac{\partial^2 u_x}{\partial x \partial y} + \frac{\partial^2 u_y}{\partial y^2} + \frac{\partial^2 u_z}{\partial y \partial z} \right) = \frac{\gamma^{(x)}}{C^{l(x)}} \frac{\partial \mu^l}{\partial y} \quad (4.3)$$

Dimensional change in the z-direction:

$$M \left(\frac{\partial^2 u_z}{\partial x^2} + \frac{\partial^2 u_z}{\partial y^2} + \frac{\partial^2 u_z}{\partial z^2} \right) + \mathbf{M} + A^* \left(\frac{\partial^2 u_x}{\partial x \partial z} + \frac{\partial^2 u_y}{\partial y \partial z} + \frac{\partial^2 u_z}{\partial z^2} \right) = \frac{\gamma^{(x)}}{C^{l(x)}} \frac{\partial \mu^l}{\partial z} \quad (4.4)$$

Moisture potential in the drying body:

$$\frac{\partial \mu^l}{\partial t} + \frac{\gamma^{(x)}}{\rho^s} \left(\frac{\partial^2 u_x}{\partial t \partial x} + \frac{\partial^2 u_y}{\partial t \partial y} + \frac{\partial^2 u_z}{\partial t \partial z} \right) = K^{(\mu)} \left(\frac{\partial^2 \mu^l}{\partial x^2} + \frac{\partial^2 \mu^l}{\partial y^2} + \frac{\partial^2 \mu^l}{\partial z^2} \right) \quad (4.5)$$

Boundary conditions: if moisture is leaving that surface.

$$-\Lambda^{(\mu)} \frac{\partial \mu^l}{\partial x} \Big|_{Boundary} = \pm \lambda^v \left(u_n - \mu_a \right) \stackrel{>}{=} const. \quad (4.6)$$

$$-\Lambda^{(\mu)} \frac{\partial \mu^l}{\partial y} \Big|_{Boundary} = \pm \lambda^v \left(u_n - \mu_a \right) \stackrel{>}{=} const. \quad (4.7)$$

$$-\Lambda^{(\mu)} \frac{\partial \mu^l}{\partial z} \Big|_{Boundary} = \pm \lambda^v \left(u_n - \mu_a \right) \stackrel{>}{=} const. \quad (4.8)$$

Table 4.2. The scalar parameters are given for the 3D model used to evaluate the normalized moisture content, in addition to the constrained drying stresses during drying as a function of time, t .

<i>Parameters and</i>	<i>Definition</i>	<i>Units</i>	<i>Value</i>
-----------------------	-------------------	--------------	--------------

<i>initial conditions</i>			
θ^l	Moisture content %	%	Variable
$\gamma^{(x)}$	Modulus of humid expansion [†] [15]	Pa	17×10^5
M	Shear elastic modulus [‡]	Pa	4×10^9
A^*	$A - \frac{\gamma^{(x)^2}}{\rho^s C^{l(x)}}$	NA	NA
A	Bulk elastic modulus [‡]	Pa	8×10^9
ρ^s	Density of solid particles	kg/m ³	6050
K^μ	$\frac{\Lambda^\mu C^{l(x)}}{\rho^s}$	NA	NA
ε	Total strain	%	Variable
$C^{l(x)}$	Moisture content coefficient [†] [15]	J/kg	80
t	Time	seconds	0 to 3600
μ^l	liquid moisture potential	J/kg	Variable
μ_n	Saturated sample moisture potential	Fit experimentally	160
μ_a	Atmospheric moisture potential	Fit experimentally	15
Λ^μ	Coefficient of moisture mass [†] transfer [15]	kg.s/m ³	6×10^{-8}
λ^v	Coefficient of convective [†] exchange of vapor [15]	kg.s/m ⁴	9×10^{-5}

σ	Stress	Pa	Variable
u	Displacement	m	Variable
Subscripts (x,y,z)	Vector direction of displacement	NA	Unit vector direction

[†] Values are good approximations taken from the literature.

[‡] Values obtained from diametral compression testing in Appendix A.

Internal drying stress is described through Equations (4.9) to (4.11). This stress due to drying stems from capillary forces with the body, the gradient of moisture potential within the body, as well as the scalar parameters describing the system.

The internal drying stress equations:

$$\sigma_{11} = \sigma_x = M \left(\frac{\partial u_x}{\partial x} + \frac{\partial u_y}{\partial x} + \frac{\partial u_z}{\partial x} \right) + A^* \frac{\partial u_x}{\partial x} - \frac{\gamma^{(x)}}{C^{l(x)}} \mu^l \quad (4.9)$$

$$\sigma_{22} = \sigma_y = M \left(\frac{\partial u_x}{\partial y} + \frac{\partial u_y}{\partial y} + \frac{\partial u_z}{\partial y} \right) + A^* \frac{\partial u_y}{\partial y} - \frac{\gamma^{(x)}}{C^{l(x)}} \mu^l \quad (4.10)$$

$$\sigma_{33} = \sigma_z = M \left(\frac{\partial u_x}{\partial z} + \frac{\partial u_y}{\partial z} + \frac{\partial u_z}{\partial z} \right) + A^* \frac{\partial u_z}{\partial z} - \frac{\gamma^{(x)}}{C^{l(x)}} \mu^l \quad (4.11)$$

To apply this system of equations to an arbitrary domain, finite element analysis methods were employed. The system of equations was programmed into COMSOL (Comsol Multiphysics 3.5a) permitting solution of differential equations over arbitrary domains, lending itself to the problem at hand. Additionally, COMSOL allows the drying analysis to include the contact of domain surfaces with one another, just as in the case for the constrained drying problem within the LM-RIF. See Appendix C for an example Comsol Multiphysics® code used to calculate the constrained drying stresses. Figure 4.5 shows a sample domain with appropriate internal and

external conditions, along with boundary conditions for the system. Within COMSOL, drying conditions can be specified, by defining the boundary conditions, to only occur on certain domain faces. In this way, free drying can be modeled, along with drying on only one side of the part, such as the drying process inherent to the LM-RIF process.

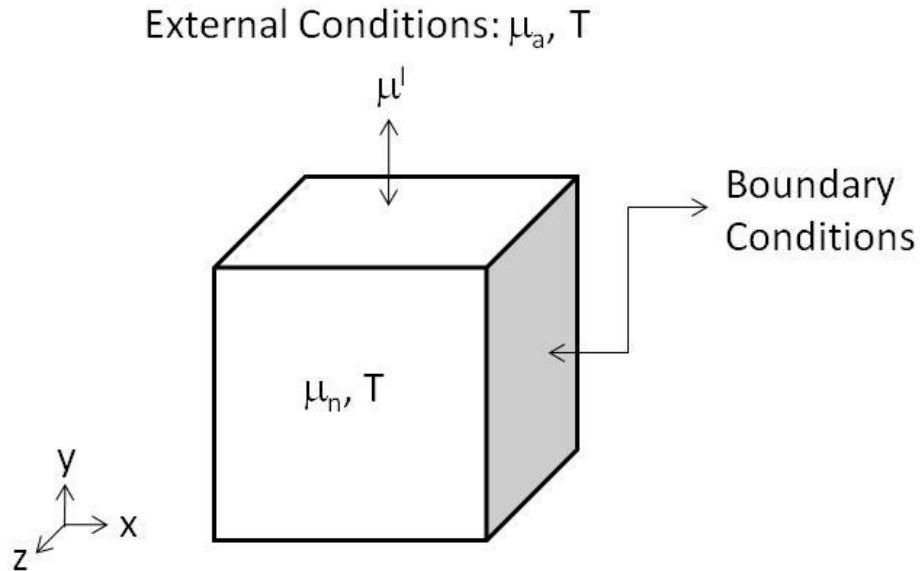


Figure 4.5. The system of partial differential equations is applied, within COMSOL, to a specific domain, such as the one shown. By defining internal moisture potential (μ_n), temperature (T), external moisture potential (μ_a), and boundary conditions, accurate predictions of drying processes can be made through the determination of the μ^l , as it ranges from initial to external moisture potential.

Model Calibration

Initially, the one sided drying of a cylindrical sample was investigated using both the one dimensional and three dimensional models. In this test case, cylindrical samples were fabricated from suspensions using the process described in Appendix A. The geometry of a test cylinder is given in Figure 4.6, where $r = 5.5\text{mm}$, and $h = 5\text{mm}$. Only the top surfaces of the cylindrical

samples were exposed to ambient conditions, making this a one sided drying problem, similar to the drying process in the LM-RIF. This test case was used to calibrate the models to the drying system at hand, as well as to qualitatively validate the drying trend. Moisture content of the samples was recorded as a function of time using an analytical balance (Sartorius MC410s) with five decimal place accuracy, interfaced to a PC via WinWedge® software (Taltech Inc.).

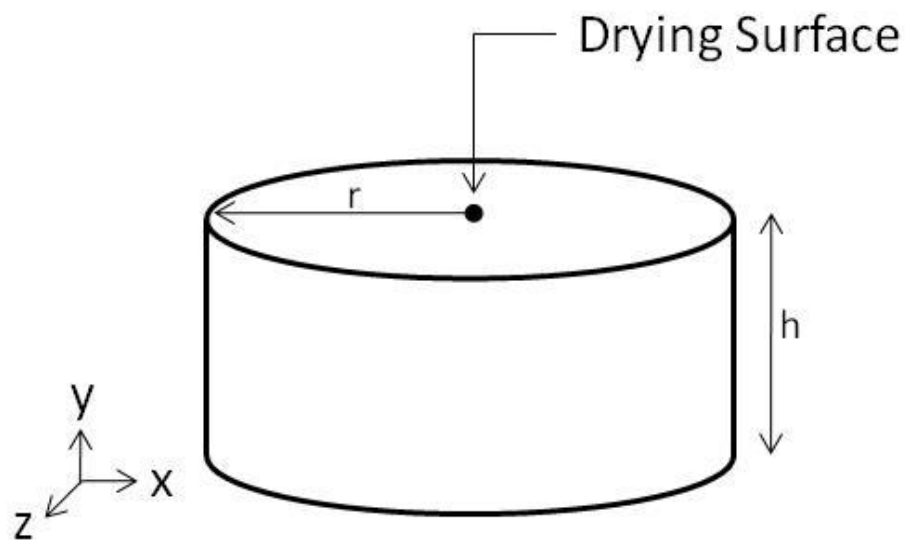


Figure 4.6. A schematic diagram of cylindrical samples used to verify the one dimensional and three dimensional drying models. Only the top face was exposed to external drying conditions, rendering both one and three dimensional drying models relevant.

In the three dimensional model, initial conditions of external and internal moisture potential were not calculated, but instead fit to experimental data, to ensure that the model accurately described the drying system. Further investigation into the calculation of these parameters, utilizing thermodynamic data is needed for application of this model to other systems, without repeating the cylindrical test sample experiments. The values of μ_n and μ_a were set to 160 and 15, respectively, and kept constant throughout the extrapolation of this model to the forceps domain shapes. Figure 4.7 provides additional details on this process. Initially, the experimental data is plotted as normalized moisture mass as a function of time. Next, the one

dimensional and three dimensional models are fit to the experimental data through manually varying μ_a and μ_n . After these values are set, the three dimensional program was then used to quantify drying stresses in the forceps domain shape. In this calculation, it is assumed that the internal moisture potential of the suspension is the same as in the cylindrical test sample. This assumption is considered valid, as the same suspensions were used to cast cylindrical calibration samples as well as the forceps shapes. If changes to the suspension are made, a new calibration test should be conducted. Furthermore, due to assumption 5 listed above for the three dimensional model, scaling of the domain size within FEA will hold valid as long as the system can still be described with a continuum approach. The maximum drying stress for all samples occurs at the end of drying stage 1. At this point, the capillary forces have reached a maximum, and the dimensional shrinkage of the part has reached a maximum, giving rise to the highest constrained stress experienced during the drying process within the LM-RIF.

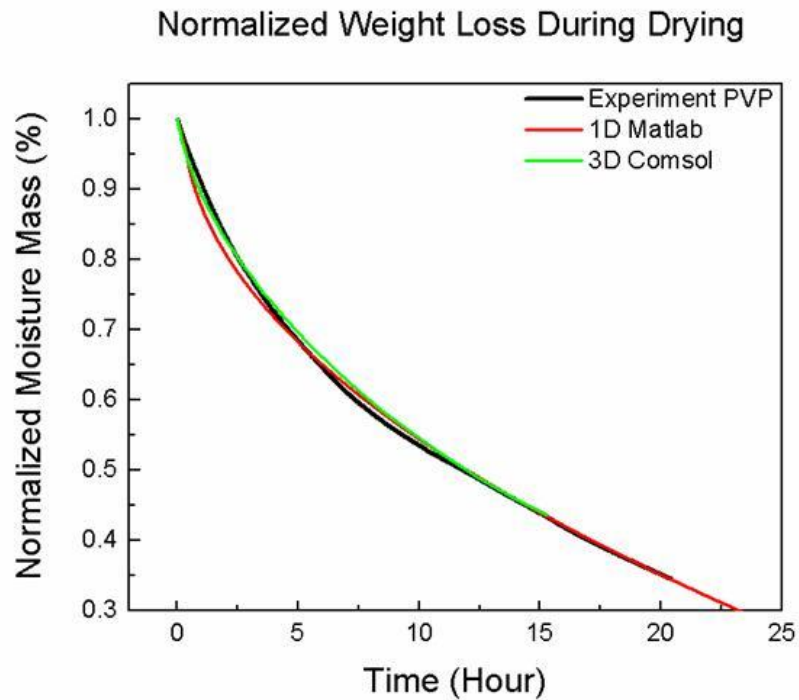


Figure 4.7. The normalized moisture mass as a function of time is plotted for the experimental cylindrical sample. In addition, the one dimensional and three dimensional drying models were used to describe the one sided drying process of the cylindrical test sample. Good agreement can be seen between the drying trends of both models and the experimental data. In the case of the three dimensional model, the internal and external moisture potential parameters were varied in order to get the fit shown above. These parameters were then carried forward in the predictions of stresses within forceps domain geometries.

In Figure 4.8, the three dimensional model is used to plot internal moisture potential μ^1 , as a function of time for the test cylinder. Drying is taking place from the top surface, with μ^1 decreasing close to the ambient moisture potential after 15 hours.

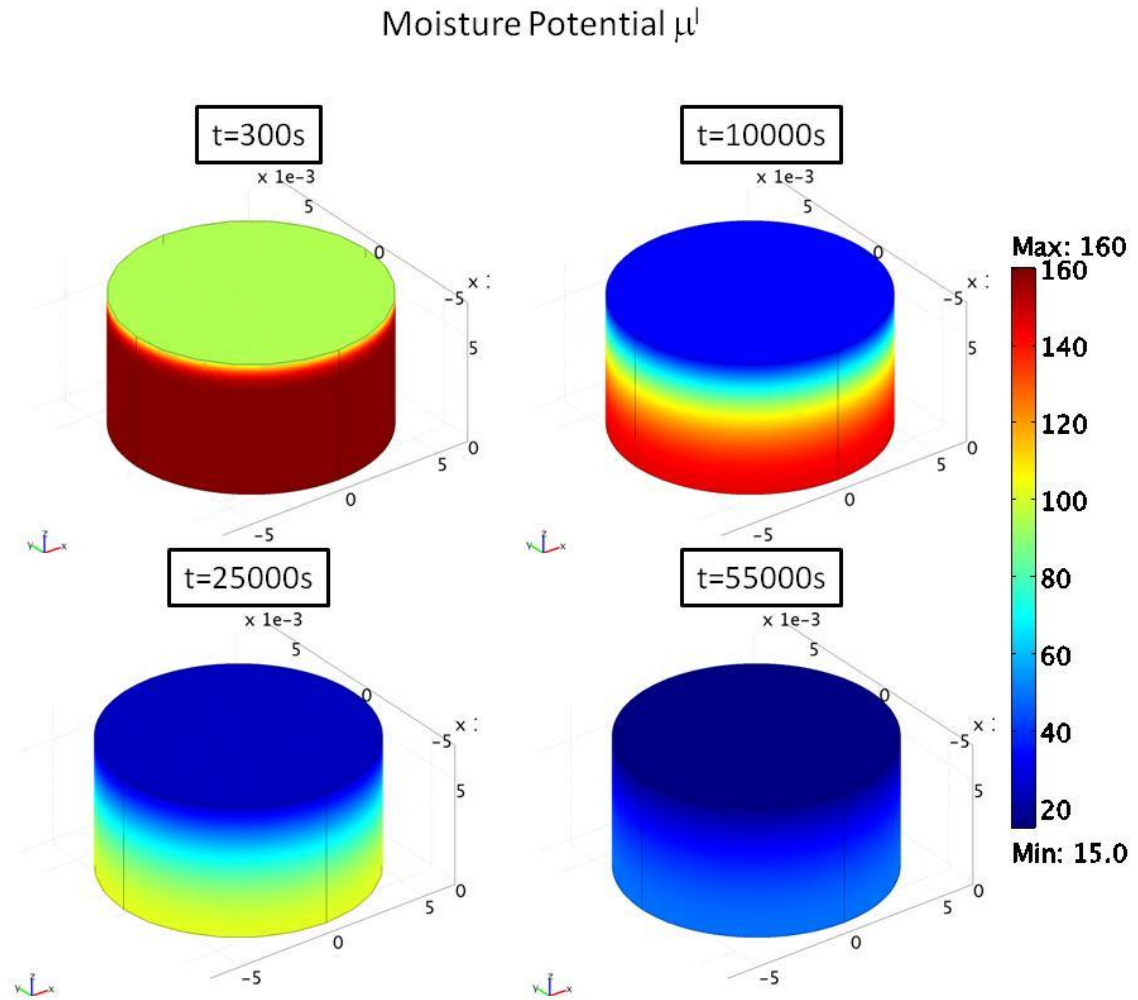


Figure 4.8. Internal moisture potential is plotted at four separate times during the drying process. The moisture potential decreases from the initial value of 160, to the external moisture potential of 15. At $t=300$ seconds, the first stage of drying is apparent, as the moisture potential has no gradient through the thickness of the part, and drying is occurring at the surface. As drying continues, the drying front moves into the sample, and finally, equilibrium with the surrounding atmosphere occurs after 15 hours.

Forceps Test Case

The constrained drying of forceps with an aspect ratio of 1:40, in a curved: without teeth, and straight: without teeth geometries were modeled using the three dimensional code developed

the shrinking part. The constrained drying thus generates mechanical stress, calculated internally with the COMSOL package. The interaction of the mold wall with the part wall is modeled as frictionless contact, with the mold walls set as fixed boundaries, eliminating deformation of the mold wall. In drying experiments, no mold deformation was apparent during drying supporting the assumption of frictionless contact and fixed wall boundaries. Total constrained drying stress is calculated, using COMSOL, as the addition of the internal drying stress field, and the mechanical stress field, due to the interaction of the shrinking part with the mold wall.

The data in Figure 4.10 demonstrates that the shape of the forceps significantly affects the maximum constrained drying stresses at the end of drying stage 1. Just as in the pure drying stress case (Figure 4.9), the large stress located at the base of the forceps is an artifact in the way the problem is constrained in Comsol. The curved forceps arms experience an order of magnitude less constrained force than the straight forceps. This is attributed to the fact that the curved forceps can deform more freely within the mold cavity, thus minimizing the constrained drying stress.

Cracking during the drying process will occur at the end of stage 1 drying, when the internal drying stress and constrained drying stress reach a maximum. At this stage, the entire forceps is under a state of stress, and cracks will be located at the weakest point. Experimentally, as shown in Figure 4.2, multiple cracks may form, due to small imperfections in the morphology of the green body, such as a large pore, or slight mold defect.

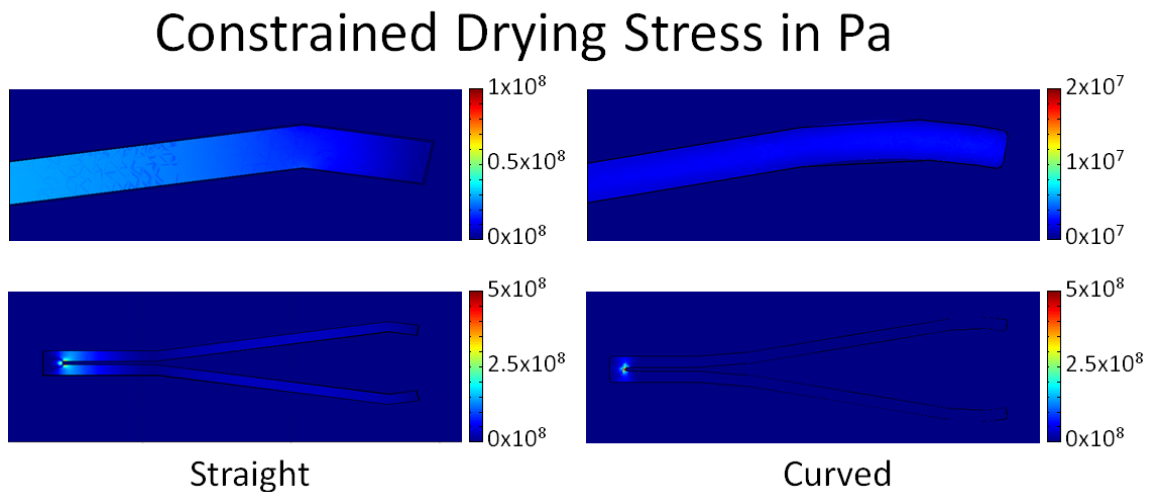


Figure 4.10. The constrained drying stress is depicted for the curved and straight forceps designs. The state of stress experienced by the curved forceps shape is an order of magnitude less than that of the straight forceps. Therefore, the shape of the part being manufactured with the LM-RIF process greatly affects the constrained drying stress, thereby affecting the final part yield. Also, the large drying stress located at the base of the forceps is artificial, and stems from the mechanical boundary conditions defined within COMSOL. The stress is shown for a time of 360 seconds, corresponding to the end of the constant drying rate period, and also the maximum state of drying stress.

Conclusions

In conclusion, the drying stress, and constrained drying stress of complex molded shapes has been evaluated with one dimensional and three dimensional models. While the one dimensional model is faster to implement, the one dimensional model only accounts for relative moisture mass in the sample as a function of time, while the three dimensional model can calculate drying time, drying stress, and constrained drying stress. The forceps shape plays a large role in the magnitude of the constrained drying stress experienced by the part during fabrication. Modifications to part geometry can be made to minimize stresses during drying and maximize final part yield with the ability to evaluate the constrained drying stress of a part manufactured within the LM-RIF process.

References

1. Singh, K.B. and M.S. Tirumkudulu, *Cracking in drying colloidal films*. Physical Review Letters, 2007. 98(21): p. 4.
2. Scherer, G.W., *Theory of Drying*. Journal of the American Ceramic Society, 1990. 73(1): p. 3-14.
3. Scherer, G.W., *Drying Gels .1. General-Theory*. Journal of Non-Crystalline Solids, 1986. 87(1-2): p. 199-225.
4. Scherer, G.W., *Correction of Drying Gels .1. General-Theory*. Journal of Non-Crystalline Solids, 1987. 92(2-3): p. 375-382.
5. Scherer, G.W., *Drying Gels .5. Rigid Gels*. Journal of Non-Crystalline Solids, 1987. 92(1): p. 122-144.
6. Scherer, G.W., *Drying Gels .3. Warping Plate*. Journal of Non-Crystalline Solids, 1987. 91(1): p. 83-100.
7. Scherer, G.W., *Drying Gels .4. Cylinder and Sphere*. Journal of Non-Crystalline Solids, 1987. 91(1): p. 101-121.
8. Scherer, G.W., *Drying Gels .2. Film and Flat-Plate*. Journal of Non-Crystalline Solids, 1987. 89(1-2): p. 217-238.
9. Scherer, G.W., *Drying Gels .6. Viscoelastic Plate*. Journal of Non-Crystalline Solids, 1988. 99(2-3): p. 324-358.
10. Scherer, G.W., *Drying Gels .8. Revision and Review*. Journal of Non-Crystalline Solids, 1989. 109(2-3): p. 171-182.
11. Scherer, G.W., *Drying Gels .7. Diffusion During Drying*. Journal of Non-Crystalline Solids, 1989. 107(2-3): p. 135-148.
12. Kowalski, S.J., *Thermomechanics of Constant Drying Rate Period*. Archives of Mechanics, 1987. 39(3): p. 157-176.
13. Kowalski, S.J., *Toward a thermodynamics and mechanics of drying processes*. Chemical Engineering Science, 2000. 55(7): p. 1289-1304.
14. Kowalski, S.J., *Thermomechanical approach to shrinking and cracking phenomena in drying*. Drying Technology, 2001. 19(5): p. 731-765.
15. Kowalski, S.J., *Thermomechanics of Drying Processes*. Lecture Notes in Applied and Computational Mechanics, ed. W. Pfeiffer. Vol. 8. 2003, New York: Springer.
16. Kowalski, S.J. and K. Rajewska, *Drying-induced stresses in elastic and viscoelastic saturated materials*. Chemical Engineering Science, 2002. 57(18): p. 3883-3892.

17. Kowalski, S.J. and A. Rybicki, *Rate of drying and stresses in the first period of drying*. *Drying Technology*, 2000. 18(3): p. 583-600.
18. Katekawa, M.E. and M.A. Silva, *A review of drying models including shrinkage effects*. *Drying Technology*, 2006. 24(1): p. 5-20.
19. Metzger, T., M. Kwapinska, M. Peglow, G. Saage, and E. Tsotsas, *Modern modelling methods in drying*. *Transport in Porous Media*, 2007. 66(1-2): p. 103-120.
20. Ghosal, S., A. Emami-Naeini, Y.P. Harn, B.S. Draskovich, and J.P. Pollinger, *A physical model for the drying of gelcast ceramics*. *Journal of the American Ceramic Society*, 1999. 82(3): p. 513-520.

Chapter 5

Non-Aqueous Processing of Metal Materials via the LM-RIF Process

Introduction

Of the many benefits of the LM-RIF process over existing mesoscale fabrication techniques, a key aspect is the ability to fabricate devices from a wide range of materials. In this chapter, the non-aqueous colloidal suspension formulation of 300 series stainless steel, as well as a composite 3mol% yttria stabilized zirconia (3YSZ), with 300 series stainless steel is discussed. These suspensions are utilized within the LM-RIF process to produce prototype devices and mechanical test specimens which have been evaluated. The work involving the non-aqueous processing for metal and metal matrix composite materials manufactured via the LM-RIF process has led to several peer review publications[†].

Powder metallurgy (PM) techniques have existed in North America, starting on the laboratory scale, since the 1930's [1]. The powder metallurgy industry has grown considerably, as unique areas of application have been discovered. Advantages of PM include its ability to form unique geometries, easily form composites of metals and non-metals, as well as metal alloys through powder mixing instead of melting, as well as the ability to form materials with

[†] Published work includes:

- Aguirre, M., G. Hayes, M. Frecker, J. Adair, and N. Antolino. *Fabrication and Design of a Nanoparticulate Enabled Micro Forceps*. in *ASME 2008 International Design Engineering Technical Conferences & Computers and Information in Engineering Conference*. 2008. New York, NY.
- Aguirre, M., G. Hayes, C. Yuangyai, M. Frecker, J. Adair, and N. Antolino. *Fabrication and Strength-Based Design of a Meso-Forceps*. in *ASME 2009 International Design Engineering Technical Conferences*. 2009. San Diego, CA.
- Aguirre, M.E., G. Hayes, R. Meirum, M. Frecker, C. Muhlstein, J.H. Adair, and J.A. Kerr, *The Design and Fabrication of Narrow-Gauge (1 mm Diameter) Surgical Instruments for Natural Orifice Translumenal Endoscopic Surgery*. To be submitted to the *Journal of Mechanical Design*.
- Cirone, S., Hayes, G.H., Babcox, B., Adair, J.H., Lesieutre, G.A., Frecker, M.I. *Design, Fabrication and Testing of Contact-Aided Compliant Cellular Mechanisms with Curved Walls*. in *SPIE Smart Structures/NDE*. 2011. San Diego, CA, USA.
- Mehta, V., Hayes, G.H., Frecker, M.I., Adair, J.H., *Design, Fabrication, and Testing of Meso-scaled Cellular Contact-aided Compliant Mechanisms*, in *ASME 2010 Conference on Smart Materials, Adaptive Structures and Intelligent Systems, SMASIS2010*. 2010: Philadelphia, Pennsylvania, USA.
- Neibel, C., A.C. Rau, M. Frecker, A. Mathew, and G. Hayes. *Design of an Endoscopic Biopsy Needle*. in *Design of Medical Devices Conference*. 2010. Minneapolis, MN.

customized properties (e.g. corrosion resistance, and mechanical properties.) [1]. PM techniques have been used in areas where corrosion resistance is critical such as the aerospace, automotive, chemical processing, medical, and recreational industries, to form complex desired device shapes from corrosion resistant materials [1].

Within the LM-RIF process, metal powder suspensions can be easily cast into the lithography based molds. 316L series stainless steel (316LSS) is austenitic, high chromium, low carbon series steel, making it strong, corrosion resistant, and an ideal material for both surgical instruments and C3M devices. The specific alloying composition is given in Table 5.1. The key additive in 316LSS is Cr which produces corrosion resistant chromate surfaces resistant to corrosion. The low carbon content in the ‘L’ designated stainless steels indicates the low carbon content. In the 316L series modification, carbon content is low, nominally at 0.03 atomic %. The low carbon content permits the welding of the alloy without precipitation of the deleterious chromium carbide phase. Precipitation of chromium carbide in stainless steel leads to loss of corrosion protection.

Table 5.1. The nominal elemental composition of 316L stainless steel powder is listed in at% [2].

<i>Grade</i>	<i>Fe</i>	<i>Cr</i>	<i>Ni</i>	<i>Mn</i>	<i>Si</i>	<i>S</i>	<i>C</i>	<i>P</i>	<i>Mo</i>	<i>N</i>
300 series	Balance	16-18	10-14	0.1-2	0-1	0-0.03	0.03	0-0.04	2-3	0-0.03

Powder metallurgy techniques focused on forming metal and metal matrixes have been examined thoroughly in the literature [3-5]. Recently, PM microfabrication techniques specifically for stainless steels have been recently explored by Imbaby [6, 7], Fu [8], and Garino [9], however, to date, a microfabrication approach with 3D capabilities, along with the ability to simultaneously produce a large number of parts has not been reported.

In addition to powder metallurgy, composite formulation from particulate materials is also possible within the LM-RIF process. Composites are a unique class of materials that combine more than one type of material while incorporating properties from each of the constituents. Stainless steel and zirconia are both used in thousands of products due to their desirable characteristics including high strength, corrosion resistance, deformation resistance, and biocompatibility. Stainless steel is currently being used in industries such as automotive, aerospace, and as a construction material in large buildings. It is also used to make products such as cookware, cutlery, hardware, appliances, industrial equipment, and surgical instruments such as scalpels and hemostats. Zirconia is used as a diamond simulant, a semiconductor, and dental restoration material for crowns and bridges. One application that stainless steel and zirconia both have in common is their biocompatibility. Several varieties of hip and knee prostheses are manufactured using stainless steel and zirconia as well as variety of surgical screws, pins, and plates [10].

In this work, a 316L series stainless steel suspension was incorporated into the LM-RIF process. The rheological properties, state of dispersion, and mechanical properties of the material were also investigated. Following device fabrication, prototype testing, and chemical analysis of the 300 series stainless steel devices was performed.

Application 1: NOTES Surgical Forceps

As previously discussed in Chapter 1 and Chapter 2, new surgical instruments for NOTES procedures are currently being developed. The surgical instrument in question, designed by Aguirre et al. [11] is shown again in Figure 5.1. This forceps design is an ideal application of the LM-RIF process, as the size scale and complexity of the design eliminates other fabrication approaches.

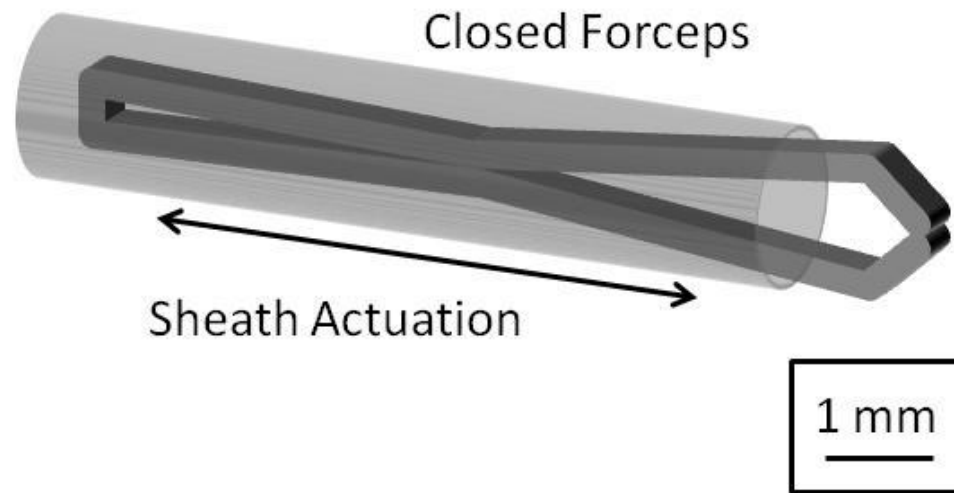


Figure 5.1. The design of the NOTES forceps/cutting surgical instrument to be fabricated with the LM-RIF process is shown. A description of the forceps is given in Chapter 1. The forceps is shown in the closed state with the sheath fully extended to close the distal end of the surgical forceps instrument.

In the following sections, the fabrication and mechanical integrity of the forceps instrument is described within the context of the LM-RIF process utilizing 300 series stainless steel. Furthermore, validation of the design by endoscopic surgeons will be discussed.

Application 2: High Stiffness-High Elastic Strain C3M device.

As discussed in Chapter 1 and Chapter 2, there is a current interest in developing materials with high stiffness and large elastic strain. A C3M unit cell is shown in the inset of Figure 5.2, where this design allows the engineering of structures that fall into this region of designed materials. This C3M design lies in the ideal size scale for fabrication utilizing the LM-RIF process. C3M devices were fabricated using the LM-RIF process and 300 series stainless

steel. In the following sections, prototype parts are tested and compared against the predicted performance curves.

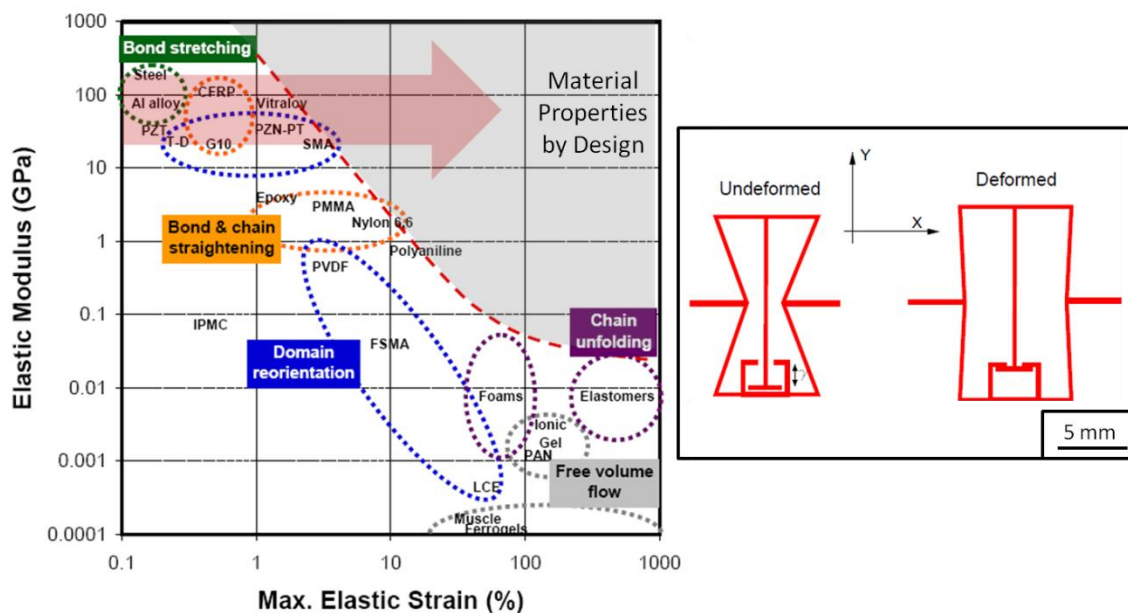


Figure 5.2. There is a region of interest for new materials properties with high stiffness and large elastic strain shown in grey. New material designs aim to shift the current maximum elastic strains to higher values, as indicated by red arrow. A C3M unit cell is shown on the right hand side, for Left: the undeformed unit cell, and Right: the fully elastically deformed cell. The Young's modulus for stainless steel and YTZP (containing 3 mole percent yttria) is 200 GPa. The predicted C3M device strains are 12 to 15%. In contrast, typical pure elastic strain in high stiffness materials is approximately 0.2%. Thus, high elastic strain devices can be produced by optimized design of relatively inelastic materials [12, 13].

Colloidal Processing

Non-aqueous 316L series stainless steel colloidal suspensions were formulated with Micro-Melt[®] -22 μm 300 series stainless steel microparticles (Carpenter Powder Products, Wyomissing, PA). The non-aqueous processing environment was employed to limit oxidation of the metallic particles prior to sintering [14]. A flow chart of the suspension preparation is given in Figure 5.3. The order of addition of the solvent, dispersant, and powder is shown in the upper

left corner of the boxes in the flow chart.

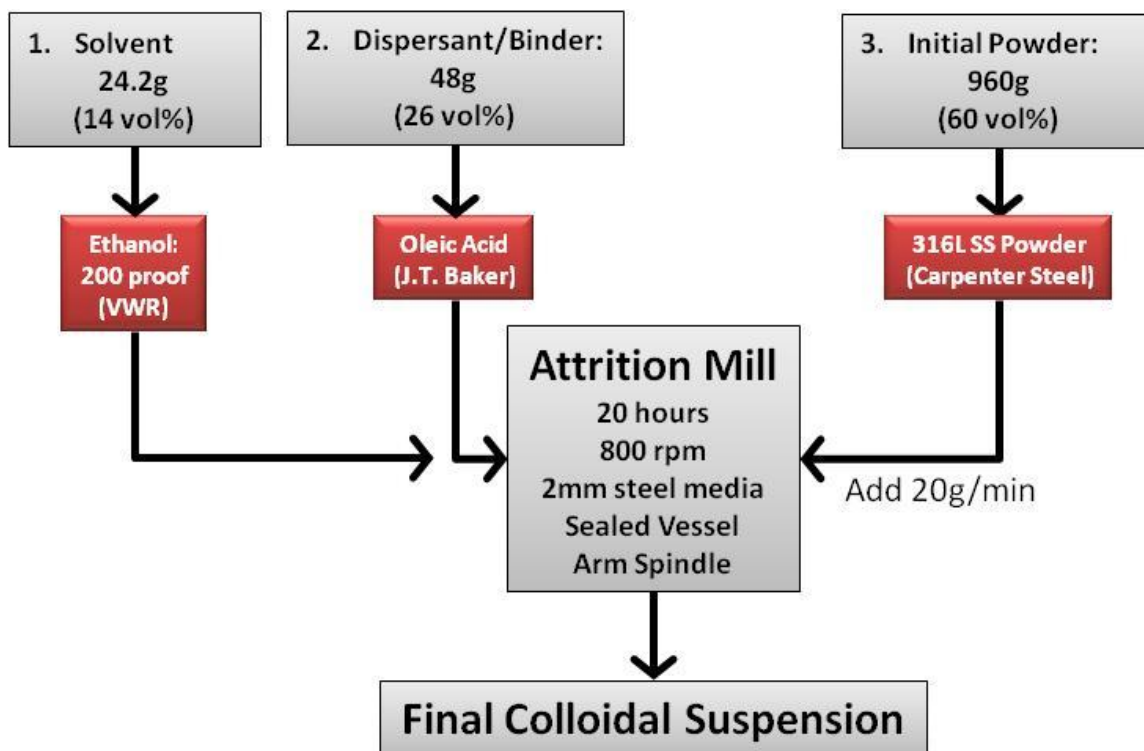


Figure 5.3. The formulation flow chart of non-aqueous colloidal suspensions is shown. The order of addition is shown in the upper left corner of the component boxes. The attrition mill is kept at 10°C and sealed to limit evaporation of any solvent during milling. A typical formulation sheet is shown in Figure 5.4.

316L series stainless steel colloidal suspensions were formulated in 200 proof ethanol (VWR International, West Chester, PA) at 60 vol% powder, with oleic acid (J. T. Baker, Phillipsburg, NJ) as the dispersant and lubricant at 5wt% of the powder. A typical suspension formulation tracking sheet is given in Figure 5.4. The tracking sheet permits ready variation and documentation of suspension parameters. The suspensions were prepared in a Szegvari 01-HDDM attrition mill equipped with a stainless steel spindle and vessel (Union Process, Inc., Akron, OH). After the dispersant was added to the ethanol, the solvent and dispersant solutions were added to the attrition mill loaded with 2mm stainless steel media. Powder was added at 20g

per minute at 430 rpm and 10°C. Once all of the powder was added, the mill speed was increased to 800 rpm and held for 20 hours. To prevent evaporation of the ethanol, the temperature was held at 10°C for the duration of the milling time, while the mill vessel was equipped with a sealed lid. After milling was completed, particle size analysis via sedimentation with a CAPA 700 (Horiba Ltd.) and rheological properties were determined.

Figure 5.5 shows the particle size distributions determined via a sedimentation method (Horiba CAPA 750, Irvine, CA), and scanning electron microscopy (SEM) photomicrographs of the as prepared and milled suspensions. The particle shape changes from a spherical starting powder, to deformed, platelet like particles as mill time is extended. This change in particle shape is responsible for the observed change in particle size, as the platelet-like shaped particles skew the sedimentation sizing data towards lower values [15] because the hydrodynamic retardation is greater for platelet particles relative to spherical particles for a given mass. Additionally, no major agglomeration, or cold welding occurred during the milling process based on the inspection of the suspensions observed in the SEM photomicrographs. Furthermore, the oleic acid dispersant is bound to the surface of the particles, and did not form segregated agglomerates of organic material.

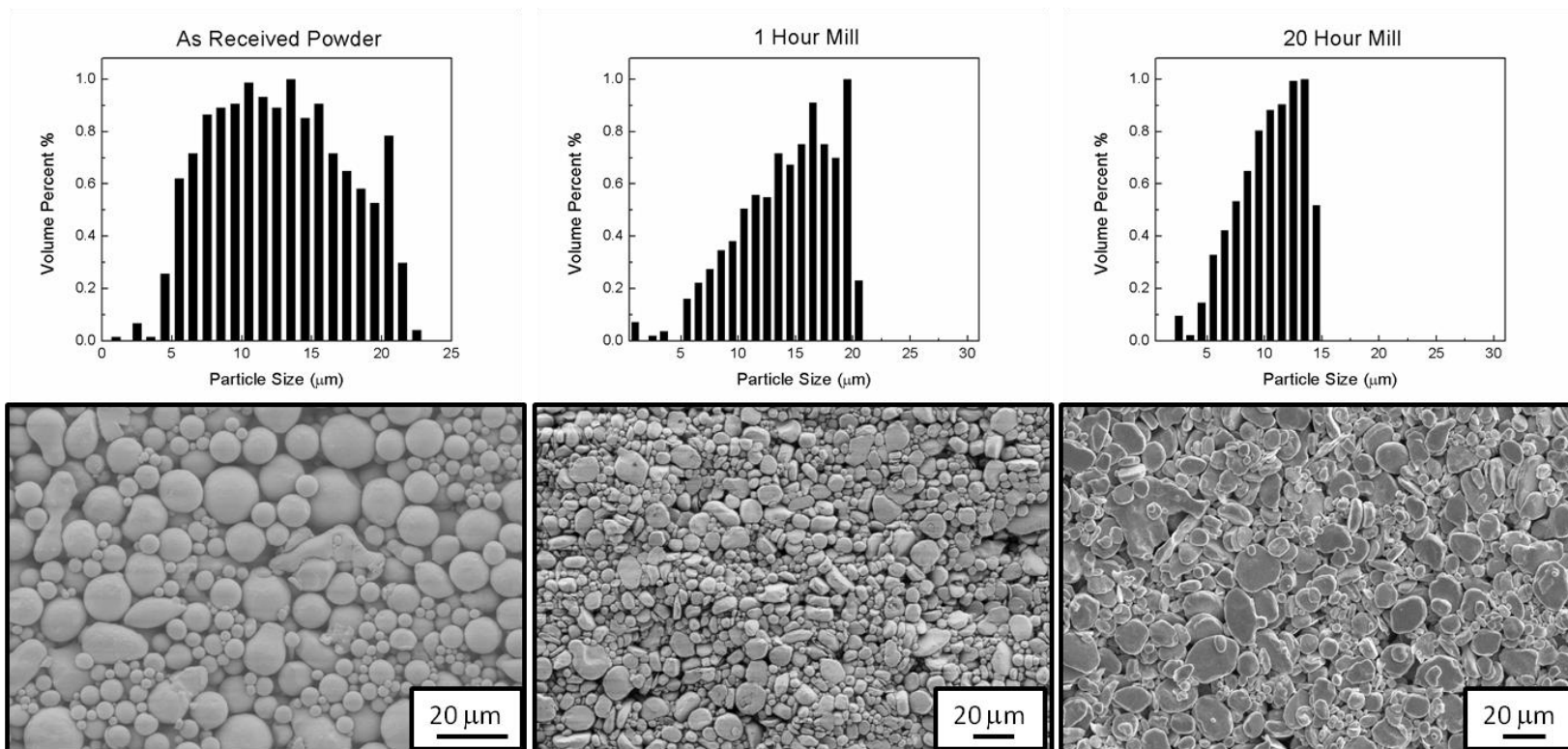


Figure 5.5. Top: particle size, measured using the sedimentation approach with a commercial particle size analyzer (Horiba CAPA 700, Irvine, CA), is shown for the as received powder, and the milled powder after 1 and 20 hours of milling. A decrease in the recorded size is evident; however, this is expected due to the change in particle shape from spherical to platelet-like. Bottom: Scanning electron micrographs of the as received and milled powder for 1 hour and 20 hours is shown. The change in particle shape from spherical to platelet-like is evident. No major agglomeration, or cold welding occurred during the milling process. Furthermore, the oleic acid dispersant is bound to the surface of the particles, and does appear to have formed segregated agglomerates of organic material.

Rheology

The viscosity of the metallic suspensions plays an important role in successful casting into the molds used in the LM-RIF process. Many factors contribute to the determination of the viscosity of a suspension, including particle size distribution, particle shape, as well as volume fraction of solids in the system. Shear stress and viscosity were measured as a function of shear rate for the 60 vol% stainless steel suspension with a Malvern Instruments Bohlin Visco88 with a 14 mm concentric cylinder system at 25 °C. By extrapolating a linear fit of the viscosity data at high shear to zero shear rate, the apparent viscosity of the suspension was obtained. Similarly, extrapolating a linear fit of the high shear, shear stress data back to zero shear rate, the Bingham yield point was established. Figure 5.6 shows the viscosity and shear stress for the 60vol% colloidal suspension milled for 20 hours. The Bingham yield point of 117 Pa and high shear viscosity of 2.1 Pa.s allows the suspension to be successfully cast into the molds during the LM-RIF processing as defined by Antolino [16]. The casting process for the LM-RIF process is currently done manually, therefore the typical LM-RIF processing shear rates of 500 s⁻¹ are sufficient to achieve the lower viscosity of the suspension at the high shear for LM-RIF casting processes rate as well as overcoming the Bingham yield stress.

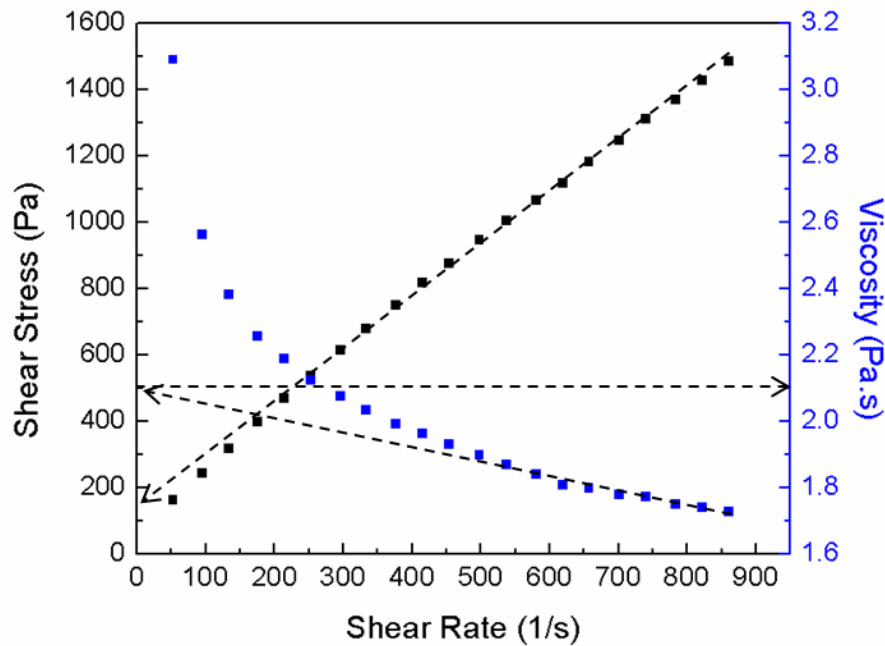


Figure 5.6. The viscosity and shear stress vs shear rate is shown for a 60 vol% 300 series stainless steel suspension in ethanol with oleic acid at 5wt% of the powder as the dispersant. At high shear, the viscosity of 2.1 Pa.s is able to be cast into the molds, while the Bingham yield point of 117 Pa is also able to be overcome in the LM-RIF processing. The method for determining Bingham yield point, and high shear viscosity is indicated by the black dashed arrows.

State of Dispersion

The state of dispersion can be estimated by considering the attractive and repulsive energy interactions in colloidal system [17]. The superposition of the attractive and repulsive interactions, V_{total} , given by Equation (5.1) provides the overall interaction energy as a function of separation distance (d) for two particle interactions. In general, the attractive energy is due to a combination of Keesom (dipole-dipole), Debye (dipole-induced dipole) and London (electronic polarization) forces. For conductors such as the stainless steel, the London dispersion forces are the most important. Krupp provides an overview on calculation schemes for a variety of material

systems including metals and semi-conductors [18]. Adair et al. have shown that the Hamaker constant for a semi-conductor such as CdS increases as nanoscale regimes are met [19]. In the current study, stainless steel particles are large enough that there are no quantum confinement effects that need to be considered. Visser has calculated the Hamaker constant for steel as 2.12×10^{-19} J [20].

The attractive interactions due to van der Waals forces, V_{vdW} , given in equation (5.2) were described by Gregory [21]. The steric barrier to agglomeration, V_{steric} , due to the oleic acid dispersant, given by equation (5.3), was described by Bergstrom [22], which accounts for the thickness of an adsorbed polymer layer on the particles.

$$V_{total} = V_{vdW} + V_{electrostatic} + V_{steric} \quad (5.1)$$

$$V_{vdW} = V_{gre}(d) = \frac{A_H}{6} \frac{a_1 a_2}{d(a_1 + a_2)} \left[1 - \frac{5.32d}{100 \cdot 10^{-9}} \ln \left(1 + \frac{100 \cdot 10^{-9}}{5.32d} \right) \right] \quad (5.2)$$

$$V_{steric} = V_{bergstrom}(d) = \begin{cases} d < d_a : & \infty \approx 10^6 \\ d_a \leq d \leq 2d_a : & \frac{2a_2}{a_1 + a_2} \left[\frac{\pi a_1 kT}{V\phi^2} \left(\frac{1}{2} - \chi \right) \left(d_a - d \right) \right] \\ d > 2d_a : & 0 \end{cases} \quad (5.3)$$

Table 5.2. The parameters used in equations (5.1) to (5.3) are provided.

Parameters and initial conditions	Definition	Units	Value
V_{total}	Total interaction energy	kT	Variable
V_{vdW}	van der Waals interaction energy also written as V_{gre}	kT	variable
$V_{electrostatic}$	Electrostatic interaction energy	kT	Variable

V_{steric}	Steric barrier interaction energy also written as $V_{bergstrom}$	kT	variable
d	Interparticle separation distance	m	Variable
d_a	Thickness of adsorbed polymer layer	m	Variable
A_H	Hamaker constant [20]	Joule	Variable
a_1 and a_2	Particle diameter, for particle 1 and particle 2, respectively	m	Variable
T	Temperature	Kelvin	Variable
ϕ	Volume Fraction of polymer in steric barrier	NA	0.5
χ	Solvent absorbent interaction parameter	NA	0.3
k	Boltzmann's Constant	$m^2.kg.s^{-2}.K^{-1}$	1.38065×10^{-23}

Non-aqueous suspensions are notoriously hard to engineer into a well dispersed state. The lack of polarity in the solvent leads to minimal repulsive forces among the particles, and the state of dispersion relies heavily on steric barriers to agglomeration. In this system, the low dielectric constant of ethanol provides little electrostatic repulsion among particles. Therefore, $V_{electrostatic}$ in the current material system is assumed to be zero due to a zero ζ -potential value in the non-aqueous environment. However, steric repulsion forces are present, with the thickness of the steric barrier used in the system estimated at 1.4 nm, assuming a 45° bonding angle of oleic acid with the surface of the particle [23]. The size of oleic acid was estimated via ACDLabs Chems sketch, and shown in Figure 5.7. Finally, the particle surface roughness is assumed to be 25 nm, due to the large particle diameter and long mill duration, the volume fraction of polymer in

the steric layer is assumed to be 0.5, and the solvent adsorbent interaction parameter is assumed to be 0.3 [24, 25]. The total interaction energy is the addition of the attractive and repulsive energies with the theoretical calculation for V_{Total} as a function of separation distance shown in Figure 5.8, utilizing the parameters listed in Table 5.3.

Table 5.3. The parameters used to theoretically calculate the interaction energy between two 300 series stainless steel particles in suspension. The program Hamaker 2.1 was used to carry out the calculation [26].

<i>Parameter</i>	<i>Value</i>
ζ -potential	0.0 mV
Thickness of adsorbed polymer layer	1.4nm
Hamaker constant [20]	2.12×10^{-19} J
Particle diameter	11 μ m
Ethanol dielectric constant [27]	24.3
Temperature (T)	300°K
Volume Fraction of polymer in steric barrier(ϕ)	0.5
Solvent adsorbent interaction parameter(χ)	0.3
Boltzmann's Constant (k)	$1.3806503 \times 10^{-23}$

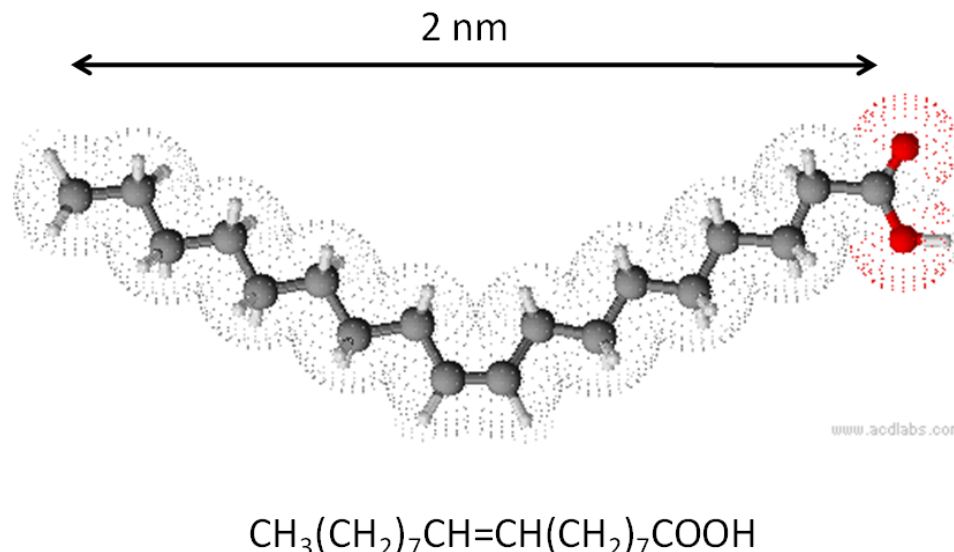


Figure 5.7. Oleic acid, depicted here by ACDLabs ChemsSketch, is approximately 2nm long, bonding to the surface of the metal particle via the carboxylic acid head group shown on the right hand side. The bond angle of the oleic acid with the particle surface is assumed to be 45°, yielding a final steric barrier of 1.4nm.

In Figure 5.8, there is a deep energy well around the 50 nm separation distance between the particles, where twice the surface roughness and steric barrier come into contact with one another. The low dielectric constant of ethanol, as well as the large particle size of the stainless steel powder contributes to this effect. While this system is not classically considered well dispersed, it is typical of a non-aqueous dispersion scheme, relying on steric interactions to keep particles separated. Hunter and co-workers have shown that the depth of the secondary minimum is directly related to the Bingham yield point of a suspension [28, 29]. From a practical viewpoint, the energy well can also be overcome at shear stresses above the Bingham yield point[28], allowing the suspension to infiltrate the molds during LM-RIF processing. The Bingham yield point in a suspension is a useful characteristic ensuring that flow into the mold

cavity takes place only during shear. Once shear is removed, the cast suspension remains in place in the mold cavity.

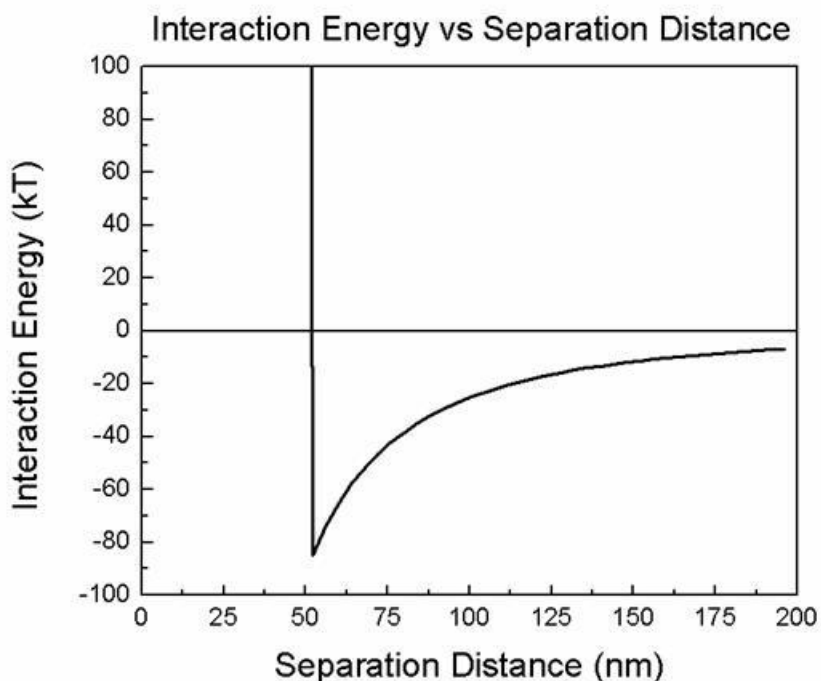


Figure 5.8. The calculated interaction energy for two 300 series stainless steel particles in ethanol is shown. There is a very large minimum energy well at 50 nm separation distance, due to the low dielectric constant of ethanol and large particle size. There is also a steric barrier of 1.4 nm at 50 of separation distance due to the surface roughness of the particles and the steric repulsion of the oleic acid on the surface of the particles. Table 5.3 lists the parameters used in the calculation.

LM-RIF processing, casting and sintering parameters

As discussed in Chapter 2, combustion of the binder and mold take place at 600°C, while sintering takes place in a dissociated ammonia reducing atmosphere. Cross sectional images were taken to determine the grain morphology of the fabricated parts. Cross sectional samples were prepared by polishing parts mounted in epoxy (Allied High Tech Products, Inc.) and polishing with the steps outlined in Table 5.4.

Table 5.4. After fired parts are mounted in an epoxy (Epoxy Bond110, Allied High Tech Products, CA), cross sectional samples were prepared with the processing steps shown below. All polishing products were provided by Allied High Tech Products and polishing was performed on a MetPrep 4 Polishing Machine (Allied High Tech Products, CA).

<i>Sequential Polishing Step</i>	<i>1</i>	<i>2</i>	<i>3</i>	<i>4</i>	<i>5</i>	<i>6</i>
Abrasive	180 Grit	320 Grit	1200 Grit	3 μm	1 μm	0.05 μm
Material	SiC	SiC	SiC	Diamond	Diamond	Diamond
Carrier	Abrasive Disc	Abrasive Disc	Abrasive Disc	Suspension	Suspension	Suspension
Polishing Cloth	-	-	-	Gold Label	Diamat	Chem-Pol
Lubricant	Water	Water	Water	Green Lube®	Green Lube®	Green Lube®
Platen Speed/Direction	300 rpm Contra	300 rpm Contra	300 rpm Contra	250 rpm Contra	250 rpm Contra	250 rpm Contra
Pressure	4 lb per mount					
Time (min.)	1	1	1	1.5	1	20
Sample Mount AP-3 Speed (rpm)	150	150	150	150	150	150

Figure 5.9 shows a SEM image of the polished surface after step 6, accompanied by an optical, bright field image. There is a second phase between the metal grains in the cross section. Using ImageJ software, the percentage of porosity was found to be approximately 5.5% in the cross sectional image, as shown in Figure 5.10. However, the remaining 94.5% of material is not fully stainless steel, as a secondary phase can be located at grain boundaries. This secondary phase is seen as the light gray inclusions in Figure 5.9 right, and is easily seen in Figure 5.11. Because the porosity in the image is black, the metallic phase and secondary phase can be excluded using the threshold function in ImageJ.

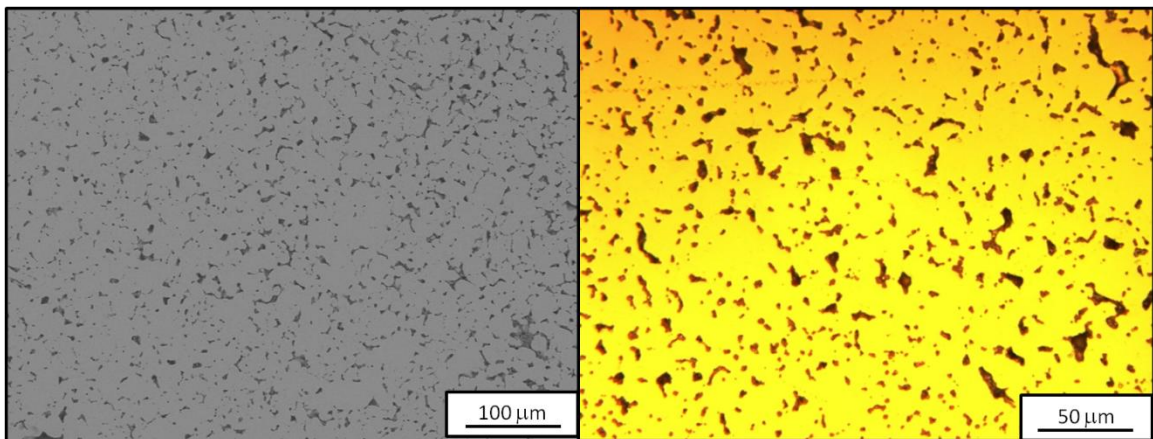


Figure 5.9. Left: Scanning electron micrograph of a cross sectional sample of the sintered 300 series stainless steel material. While minor porosity is present, no major bubbles can be found. Right: An optical micrograph of the same sample is shown. While there is an interconnected metallic phase, there is also a secondary material present at the original particle boundaries.

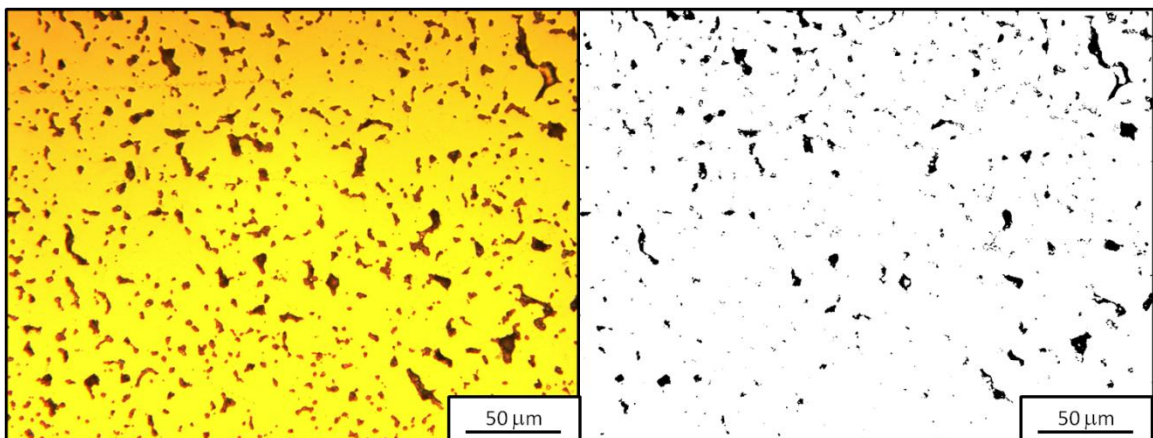


Figure 5.10. Using ImageJ [30] area analysis, there is 5.5% porosity in the sample after the sintering process. The remaining 94.5% is not fully 300 series stainless steel due to inclusions of another phase located at the original particle boundaries prior to sintering. Left: The second phase material can be seen as small light gray particles, as opposed to the larger dark pores. Right: ImageJ area analysis shows the locations of the large porosity in the cross section sample.

To quantify the secondary phase seen in the microstructure in Figure 5.9, Auger electron spectroscopy (AES) was also employed. The PHI 670 FE scanning AES instrument was operated at the analytical conditions listed in Table 5.5.

Table 5.5. The parameters of the AES system are listed. A 10 minute Argon ion sputter was used to remove any oxidation to the surface of a cross sectional sample of part of a forceps device prepared via the polishing scheme described above.

<i>Condition</i>	<i>Value</i>
System pressure	Mid 10^{-8} torr during analysis
Electron beam energy	10keV
Electron beam current	10nA
Approximate beam size	Several hundred Angstroms in diameter
Analyzer resolution	Fixed 0.7%
Step size, dwell time	1eV step size, 60 ms total dwell time, 3 scans integrated
Stage tilt	30°
Sample mounting	Screw mount
Data smoothing	5 pt. SG
Ion beam	3keV Ar ⁺ rastered 2mm x 2mm
Sputter rate	~3Å per second
Sputtering interval	10 minutes (~180nm)
Relative Intensity Factors of appropriate elements. The first number given in () is electron kinetic energy, followed by the relative intensity factor.	O(510) =0.79, C(275) = 0.28, Si(1620) = 0.27, Cr(491) = 0.84, Cr(531)=0.99, Mn(638)=0.46, Mn(592)=0.6, Mn(545)=0.46, Fe(600)=0.38, Fe(654)=0.56, Fe(705)=0.66, Ni(718)=0.2, Ni(785)=0.32, Ni(849)=0.85

Figure 5.11 shows the AES analysis of the polished cross sectional sample. There are two types of inclusions present, in addition to the bulk stainless steel matrix. The AES spectra shows that the matrix metal is rich in chromium, iron and nickel, typical of 300 series stainless steel. The first type of secondary phase present is rich in oxygen, carbon, manganese, and silicon.

These elements are present in the polishing media used to prepare the cross sectional sample. Therefore, these areas are taken to be the location of porosity. The second type of secondary phase is rich in chromium, oxygen, and manganese. Furthermore, due to the relative intensity factors of the individual elements, the ratios of chromium to oxygen to manganese cannot be determined because of the determined because of the relatively low concentrations relative to the background concentrations in the matrix. Chromium and oxygen have similar intensity factors of 0.84 and 0.79, respectively. Manganese, with an intensity factor of 0.6 will therefore have a smaller intensity peak in the spectra. Additionally, the location of the kinetic energy peaks in the spectra convolute any attempt at exact composition analysis. Thus, we are limited to conclusions that chromium rich steel is present in the bulk phase, while chromium oxygen and manganese constitute the main second phase. From the bulk areas analyzed in the metal matrix, not all of the chromium has gone into the secondary phase inclusion. Thus, the corrosion resistant properties of the stainless steel should still be present. The corrosion resistant properties also should still be present based on the chemical analysis discussed below, with final chromium content at approximately 15at%. Samples placed in a saturated sodium chloride solution for 24 hours at room temperature showed no sign of oxidation with optical microscopy.

The surface of the sample was sputter etched with an argon ion beam for 10 minutes, revealing a more detailed microstructure. The secondary phase inclusion appear only at grain boundaries, but the grain boundaries present are not located at the original particle boundaries in the dried green body, as shown by the argon etched microstructure in Figure 5.11.

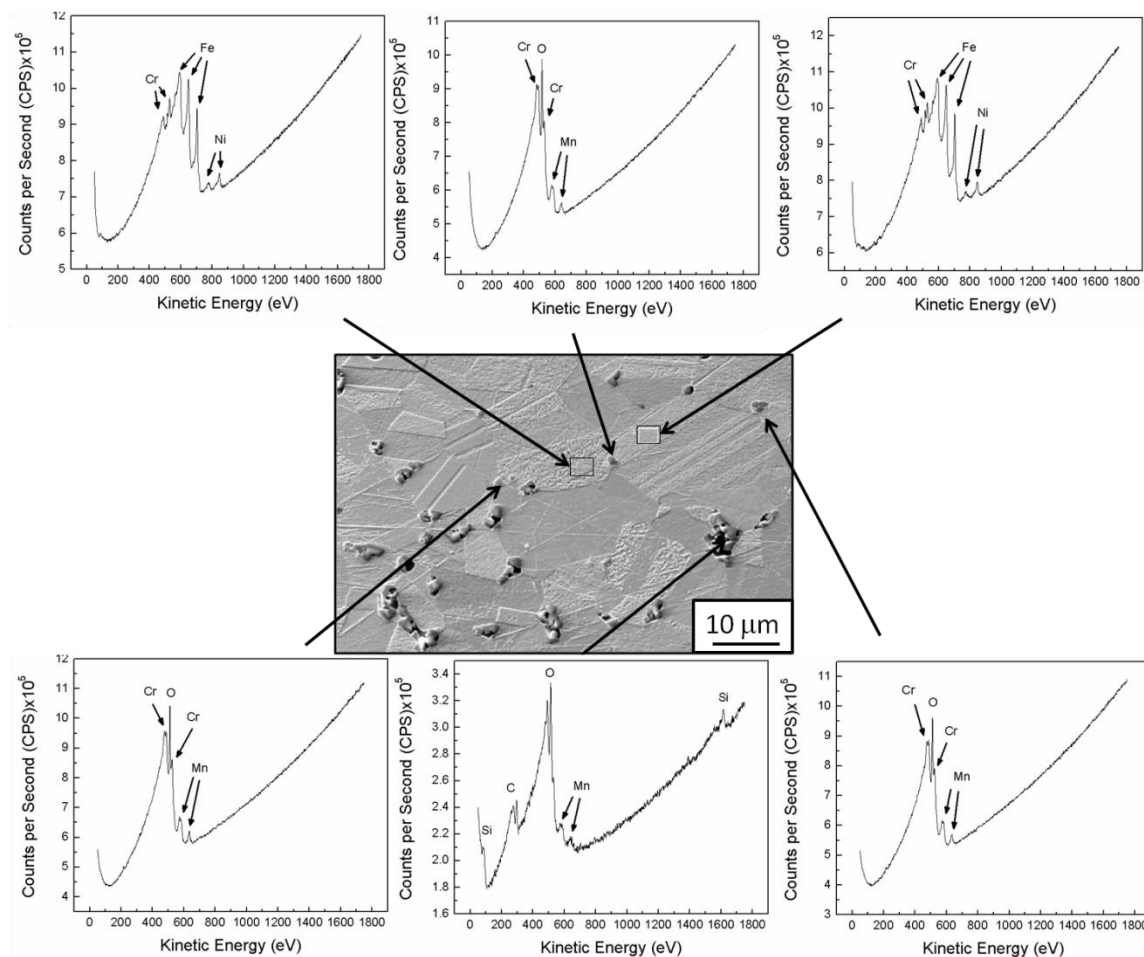


Figure 5.11. AES count rate vs kinetic energy scans are shown for the polished cross sectional sample. The bulk metal material consists of iron, chromium, and nickel, which is consistent with stainless steel, while the secondary phase inclusions are of two types. Type one, includes oxygen, manganese, carbon, and silicon, indicative of the polished preparation, while type two consists of chromium, oxygen, and manganese, indicative of a chromium rich second phase. Although there is chromium rich second phase, there is still chromium present in the main metal matrix.

Chemical Analysis

A chemical analysis was completed for the four stages of LM-RIF processing with the metallic suspension. The analysis was completed on the as received powder, after attrition milling, after organic removal at 600°C in ambient atmosphere, and after sintering in 5% H₂/N₂. Carbon and sulfur content was determined using combustion infrared detection as per ASTM E

1019-08. Oxygen and Nitrogen content was determined using inert gas fusion as per ASTM E 1019-08. Hydrogen content was determined using inert gas fusion as per ASTM E 1447-09. Chromium, manganese, molybdenum, nickel, phosphorus, and silicon content was determined using direct current plasma emission spectroscopy as per ASTM E 1019-08. All analysis was carried out by Luvak Inc. (Boylston, MA USA). Figure 5.12 Top and bottom shows the entire content of elements in the steel parts for all four stages of processing. Prior to organic removal, chromium and oxygen content are relatively stable and fall within the expected range of 316L stainless steel. After organic burnout, oxygen levels increase, and chromium levels decrease. Final oxygen content in the steel part is approximately 1.5at% by chemical analysis, with the oxygen being located in a second phase as previously determined by auger spectroscopy. Furthermore, the second phase determined via auger spectroscopy shows high oxygen, chromium, and manganese, while the chemical analysis shows a decrease in the chromium and manganese content in the bulk material after sintering.

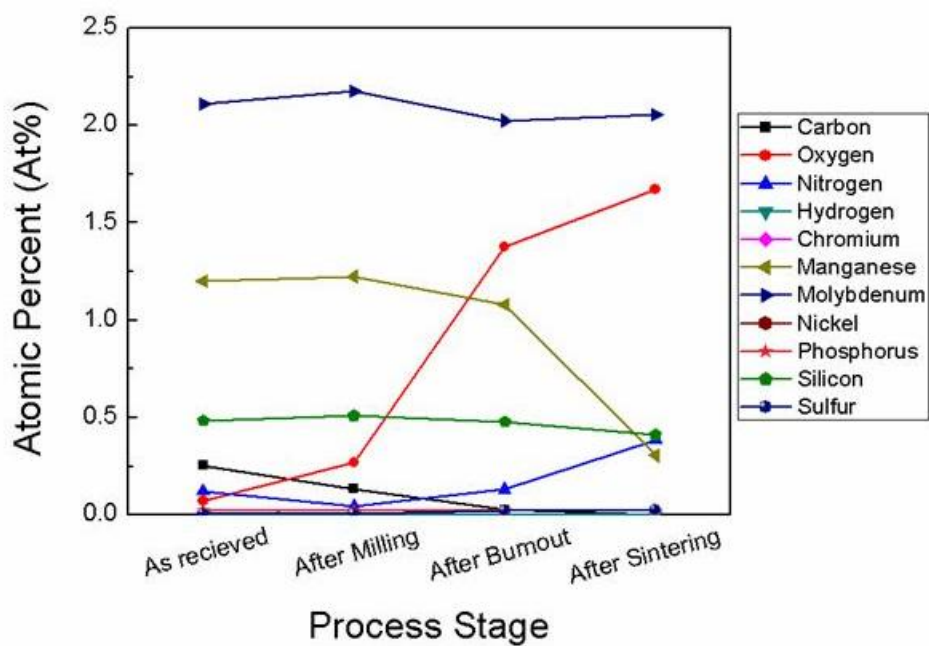
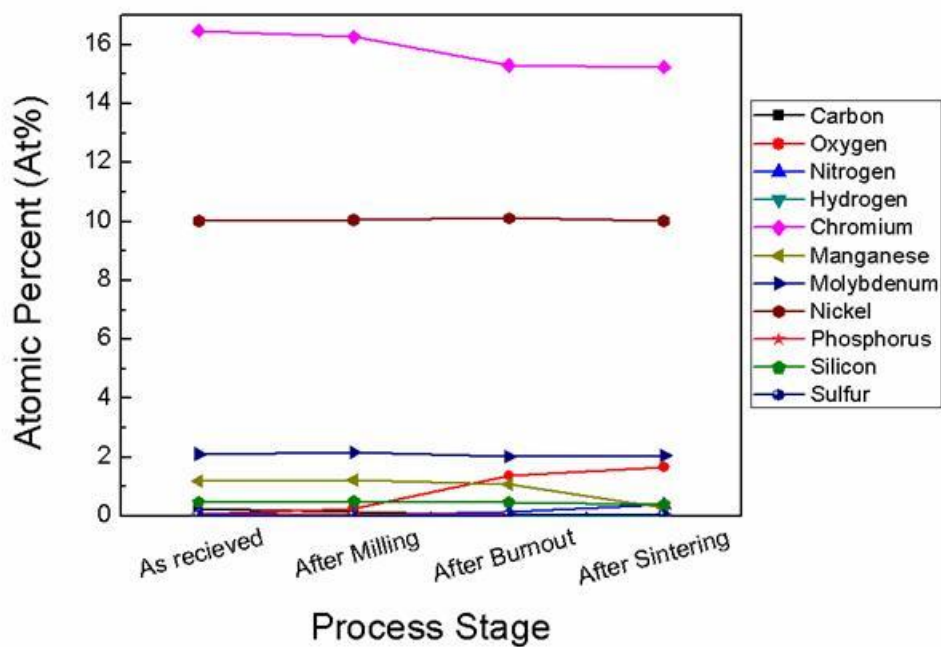


Figure 5.12. A full chemical analysis of the metallic parts was completed for all four stages of processing including the as received powder, post attrition milling, post organic burnout, and post sintering. Top: The full spectrum of elements investigated are shown, including high chromium and nickel content, indicative of 300 series stainless steel. Bottom: a restricted view is shown up to 2.5 at% to more clearly illustrate the lower at% elements.

Table 5.6. The atomic percentages of the elements found in the steel parts are given as a function of the process stage. The as received store bought powder, after milling with oleic acid dispersant, after organic removal at 600°C in ambient atmosphere, and finally, after sintering at 1300°C in 5% H₂/N₂.

<i>Element</i>	<i>As Received (At%)</i>	<i>After Milling (At%)</i>	<i>After Organic Removal (At%)</i>	<i>After Sintering (At%)</i>
Carbon	0.0255	0.134	0.027	0.002
Oxygen	0.071	0.2705	1.375	1.6725
Nitrogen	0.122	0.044	0.132	0.3865
Hydrogen	0.0009	0.0006	0.0013	0.0019
Chromium	16.475	16.27	15.305	15.245
Manganese	1.2	1.225	1.08	0.305
Molybdenum	2.11	2.175	2.025	2.055
Nickel	10.015	10.055	10.115	10.03
Phosphorus	0.022	0.0225	0.0225	0.0225
Silicon	0.485	0.51	0.48	0.41
Sulfur	0.008	0.008	0.024	0.027

Mechanical Property Evaluation of 300 series stainless steel Specimens

The LM-RIF process was utilized to fabricate mechanical test bars with dimensions 300x400x5000μm, in width, height, and length, respectively. These specimens were tested in 3-

point bending to determine the yield stress and ultimate tensile stress of the 300 series stainless steel produced with the LM-RIF process. An Instron 4858 mechanical testing system was used to complete the 3point bend testing in Dr. Muhlstein's laboratory. The mechanical testing was provided courtesy of Roi Meirum in Dr. Muhlstein's laboratory. The test system consists of an electromechanical load frame with a high-resolution digital encoder at 20 nm resolution. A $10\text{N}\pm 0.1\%$ load cell was used to measure the force applied to specimens. Real-time imaging of the testing process were recorded via a digital camera in conjunction with a firewire image acquisition card (Pixelink, Inc.). Ambient vibrations were minimized during testing by a mechanical damping system supporting the testing apparatus. The result of the bend tests, listed in Table 5.7, indicate that the yield stress ranges from 603 to 677MPa, with ultimate tensile strength ranging from 1.23 to 1.49GPa. These values are significantly higher than bulk 300 series stainless steel yield strength of 250MPa and ultimate tensile strength of 560MPa [31, 32].

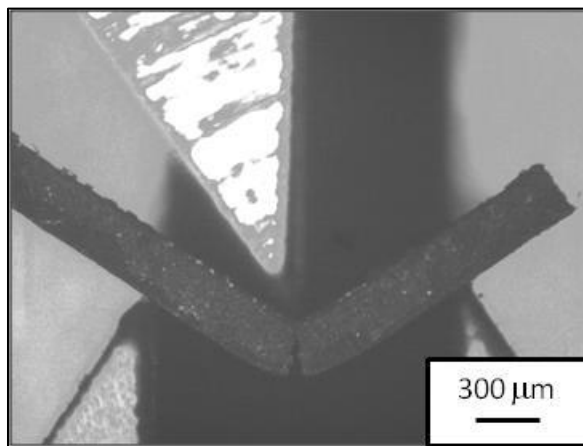


Figure 5.13. An optical image of a sample 3-point bend specimen ($300\times 400\times 5000\mu\text{m}$) is shown undergoing ductile fracture. The test specimens were fabricated using the LM-RIF process. Mechanical testing was carried out in collaboration with Professor Muhlstein, at The Pennsylvania State University.

Table 5.7. The yield stress and ultimate tensile stress are given for four samples tested in 3-point bend. In sample 4, the test was stopped before the ultimate tensile strength could be measured due to the upper loading point pinching the test bar against the lower loading point. This problem was fixed, and the other tests were successfully completed [33]. The 95% confidence interval is given for both the yield stress and ultimate tensile stress.

<i>Sample</i>	<i>Yield Stress (MPa)</i>	<i>Ultimate Tensile Strength (GPa)</i>
1	677	1.23
2	622	1.49
3	603	1.26
4	616	Test Stopped
Average	630 ± 52	1.33 ± 0.35

Prototype Testing

Forceps Prototype Devices

In a concurrent study by Aguirre et al. [33], forceps fabricated in the Adair labs by Hayes using the LM-RIF process, as shown in Figure 5.14, were assembled into functioning prototypes with aspect ratio of 1:40. Following fabrication, prototype fabrication and testing was carried out by Milton Aguirre and Mathew Addis. The results of their work are summarized. The prototype forceps were spot welded to a wire, which was then inserted into an actuation sheath made from 300 series stainless steel (SS hypodermic tube: 17 gauge, 0.058" OD x 0.042" ID x 0.008" wall).

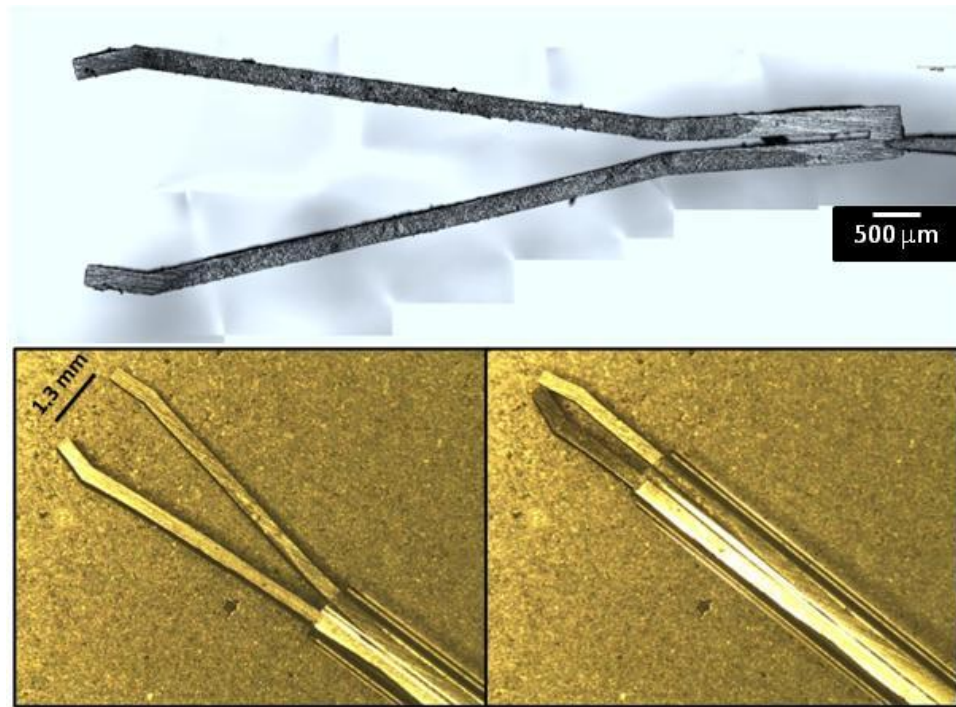


Figure 5.14. A fabricated forceps with the LM-RIF process is depicted using optical microscopy. See also Figure 3.1 for a schematic of the forceps instrument. Top: an optical image of as fabricated forceps with aspect ratio of 1:40. Bottom left: assembled forceps device in the open position, showing a total jaw opening of 1.3mm. The retracting and extending sheath composed of glass, for demonstration, can be seen in the bottom right in the optical image. Bottom right: the assembled forceps in the closed position, showing the grasping function and the fully extended sheath closing the instrument tips.

A series of evaluations were performed on the assembled prototype forceps an incremental step test to evaluate tip deflections as a function of sheath position, as well as gripping strength measured by a pull off test. In the pull off test, the forceps were actuated to grip a latex rubber tube, and the force needed to remove the tube from the closed forceps was measured. After accounting for exact dimensions, as well as any initial geometrical variations due to plastic deformation, good agreement was seen between the experimental and simulated theoretical results. Figure 5.15 shows the forceps tip location as a function of sheath actuation, with agreement between the experimentally (EXP) measured tip location and the theoretically calculated (FEA) tip location [33]. A greater tip deflection in Figure 5.15 corresponds to the

forceps closing. For a detailed review of the prototype validation, readers are referred to Aguirre et al. [33].

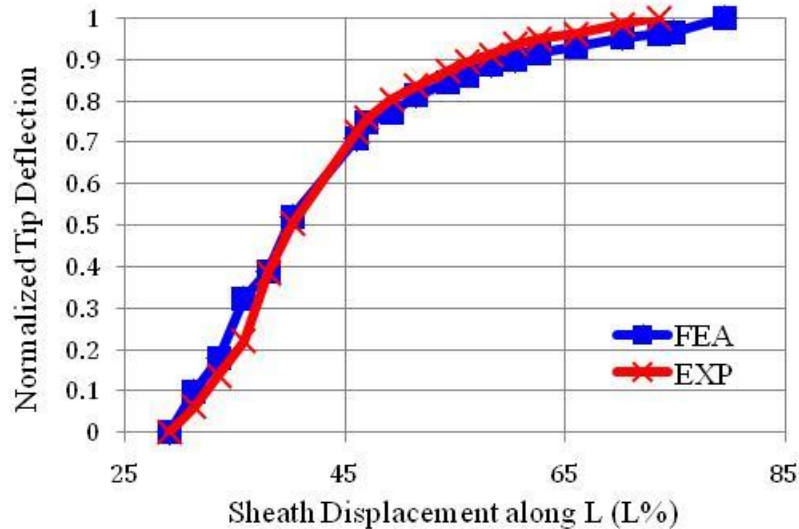


Figure 5.15. The tip location of an actuated forceps is plotted as a function of sheath location. Good agreement is seen between the Finite Element Analysis (FEA) theoretically calculated tip location, and experimentally (EXP) observed tip location. The observed tip location was measured in real time via photos captured with a digital camera (Pixelink, Inc.). A larger tip location corresponds to the forceps closing. Figure courtesy of Aguirre et al. [33]

Forceps Validation at Penn State's Hershey Medical Center

In addition to laboratory prototype testing, validation of the forceps overall function was also carried out in a test trial with endoscopic surgeons at Hershey Medical Center [34]. The forceps fabricated with the LM-RIF process, were assembled into NOTES instruments by attaching the forceps and sheath mechanism via a cable, to an actuation handle. Through the handle, shown in Figure 5.16, the forceps instrument was actuated by surgeons in a series of validation experiments.

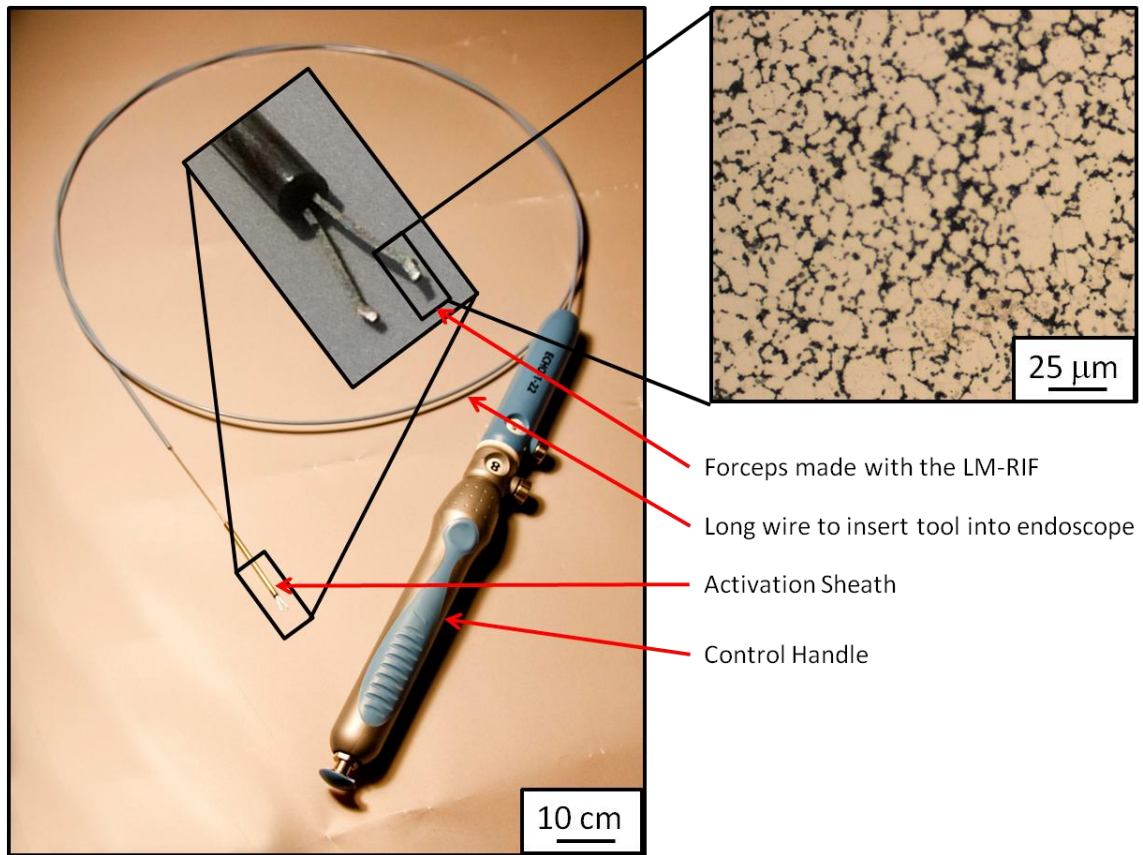


Figure 5.16. Prototype forceps assembled into a NOTES device for hospital testing. An inset is shown highlighting that the microstructure of the prototype device is similar to the previously analyzed microstructure. The forceps device, after being spot welded to an actuation cable, is connected to a handle, shown in blue. With this handle, surgeons are able to actuate the sheath, opening and closing the forceps. The entire forceps and actuation wire are meant to work within an endoscope, as described in Chapter 2 [33].

The validation experiments consist of tests to qualify the dexterity of the instrument, the gripping pulling force of the forceps, as well as the functioning of the forceps as a biopsy tool. The tests carried out are listed in Table 5.8. Twelve participants evaluated the prototype forceps, as well as a standard endoscopic tool. Among the features most interesting about the new forceps, fabricated with the LM-RIF process, is the ability to control the closing and opening of the device, as opposed to having just two settings, open or closed.

Table 5.8. The endoscopic tool evaluation tests are listed along with their description, and the intended feature/ability tested. Data was collected via a survey given to participating surgeons after the tests were completed [34].

<i>Test Name</i>	<i>Feature/Ability Tested</i>	<i>Description</i>
Fuzzy Ball	Dexterity/Handling	Picking up a fuzzy ball by as few hairs as possible
Cup Drop	Dexterity/Gripping Force	Picking up small fuzzy balls and placing them in a cup
Material Pull	Pulling Force/Gripping Force	Removing pins with fabric attached from a sheet of foam
Force Gauge	Pulling Force	Pulling on a piece of latex attached to a force gauge
Biopsy	Tissue Removal	Removing pieces of foam from a foam block, the number of attempts necessary to remove the dot will be counted
Ring Around	Gripping Force/Handling	Picking up rings and placing them around a pin in a piece of wood

Results of the forceps prototype testing are shown in Figure 5.17 [34]. The prototype instrument performed as well as, or better than, the standard instrument in almost all of the tasks undertaken. The prototype testing illustrates the LM-RIF capabilities to fabricate devices on a size scale that was previously unattainable and validates the need for a mesoscale fabrication process that is closely linked with mechanical design and testing.

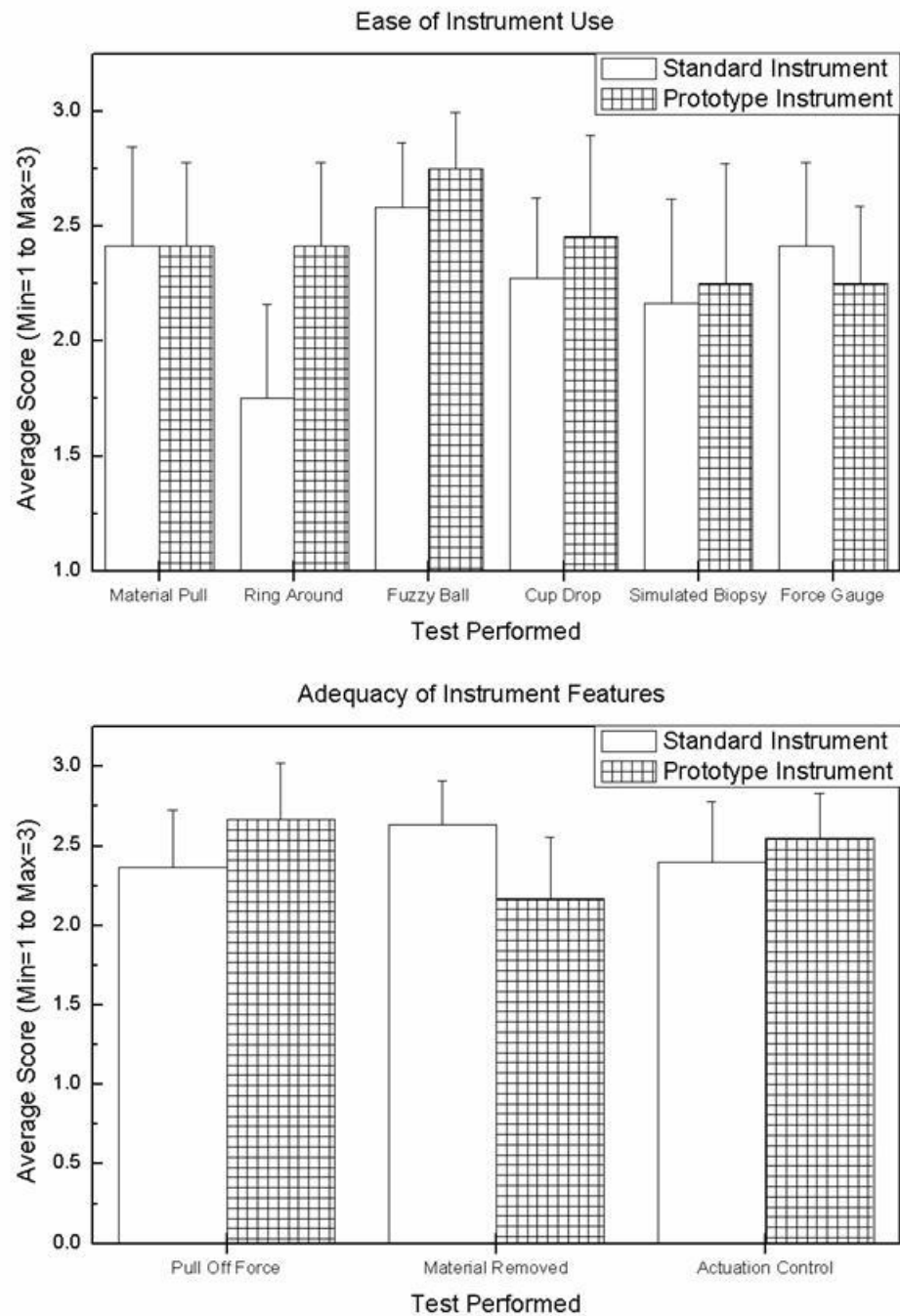


Figure 5.17. The prototype forceps was tested against an industry standard instrument in a variety of real-life simulations shown in both the Top and Bottom comparisons. Endoscopic surgeons ranked the performance of the prototype forceps against the standard instrument for all

tests completed. The forceps instrument performed as well as, or better than, the standard instrument in almost all of the tasks at hand. This validates the LM-RIF process as an important step in designing and fabricating devices on size scales that were previously unattainable [34]. The ability of the LM-RIF to allow design engineers to re-engineer the opening and closing mechanism of the forceps, allowing more precise gripping control, facilitated the preference of the prototype instrument over the standard instrument.

C3M Prototype Devices

Prototype C3M devices were successfully fabricated utilizing the LM-RIF process, as well as mechanically tested and compared against theoretically calculated performance.

Prototype C3M devices consisting of 9 unit cells each are shown in Figure 5.18.

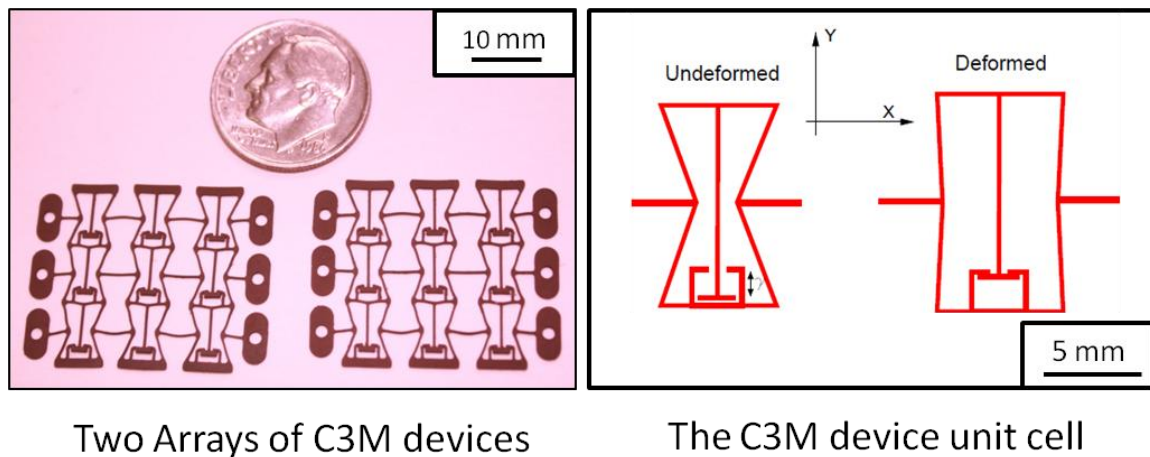


Figure 5.18. Prototype C3M arrays consisting of 9 unit cells each are shown in the optical image. A U.S. dime is included for perspective. These devices, fabricated with the LM-RIF process are over 2 centimeters in width, 400 μ m in thickness, and have features as small as 50 microns in the contact mechanism [13, 35]. The contact mechanism can be seen in the right hand figure, where the dash pot mechanism contacts itself in as the cell deforms.

To mechanically evaluate the performance of C3M devices, a small scale test rig was developed and reported by Mehta et al. [35]. This unique test rig, shown in Figure 5.19, has the capability to test the C3M devices through a specialized mounting system that accounts for the auxetic mechanical behavior of the C3M device.

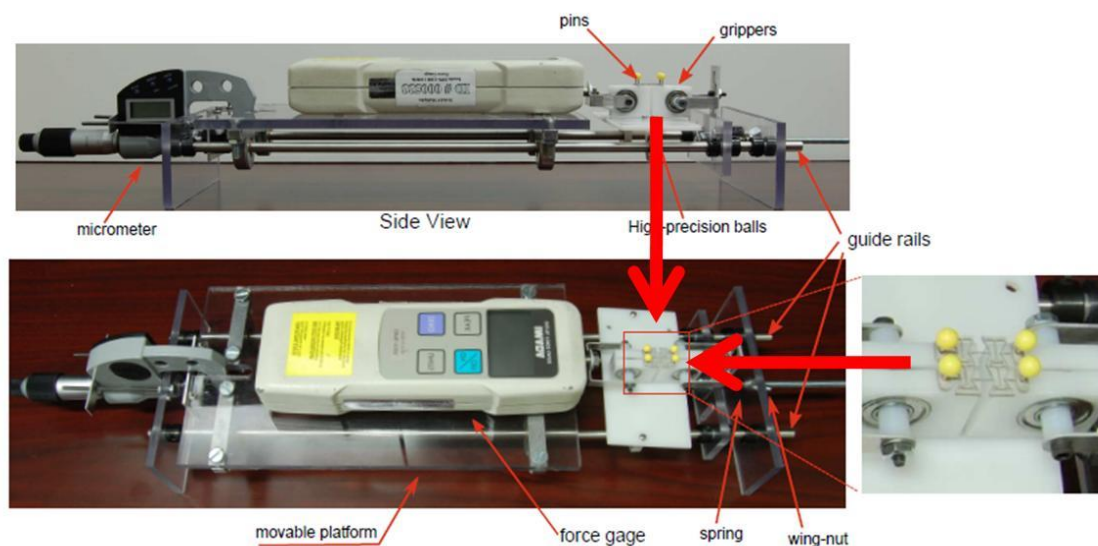


Figure 5.19. A specialized test rig, shown from the top view and side view was developed to mechanically evaluate the C3M devices. The rig consists of a force gauge to monitor the force as a function of deformation. The deformation is controlled using a micrometer. Right: the sample mounting rig is able to support the C3M device, apply a load, and comply with the auxetic deformation of the cellular array [35].

The experimentally measured force displacement curves were compared to the theoretically calculated curves in Figure 5.20. Good agreement between experimentally measured values and theoretically calculated data occurs when an elastic modulus of 150 GPa is assumed for the 300 series stainless steel fabricated with the LM-RIF process. Furthermore, an elastic modulus of 150 GPa is well within expected values for the material system processed. Although the elastic modulus is lower than that of bulk stainless steel, processing parameters affecting grain size, density, and composition could give rise to the lower value. Additional mechanical testing is proposed, outlined in Chapter 6, which includes independent determination of the elastic modulus.

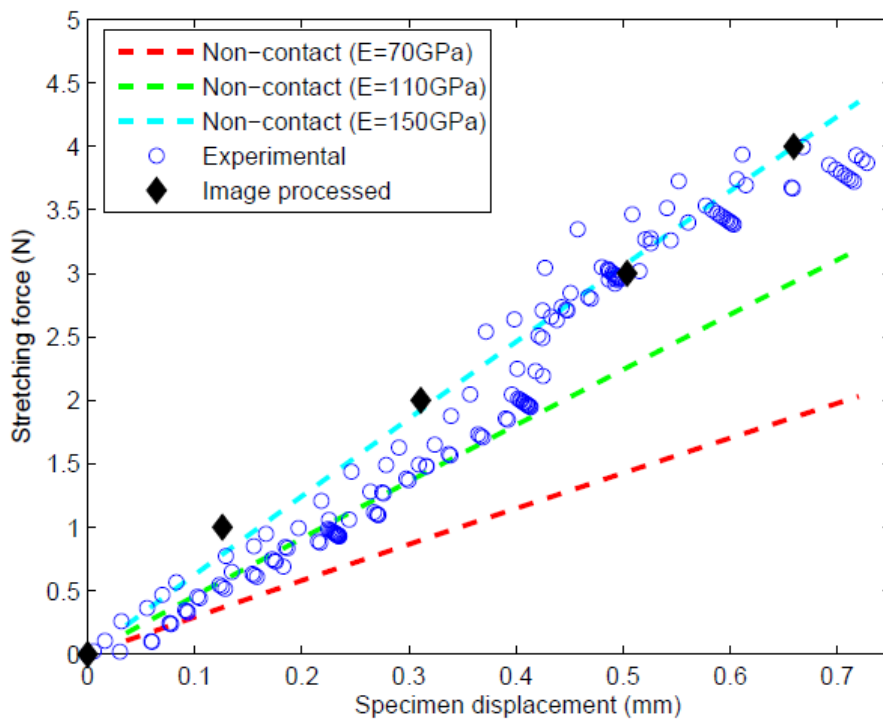


Figure 5.20. Experimentally determined force displacement data is compared to theoretically calculated data for assumed elastic moduli of 100, 110, and 150GPa. Relatively good agreement is obtained for the experimentally measured data and the theoretical data calculated with $E=150\text{GPa}$. The experimental data is from the digital micrometer read out, while the image processed specimen displacement data is measured through an external camera system above the test rig [35].

The C3M prototype testing illustrates the LM-RIF capabilities to fabricate devices on a size scale that was previously unattainable by any microfabrication approach. In addition, the LM-RIF process has the capability to produce larger arrays, with more intricate geometries. The successful prototype testing of the C3M devices further validates the need for a mesoscale fabrication process that is closely linked with mechanical design and testing.

Conclusion

The formulation of non-aqueous 300 series stainless steel suspensions was successfully completed, and these suspensions were implemented into the LM-RIF process. Initially, the length of attrition milling plays an important role in the final particle shape, as long mill time results in less spherical particles. Furthermore, the non-aqueous environments rely strictly on steric repulsive forces to maintain a viscosity low enough to be cast in molds during LM-RIF processing. After sintering, a chromium and oxygen rich secondary phase was found via AES analysis, however, residual chromium still remained within the matrix of the metal part.

The average yield stress in 3-point bending of 300 series stainless steel fabricated parts is 628 MPa, with ultimate tensile strength of 1.33GPa. Prototype designs of both a forceps device, and a C3M component were successfully fabricated and testing and validation was completed for the designs. It was found that in both cases, the devices performed as expected theoretically. In addition, the forceps device performed well in a comparison study at Hershey Medical Center.

References

1. *POWDER-METALLURGY - APPLICATIONS, ADVANTAGES, LIMITATIONS* - KLAR,E. International Journal of Powder Metallurgy, 1983. 19(4): p. 315-316.
2. Erhard, K. and P.K. Samal, *Powder Metallurgy Stainless Steels: Processing, Microstructures, and Properties*. 2007: ASM International.
3. Ye, H.Z., X.Y. Liu, and H.P. Hong, *Fabrication of metal matrix composites by metal injection molding - A review*. Journal of Materials Processing Technology, 2008. 200(1-3): p. 12-24.
4. Schatt, W., K.P. Wieters, and A. European Powder Metallurgy, *Powder metallurgy: processing and materials*. 1997: European Powder Metallurgy Association.
5. Thummler, F. and R. Oberacker, *An introduction to powder metallurgy*. 1993: Institute of Materials.

6. Imbaby, M.F. and K. Jiang, *Stainless steel-titania composite micro gear fabricated by soft moulding and dispersing technique*. *Microelectronic Engineering*. 87(5-8): p. 1650-1654.
7. Imbaby, M., K. Jiang, and I. Chang, *Net shape fabrication of stainless-steel micro machine components from metallic powder*. *Journal of Micromechanics and Microengineering*, 2008. 18(11): p. 7.
8. Fu, G., N.H. Loh, S.B. Tor, B.Y. Tay, Y. Murakoshi, and R. Maeda, *Injection molding, debinding and sintering of 300 series stainless steel microstructures*. *Applied Physics a-Materials Science & Processing*, 2005. 81(3): p. 495-500.
9. Terry J. Garino, A.M., Thomas Buchheit, and Brad Boyce *Fabrication of Stainless Steel Parts for MEMs*. in *MRS Fall Meeting*. 2001. Boston, MA.
10. Hernigou, P. and T. Bahrami, *Zirconia and alumina ceramics in comparison with stainless-steel heads - Polyethylene wear after a minimum ten-year follow-up*. *Journal of Bone and Joint Surgery-British Volume*, 2003. 85B(4): p. 504-509.
11. Aguirre, M.E., G. Hayes, R. Meirom, M. Frecker, C. Muhlstein, J.H. Adair, and J.A. Kerr, *The Design and Fabrication of Narrow-Gauge (1 mm Diameter) Surgical Instruments for Natural Orifice Translumenal Endoscopic Surgery*. Under review in *The Journal of Mechanical Design*, 2011.
12. Henry, C. and G. McKnight. *Cellular variable stiffness materials for ultra-large reversible deformations in reconfigurable structures*. in *Smart Structures and Materials: Active Materials: Behavior and Mechanics*. 2006.
13. Mehta, V., M. Frecker, and G.A. Lesieutre, *Stress Relief in Contact-aided Compliant Cellular Mechanisms*. *ASME Journal of Mechanical Design*, 2009. 31(9): p. 1-11.
14. Sushumna, I., R.K. Gupta, and E. Ruckenstein, *EFFECTIVE DISPERSANTS FOR CONCENTRATED, NONAQUEOUS SUSPENSIONS*. *Journal of Materials Research*, 1992. 7(10): p. 2884-2893.
15. Adair J.H., R.A.J., McCoy L.G. *Particle size analysis of ceramic powders*. in *Processing for Improved Productivity, Advances in Ceramics*. 1984. Columbus, Ohio: The American Ceramic Society.
16. Antolino, N.E., *Lost Mold-Rapid Infiltration Forming: Strength Control in Mesoscale 3Y-TZP Ceramics*, Doctor of Philosophy, dissertation in Materials Science and Engineering, The Pennsylvania State University, University Park, 2010.
17. Hunter, R.J., *Foundations of colloid science*. 2 ed. 2001, New York: Oxford University Press.
18. Krupp, H., *Particle Adhesion Theory and Experiment*. *Advan. Colloid Interface Sci.*, 1967. 1: p. 111-239.

19. Adair, J.H., R. Kumar, N. Antolino, C.J. Szepesi, R.K. Kimel, and S.M. Rouse. *Colloidal Lessons Learned for Dispersion of Nanosize Particulate Suspensions*. in *Lessons in Nanotechnology from Traditional and Advanced Ceramics, Proceedings of the World Academy of Ceramics*. 2005. Faenza, Italy: Techna Group S.I.
20. Visser, J., *On Hamaker constants: A comparison between Hamaker constants and Lifshitz-van der Waals constants*. *Advances in Colloid and Interface Science*, 1972. 3(4): p. 331-363.
21. Gregory, J., *APPROXIMATE EXPRESSIONS FOR RETARDED VANDERWAALS INTERACTION*. *Journal of Colloid and Interface Science*, 1981. 83(1): p. 138-145.
22. Bergstrom, L., C.H. Schilling, and I.A. Aksay, *CONSOLIDATION BEHAVIOR OF FLOCCULATED ALUMINA SUSPENSIONS*. *Journal of the American Ceramic Society*, 1992. 75(12): p. 3305-3314.
23. Allara, D.L. and R.G. Nuzzo, *SPONTANEOUSLY ORGANIZED MOLECULAR ASSEMBLIES .1. FORMATION, DYNAMICS, AND PHYSICAL-PROPERTIES OF NORMAL-ALKANOIC ACIDS ADSORBED FROM SOLUTION ON AN OXIDIZED ALUMINUM SURFACE*. *Langmuir*, 1985. 1(1): p. 45-52.
24. Bergstrom, L., *Hamaker constants of inorganic materials*. *Advances in Colloid and Interface Science*, 1997. 70: p. 125-169.
25. Bergstrom, L., E. Blomberg, and H. Guldborg-Pedersen, *Interparticle forces and rheological properties of ceramic suspensions*, in *Novel Synthesis and Processing of Ceramics*. 1999. p. 119-126.
26. Aschauer U., B.-M.O., Moreno R., Bowen P., *Hamaker 2: A toolkit for the calculation of particle interactions and suspension stability and its application to mullite synthesis by colloidal methods*. *Journal of Dispersion Science and Technology*, In Press.
27. *CRC Handbook of Chemistry and Physics*. 87 ed. 2006-2007, Boca Raton, FL: CRC Press.
28. Firth, B.A. and R.J. Hunter, *FLOW PROPERTIES OF COAGULATED COLLOIDAL SUSPENSIONS .1. ENERGY-DISSIPATION IN FLOW UNITS*. *Journal of Colloid and Interface Science*, 1976. 57(2): p. 248-256.
29. Vandeven, T.G.M. and R.J. Hunter, *ENERGY-DISSIPATION IN SHEARED COAGULATED SOLS*. *Rheologica Acta*, 1977. 16(5): p. 534-543.
30. Rasband, W.S., *ImageJ*, B. National Institutes of Health, MD, USA, Editor. 1997-2009.
31. Hertzberg, R.W., *Deformation and fracture mechanics of engineering materials*. 1996: J. Wiley & Sons.
32. Matweb. www.matweb.com. 2011 [cited 2011]; Available from: <http://www.matweb.com/search/DataSheet.aspx?MatGUID=1336be6d0c594b55afb5ca8bf1f3e042&ckck=1>.

33. Aguirre, M., G. Hayes, C. Yuangyai, M. Frecker, J. Adair, and N. Antolino. *Fabrication and Strength-Based Design of a Meso-Forceps*. in *ASME 2009 International Design Engineering Technical Conferences*. 2009. San Diego, CA.
34. Addis, M., *Evaluation of Surgical Instruments for Use in Minimally Invasive Surgery*, B.S. Honor Thesis, dissertation in Department of Mechanical and Nuclear Engineering, The Pennsylvania State University, University Park, PA, 2010.
35. Mehta, V., Hayes, G.H., Frecker, M.I., Adair, J.H., *Design, Fabrication, and Testing of Meso-scaled Cellular Contact-aided Compliant Mechanisms*, in *ASME 2010 Conference on Smart Materials, Adaptive Structures and Intelligent Systems, SMASIS2010*. 2010: Philadelphia, Pennsylvania, USA.

Chapter 6

Conclusions and Future Work

A collaborative effort among mechanical engineering and materials science engineering and surgeons at Penn State's Hershey Medical Center has been presented that furthered the development of two devices: 1; a minimally invasive surgical instrument tool tip, and 2; a contact-aided compliant cellular mechanism. Additionally, it was demonstrated that mechanical design influences the formulation of colloidal suspensions and processing parameters in the materials fabrication areas, while measured material properties, along with processing yield results, and processing constraints influenced the mechanical design.

The overarching objective of this dissertation was to further develop the novel microfabrication, LM-RIF process, invented over the past five years at Penn State in conjunction with mechanical design, with materials science properties dictating the process parameters and constraints on mechanical design. The LM-RIF technique has the capability to produce large arrays of free standing parts, have the desired large aspect ratios, maintain good resolution, be applicable to 3-dimensional structures, and permits a wide range of materials to be developed based on particulate materials.

The hypothesis that a combination of lithography molding techniques, colloidal science, and mechanical testing, leads to a new fabrication process able to work with particulate material systems to manufacture meso-scale devices has been demonstrated in this dissertation. Additionally, it has been shown that incorporating an analysis of the predicted stresses due to drying into the original device design alters the final mold design, and increases the yield and properties of future instruments. Lastly, it was shown that both metallic and ceramic particulate material systems can be incorporated into the fabrication process, as well as stacking of photoresist molds to create 3-dimensional shapes. A summary of the main research contributions

are given in Table 6.1. The contributions are separated by the LM-RIF processing step affected by the work.

Conclusions

An introduction to the design and fabrication of mesoscale devices was given, demonstrating that the LM-RIF process is the most viable fabrication approach to the devices in question. A description of the non standard lithography methods used to create molds for the LM-RIF process was provided, along with the procedure to stack lithography molds to create three dimensional structures, shown in Chapter 3.

The LM-RIF process was shown to; (1) fabricate large arrays of surgical instruments; (2) be complementary to particulate based material systems; and, (3) have 3 dimensional capabilities. Furthermore, using this manufacturing technique for both surgical instrument and C3M device design is attractive because free standing parts are fabricated with the desired large aspect ratios while retaining good resolution on the micron scale stemming from the lithographic based molds and colloidal infiltration processes.

The formulation and characterization of non-aqueous 300 series stainless steel colloidal suspensions is provided in Chapter 3. Following the incorporation of the non-aqueous suspension into the LM-RIF process, prototype forceps and C3M devices were fabricated and tested for both material strength, and device performance. It was found that in both applications, the devices performed as expected, while in the in the case of the forceps, the prototype design was better or equal to existing surgical forceps. The properties of the initial slurry composition are important in determining final particle shape and size, even under the same milling procedures. By altering the amounts of solvents, dispersants, and organic additives, the colloidal suspension can be tailored to work within the LM-RIF process.

Furthermore, non-aqueous 3Y-TZP and 300 series stainless steel suspensions were able to be combined, forming composites. These composite materials show promise to produce desirable characteristics such as high strength and graceful failure. Through the determination of the rheological properties of the composite suspensions, the concentration of particles in a suspension increases the overall viscosity. Also, the apparent viscosity of the composite suspension decreases as the ratio of micro-stainless steel to zirconia increases at constant total solids loading. This is attributed to the interaction between particles in a suspension with two particle size distributions.

The prediction of constrained drying stress was calculated analytically with both a one dimension and three dimensional model, in Chapter 4. While the one dimensional model is faster to implement, it only accounts for relative moisture mass in the sample as a function of time, while the three dimensional model, can calculate drying time, drying stress, and constrained drying stress. The three dimensional model, written in Comsol® was used to demonstrate that the constrained drying stresses are dependent of forceps shape. A decrease in the total constrained drying stress is seen with a more forgiving, curved design, compared to a straight segmented design. Predicting the constrained drying stress of parts manufactured within the LM-RIF allows changes to be made to the part shape prior to fabrication, thereby minimizing stresses during drying, and maximizing final part yield.

The formulation and characterization of two new gel-binder systems, used in the aqueous colloidal suspension preparation of 3Y-TZP, are given in Appendix A. These binder systems were formulated to increase part yield, to accommodate the large constrained drying stresses for the LM-RIF process. The sintered yield of forceps increased from 0% to 40.6% for small aspect ratio designs. Green body strength increased from 1Mpa to 4MPa by diametral compression testing, while viscosity increased dramatically. Both binder systems showed complete removal via combustion, while the mold material is removed at a higher temperature. This indicates that

the binder system is only actively supporting the green part through the drying process. Residual closed porosity and bubbles in the final parts resulted in relatively weak parts, but there is ongoing work to remedy this problem. As the LM-RIF process is iterative, future strength improvements, as well as improvements in aspect ratio, can lead to better forceps designs.

Appendix B provides a synopsis of a design project used to topologically design a forceps instrument that can be manufactured using the LM-RIF process in 3 layers. Within this topology optimization scheme, the number of layers can be increased to a desired level, constrained only by practical manufacturing limits.

The Comsol[®] Multiphysics 3.5a, and Matlab[®] computer codes used for the drying modeling discussed in Chapter 4 are provided in Appendix C.

Table 6.1. The main research contributions of this dissertation are given as they correspond to the LM-RIF process. Each contribution helped to further advance the capabilities of the LM-RIF process.

<i>LM-RIF Process Step</i>	<i>Contribution</i>	<i>Advantages</i>	<i>Remaining Limitations</i>
SU8 Mold Fabrication	Adapted ultra thick and laminating SU8 technologies to work with refractory substrates	Molds 10 to >1000 microns in thickness, as well as laminating mold layers possible	The smallest possible feature size increases with increased mold thickness
Aqueous 3YSZ Colloidal Suspensions	Formulated novel gel-binder system for aqueous processing	Increased green strength, and part yield for complex shapes	High viscosity entraps air bubbles during casting, lowering strength
Non-Aqueous 300 series stainless steel Colloidal	Formulated high solids loading suspensions utilizing oleic acid and attrition milling	High solids loading and low viscosity for casting into complex shapes	Green part density is a function of maximum solids loading

Suspensions			
Composite 300 series stainless steel and 3YSZ Colloidal Suspensions	Formulated composite suspensions able to be incorporated into the LM-RIF process	Harder materials, along with tailored material properties	Composite suspensions must have same solvent
Constrained Drying Stress Modeling	Extended drying model to 3D, included stresses from mold walls during shrinking	Constrained drying stress can be assessed via part shape, size, thickness, and material	System parameters need to be determined experimentally prior to modeling

Future Work

Extensions and improvements to the LM-RIF process, and the supporting materials science research fall into the following categories: 1) Manufacture of three dimensional structures, 2) Improvement of the yield of C3M devices through redesign of the mechanisms to include curved segmented structures, instead of straight segmented structures, 3) Improvement of the yield of aqueous based colloidal suspensions through minimizing drying stresses via critical point drying, 4) Further improving the ability of the constrained drying model to predict drying stresses by experimentally determining parameters, 5) Improving device performance through the incorporation of two or more materials in one device, and 6) Additional testing of the mechanical properties of the metal, ceramic, and composite components via theta-test specimens and tensile test specimens.

Three dimensional part design

In Chapter 2, the processing steps are described to fabricate and laminate photoresist molds together, creating three dimensional devices. A simple test case for this process is the fabrication of a three dimensional biopsy needle device, designed by Neibel et al. [1]. In this design, shown in Figure 6.1, a two dimensional biopsy needle design is used to create three individual mold layers. Each of these layers is then stacked, with additional layers offset along the length of the needle, creating a sequence of barbs along the side of the device. This is an ideal test case for fabricating structures in three dimensions with LM-RIF process due to the simplicity of the design, along with the inherent ease of alignment during the laminating process. With this simple test case design, the three possible fabrication methods to create three dimensional structures should be evaluated to determine the best path forward in multi-layer device fabrication.

Three Dimensional Instrument Design

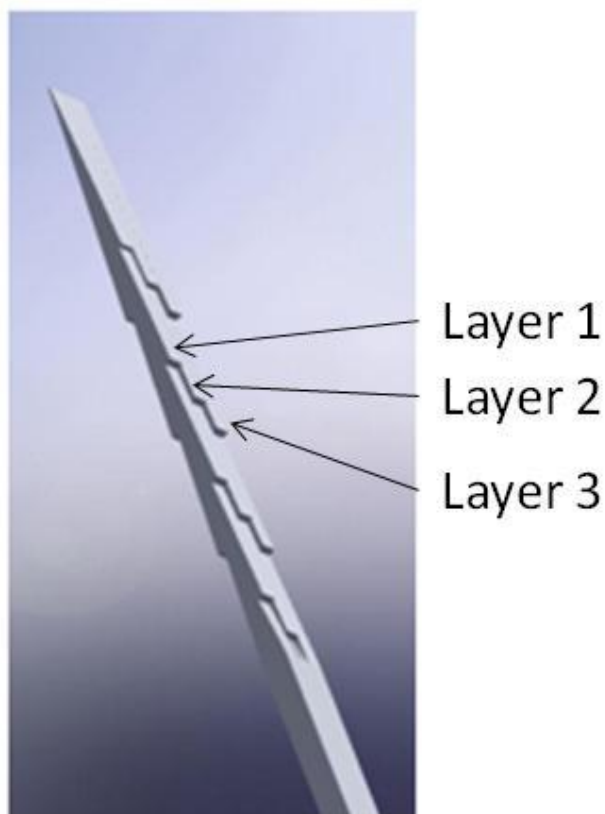


Figure 6.1. A computer aided design drawing of a three layer biopsy needle device is shown. This device is an ideal candidate to evaluate the mold multi-layering scenarios described in Chapter 2. In this test case, three layers are stacked on top of one another, with additional layers offset along the length of the needle, giving rise to the sequence of barbs along the side of the needle [1].

Curved segmented C3M devices

Future work on the design and fabrication of C3M devices includes the incorporation of constrained drying modeling, as well as further fine tuning the LM-RIF process to produce large arrays of C3M devices. In current research by Cirone et al. [2], shown in Figure 6.2, a new curved walled C3M device has been developed, giving rise to an increase in global strain. This curve walled design was inspired through the constrained drying modeling completed on the

forceps instruments. It can be seen in Figure 6.2, courtesy of Cirone et al. [2], that the curved cells exhibit better global strain performance than their straight walled counterparts.

Furthermore, the curved wall cells should show a decrease in constrained drying stress.

		Geometry	$h/l = 0.2$ $\theta = 4^\circ$	$h/l = 0.3$ $\theta = 2^\circ$	$h/l = 0.6$ $\theta = 10^\circ$	$h/l = 0.8$ $\theta = 20^\circ$	$h/l = 1.0$ $\theta = 20^\circ$	$h/l = 1.2$ $\theta = 30^\circ$	Variables Defining Geometry
Non Curved Global Strains	Shape	geometry not possible							
	Non-Contact		12.6%	7.2%	6.5%	3.9%	3.5%		
	Contact-Aided		12.6%	7.2%	7.3%	4.4%	3.8%		
Curved Global Strains	Shape								
	Non-Contact	32.4%	18.2%	12.2%	11.1%	7.3%	5.7%		
	Contact-Aided	32.4%	19.7%	13.4%	12.2%	7.9%	6.3%		

Figure 6.2. The next generation curved wall C3M devices are compared to the original straight walled designs. The curve walled design topology shows an increase in the performance of the device in terms of global strain, and should show a decrease in the constrained drying stress experienced by the part during LM-RIF processing [2].

Incorporating the new C3M device designs into the LM-RIF process is currently being undertaken. In Figure 6.3, the photolithography mask layout is shown, demonstrating the ability to fabricate multiple C3M array sizes, in addition to the various cell designs. Even with limitations on the photolithography mask size available, more than 75 arrays of C3M devices fit on a standard 6 inch mask.

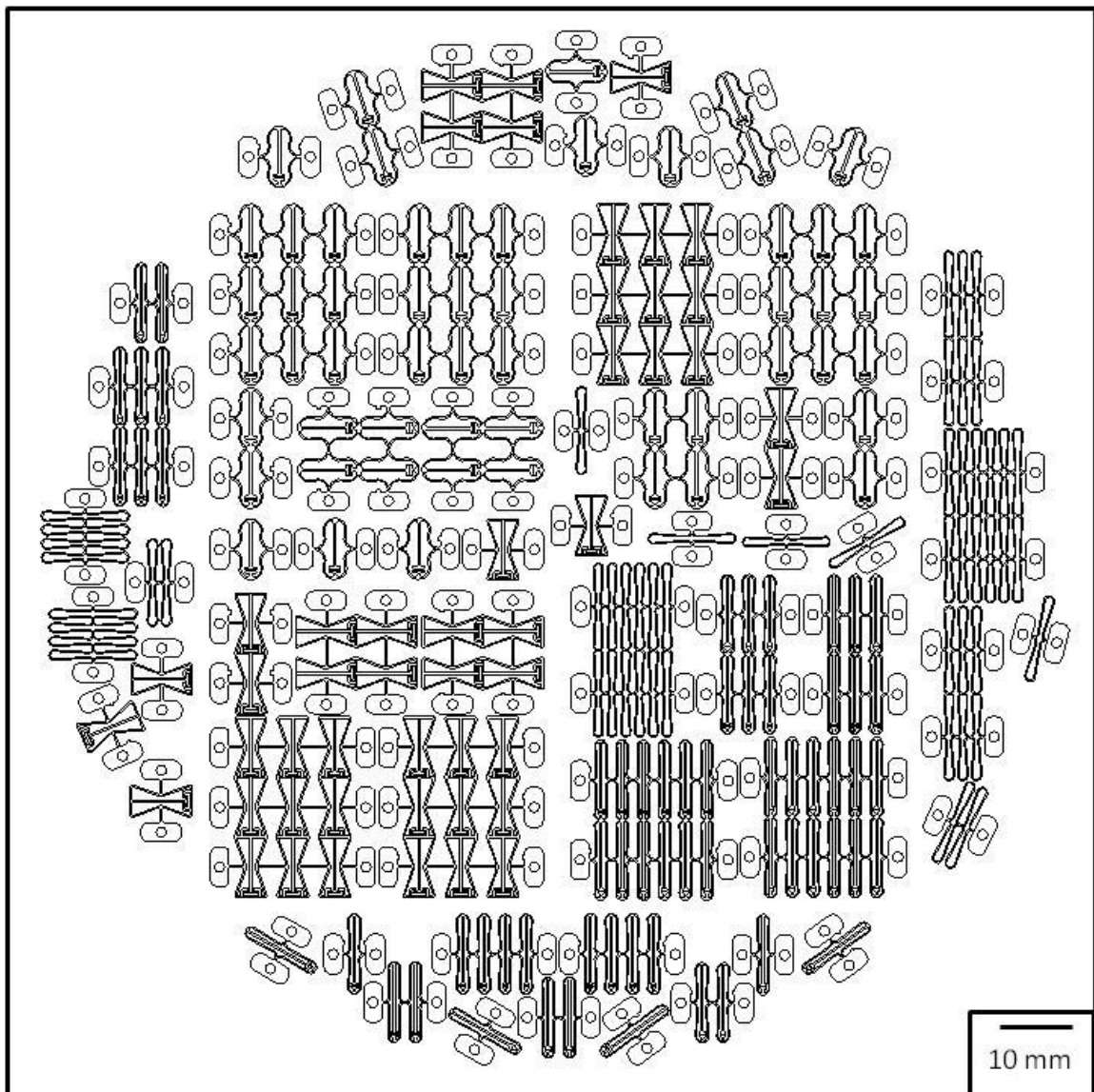


Figure 6.3. The photolithography mask layout for the curved C3M devices is depicted. More than 75 arrays of C3M devices, consisting of the curved and straight C3M designs are present on the mask. Once LM-RIF processing is carried out, mechanical testing, and evaluation of the devices will be performed.

Optical microscopy images of initial prototyped parts for the curved wall C3M devices are shown in Figure 6.4. In (A) and (B) the contact mechanism has good edge resolution, while an intact unit cell is shown in (C). Through the incorporation of the curve walled C3M devices, the adaptability of the LM-RIF process to various geometries is demonstrated. Future work in

collaboration with Cirone includes mechanical testing of the devices on a custom test rig to measure force as a function of global strain. These global strain values will then be compared to the theoretical values, just as in the straight walled C3M device case. Preliminary testing has shown that good agreement is expected.

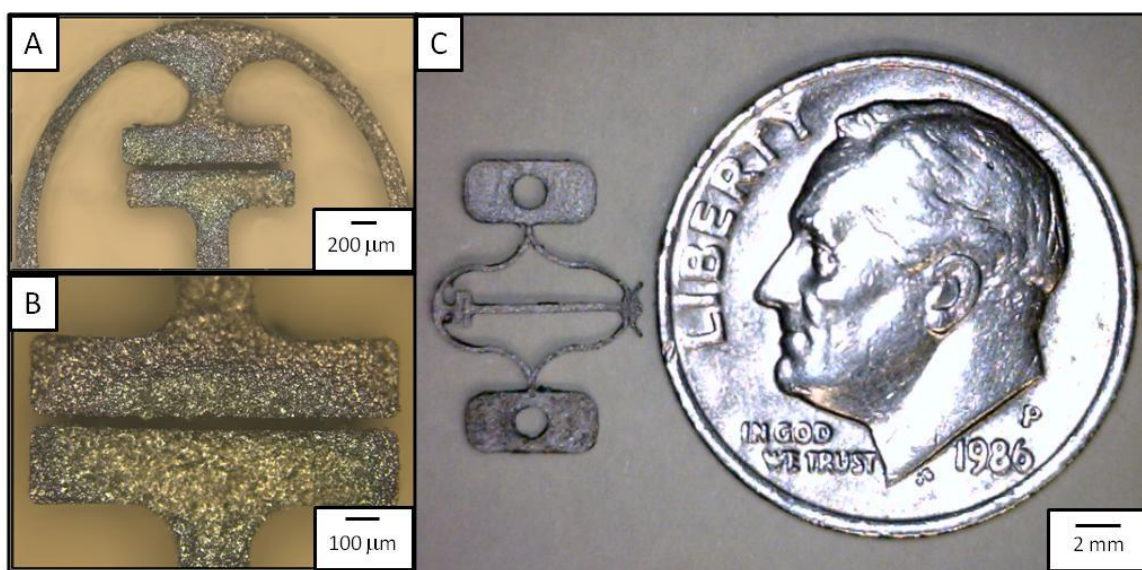


Figure 6.4. Optical microscopy images of curved C3M unit cells are shown. In (A) and (B) the contact mechanism shows good edge resolution, along with minimal distortion. In (C) a complete unit cell is shown with a US dime for scale reference. By fabricating curved C3M devices, the adaptability of the LM-RIF process has been demonstrated. Future work includes the mechanical testing and validation of the curved designs.

Incorporation of critical point drying into the LM-RIF process

A discussion of the constrained drying stress on devices made within the LM-RIF process is given in Chapter 4. These stresses arise mainly due to capillary forces within the drying green ceramic body, forcing the drying part to shrink. The approach taken in Appendix A was to support the drying part through the incorporation of a gelled matrix, along with binder. One possible way to further minimize the stresses seen during drying is to eliminate the capillary forces acting on the part during drying. In this way, the incorporation of critical point drying into

the LM-RIF could greatly increase the yield of intact parts. Furthermore, critical point drying would allow the simultaneous decrease in gel and binder necessary to obtain intact parts after processing, thereby eliminating a source of defects in the sintered parts.

Critical point drying was initially developed for the synthesis of aerogels [3], where capillary forces destroy the aerogel during drying. The effective stresses experienced by a material going through the critical point drying process, while minimized in comparison to standard drying, have also been investigated by Scherer et al. [4]. Critical point drying is also utilized in drying organic materials for electron microscopy, in order to preserve delicate membranes in the structures [5], and in the past two decades, has been incorporated into ceramics [6].

The critical point drying process is depicted in Figure 6.5, and could be incorporated into the LM-RIF process in the following manner. After casting, and prior to drying, the molded, wet, green part would go through a solvent exchange process to replace water in the system with either ethanol, or methanol. This step is necessary to ensure that the solvent in the green part is miscible with liquid CO₂; the solvent used in the critical point drying process. In a pressure vessel, a second solvent exchange is performed on the molded green part, where liquid CO₂ replaces the ethanol (or methanol) in the system. At this point, Figure 6.5 (A), the part is located within the pressure vessel and is saturated with liquid CO₂ at elevated pressure, and approximately 10°C. Next, the pressure and temperature are increased, moving from Figure 6.5(B) to Figure 6.5(C). Figure 6.5(C) is within the supercritical fluid area, above the critical point, on the pressure temperature phase diagram. By operating above the critical point of the liquid, evaporation and capillary forces can be effectively eliminated from the drying system. Moving out of the supercritical fluid area from Figure 6.5(C) to Figure 6.5(D), a capillary free transition from liquid to gas is obtained. CO₂ is the most commonly used liquid for critical point drying, due to a relatively low critical point temperature and pressure, of 31°C and 72.8atm, respectively.

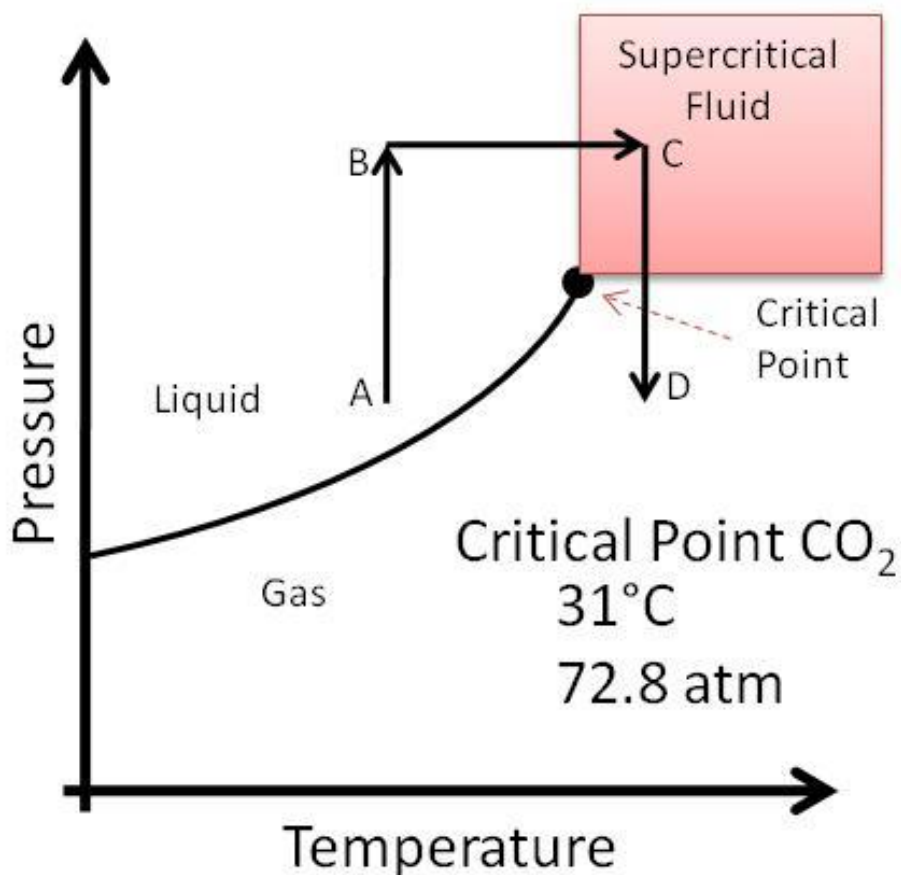


Figure 6.5. A pressure-temperature phase diagram, reproduced from Matson et al. [6] is shown, along with the description of the critical point drying process (A-D). In critical point drying, the transition from liquid to gas takes place at a temperature and pressure above the critical point of the fluid, eliminating capillary forces during drying. The process starts at point A, and with an increase in pressure and temperature moves to point B and C. In the CO₂ system, the temperature and pressure must be above 31°C and 72.8atm in order to transition into the supercritical fluid regime. Once above the critical point, the pressure is reduced (point D), and the dry part can be removed from the pressure vessel.

Constrained Drying Modeling and Stresses

In the development of the three dimensional analytical model that accurately describes the drying of particulate bodies, the most simplified version of a complete model was chosen for programs in Comsol Multiphysics®. To this end, there are many directions that the model can be expanded, made more accurate, and more complete.

Within the current working model, there are also many interesting questions that can be asked. First, how does constrained drying stress change as a function of part thickness, aspect ratio, and wall curvature? Secondly, how does constrained drying stress vary as function of number of layers in a multilayer design? Also, does the constrained drying stress vary if the part is allowed to dry from different surfaces and not just the top surface?

To improve the model, it is recommended that the following aspects of drying modeling be taken into account. First, the current model does not account for changes in temperature during drying. This is achievable through addition of one more relationship in the system of partial differential equations describing drying. Secondly, the current model does not account for changes in the mechanical properties of the suspension as a function of saturation. Diametral compression testing can be used to measure the increase in strength as percent saturation decreases, and this data can be incorporated in the Comsol® interface. Finally, while good approximations were used for all of the defining variables and coefficients describing the drying system, Kowalski [7], outlines a series of experiments that can be carried out to better approximate the system of interest. In this way, a relationship between constrained drying stress, green strength, particle size, surface tension, and even particle size distribution can be determined.

Multi-Material Components and Mechanical Testing

Hybrid Forceps Design

Recent progress on the design of forceps instruments to be manufactured with the LM-RIF process requires a hybrid material design. Shown in Figure 6.6, a material with a low elastic modulus, or flexible material is located on one side of the instrument, which is then bonded to a

material of high elastic modulus, or stiff material. Unlike the three dimensional modeling scenarios presented in Chapter 2, the fabrication of a hybrid material design requires additional lithography processing to be successfully completed.

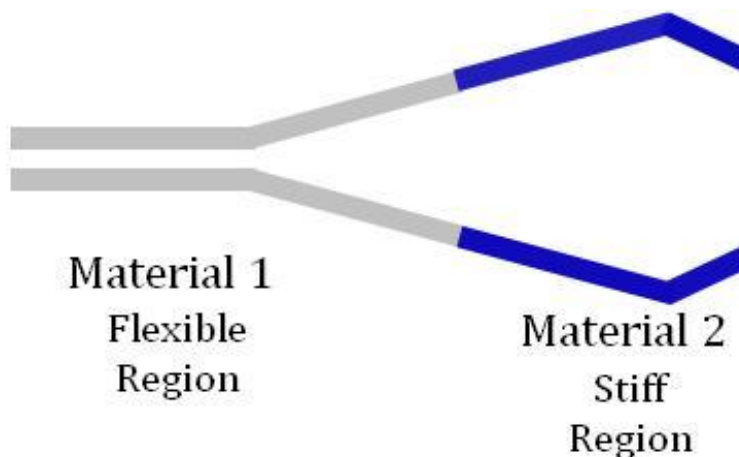


Figure 6.6. The schematic representation of a hybrid material forceps instrument is shown. In this device, in a single lithography layer, a flexible material would be located on one side of the instrument, while a stiff material would be bonded to that material in plane, and located on the other side of the device. This hybrid design requires that the two materials are able to successfully bonded together, as well as additional lithography and casting processes to successfully fill a mold cavity with two different colloidal suspensions [11].

In this way, additional modification to the LM-RIF process include a casting scheme to successfully infiltrate colloidal suspensions in areas of interest, in a single lithography mold layer. The proposed method to complete this task is shown in Figure 6.7. In this method, two photoresists are required, a negative photoresist, SU8 (Microchem, USA) is used to make the main mold cavity. In addition, a positive photoresist, SIPR 7120M-20 (Shin Etsu Microsi) is needed to serve as place holder in the mold during casting. In Figure 6.7, starting from the top left, and proceeding row by row, the process is as follows. 1) Fabricate SU8 mold on refractory substrate utilizing mask A, as described in Chapter 2. 2) Fill the entire mold cavity with the positive photoresist place holder. 3) Expose desired regions of positive photoresist through mask

B. 4) Develop away the treated positive photoresist. At this point, an SU8 mold is partially empty and partially filled with positive photoresist. 5) Cast material 1 into the empty cavities in the SU8 mold. 6) Dissolve the positive photoresist, opening the rest of the original SU8 mold cavity. 7) Cast material 2 into the open areas in the SU8 mold. 8) A burnout process will be needed to remove the mold and any binder present. 9) The final hybrid material device will be left on the refractory substrate. In the mask design, a mechanical interlocking design between the two materials was designed to help bind the two materials.

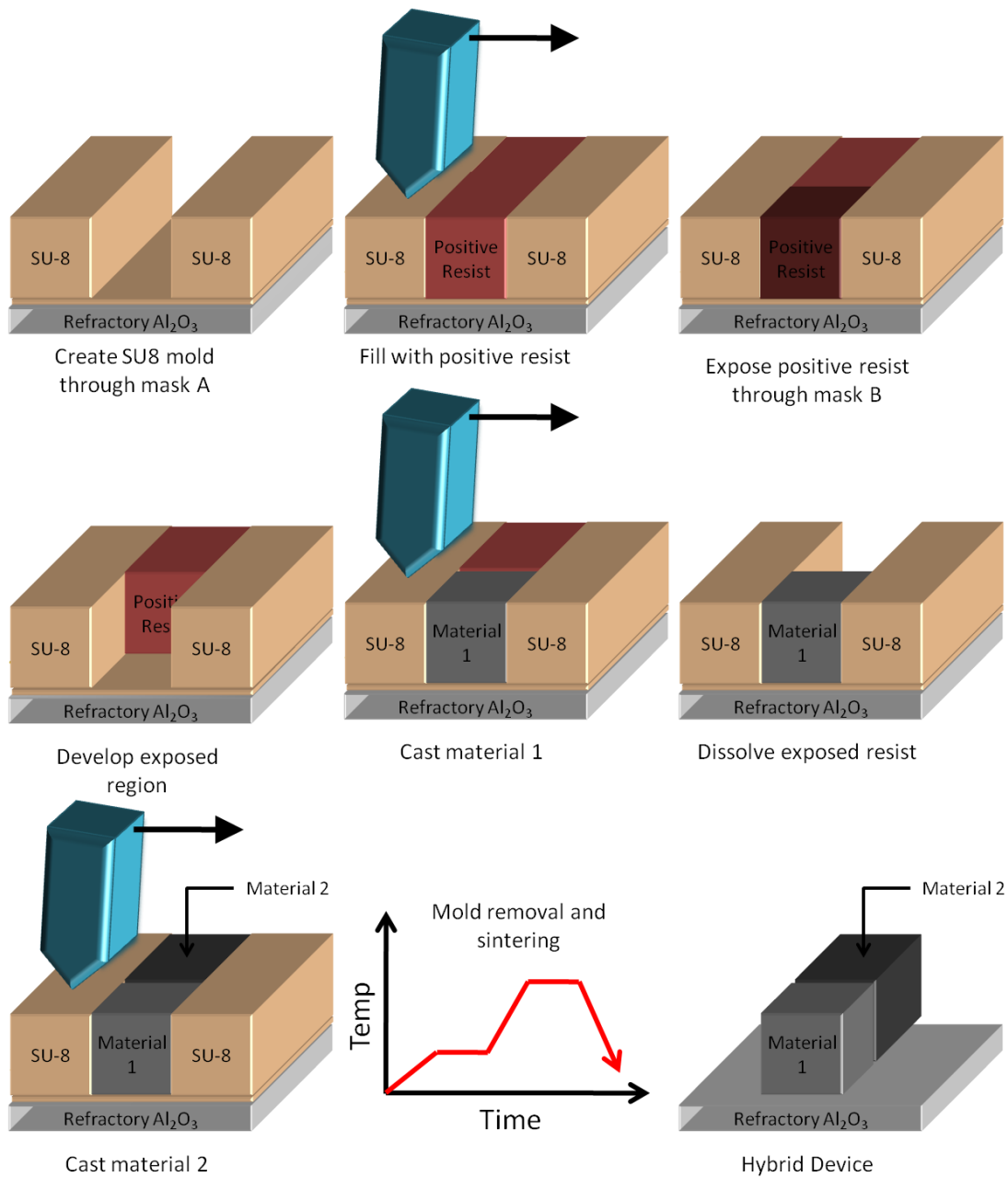


Figure 6.7. Starting from the top left, and proceeding row by row, the process presented to fabricate hybrid devices is as follows. 1) Fabricate SU8 mold on refractory substrate utilizing mask A, as described in Chapter 2. 2) Fill the entire mold cavity with the positive photoresist place holder. 3) Expose desired regions of positive photoresist through mask B. 4) Develop away the treated positive photoresist. At this point, an SU8 mold is partially empty and partially filled with positive photoresist. 5) Cast material 1 into the empty cavities in the SU8 mold. 6) Dissolve the positive photoresist, opening the rest of the original SU8 mold cavity. 7) Cast material 2 into the open areas in the SU8 mold. 8) A burnout process will be needed to remove the mold and any binder present. 9) The final hybrid material device will be left on the refractory substrate.

Figure 6.8 (A) shows a schematic of the photomask designed to facilitate the hybrid material designs. The upper right section of the photomask is expanded in Figure 6.8 (B) and Figure 6.8 (C), where it can be seen that the first lithography step will be carried out utilizing the full design (mask A), highlighted in black, and the second lithography step will be completed using the partial design (mask B), highlighted in red. When the two designs are overlapped on the photomask, the interface between the two materials can be seen in Figure 6.8 (C). To strengthen the bond between the two materials, several mechanical interlocking mechanisms have been designed, and incorporated into the photolithography mask layout. Future work includes determining if these mechanical interlocking mechanisms between the two materials are necessary, as well as qualifying which designs are more successful than others.

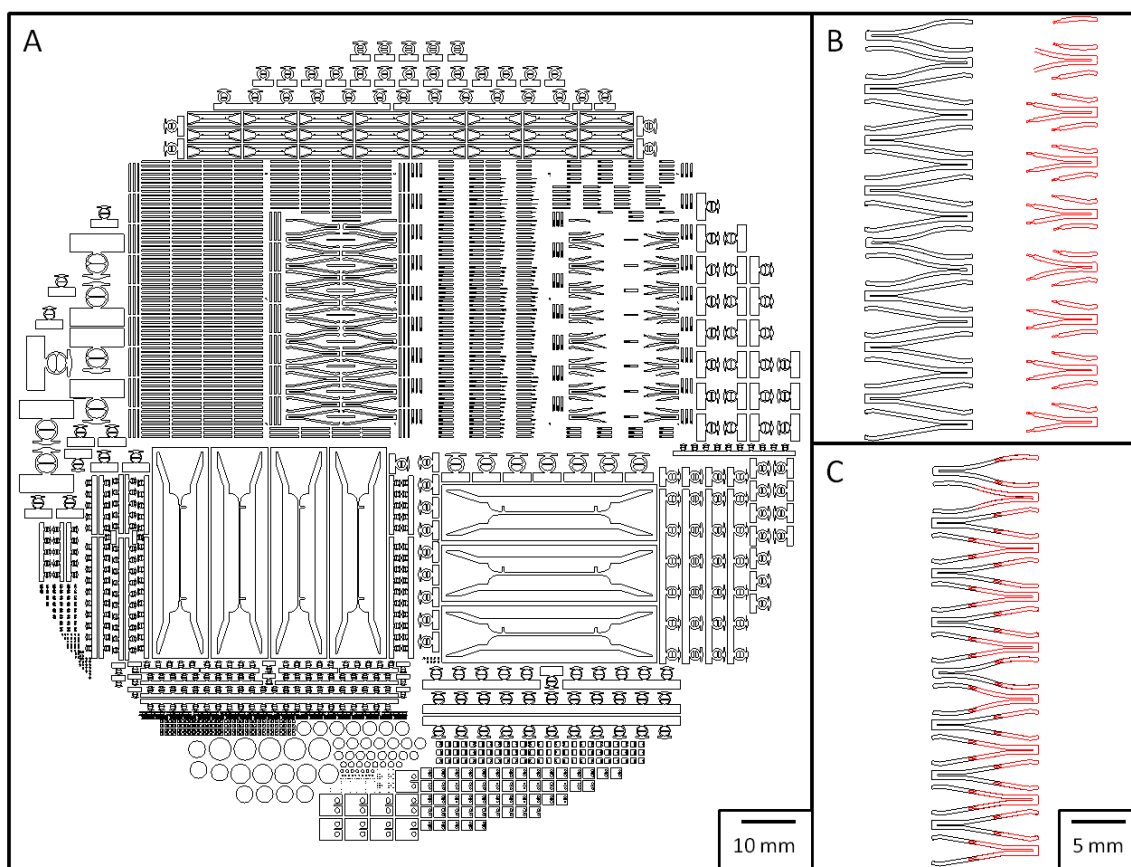


Figure 6.8. (A) The designed photomask for fabricating hybrid material components as well as mechanical property test structures within the LM-RIF process is shown. The top half of the photomask is dedicated to the fabrication of hybrid forceps designs, while the bottom half of the mask is dedicated to mechanical test specimens for standard tensile testing, as well as theta geometry tensile test specimens. Details of the mechanical testing structures are given in Figure 6.9. In (B) and (C) the photomask layout is shown in detail for the hybrid material instruments. The first lithography step is performed with the entire design (mask A, shown in black), while the second lithography step is performed with the partial design (mask B, shown in red). The final hybrid design is shown in (C), where the intersection between the black and red designs corresponds to the intersection between the two materials in the hybrid forceps. The mask layout was developed in collaboration with Brian Babcox.

Mechanical testing

Determination of the mechanical properties of materials fabricated with the LM-RIF process is necessary to verify the strength of the material being processed, as well as provide mechanical property data used in device design. Due to the size scale of the parts in question,

conventional mechanical testing is not a viable option, therefore, alternative testing techniques need to be developed. Shown in Figure 6.9 top, a modified tensile test specimen, designed by Professor Muhlstein (The Pennsylvania State University) will be used to test ductile materials. This test specimen is equipped with tabs at the top and bottom of the specimen, so that video calibration can be used to adequately track strain. Additionally, brittle material tensile test specimens have been designed, based on the initial theta-test specimens proposed by the National Institute of Standards and Technology (NIST) [8-10]. The geometry of the theta-like test specimens is similar to geometries already produced by the LM-RIF. Furthermore, on a single 5x5 cm substrate, hundreds of theta test specimens can be produced. The theta specimen, depicted in the bottom of Figure 6.9, produces a tensile force in the horizontal member of the theta shape when the entire theta specimen is placed under compression. Future work in properly evaluating the stress to failure of the theta specimens includes the development of standards and test protocols, as no industry standard exists to date.

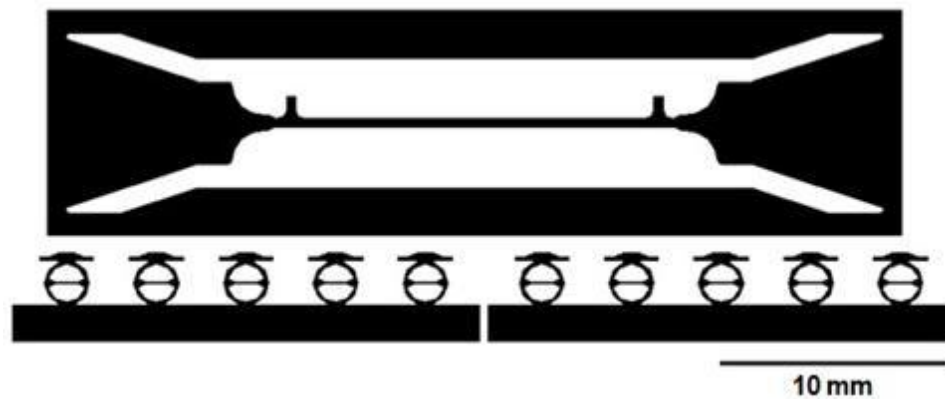


Figure 6.9. Tensile and theta mechanical test specimen to be used for evaluation of the material properties. The specimen are indicated in black. Top, a tensile test specimen is shown. Prior to testing, the four corners of the test specimen will be cut, leaving just the tensile specimen present in the test rig. The reason for having the surrounding material prior to testing is to provide support for the small and then sample, during sample loading. Bottom, theta tensile test specimens are utilized to test tensile strength while using a compressive force. This geometry

facilitates tensile testing of small, delicate samples. Multiple theta specimens can be tested in succession.

References

1. Neibel, C., A.C. Rau, M. Frecker, A. Mathew, and G. Hayes. *Design of an Endoscopic Biopsy Needle*. in *Design of Medical Devices Conference*. 2010. Minneapolis, MN.
2. Cirone, S., Hayes, G.H., Babcox, B., Adair, J.H., Lesieutre, G.A., Frecker, M.I. *Design, Fabrication and Testing of Contact-Aided Compliant Cellular Mechanisms with Curved Walls*. in *SPIE Smart Structures/NDE*. 2011. San Diego, CA, USA.
3. Kistler, S.S., *Coherent expanded aerogels*. Journal of Physical Chemistry, 1932. 36(1): p. 52-64.
4. Scherer, G.W., *Stress Development During Supercritical Drying*. Journal of Non-Crystalline Solids, 1992. 145(1-3): p. 33-40.
5. Anderson, T.F., *TECHNIQUES FOR THE PRESERVATION OF 3-DIMENSIONAL STRUCTURE IN PREPARING SPECIMENS FOR THE ELECTRON MICROSCOPE*. Transactions of the New York Academy of Sciences, 1951. 13(4): p. 130-134.
6. Matson, D.W. and R.D. Smith, *SUPERCritical FLUID TECHNOLOGIES FOR CERAMIC-PROCESSING APPLICATIONS*. Journal of the American Ceramic Society, 1989. 72(6): p. 871-881.
7. Kowalski, S.J., *Thermomechanics of Drying Processes*. Lecture Notes in Applied and Computational Mechanics, ed. W. Pfeiffer. Vol. 8. 2003, New York: Springer.
8. Fuller Jr., E.R., D.L. Henann, and L. Ma, *Theta-like specimens for measuring mechanical properties at the small-scale: effects of non-ideal loading*. Int. App. J. Res., 2007. 98(8): p. 729-734.
9. Durelli, A.J., S.M., and V. Parks, *The Theta Specimen for Determining Tensile Strength of Brittle Materials*. Materials Research and Standards, 1962. 2: p. 114-117.
10. Gaither, M.S., F.W. DelRio, R.S. Gates, E.R. Fuller Jr, and R.F. Cook, *Strength distribution of single-crystal silicon theta-like specimens*. Scripta Materialia, 2010. 63(4): p. 422-425.
11. Aguirre, M. and Frecker, M. *Design and Optimization of a Hybrid Compliant Narrow-Gauge Surgical Forceps*. 2010. Proceedings of the ASME Conference on Smart Materials, Adaptive Structures, and Intelligent Systems (SMASIS), Philadelphia, PA.

Appendix A

Aqueous Colloidal Processing for the LM-RIF Process

The work involving the aqueous gel/binder system incorporation in the LM-RIF process has led to peer review publication[†].

As discussed in Chapter 1, there is a need for more versatile, more intricate, and smaller surgical instruments for natural orifice transluminal endoscopic surgery (NOTES) [1, 2]. Initial fabrication of ceramic devices was undertaken by Antolino and Hayes et al. [3-5], in the early developmental stages of the lost mold-rapid infiltration forming process. The LM-RIF process is an iterative technique, facilitating the improvement of the overall process in every cycle. Thus, recent progress has been made in moving the process away from the fabrication of small scale (25x25x300 μ m) test bars, and into larger parts, with more intricate geometries. Specifically, these intricate parts include the fabrication of surgical instruments designed by Aguirre et al. [6-8], shown in Figure A.1.

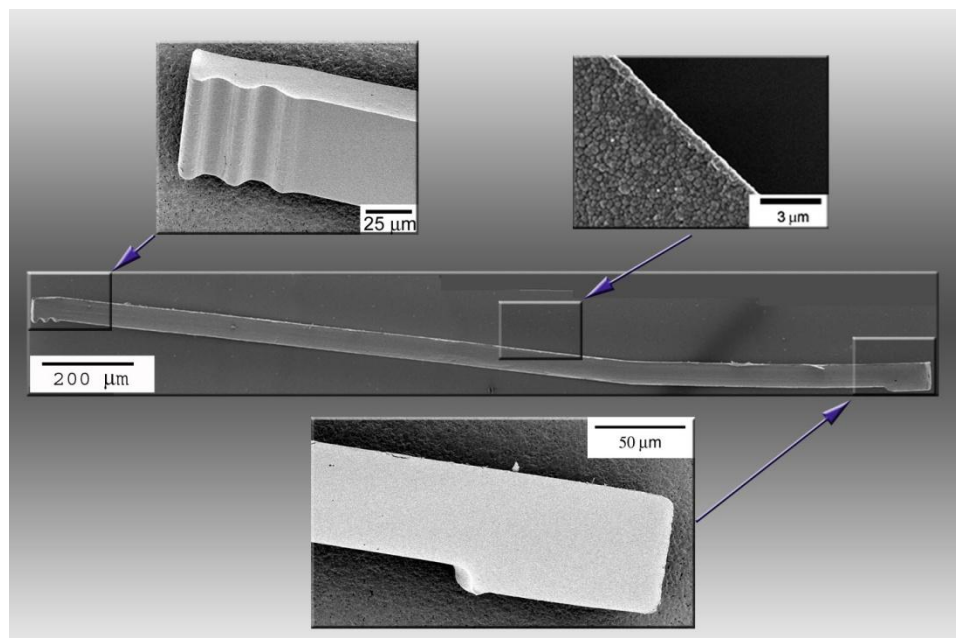


Figure A.1. To successfully fabricate intricate parts using the LM-RIF process, such as the forceps arm shown here, green bodies have to be formed that do not undergo a dimensional change during processing. Therefore, new binder systems were developed to work within the LM-RIF process.

The initial need for a scale-up (from 25 μ m to 400 μ m part thickness) of the fabrication process was to fabricate instruments that are surgically useful; centimeters in length with micron scale resolution. While these surgical instruments are much larger than the previously fabricated test bars, the LM-RIF process was still applicable, as other manufacturing techniques, discussed in Chapter 1, involved greater limitation on part size, material choice, and number of parts manufactured. Figure A.2 illustrates in the differences in size scale that the scale up entailed. The previously fabricated bend bars were 300 μ m in length, while the current forceps designs are 300 μ m in width.



Figure A.2. The magnitude of the scale up process is demonstrated, as previously fabricated bend bars were 300 μm in length, the forceps designs were 300 μm in cross sectional width. This scale up led to many challenges, including mold fabrication, and green body formation.

Fabricating forceps with prior LM-RIF techniques, as outlined by Antolino et al. [3] led to severe cracking during the drying stage. Cracking during drying can result from non-uniform drying, fast evaporation, and high capillary forces inside the drying green body [9-12]. The stresses that the green body must endure during drying stem from the fact that the part is constrained through the drying process. On the left side of Figure A.3, it can be seen that standard fabrication methods allow parts to dry following a demolding step, thus any shrinking and deformation that occurs during drying may not lead to catastrophic failure. One consequence of the LM-RIF process is that drying must take place while the green ceramic part is still contained in the mold. For simple shapes, such as a rectangular prism, this does not prove to be an issue, as the geometry allows shrinkage in all directions without constraint. However, as seen

on the right of Figure A.3, even slightly more complicated shapes, such as an annulus, experience constrained drying and are therefore prone to catastrophic failure during drying.

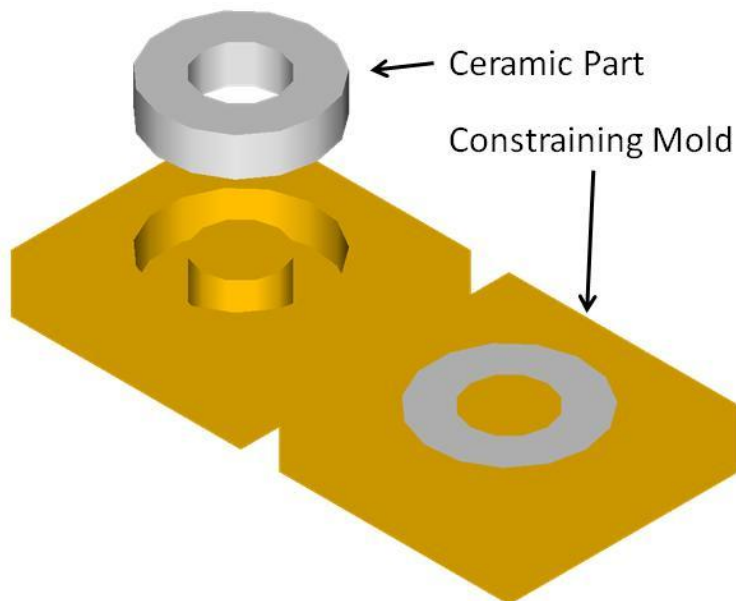


Figure A.3. Unlike traditional forming techniques, where the cast green part can be removed from the mold prior to drying (left), the LM-RIF process requires that the green part stay molded throughout the drying process (right), leading to stresses that occur when the part starts to shrink.

These constrained stresses exist during the drying of other complex geometries, such as the forceps design. Figure A.4 A shows a typical unsuccessful forceps fabricated using the LM-RIF process as described by Antolino et. al. Possible solutions to alleviate drying defects include the addition of polymer binders [13-15], the use of gelling agents [16-20], combination gelling and polymer binders [21-23], and solvent exchange drying [24, 25]. Within the LM-RIF process, it is desirable to maintain an aqueous based colloidal suspension preparation method for good dispersion properties, as well as keep any additional binder to a minimum to obtain high density final parts. A multitude of solutions was investigated, including a stronger gel casting system, critical point drying, freeze drying, drying desiccant bath, suspension solvent change, a wax based injection molding technique, and aqueous and non-aqueous tape casting techniques.

Initially, wax based injection molding, non-aqueous tape casting, and solvent change techniques were eliminated due to poor dispersion. The mismatch in the coefficients of thermal expansion for the mold and substrate is too large for freeze drying, as the mold deforms and fractures upon freezing. Critical point drying proved promising; however, the small chamber size of the critical point dryer available did not allow fabrication of large arrays of parts. The drying desiccant bath, stronger gel casting system, and aqueous tape casting techniques all proved promising; however, none of the existing processes were able to fabricate forceps that would remain intact through the drying process, as shown in Figure A.4 B. In this chapter, 2 new gel-casting binder systems are described. These systems were used to fabricate large parts with micron scale resolution, as shown in Figure A.4C. Rheological, thermal, and strength properties of green body formation process are examined herein, as well as final part yield and final part mechanical strength. The gel casting system used in both gel casting binder systems is a binary monomer system of Methacrylamide and 1-vinyl-2-pyrrolidone, along with the crosslinking agent N,N'-methylenebisacrylamide in a 1.5:1.5:1 ratio. Gel-casting binder system 1 is the aforementioned gel-casting system with a plasticized polyvinyl alcohol (PVA) binder system, while gel-casting system 2 is the same gel-casting system with a plasticized polyvinyl pyrrolidone (PVP) binder system, known herein as Binder system 1 and Binder system 2, respectively.

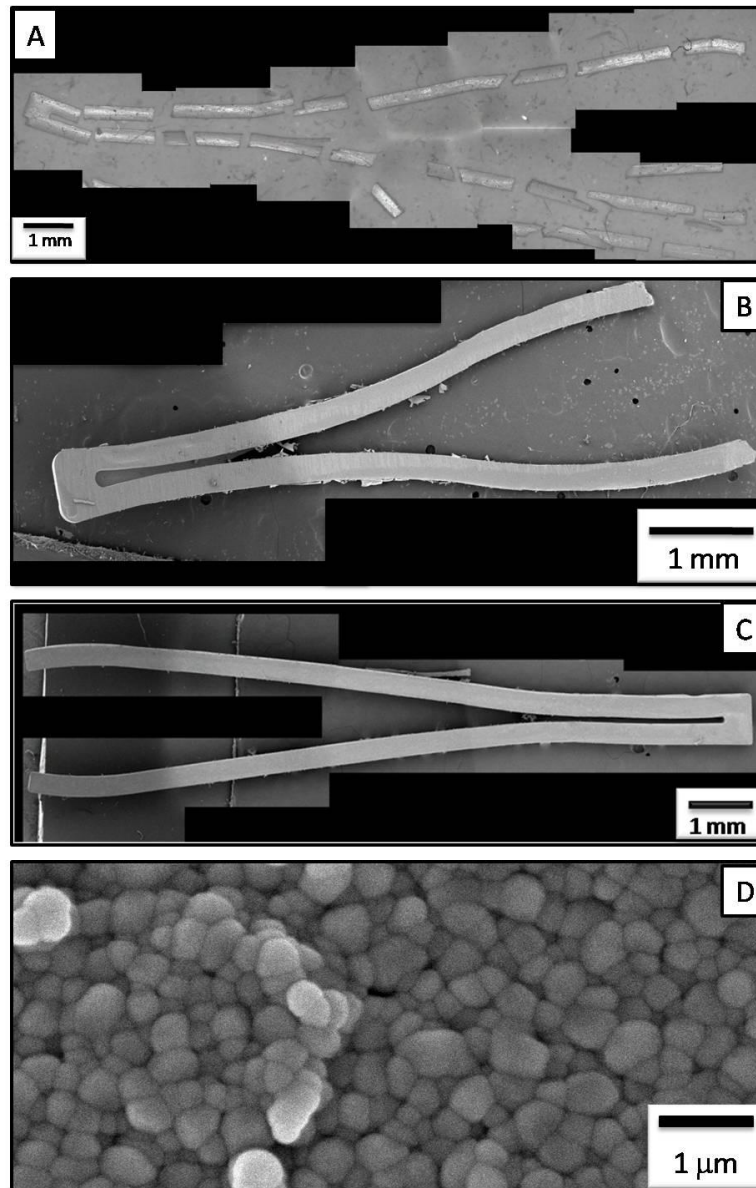


Figure A.4. A: Catastrophic failure of forceps due to drying cracking is shown as the starting point, and the need for improved processing, B: Fractured forceps due to drying cracking but with additional binder and gel present, C: Intact forceps fabricated with ideal binder and gel levels as per DOE experimentation, and D: microstructure of the forceps shown in C.

Transformation toughened zirconia exhibits mechanical properties that are more desirable than traditional materials in surgical instrument applications, such as high stress to failure [26].

Additionally, ceramic materials are more attractive on the micron scale than conventional surgical

instrument materials due to their ability to be easily formed into complex shapes via powder processing. In order to obtain precise cutting and grasping surfaces, micron scale resolution is needed, therefore dictating that the final grain size of the dense ceramic must be sub-micron. The initial particle size must also then lie in the nanometer size range to satisfy the final grain size requirements. Additionally, nanometer sized particles facilitate complex mold filling.

Well dispersed, high solids loading slurries are required to fabricate dense ceramic parts using the gel-casting binder systems. In the LM-RIF process, Ytria partially stabilized zirconia (Tosoh Corporation 3Y-TZP) is dispersed and concentrated by chemically-aided attrition milling (CAAM). During CAAM, the as-received, spray dried commercial powder is added to DI water with ammonium polyacrylate at pH 9 (RT Vanderbilt, Darvan 821A) on a 1.5wt% dry basis as the dispersant, and milled using 2mm zirconia media. Particle diameter based on the volume distribution is reduced from 60 μ m to 136nm as measured by dynamic light scattering (Nano-S, Malvern Instruments, Southborough, MA), while electrosteric dispersion of the ceramic colloid is maintained at close particle separation distance by a high ζ -potential at pH 9, (-49mV, ZetaPALS, Brookhaven Instruments Corp, Holtsville, NY).

After satisfactory suspensions are obtained, gel-casting monomers and crosslinker, as well as binder and plasticizer are added to the system. In Binder system 1, a binary monomer system of Methacrylamide (Sigma-Aldrich), and 1-vinyl-2-pyrrolidone (Sigma-Aldrich), along with the crosslinking agent N,N'-methylenebisacrylamide (Sigma-Aldrich), are used in a 1.5:1.5:1 ratio. Additionally, polyvinyl alcohol (80% hydrolyzed, Sigma-Aldrich) and polyethylene glycol (MW 400, Carbowax Incorporated) are added in a 1:1 ratio as a binder/plasticizer system. In Binder system 2, a binary monomer system of Methacrylamide (Sigma-Aldrich), and 1-vinyl-2-pyrrolidone (Sigma-Aldrich), along with the crosslinking agent N,N'-methylenebisacrylamide (Sigma-Aldrich), are used in a 1.5:1.5:1 ratio. Additionally,

polyvinyl pyrrolidone (MW=55000, Sigma-Aldrich) and triethylene glycol (MW=150, Sigma-Aldrich) are added in a 1:0.5 ratio as a binder/plasticizer system.

In an effort to optimize the yield of parts obtained from this slurry, varying amounts of gel-casting precursors, and binder/plasticizer were added to the system. Design of Experiments was utilized to optimize the system, and more details can be found in Yuangyai et al. [27]. The total amount of binder ranged from 2 to 8 vol% of the entire system, while gel precursors were added at 5 to 20 wt% of the water in the system. A 10:1 mass ratio of ammonium peroxydisulfate (Sigma-Aldrich) and N',N',N',N'-tetramethylethylenediamine (Sigma-Aldrich) was used to initiate and catalyze the monomers. The initiator and catalyst were added at 5wt% of the total monomer content. Following the DOE investigation, gel content was set to 2.5vol%, binder content was set to 8vol%, solids loading at 40vol%, and dispersant at 1.5wt% of the dry powder. Figure A.5 shows the processing steps used to create colloidal suspensions using CAAM with Binder system 1, while Figure A.6 shows the processing steps used to create colloidal suspensions of Binder system 2.

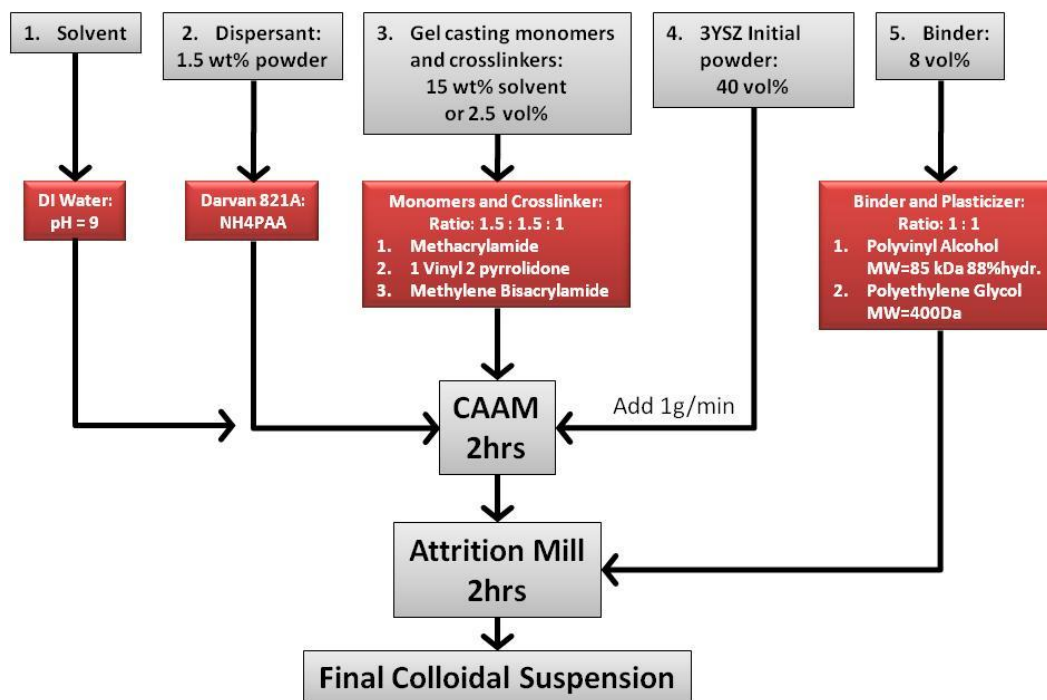


Figure A.5. The process flow diagram is shown for Binder system 1. The order of addition of components is given by the numbers in the top left corner of the gray boxes, noting that polymer binder is the final addition.

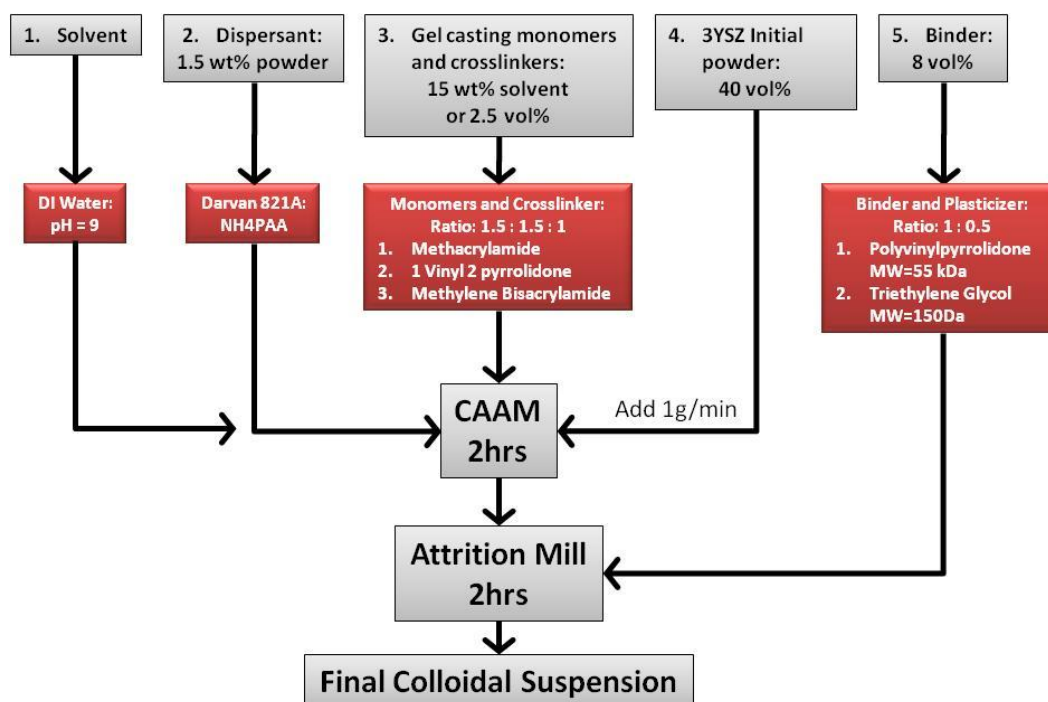


Figure A.6. The process flow diagram is shown for Binder system 2. The order of addition of components is given by the numbers in the top left corner of the gray boxes, noting that polymer binder is the final addition.

LM-RIF Processing

Prior to mold infiltration, the gelation reaction was initiated, leaving a working time of approximately 25 min. The gelation reaction formed a network of cross-linked polymer between particles which provided additional green strength during the drying and mold removal steps. Additionally, a silicone mold release layer was applied to the mold prior to infiltration to minimize part to mold wall adhesion. Following initiation of the gel, slurry was cast into the molds via a screen printing squeegee at a rate of 10cm/s. During this infiltration process, an excess of ceramic slurry was placed on top of the mold and worked into the mold cavities with the squeegee, while simultaneously removing any bubbles in the slurry. Multiple passes with the squeegee were needed to ensure complete mold filling with no entrapped air pockets, with the

final squeegee pass leaving a thin ($< 1\text{mm}$) layer of excess slurry on top of the mold. Gelation was carried out in 100% relative humidity N_2 environment, to minimize drying and allow the reaction to be carried to completion. Following gelation, the samples were placed directly into an ethanol bath, allowing the ethanol to displace the water in the green gelled body. The addition of the ethanol solvent exchange step limited cracking in the green body due to capillary drying forces. After 4 hours in an ethanol bath, samples were allowed to dry completely in ambient atmosphere. The excess slurry on top of the mold was removed via planarization with 2400 grit polishing paper, again, using ethanol as the planarizing liquid. Dishing out of slurry from within the mold cavity was minimized to less than $5\mu\text{m}$. Dry intact green parts, still contained in the mold, were put through a mold removal and sintering step, during which the mold was removed via combustion, followed by the sintering of the ceramic prototype part. To complete the LM-RIF process iteration, parts were mechanically tested, and this information was fed back into the device design.

Colloidal Suspension Properties

Particles in suspension experience attractive van der Waals forces, namely London dispersion, permanent dipole, and induced dipole. Additionally, they experience repulsive forces, namely electrostatic and steric interaction. The summation of these forces, known as the DLVO theory after the scientists Derjaguin, Landau, Verwey, and Overbeek, can help theoretically determine the stability of a suspension [28]. Figure A.7 shows the process through which particles exude an electrical charge while in an ionic medium, forming the basis for double layer theory. The bulk solution is a medium of known ionic strength. In this case, the positively charged particles will interact with the solution, and a tightly bound layer of negative ions will form the Stern layer, moving away from the particle, after the Stern layer, loosely bound,

primarily negative ions form a diffuse layer. The shear plane, or interface between the Stern layer and diffuse layer, is the maximum in electrical potential, denoted as the ζ -potential [29]. The ζ -potential can be used to approximate the net repulsive forces between particles in a suspension. Generally speaking, the size of the diffuse layer can be manipulated with a change in the ionic strength of the bulk solution, while the ζ -potential can be manipulated through changes in pH [29].

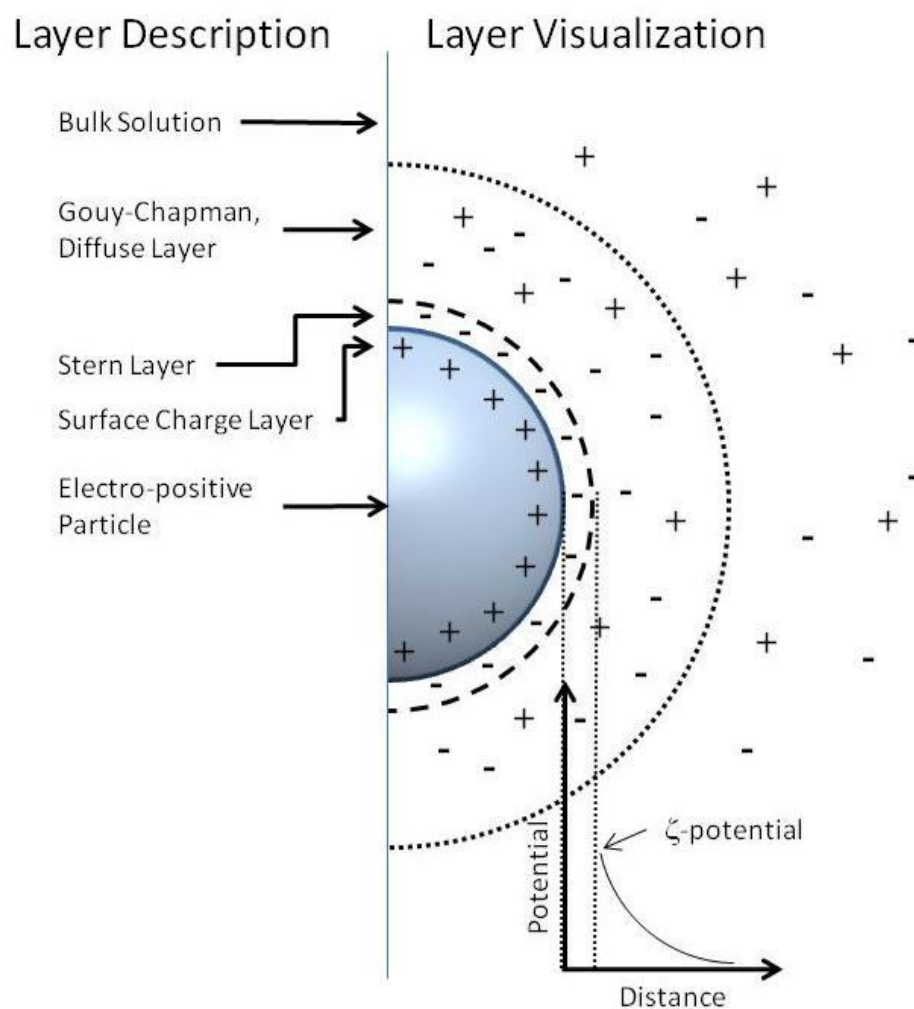


Figure A.7. The electric interaction of a particle with an ionic solvent is shown for an electro-positive particle. Positive and negative ions in solution are represented with a (+) and (-), respectively. The measured ζ -potential, or electric potential at the intersection of the Stern layer and diffuse layer, is labeled in the bottom right. ζ -potential is a key parameter in calculating the

interaction energy barriers between particles in suspension. This figure was re-created from Adair et al. [30].

The attractive van der Waals forces in our system are described by Gregory [31]. The attractive energy, V_{vdW} , is a function of the particle separation distance, the particle radii, and the effective Hamaker constant for the system. The repulsive electrostatic forces, $V_{electrostatic}$, are given by the Hogg-Healy-Fuerstenau [32] relationship taking into consideration the ionic strength, the dielectric constant of the medium, the particle radii, and the ζ -potential. Steric repulsion forces, V_{steric} , are considered using the Bergstrom approach [33], which accounts for the thickness of an adsorbed polymer layer on the particles. The total interaction energy then, as a function of particle separation distance is

$$V = V_{vdW} + V_{electrostatic} + V_{steric} . \quad (6.1)$$

The required barrier energy to having particles collide is calculated from Israelachvili [29] and is considered the stability of the suspension; depicted in Figure A.8 as the horizontal dotted line for 20°C. Figure A.8 shows the total interaction energy for the 3Y-TZP system prior to the addition of the Binder systems 1 and 2. The parameters used to calculate the interaction energy curve are given in Table A.1.

It can be seen that the system is very stable in a dispersed state, under the conditions used during processing. Now that the colloidal suspension is not prone to agglomeration, further processing can be carried out including the addition of gel-casting precursors, as well as a binder system. The completed formulations of Binder systems 1 and 2 will be characterized in the following sections.

Table A.1. The parameters used to theoretically calculate the interaction energy between two 3Y-TZP particles in solution. The program Hamaker 2.1 was used to carry out the calculation [34].

<i>Parameter</i>	<i>Value</i>
ζ -potential	-49 mV
Thickness of adsorbed polymer layer	2 nm
Electrolyte composition	0.1M
Hamaker constant [35]	7.2×10^{-20} J
Particle diameter	114 nm

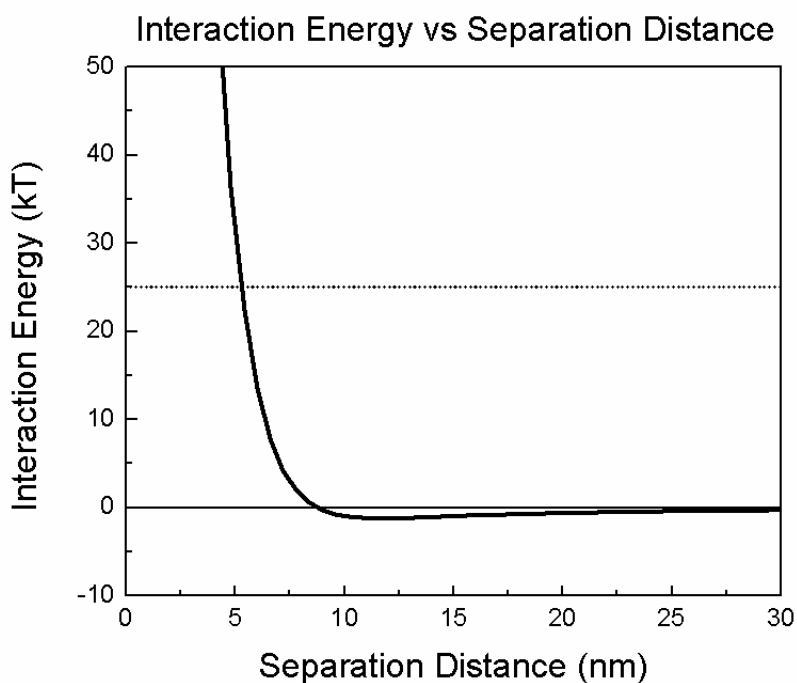


Figure A.8. The total interaction energy curve for the 3Y-TZP particles is shown as a function of distance. Electrosteric dispersion creates a high barrier energy to agglomeration around 6nm separation distance, while a steric barrier prevents the particles from approaching the primary minimum at a separation distance of zero. This theoretical curve is determined using the parameters appropriate to the LM-RIF process.

Rheology

A previous study by Antolino [3] showed that at 43 vol% solids content, the Bingham yield point of the pure gel-casting system is 160 Pa, while the high shear viscosity is 0.65 Pa.s. The rheological behavior of the suspensions in the form of Binder system 1 and Binder system 2 was analyzed at 40 vol% solids loading using a parallel plate rheometer (Rheometrics: RDS II Rheometer) with a 2-degree plate and cone geometry. It appeared that the addition of binder to the system dramatically increased the viscosity. As shown in Figure A.9, for Binder system 1, the high shear viscosity and Bingham yield point is 15Pa.s and 600 Pa, respectively. For Binder system 2, the high shear viscosity and Bingham yield point is 4.3 Pa.s and 186 Pa, respectively. Both show shear thinning behavior, which makes both binder systems applicable to the casting steps in the LM-RIF process. Although these viscosities are much higher than the pure gel system, the suspensions are still able to cast into the molds, and final intact parts were produced.

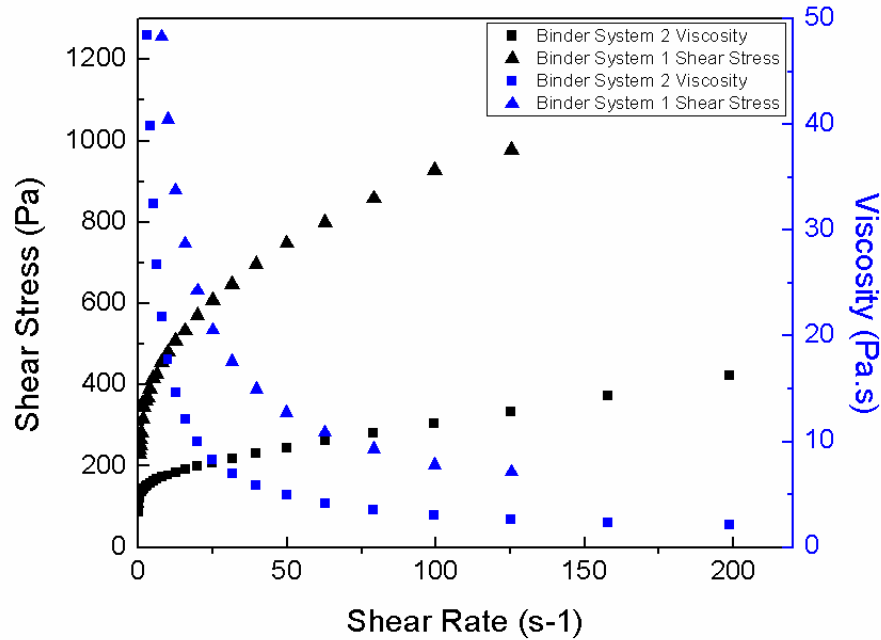


Figure A.9. The shear stress and viscosity is plotted against shear rate for both Binder system 1 and Binder system 2. For Binder system 1, the high shear viscosity and Bingham yield point are 15Pa.s and 600 Pa, respectively. For Binder system 2, the high shear viscosity and Bingham yield point are 4.3 Pa.s and 186 Pa, respectively.

Green strength

Diametral compression testing was employed to determine the increase in green body strength due to the addition of Binder systems 1 and 2. In diametral compression testing, the application of a compressive load on an upright disk results in tensile forces on the vertical centerline of the disk sample. The maximum stress can be calculated at the center of the disk by Equation (A.2), where σ_{max} is the maximum tensile stress, P is the applied load, D is the diameter of the disk, and t is the thickness of the disk.

$$\sigma_{\max} = \frac{2P}{\pi Dt} \quad (\text{A.2})$$

In Table A.2, through the addition of both binder systems, the green strength is increased. This increase in strength can be seen in the resulting increase in part yield in the LM-RIF fabrication process with the binder systems. This increase in strength is especially pertinent during the drying process, as weak parts in constrained drying scenarios exhibit cracking.

Table A.2. Diametral compression testing of dry green disks.

<i>Gel-Binder Formulation</i>	<i>Maximum Stress, σ_{ult} (MPa)</i>	<i>Elastic Modulus E (GPa)</i>
Gelcast system only	1.3 ± 0.69	3.5 ± 1.5
Binder system 1	4.06 ± 0.44	7.9 ± 1.6
Binder system 2	2.50 ± 0.33	17.5 ± 2.5

Thermal Analysis

Thermal gravimetric analysis (TGA) (TA Instruments, TGA 2050) was used to determine at what temperature, and in what order, the binder system undergoes combustion during the burnout and sintering steps of the LM-RIF. TGA was carried out in ambient air atmosphere, at 5°C per minute to 100°C. In Figure A.10 it can be seen that both Binder system 1 and Binder system 2 undergo complete removal during combustion. In addition, the SU8 mold is removed at a higher temperature than the binder systems, resulting in a temperature range in which the green body must withstand the SU8 mold removal process without binder present. Additionally, the binder systems only provide support to the green part in the drying process steps, prior to mold removal.

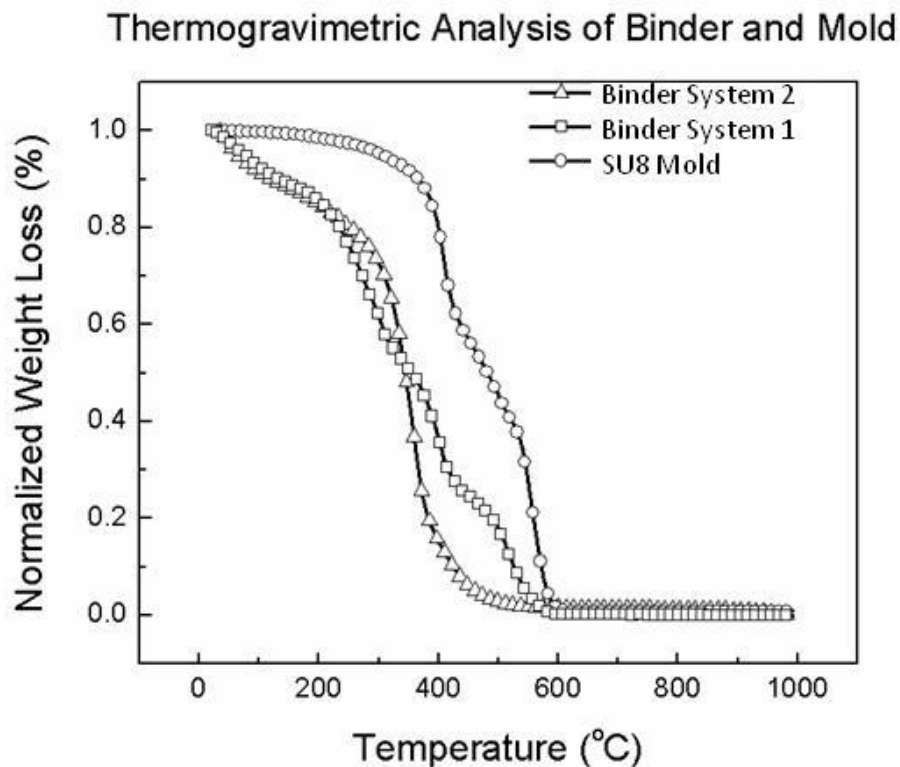


Figure A.10. Thermogravimetric analysis of Binder systems 1 and 2 and the mold material SU8 are compared. All show complete removal by 600°C, however, the binder systems undergo combustion prior to the mold material, indicating that the binder systems only provide support to the green part during the drying process.

Differential scanning calorimetry (DSC) (TA Instruments DSC 2910) was employed to examine the possibility of the binder systems undergoing a glass transition temperature (T_g) during processing. While both binder systems are chemically cross-linked, there is no indication that a T_g exists for either binder system, as shown in Figure A.11.

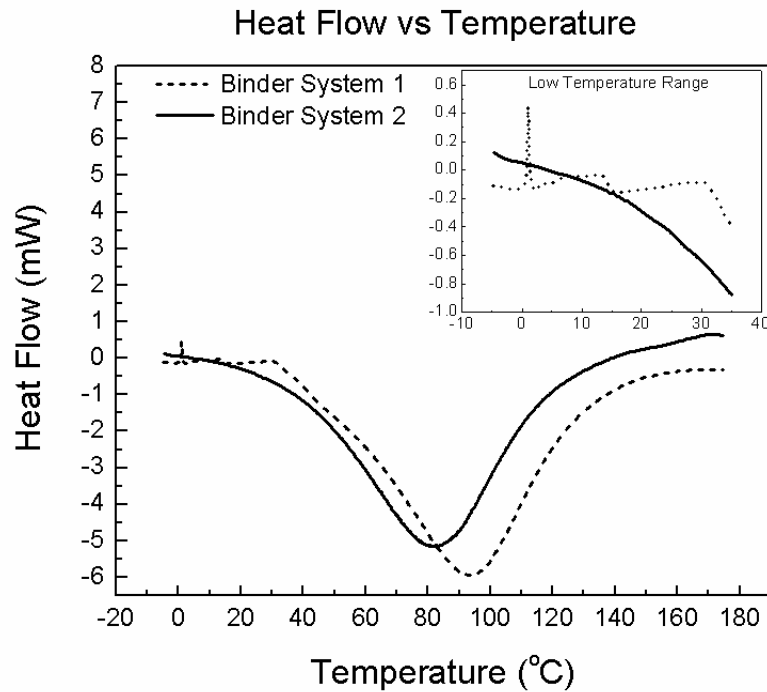


Figure A.11. Differential scanning calorimetry indicates that there is no real glass transition temperature in Binder systems 1 and 2 in the temperature range of interest. As these binder systems are in the presence of chemically initiated gelled matrix, it is not expected that there would be a glass transition temperature.

Using the LM-RIF process for surgical instrument design is advantageous in creating free standing parts fabricated with the desired large aspect ratios (up to 1:40) and sharp edges (~ 1 micron) while retaining a resolution of 2 microns, as seen in Figure A.12. Complex geometries that undergo constrained drying stresses during fabrication have been successfully manufactured. The current limitations of this technology include defects, such as cracking and spallation in some parts that are introduced during the manufacturing process. Thus, accurate prediction of the material strength and proper design of the surgical instruments are quite important.

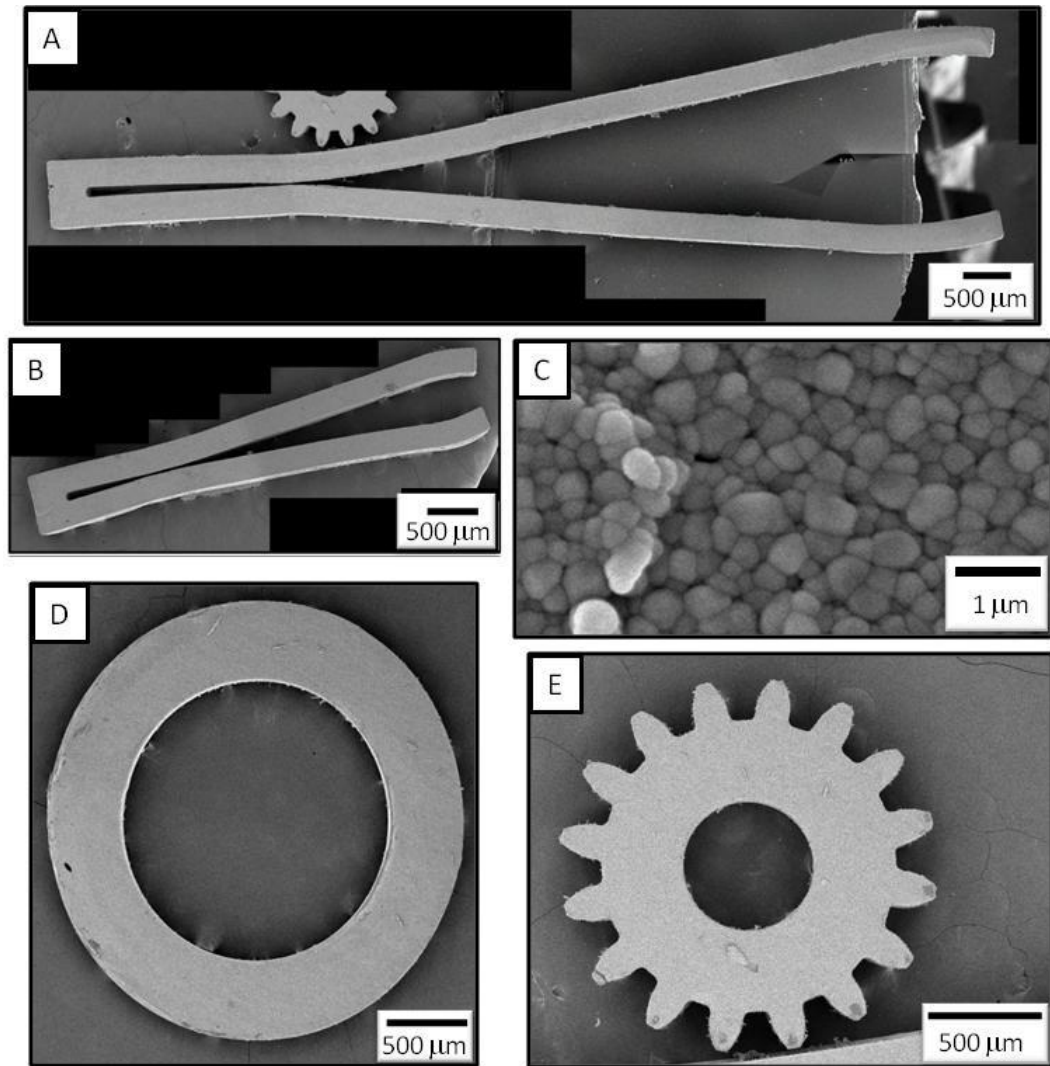


Figure A.12. Final sintered parts using Binder system 1 with complex geometries that underwent constrained drying during processing. A: a splined forceps design with aspect ratio 1:40. B: a splined forceps design with aspect ratio of 1:20. C: closed porosity exists in the microstructure, limiting strength and decreasing reliability. D and E show an annulus and a gear to demonstrate the range of geometries possible with the LM-RIF process.

The yield of final sintered parts from the LM-RIF process with Binder system 1 was quantified as a function of forceps shape and aspect ratio. The aspect ratio of the forceps is defined as the width of one forceps arm by the length of the entire forceps. Shown in Figure A.13, there are three separate forceps shapes considered. The first design is a straight linkage

design, with a flat surface at the gripping end. Secondly, a straight linkage design is used with curved teeth at the gripping end to improve grasping capabilities. Lastly, there is a splined geometry, designed to limit the constrained drying stresses, which has a flat gripping end as well.

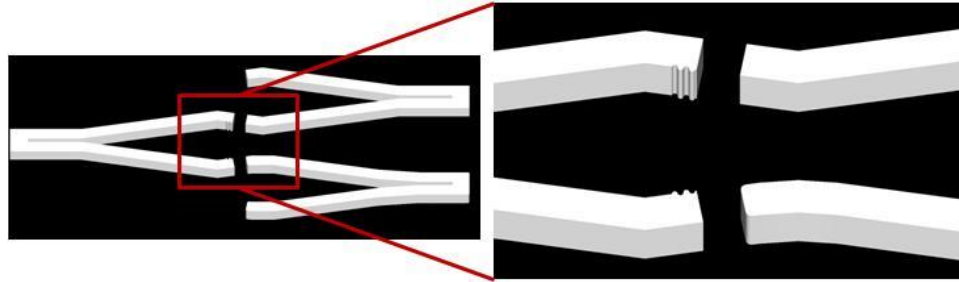


Figure A.13. Left: three forceps designs are shown with an aspect ratio of 1:20. Right: the differences of the three forceps designs are highlighted: straight linkage with gripping teeth, straight linkage without gripping teeth, and splined linkage without gripping teeth.

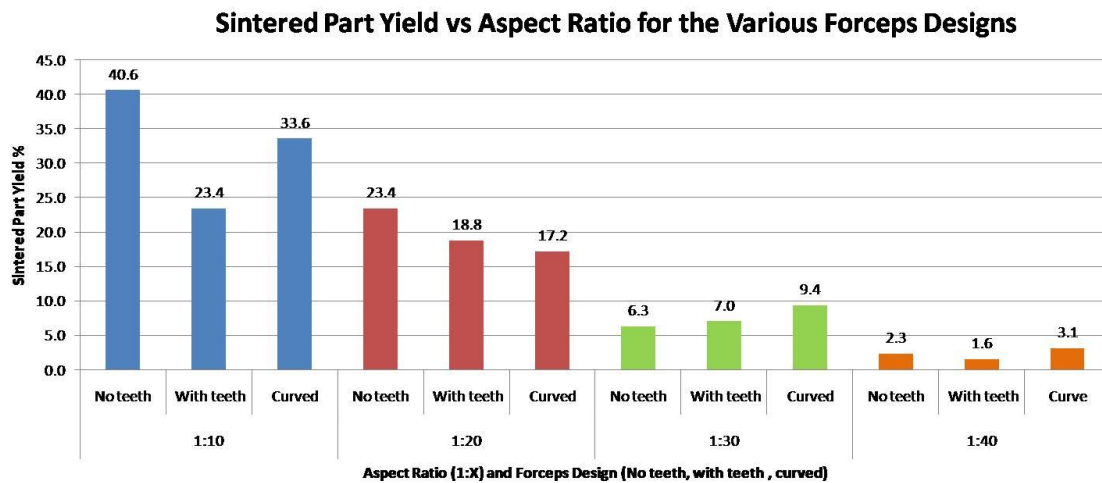


Figure A.14. Sintered part yield is shown as a function of aspect ratio (1:10, 20, 30, 40) for the various forceps designs; straight linkage with gripping teeth, straight linkage without gripping teeth, and splined (curved) linkage without gripping teeth.

Initial results indicate that the addition of gel, binder, and a tailored solids loading significantly increases part yield from no part yield to 20-40% depending on aspect ratio and

forceps design. Aspect ratio of the forceps was varied from 1:10 to 1:40. Figure A.14 shows the sintered part yield as a function of aspect ratio and forceps design. Results of yield quantification show that green part yield increases with higher binder content, lower gel content, and lower solids loading. Higher green part yield with increasing organic content was expected, but these results also show that the system favors the less rigid (cross linked) binder to the more rigid (high cross linked density) gelled monomer. Of course, the downside to higher organic content is porosity in the sintered body. We have found that the solids loading needs to be higher than 35 vol% in order to obtain dense ceramics parts after sintering. Additionally, the binder content is limited to 10 vol% due to solubility restrictions and the gel content must be at least 5% otherwise yield significantly decreases.

Additionally, it can be seen in Figure A.14 that the sintered part yield decreases as the aspect ratio of the forceps is increased. In most cases, the splined geometry forceps show an order of magnitude lower stress during drying (see Chapter 4) and show an increase in sintered part yield after processing is complete.

Binder systems 1 and 2 were used within the LM-RIF to fabricate 3-point bend specimens. It can be seen in Table A.3 that while the strength of binder system 1 is slightly higher than the strength of binder system 2, both final part strengths are relatively weak compared with literature values of 3Y-TZP ceramics [26]. Due to the viscosity of the suspensions, and the amount of binder present in both systems, residual porosity and bubbles are currently causing a decrease in final part strength. Future work includes the de-airing of suspensions prior to casting in order to improve strength values.

Table A.3. Three Point bend test strength results for Binder systems 1 and 2.

<i>Gel-Binder Formulation</i>	<i>Maximum Stress, σ_{ult} (MPa)</i>
Binder system 1	423 \pm 81

Binder system 2	419 ± 96
-----------------	----------

Conclusion

Complex ceramic forming methods such as the LM-RIF, which undergo constrained drying processes, require unique binder systems in order to successfully fabricate devices. The comparison of two gel-binder systems utilizing the properties of both gel-casting and tape-casting binder formulation successfully increased the yield of parts fabricated using the LM-RIF from 0% to 40.6% for small aspect ratio forceps. Green body strength increased from 1Mpa to 4MPa by diametral compression testing, while viscosity increased dramatically. Both binder systems showed complete removal via combustion, while the mold material was removed at a higher temperature. This indicates that the binder system is only actively supporting the green part through the drying process. Residual closed porosity and bubbles in the final parts resulted in fairly weak parts, however, there is ongoing work to remedy this problem. As the LM-RIF process is iterative, future strength improvements, as well as improvements in aspect ratio, are likely to lead to improved forceps designs.

References

1. Rattner, D. and A. Kalloo, *ASGE/SAGES working group on natural orifice transluminal endoscopic surgery - October 2005*. Surgical Endoscopy and Other Interventional Techniques, 2006. 20(2): p. 329-333.
2. Rattner, D.W., *NOTES: 'where have we been and where are we going' (2008:22(5)1143-1145) and 'transvaginal endoscopic appendectomy in humans: a unique approach to NOTES 'world's first' (2008:22(5)1343-1347)*. Surgical Endoscopy and Other Interventional Techniques, 2008. 22(10): p. 2327-2327.
3. Antolino, N.E., G. Hayes, R. Kirkpatrick, C.L. Muhlstein, M.I. Frecker, E.M. Mockensturm, and J.H. Adair, *Lost Mold Rapid Infiltration Forming of Mesoscale*

- Ceramics: Part 1, Fabrication*. Journal of the American Ceramic Society, 2009. 92(1): p. S63-S69.
4. Antolino, N.E., G. Hayes, R. Kirkpatrick, C.L. Muhlstein, M.I. Frecker, E.M. Mockensturm, and J.H. Adair, *Lost Mold-Rapid Infiltration Forming of Mesoscale Ceramics: Part 2, Geometry and Strength Improvements*. Journal of the American Ceramic Society, 2009. 92(1): p. S70-S78.
 5. U.S. Patent, Patent Pending 61/150,568, J. H. Adair, M.F., C. Muhlstein, E. Mockenstrum, H. B. Nembhard, R. S. Haluck, A. Mathew, N. Antolino, G. Hayes, M. Aguirre, R. Kirkpatrick, and C. Yuangai. *Polycrystalline Complex-Shaped Meso-scale Components*, 2009.
 6. Aguirre, M., G. Hayes, M. Frecker, J. Adair, and N. Antolino. *Fabrication and Design of a Nanoparticulate Enabled Micro Forceps*. in *ASME 2008 International Design Engineering Technical Conferences & Computers and Information in Engineering Conference*. 2008. New York, NY.
 7. Aguirre, M., G. Hayes, C. Yuangyai, M. Frecker, J. Adair, and N. Antolino. *Fabrication and Srength-Based Design of a Meso-Forceps*. in *ASME 2009 International Design Engineering Technical Conferences*. 2009. San Diego, CA.
 8. Aguirre, M.E., G. Hayes, R. Meirom, M. Frecker, C. Muhlstein, J.H. Adair, and J.A. Kerr, *The Design and Fabrication of Narrow-Gauge (1 mm Diameter) Surgical Instruments for Natural Orifice Transluminal Endoscopic Surgery*. To be submitted to the Journal of Mechanical Design, 2009.
 9. Scherer, G.W., *Stress and Fracture During Drying of Gels*. Journal of Non-Crystalline Solids, 1990. 121(1-3): p. 104-109.
 10. Scherer, G.W., *Theory of Drying*. Journal of the American Ceramic Society, 1990. 73(1): p. 3-14.
 11. Banaszak, J. and S.J. Kowalski, *Theoretical and experimental analysis of stresses and fractures in clay like materials during drying*. Chemical Engineering and Processing, 2005. 44(4): p. 497-503.
 12. Kowalski, S.J., K. Rajewska, and A. Rybicki, *Destruction of wet materials by drying*. Chemical Engineering Science, 2000. 55(23): p. 5755-5762.
 13. Christian and P.J.A. Kenis, *Fabrication of ceramic microscale structures*. Journal of the American Ceramic Society, 2007. 90(9): p. 2779-2783.
 14. Ma, J.T., Z.P. Xie, H.Z. Miao, L.J. Zhou, Y. Huang, and Y.B. Cheng, *Elimination of surface spallation of alumina green bodies prepared by acrylamide-based gelcasting via poly(vinylpyrrolidone)*. Journal of the American Ceramic Society, 2003. 86(2): p. 266-272.

15. Albano, M.P. and L.B. Garrido, *Aqueous tape casting of yttria stabilized zirconia*. Materials Science and Engineering a-Structural Materials Properties Microstructure and Processing, 2006. 420(1-2): p. 171-178.
16. Janney, M.A., O.O. Omatete, C.A. Walls, S.D. Nunn, R.J. Ogle, and G. Westmoreland, *Development of low-toxicity gelcasting systems*. Journal of the American Ceramic Society, 1998. 81(3): p. 581-591.
17. Omatete, O.O., M.A. Janney, and R.A. Strehlow, *Gelcasting - a New Ceramic Forming Process*. American Ceramic Society Bulletin, 1991. 70(10): p. 1641.
18. Young, A.C., O.O. Omatete, M.A. Janney, and P.A. Menchhofer, *Gelcasting of Alumina*. Journal of the American Ceramic Society, 1991. 74(3): p. 612-618.
19. Potoczek, M. and E. Zawadzak, *Initiator effect on the gelcasting properties of alumina in a system involving low-toxic monomers*. Ceramics International, 2004. 30(5): p. 793-799.
20. Xiang, J.H., Z.P. Xie, and Y. Huang, *Processing of Al₂O₃ sheets by the gel-tape-casting process*. Ceramics International, 2002. 28(1): p. 17-22.
21. Huha, M.A. and J.A. Lewis, *Polymer effects on the chemorheological and drying behavior of alumina-poly(vinyl alcohol) gelcasting suspensions*. Journal of the American Ceramic Society, 2000. 83(8): p. 1957-1963.
22. Ma, L.G., Y. Huang, J.L. Yang, H.R. Le, and Y. Sun, *Effect of plasticizer on the cracking of ceramic green bodies in gelcasting*. Journal of Materials Science, 2005. 40(18): p. 4947-4949.
23. Ma, J.T., Z.P. Me, H.Z. Miao, Y. Huang, and Y.B. Cheng, *Gelcasting of ceramic suspension in acrylamide polyethylene glycol systems*. Ceramics International, 2002. 28(8): p. 859-864.
24. Barati, A., M. Kokabi, and M.H.N. Famili, *Drying of gelcast ceramic parts via the liquid desiccant method*. Journal of the European Ceramic Society, 2003. 23(13): p. 2265-2272.
25. Barati, A., M. Kokabi, and N. Famili, *Modeling of liquid desiccant drying method for gelcast ceramic parts*. Ceramics International, 2003. 29(2): p. 199-207.
26. Rogner, J., B. Okolo, S. Kurzenhauser, M. Muller, W. Bauer, H.J. Ritzhaupt-Kleissl, E. Kerscher, and V. Schulze, *Relationships between process, microstructure and properties of molded zirconia micro specimens*. Microsystem Technologies-Micro-and Nanosystems-Information Storage and Processing Systems, 2008. 14(12): p. 1831-1837.
27. Yuangyai, C., Hayes, G., Antolino, N., Nembhard, H. B., and Adair, J. H. , *Yield Improvement for Lost Mold Rapid Infiltration Forming Process by a Multi-Stage Fractional Factorial Split Plot Design*. International Journal of Nanomanufacturing, 2009. 3(4): p. 351-367.
28. Hunter, R.J., *Foundations of colloid science*. 2 ed. 2001, New York: Oxford University Press.

29. Israelachvili, J.N., *Intermolecular and Surface Forces*. 2 ed. 1991, San Diego: Elsevier.
30. Adair, J.H., E. Suvaci, and J. Sindel, *Surface and Colloid Chemistry of Advanced Ceramics*, in *Encyclopedia of Materials: Science and Technology*. 2001, Elsevier Science Ltd: Oxford. p. 8996-90065.
31. Gregory, J., *APPROXIMATE EXPRESSIONS FOR RETARDED VANDERWAALS INTERACTION*. *Journal of Colloid and Interface Science*, 1981. 83(1): p. 138-145.
32. Hogg, R., T.W. Healy, and Fuersten.Dw, *MUTUAL COAGULATION OF COLLOIDAL DISPERSIONS*. *Transactions of the Faraday Society*, 1966. 62(522P): p. 1638-&.
33. Bergstrom, L., C.H. Schilling, and I.A. Aksay, *CONSOLIDATION BEHAVIOR OF FLOCCULATED ALUMINA SUSPENSIONS*. *Journal of the American Ceramic Society*, 1992. 75(12): p. 3305-3314.
34. Aschauer U., B.-M.O., Moreno R., Bowen P., *Hamaker 2: A toolkit for the calculation of particle interactions and suspension stability and its application to mullite synthesis by colloidal methods*. *Journal of Dispersion Science and Technology*, In Press.
35. Bergstrom, L., *Hamaker constants of inorganic materials*. *Advances in Colloid and Interface Science*, 1997. 70: p. 125-169.

Appendix B

Multilayer Topology Optimization for the LM-RIF Process

Introduction

The Lost Mold Rapid-Rapid Infiltration Forming (LM-RIF) process, described in Chapter 3, can be used to fabricate structures on the meso-scale. In this project, the drawbacks of the LM-RIF process, as it consists of layers, are highlighted, and a design algorithm is presented that is tailored to designing structures within the LM-RIF process itself.

A disadvantage to using the LM-RIF process is that molds are formed in only "2.5D". One mold layer can have good resolution in plane, and then mold thickness is determined by the original layer thickness. To create 3D molds, multiple mold layers can be stacked onto one another, as described in Chapter 3, and processing can continue. Herein, a topological optimization scheme was employed to help design instruments that are compatible with a new meso-scale manufacturing process: A micro-fabrication technique is used which combines deep UV lithography with ceramic powder processing to produce free standing meso-scale parts.

In the current work, forceps instruments for use in minimally invasive surgery have been designed as a monolithic compliant mechanism that can be manufactured using the LM-RIF fabrication process, as shown in Figure B.1 [1]. Optimization techniques using finite element analysis were used to determine the effect of dimensional parameters and material strength on the performance of the compliant micro forceps [1, 2]. Specifically, these 2 dimensional forceps have been optimized to give sufficient tip detection while minimizing the aspect ratio (length/width), and also to maximize the forceps opening. The applied design is 2 dimensional with thickness being constant as determined by using only a single mold layer with the fabrication method.

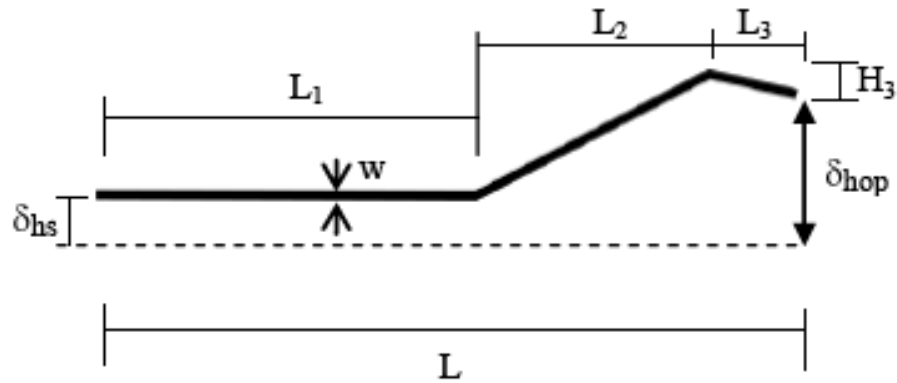


Figure B.1. One arm of a forceps design is shown with parameters length (L), width (w), instrument opening (δ_{hop}), arm separation (δ_{hs}) and angled tip distance (H_3) labeled. This arm is made from a monolithic material, currently having a constant thickness throughout.

The major drawbacks of this design are that it is limited to 2 dimensions (plus thickness), and the thickness is constant throughout the instrument. Additionally, the width is set to be constant throughout the mechanism. Using the fabrication method described in Chapter 3 [3, 4], it is possible to create layered molds, giving rise to 3D structures; with each layer having constant thickness, and width and length being allowed to vary. This is illustrated in Figure B.2.

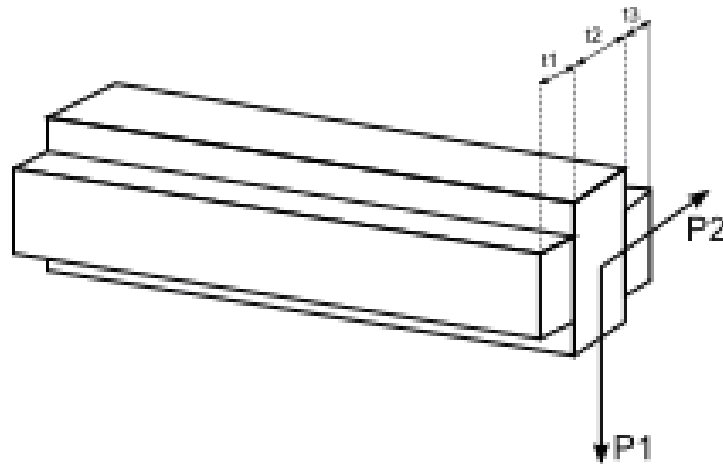


Figure B.2. An example of a 3 layer cantilever beam is shown, with each layer having a thickness of t and the loads P_1 and P_2 , for demonstration are placed at the right end of the beam. While the thickness of each of the layers is constant within each layer, the width and length of the layers are allowed to vary.

Using topology optimization and the solid isotropic material with penalization (SIMP) method [5], the distribution of a material in a given design space can be determined. Topology optimization using the SIMP method outputs a given topology within a design space in terms of the stiffness of each discretized element. With SIMP, element stiffness is depicted on a gray scale, with black representing 100% of the material stiffness and white representing 0% of the material stiffness. This stiffness distribution can then be interpreted to represent the structure topology, in the region of 100% material stiffness, and empty space, in the regions of 0% material stiffness. A penalization factor and filter is used to determine the final topologies of the designs by eliminating elements that require only partial stiffness, or “gray” elements. In this way, a structure’s topology within a design space depends on many factors, including the amount of material available, the application of forces or constraints in the design space, and the objective function used to optimize the topology (i.e. Minimize the compliance of a structure in a given direction)[6]. In this work, the distribution of material within a design space is determined for two validation problems, as well as for an applied problem of a three dimensional forceps able to be manufactured with the LM-RIF method.

Problem Statement

3D topology optimization has been employed to improve the design of the forceps design, described in Chapter 2, by allowing for variations in width while including the addition of layers, creating more complex structures. For simplification and feasibility within the scope of this project, the following steps were taken.

1. Update the 99 line Matlab® code by Sigmund et al [7] to account for 3 dimensions and multiple loads. Verify the code using a simple cantilever beam in minimum compliance.
2. Adapt the 3D code to optimize compliant mechanisms and test it using a standard inverter problem.
3. Apply the 3D compliant mechanism code to design a new forceps device to build on the existing research.

3D Compliance Minimization

Formulation

In the current project, the topology optimization of layered structures was completed using the Solid Isotropic Material with Penalization (SIMP) method. To do so, a 99 line optimization code written in Matlab by Sigmund et al. [7] was modified to account for a 3 dimensional analysis as well as the constraints listed below. User inputs for the code include the number of elements in the x, y, and z directions, the volume fraction of the design space to be used, the penalization factor used to eliminate "gray" elements, and the r_{\min} value denoting filter size. A key aspect of this design problem is the finite element allocation of the beam into 3 layers, making the design compatible with a 3 layer lithography process that can be used to build the instrument. Figure B.3 shows the changes made to number nodes and elements from 2D to 3D. The actual calculation of the stiffness matrix in 3D is included can be found in accompanying Matlab code [8].

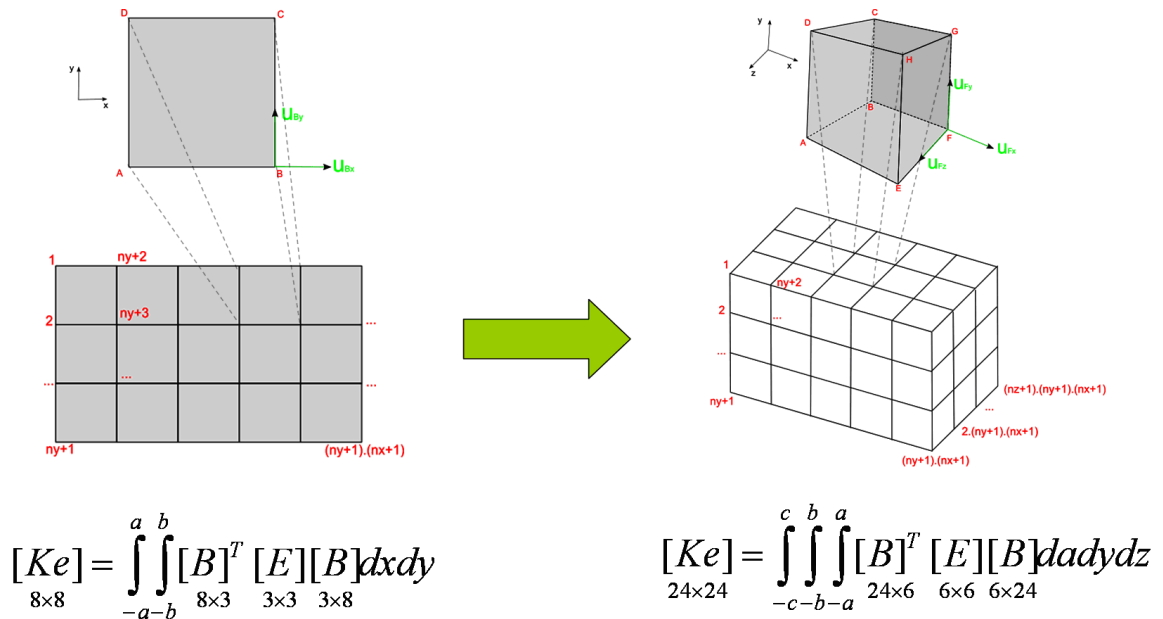


Figure B.3. The updating scheme for the stiffness matrix is depicted along with node numbering, from 2D to 3D, with details shown in the accompanying Matlab code.

Additionally, Table B.1 shows the elements of the 99 line code that were changed or left unchanged for the 3D code. The optimization problem is then to find the best set of design variables that satisfies the objective function given a set of constraints on this 3D layered beam. The design variables are simply the element densities for this problem set-up.

Table B.1. Comparison table showing which items were changed when modifying the 99 line code into 3 dimensions.

Function	99 line code	3D code
Main function (<i>top</i>)	Compliance and sensitivities for 1 load case and for 2D structure	Compliance and sensitivities for multiple loads case and 3D structure
Optimality Criteria (<i>OC</i>)	Bi-sectioning method	unchanged
Filter (<i>Check</i>)	Mesh independency filter (Sigmund)	Unchanged, assumed to be correct in 3D
Ke Matrix (<i>Ik</i>)	Element stiffness matrix for square elements, 2 displacements per node	Element stiffness matrix for cube elements, 3 displacements per node
FE Analysis (<i>FE</i>)	2D analysis	3D analysis, multiple loads definitions

To verify the 3D code, a test problem was considered in which the topology of a cantilever beam was determined such that its compliance under loading was minimized. The objective functions and constraints on the problem are listed in Figure B.4: concisely, the layer thicknesses must be preset but can be manually varied, the volume fraction must be preset but can be manually varied, the element densities (stiffness) must range from almost zero to 1, and the system must be in equilibrium. This problem was considered in order to show that a classical problem with a known answer can be solved using this approach.

$$\min_x : c(x) = \sum_{i=1}^n U_i^T K U_i = \sum_{i=1}^n \sum_{e=1}^N (x_e)^p \mathbf{u}_{ei}^T \mathbf{k}_o \mathbf{u}_e \quad \text{Objective (multiple loads)}$$

s.t.

$$: \frac{V(x)}{V_o} = f \quad \text{Volume constraint}$$

$$: K U = F \quad \text{Equilibrium}$$

$$: 0 < x_{\min} \leq x \leq 1 \quad \text{Design Variable (element density)}$$

Figure B.4. The problem statement is given for the 3D compliance minimization formulation. Where x is the vector of design variables with x_{\min} being the minimum relative density, U , F , and K are the global displacement, force, and stiffness matrices, $V(x)$ and V_0 are the material volume and design domain volume, and f is the allowed volume fraction.

Results and Validation

The design space for the cantilever beam problem is shown Figure B.5 with 3 elements used in the thickness direction in order to represent 3 layers. The left side of the design space is fixed in order to obtain a cantilever scenario. Two loads are applied at the far corners in order to maintain symmetry in the solution. Since forces and displacements must be applied at node points, symmetry cannot be obtained with 3 layers, as there is no node point in the center. The design space was discretized into (50x20x3) 3D elements. The volume fraction was set at 0.4, the penalization factor used was 3, and r_{\min} was 1.2.

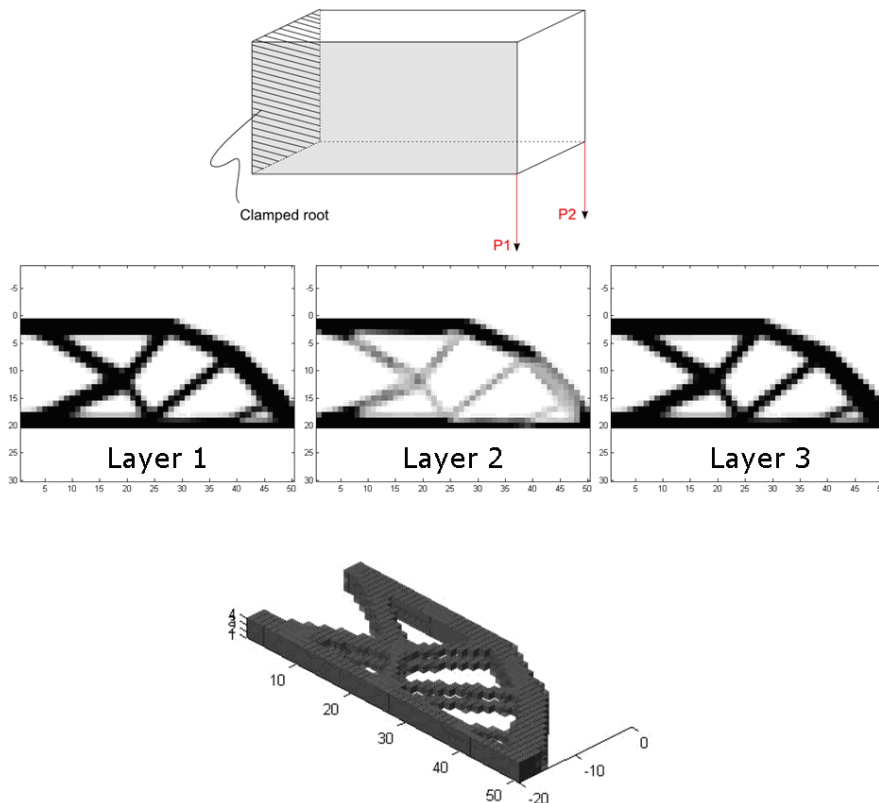


Figure B.5. Top: Design space for the 3D cantilever beam problem; the left side of the design space is fixed (clamped), and loads P1 and P2 are applied downward on the right side. Additionally, the design space is discretized into 3 layers with the layer 1 comprising the front shaded face of the design space, layer 2 being in the center of the design space, and layer 3 at the far side, comprising load P2. Middle: Resulting topologies of each individual layer are shown. As load P1 and P2 are applied to layer 1 and layer 3 respectively, layer 2 does not directly interact with the applied loads. Therefore some areas of layer 2 can be excluded from the final design through the density filter. Bottom: the assembled 3D final truss structure with 3 layers is shown.

A symmetrical result was obtained with layers 1 and 3 being almost identical. Layer 2 consists of gray elements, possibly indicating that a second material, of lower elastic modulus could be used in this specific problem formulation. The final solution represents the classical Michell truss result, validating the 3D code. In the following sections, it will be described how this 3D code was further modified to include compliant mechanism design, tested, and applied to a specific problem.

3D Compliant Mechanism Design

Objectives

The objective of this problem was to validate a 3D compliant mechanism code in order to gain insight into a possible compliant mechanism design for the surgical instrument. Since a linear model was used for the analysis of this problem, the solutions obtained are not accurate enough to be applied to a real application. A non-linear model would be more accurate in predicting large deflections; however, this linear analysis will provide some insight. A topology design approach was used. The input loads and output displacements are specified as shown in the Figure B.6, which represents a sample design space with boundary conditions. Dummy loads are set on the output points in order to keep some stiffness in the structure, and avoid a zero material solution: The compliant mechanism design problem is a compromise between stiffness

and flexibility. The objective of a compliant mechanism design is to maximize the output displacements given a set of input loads. This is done by setting the structure as flexible as possible, thus as soft as possible. Springs are used to impose a stiffness on the output forces.

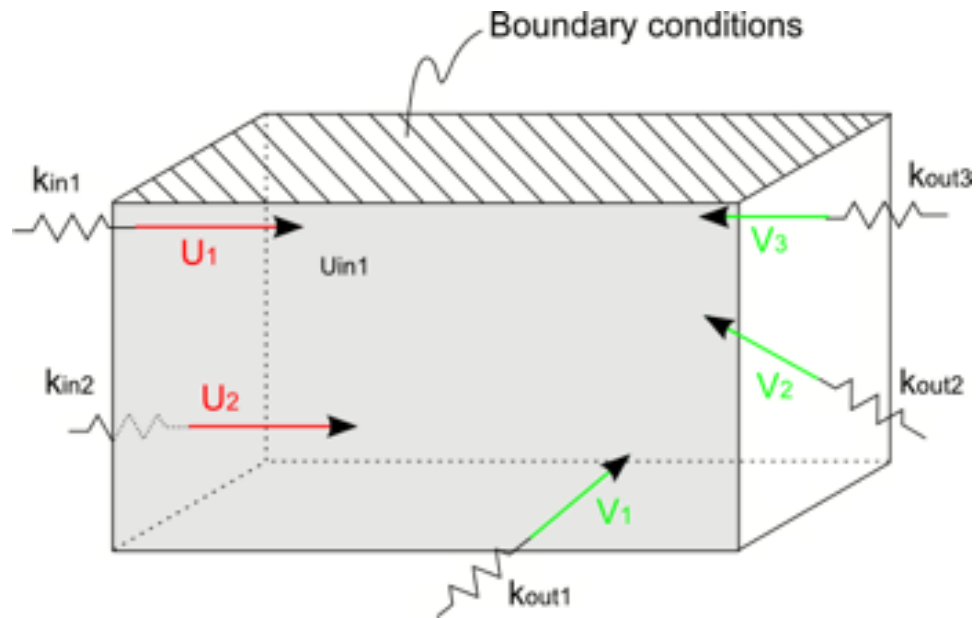


Figure B.6. An example of a design space used for compliant mechanism topology optimization is shown. Within the design space, input forces, output forces, boundary conditions, and number of elements in each direction can be prescribed.

A brief validation of the 3D compliance minimization code was performed and validated the modifications applied to the 99 line code to take account for the 3D analysis. To go into further detail in the design of the surgical instrument, a compliant mechanism design had to be investigated. Following the 105 line code written by Sigmund et al. for a compliant mechanism design problem, and based on the 99 line code, modifications in the Matlab code that had to be performed concerned the main function, which included the objective function. The compliance was calculated in the previous problem. In calculating compliance, the mutual potential energy was sought for each input and output of the 3D structure. In terms of sensitivities, the function

remained almost the same, while modifying the damping factor from 0.5 to 0.3 to stabilize the convergence. Furthermore, the sensitivity values could now be positive. The filtering function was assumed to work well for the 3D analysis and the Finite Element Analysis (FEA) was left the same since it was validated.

Formulation

The objective function is to maximize the output displacements given a set of constraints.

The formulation of this optimization problem can be written as follows:

$$\begin{aligned} & \max(\sum u_{out}) \\ \text{such that } & Ku_j = F_j \\ & Kv_i = G_i \\ & V - V^* = 0 \end{aligned}$$

The objective function could be improved by considering the maximization of the minimum displacement. Indeed, one of the displacements could be much greater than the other, and thus could dominate the sum. The maximization of the displacements is equivalent to the maximization of the work generated by the inputs and outputs, which can be written in terms of mutual potential energy. The problem is then to minimize the opposite of the sum of every mutual potential energy. The objective function can be written as follows, with the constraints being equilibria and the volume fraction, considering every element, and using the SIMP method with x_e the density and p the penalization factor:

$$\min \left(- \sum_i \sum_j \sum_e (x_e)^p v_{ei}^T k_e u_{ej} \right)$$

$$\text{such that } \begin{aligned} Ku_j &= F_j \\ Kv_i &= G_i \\ V - V^* &= 0 \end{aligned}$$

Design Space

In an attempt to validate the code produced, a common example has been considered: the inverter problem. The solution to this problem is known for a 2D case. By applying symmetric loads on a 3D layered-structure, a similar solution could be obtained. The design space of this example is represented in Figure B.7.

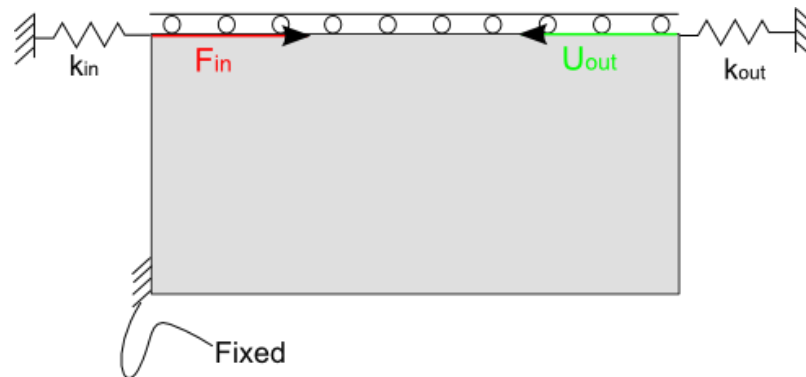


Figure B.7. The design space used in the validation of the final code using the inverter problem is shown. This test problem works well, as the solution to the inverter problem is well understood [5].

An input force is applied at the top left of the design space. The output displacement is set to be in the opposite direction of the input. The structure is fixed at the bottom left and the upper part can only translate in the x direction. In the 3D case, the design space is exactly the same, and the loads are symmetrically applied with respect to thickness.

Results and Validation

The obtained results match very closely the results for a 2D case [5]. The solution is symmetrical in the z direction. The 3D compliant mechanism design code is then verified as properly working.

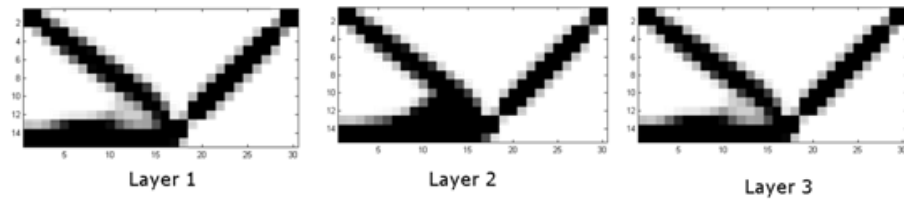


Figure B.8. Optimization results for the topology of a force inverter are shown as function of 3 layers. These results match the well known results for the force inverter problem.

Application to Forceps Design and Results

Boundary Conditions

Since validations were successfully performed, the code has been applied to a design space modeling half of a forceps, which is one of the forceps' arms. The forceps structure was symmetric, thus only the half upper part was considered for the optimization.

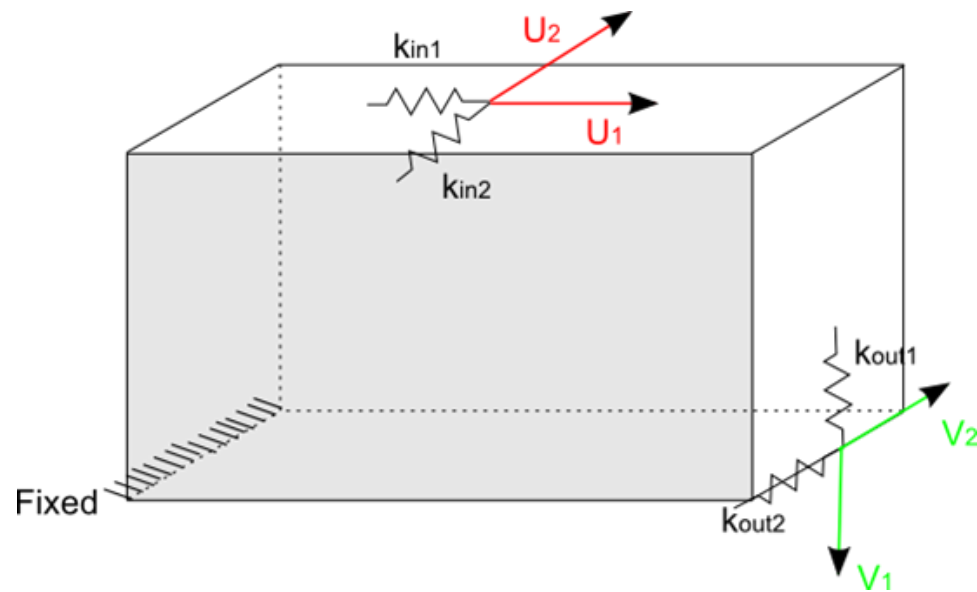


Figure B.9. Design space of one of a forceps arms is shown. Input forces, shown in red, were applied at the top of the space, and could be in one of two directions. Output forces, shown in green, were the desired responses of the input forces. The output forces and directions were required for appropriate forceps articulation.

To understand the boundary conditions, it has to be realized that the forces applied on the surgical instrument are actuated by a sheath that can translate and rotate around the forceps, as discussed in Chapter 2. In Figure B.9, U_1 models the translation of the sheath that has to produce a maximum output displacement V_1 . U_2 represents the rotation of the sheath that has to induce a maximum output displacement V_2 . The forceps is fixed at the bottom left of the design space. Again, this only represents half of the forceps.

Results

After applying those boundary conditions and setting a design space grid of $40 \times 20 \times 3$, a resulting optimized topology was obtained. The run time was quite high considering the resolution of the design space: 9 hours were necessary to obtain a converged solution, see Figure B.10. The convergence criteria could be improved. It was set to 1% of the maximum changes in

the densities. A criterion of at least 0.1% would have been better but such a criterion would also imply a greater run time. The final design obtained is presented in the Figure B.11. The solution is not symmetric since the loads are not symmetrically applied. Some gray elements are still present and they might be avoided by using a greater penalization factor or by decreasing the convergence criterion. It also can be noted that for too high a value of the penalization factor, convergence could not be obtained as some singularities appeared in the stiffness matrix. Nevertheless, the solution is physically sensible.

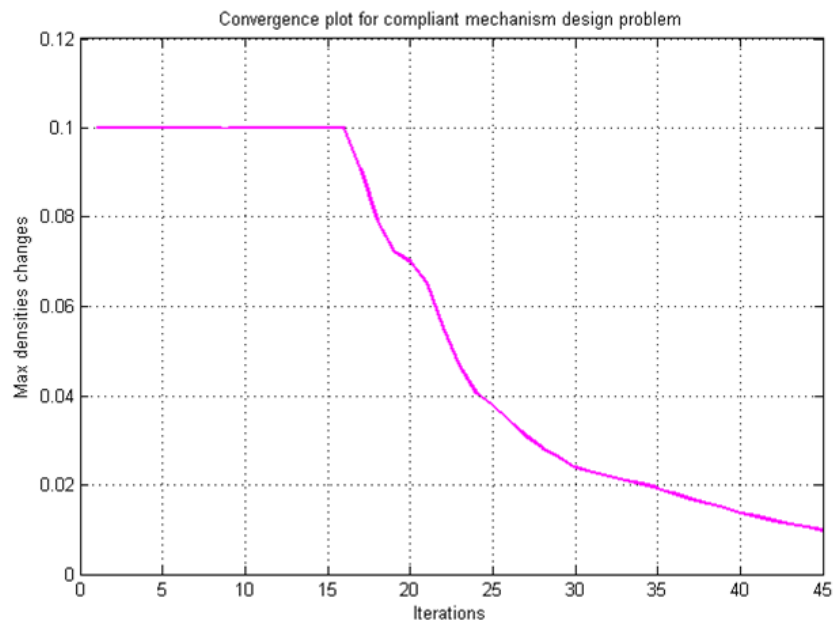


Figure B.10. Final convergence occurred after roughly 45 iterations, and 9 hours.

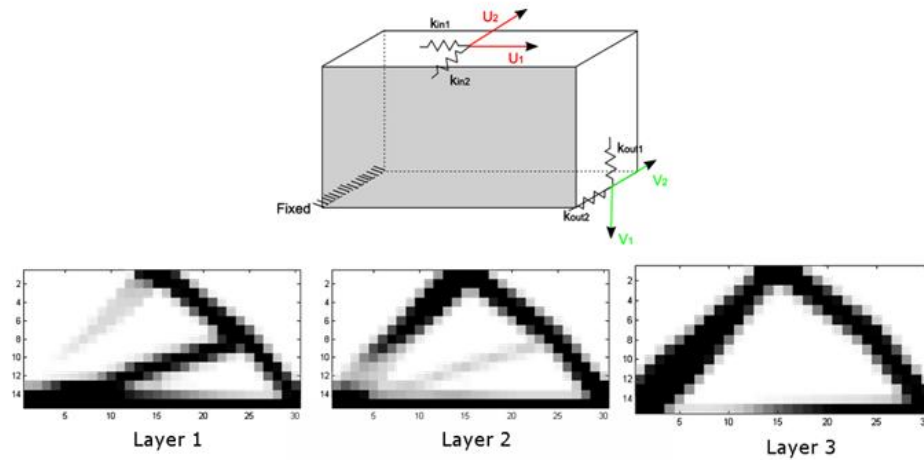


Figure B.11. Final forceps design is shown as a function of the 3 layers. Layer 1 corresponds to the front shaded face of the design space. Layer 2 comprises the input and output forces, and layer 3 corresponds to the face opposite the gray shaded face of the design space. Stacking layer 1, 2, and 3 to form the final complete topology would create one forceps arm.

Conclusions and Recommendations

In summary, a topological optimization routine, using the SIMP method, was instituted in order to design devices that are compatible with a new mesoscale manufacturing process. Initially for simplification, a three layer cantilever beam was considered as a minimum compliance problem. Following validation, the 3D code was updated to consider compliant mechanism design, and this final code was applied to the design of a surgical instrument. Although the results obtained are feasible designs, the run time for 40x20x3 design space was approximately 9 hrs, with the convergence set at 0.01. Some recommendations can be made in order to obtain more reliable results:

1. To achieve a more realistic surgical instrument, some material could be taken out near the tip in the solution design.
2. The optimality criterion was left the same for simplicity. A Method of Moving Asymptotes (MMA) may be more efficient in the convergence process.

3. A non-linear analysis would have to be considered in order to get reliable results, and not only an 'insight'. Without such an analysis, the here obtained results cannot be considered as applicable designs.
4. The effect of the thickness of each layer was not investigated. A size optimization could be performed.

References

1. Aguirre, M.E., G. Hayes, M. Frecker, N. Antolino, and J. Adair. *Fabrication and Design of a Nanoparticulate Enabled Micro Forceps*. in *32nd Annual Mechanisms and Robotics Conference (MR) Topic: MR-8 Medical Devices and their Applications*. 2008.
2. Aguirre, M.E., G. Hayes, R. Meirom, M. Frecker, C. Muhlstein, J.H. Adair, and J.A. Kerr, *The Design and Fabrication of Narrow-Gauge (1 mm Diameter) Surgical Instruments for Natural Orifice Translumenal Endoscopic Surgery*. To be submitted to the Journal of Mechanical Design, 2009.
3. Antolino, N.E., G. Hayes, R. Kirkpatrick, C.L. Muhlstein, M.I. Frecker, E.M. Mockensturm, and J.H. Adair, *Lost Mold Rapid Infiltration Forming of Mesoscale Ceramics: Part 1, Fabrication*. Journal of the American Ceramic Society, 2009. 92(1): p. S63-S69.
4. Antolino, N.E., G. Hayes, R. Kirkpatrick, C.L. Muhlstein, M.I. Frecker, E.M. Mockensturm, and J.H. Adair, *Lost Mold-Rapid Infiltration Forming of Mesoscale Ceramics: Part 2, Geometry and Strength Improvements*. Journal of the American Ceramic Society, 2009. 92(1): p. S70-S78.
5. Bendsoe, M.P. and O. Sigmund, *Optimization of structural topology, shape, and material*. 1995: Springer.
6. Haftka, R.T. and Z. Gurdal, *Elements of structural optimization*. 1992: Kluwer Academic Publishers.
7. Sigmund, O., *A 99 line topology optimization code written in Matlab*. Structural and Multidisciplinary Optimization, 2001. 21(2): p. 120-127.
8. *Matlab*, in *R2007a*. 2007, The Mathworks.

Matlab Scripts

```

%% 3D COMPLIANT MECHANISM DESIGN CODE, BASED ON 99 LINE CODE BY OLE
%% SIGMUND
%%
%% GREG HAYES & OLIVIER LEON
%% MAY 2008

function top(nelx,nely,nelz,volfrac,penal,rmin)
% INITIALIZE

x(1:nelz,1:nely,1:nelx) = volfrac;
loop = 0;
change = 1.;
changes = [];
% START ITERATION
while change > 0.01
    loop = loop + 1;
    xold = x;
% 3D FE-ANALYSIS
    [U]=FE(nelx,nely,nelz,x,penal);
% OBJECTIVE FUNCTION AND SENSITIVITY ANALYSIS
    [KE] = lk;
    c = 0.;
    for ely = 1:nely
        for elx = 1:nelx
            for elz = 1:nelz
                n1 = (nely+1)*(elx-1) + ely + (elz-1)*(nelx+1)*(nely+1);
                n2 = (nely+1)* elx + ely + (elz-1)*(nelx+1)*(nely+1);
                n3 = n1 + (nelx+1)*(nely+1);
                n4 = n2 + (nelx+1)*(nely+1);
                dc(elz, ely,elx) = 0.;

                Ue1 = U([3*n1+1;3*n1+2;3*n1+3; 3*n3+1;3*n3+2;3*n3+3; 3*n3-2; ...
                    3*n3-1;3*n3; 3*n1-2;3*n1-1;3*n1; 3*n2+1;3*n2+2;3*n2+3; ...
                    3*n4+1;3*n4+2;3*n4+3; 3*n4-2;3*n4-1;3*n4; 3*n2-2;3*n2-1; ...
                    3*n2],1);
                Ue2 = U([3*n1+1;3*n1+2;3*n1+3; 3*n3+1;3*n3+2;3*n3+3; 3*n3-2; ...
                    3*n3-1;3*n3; 3*n1-2;3*n1-1;3*n1; 3*n2+1;3*n2+2;3*n2+3; ...
                    3*n4+1;3*n4+2;3*n4+3; 3*n4-2;3*n4-1;3*n4; 3*n2-2;3*n2-1;...
                    3*n2],2);
                Ue3 = U([3*n1+1;3*n1+2;3*n1+3; 3*n3+1;3*n3+2;3*n3+3; 3*n3-2;...
                    3*n3-1;3*n3; 3*n1-2;3*n1-1;3*n1; 3*n2+1;3*n2+2;3*n2+3; ...
                    3*n4+1;3*n4+2;3*n4+3; 3*n4-2;3*n4-1;3*n4; 3*n2-2;3*n2-1; ...
                    3*n2],3);
                Ue4 = U([3*n1+1;3*n1+2;3*n1+3; 3*n3+1;3*n3+2;3*n3+3; 3*n3-2; ...
                    3*n3-1;3*n3; 3*n1-2;3*n1-1;3*n1; 3*n2+1;3*n2+2;3*n2+3; ...
                    3*n4+1;3*n4+2;3*n4+3; 3*n4-2;3*n4-1;3*n4; 3*n2-2;3*n2-1; ...
                    3*n2],4);
            end
        end
    end
    change = max(abs(x-xold));
end

```

```

c = c + x(elz,ely,elx)^penal*Ue3'*KE*Ue1;
c = c + x(elz,ely,elx)^penal*Ue4'*KE*Ue1;
c = c + x(elz,ely,elx)^penal*Ue3'*KE*Ue2;
c = c + x(elz,ely,elx)^penal*Ue4'*KE*Ue2;

dc(elz,ely,elx) = ...
    dc(elz,ely,elx)+penal*x(elz,ely,elx)^(penal-1)*Ue3'*KE*Ue1;
dc(elz,ely,elx) = ...
    dc(elz,ely,elx)+penal*x(elz,ely,elx)^(penal-1)*Ue4'*KE*Ue1;
dc(elz,ely,elx) = ...
    dc(elz,ely,elx)+penal*x(elz,ely,elx)^(penal-1)*Ue3'*KE*Ue2;
dc(elz,ely,elx) = ...
    dc(elz,ely,elx)+penal*x(elz,ely,elx)^(penal-1)*Ue4'*KE*Ue2;
end
end
end
% FILTERING OF SENSITIVITIES
[dc] = check(nelx,nely,nelz,rmin,x,dc);
% DESIGN UPDATE BY THE OPTIMALITY CRITERIA METHOD
[x] = OC(nelx,nely,nelz,x,volfrac,dc);
% PRINT RESULTS
change = max(max(max(abs(x-xold))));
changes(loop) = change;
disp([' It.: ' sprintf('%4i',loop) ' Obj.: ' sprintf('%10.4f',c) ...
      ' Vol.: ' sprintf('%6.3f',sum(sum(sum(x)))/(nelx*nely*nelz)) ...
      ' ch.: ' sprintf('%6.3f',change )])
% SAVE DATA
x1(:, :) = x(1, :, :);
save('x1', 'x1');
x2(:, :) = x(2, :, :);
save('x2', 'x2');
x3(:, :) = x(3, :, :);
save('x3', 'x3');

end

%%%%%%%%%%%%%%%%%%%%%%%%%%%%%%%%%%%%%%%%%%%%%%%%%%%%%%%%%%%%%%%%%%%%%%%%%% OPTIMALITY CRITERIA UPDATE %%%%%%%%%%%%%%%%%%%%%%%%%%%%%%%%%%%%%%%%%%%%%%%%%%%%%%%%%%%%%%%%%%%%%%%%%%%
function [xnew]=OC(nelx,nely,nelz,x,volfrac,dc)
l1 = 0; l2 = 100000; move = 0.1;
while (l2-l1)/(l2+l1) > 1e-4 && l2 > 1e-40
    lmid = 0.5*(l2+l1);
    xnew = max(0.001,max(x-move,min(1.,min(x+move,x.*(max(1e-10, ...
        -dc./lmid)).^0.3))));
    if sum(sum(sum(xnew))) - volfrac*nelz*nelx*nely > 0;
        l1 = lmid;
    else

```

```

        l2 = lmid;
    end
end
end
%%%%%%%%%%%%%%%%%%%%%%%%%%%%%%%%%%%%%%%%%%%%%%%%%%%%%%%%%%%%%%%%%%%%%%%%% MESH-INDEPENDENCY FILTER %%%%%%%%%%
function [dcn]=check(nelx,nely,nelz,rmin,x,dc)
dcn=zeros(nelz,nely,nelx);
for i = 1:nelx
    for j = 1:nely
        for m = 1:nelz
            sum=0.0;
            for k = max(i-floor(rmin),1):min(i+floor(rmin),nelx)
                for l = max(j-floor(rmin),1):min(j+floor(rmin),nely)
                    for n = max(m-floor(rmin),1):min(m+floor(rmin),nelz)
                        fac = rmin-sqrt((i-k)^2+(j-l)^2+(m-n)^2);
                        sum = sum+max(0,fac);
                        dcn(m,j,i) = dcn(m,j,i) + max(0,fac)*x(n,l,k)*dc(n,l,k);
                    end
                end
            end
            dcn(m,j,i) = dcn(m,j,i)/(x(m,j,i)*sum);
        end
    end
end
end
%%%%%%%%%%%%%%%%%%%%%%%%%%%%%%%%%%%%%%%%%%%%%%%%%%%%%%%%%%%%%%%%%%%%%%%%% FE-ANALYSIS %%%%%%%%%%
function [U]=FE(nelx,nely,nelz,x,penal)
[KE] = lk;
K = sparse(3*(nelx+1)*(nely+1)*(nelz+1), 3*(nelx+1)*(nely+1)*(nelz+1));
F = sparse(3*(nelx+1)*(nely+1)*(nelz+1),4);
U = sparse(3*(nelx+1)*(nely+1)*(nelz+1),4);
for elx = 1:nelx
    for ely = 1:nely
        for elz = 1:nelz
            n1 = (nely+1)*(elx-1) + ely + (elz-1)*(nelx+1)*(nely+1);
            n2 = (nely+1)* elx + ely + (elz-1)*(nelx+1)*(nely+1);
            n3 = n1 + (nelx+1)*(nely+1);
            n4 = n2 + (nelx+1)*(nely+1);
            edof = [3*n1+1;3*n1+2;3*n1+3; 3*n3+1;3*n3+2;3*n3+3; 3*n3-2; ...
                    3*n3-1;3*n3; 3*n1-2;3*n1-1;3*n1; 3*n2+1;3*n2+2;3*n2+3; ...
                    3*n4+1;3*n4+2;3*n4+3; 3*n4-2;3*n4-1;3*n4; 3*n2-2;3*n2-1;3*n2];
            K(edof,edof) = K(edof,edof) + x(elz,ely,elx)^penal*KE;
        end
    end
end
end
% DEFINE LOADS AND SUPPORTS
% INPUT NODES
din1 = 3*(nely+1)*(nelx+1)+1;
din2 = 6*(nely+1)*(nelx+1)+1;
% OUTPUT NODES

```

```

dout1 = 6*(nely+1)*(nelx+1)-2-3*nely;
dout2 = 9*(nely+1)*(nelx+1)-2-3*nely;

F(din1,1) = 1;
F(din2,2) = 1;
F(dout1,3) = -1;
F(dout2,4) = -1;

K(din1,din1)=K(din1,din1)+0.1;
K(din2,din2)=K(din2,din2)+0.1;
K(dout1,dout1)=K(dout1,dout1)+0.1;
K(dout2,dout2)=K(dout2,dout2)+0.1;

fixeddofs = union([3*(nely+1):-1:3*(nely+1)-5], ...
    [3*(nely+1)*(nelx+2):-1:3*(nely+1)*(nelx+2)-5]);
fixeddofs = union( fixeddofs, ...
    [3*(nely+1)*(2*nelx+3):-1:3*(nely+1)*(2*nelx+3)-5]);
fixeddofs = union( fixeddofs, ...
    [3*(nely+1)*(3*nelx+4):-1:3*(nely+1)*(3*nelx+4)-5]);
fixeddofs = union( fixeddofs, ...
    [2:3*(nely+1):3*(nely+1)*(nelx+1)]);
fixeddofs = union( fixeddofs, ...
    [3*(nely+1)*(nelx+1)+2:3*(nely+1):6*(nely+1)*(nelx+1)]);
fixeddofs = union( fixeddofs, ...
    [6*(nely+1)*(nelx+1)+2:3*(nely+1):9*(nely+1)*(nelx+1)]);
fixeddofs = union( fixeddofs, ...
    [9*(nely+1)*(nelx+1)+2:3*(nely+1):12*(nely+1)*(nelx+1)]);

alldofs = [1:3*(nelx+1)*(nely+1)*(nelx+1)];
freedofs = setdiff(alldofs,fixeddofs);
% SOLVING
U(freedofs,:) = K(freedofs,freedofs) \ F(freedofs,:);
U(fixeddofs,:)= 0;
%%%%%%%%% ELEMENT STIFFNESS MATRIX %%%%%%%%%%
function [KE]=lk
E = 1.;
nu = 0.3;

a = 1;
b = 1;
c = 1;

% ELEMENT STIFFNESS MATRIX TOO BIG TO BE PRINTED
KE = [ .. ];

```

Mathematica® Code to Calculate Stiffness Matrix

Calculate Young Modulus Matrix called Eyoung

```

constant1 = Young / ((1 + v) (1 - 2 v));
G = Young / (2 (1 + v));
Eyoung = {{ (1 - v) constant1, v constant1, v constant1, 0, 0, 0},
          {v constant1, (1 - v) constant1, v constant1, 0, 0, 0},
          {v constant1, v constant1, (1 - v) constant1, 0, 0, 0},
          {0, 0, 0, G, 0, 0},
          {0, 0, 0, 0, G, 0},
          {0, 0, 0, 0, 0, G}}
{{ (1 - v) Young, v Young, v Young, 0, 0, 0},
  {(1 - 2 v) (1 + v), (1 - 2 v) (1 + v), (1 - 2 v) (1 + v)},
  {v Young, (1 - v) Young, v Young, 0, 0, 0},
  {(1 - 2 v) (1 + v), (1 - 2 v) (1 + v), (1 - 2 v) (1 + v)},
  {v Young, v Young, (1 - v) Young, 0, 0, 0},
  {(1 - 2 v) (1 + v), (1 - 2 v) (1 + v), (1 - 2 v) (1 + v)},
  {0, 0, 0, Young, 0, 0}, {0, 0, 0, 0, Young, 0}, {0, 0, 0, 0, 0, Young}
}

```

Form Operator Matrix for d/dx etc...

```

MatrixForm[MM = {{D[h, x] ε, 0 # ε, 0 # ε}, {0 # ε, D[h, y] ε, 0 # ε}, {0 # ε, 0 # ε, D[h, z] ε},
                 {D[h, y] ε, D[h, x] ε, 0 # ε}, {0 # ε, D[h, z] ε, D[h, y] ε}, {D[h, z] ε, 0 # ε, D[h, x] ε}}]

```

$$\begin{pmatrix}
 \partial_x h1 \epsilon & 0 h1 \epsilon & 0 h1 \epsilon \\
 0 h1 \epsilon & \partial_y h1 \epsilon & 0 h1 \epsilon \\
 0 h1 \epsilon & 0 h1 \epsilon & \partial_z h1 \epsilon \\
 \partial_y h1 \epsilon & \partial_x h1 \epsilon & 0 h1 \epsilon \\
 0 h1 \epsilon & \partial_z h1 \epsilon & \partial_y h1 \epsilon \\
 \partial_z h1 \epsilon & 0 h1 \epsilon & \partial_x h1 \epsilon
 \end{pmatrix}$$

2 | Solve for K.nb

Form N : the Shape Function matrix

```

N1 = (a-x) (b-y) (c+z) / (8 a b c);
N2 = (a-x) (b-y) (c-z) / (8 a b c);
N3 = (a-x) (b+y) (c-z) / (8 a b c);
N4 = (a-x) (b+y) (c+z) / (8 a b c);
N5 = (a+x) (b-y) (c+z) / (8 a b c);
N6 = (a+x) (b-y) (c-z) / (8 a b c);
N7 = (a+x) (b+y) (c-z) / (8 a b c);
N8 = (a+x) (b+y) (c+z) / (8 a b c);

```

```

MatrixForm[Q = {{N1, 0, 0, N2, 0, 0, N3, 0, 0, N4, 0, 0, N5, 0, 0, N6, 0, 0, N7, 0, 0, N8, 0, 0},
{0, N1, 0, 0, N2, 0, 0, N3, 0, 0, N4, 0, 0, N5, 0, 0, N6, 0, 0, N7, 0, 0, N8, 0},
{0, 0, N1, 0, 0, N2, 0, 0, N3, 0, 0, N4, 0, 0, N5, 0, 0, N6, 0, 0, N7, 0, 0, N8}}]

```

$$\begin{pmatrix}
 \frac{(a-x)(b-y)(c+z)}{8abc} & 0 & 0 & \frac{(a-x)(b-y)(c-z)}{8abc} & 0 & 0 & \frac{(a-x)(b+y)(c-z)}{8abc} & 0 & 0 & \frac{(a-x)(b+y)(c+z)}{8abc} & 0 & 0 & 0 & 0 & 0 & 0 & 0 & 0 & 0 & 0 & 0 & 0 & 0 \\
 0 & \frac{(a-x)(b-y)(c+z)}{8abc} & 0 & 0 & 0 & 0 & \frac{(a-x)(b-y)(c-z)}{8abc} & 0 & 0 & 0 & 0 & 0 & \frac{(a-x)(b+y)(c-z)}{8abc} & 0 & 0 & 0 & 0 & 0 & 0 & 0 & 0 & 0 & 0 \\
 0 & 0 & \frac{(a-x)(b-y)(c+z)}{8abc} & 0 & 0 & 0 & 0 & 0 & 0 & \frac{(a-x)(b+y)(c-z)}{8abc} & 0 & 0 & 0 & \frac{(a-x)(b+y)(c+z)}{8abc} & 0 & 0 & 0 & 0 & 0 & 0 & 0 & 0 & 0
 \end{pmatrix}$$

Form K integrand Matrix By multiplying Transpose(B)*E*B

```

B = Table[Sum[MM[[i1, j1]] / @Q[[j1]], {j1, 3}], {i1, 6}];

```

```

Greg = B'.E.young.B;

```

Form K matrix by integrating over the volume

$$K = \int_{-c}^c \int_{-b}^b \left(\int_{-a}^a \text{Greg} \, dx \right) dy \, dz // \text{MatrixForm}$$

A very large output was generated. Here is a sample of it:

(<<1>>)

Show Less Show More Show Full Output Set Size Limit...

```

Export["testy.xls", K]

```

```

testy.xls

```

```

a = 1;
b = 1;
c = 1;
Young = 1;
v = 0.3;

```

Solve for K.nb | 3

```

K // MatrixForm
{0.470085  0.160256 -0.160256  0.106838  0.0801282  0.0320513 -0.0106838 -0.0160256
0.160256  0.470085 -0.160256  0.0801282  0.106838  0.0320513  0.0160256 -0.17094
-0.160256 -0.160256  0.470085 -0.0320513 -0.0320513 -0.213675 -0.0160256  0.160256
0.106838  0.0801282 -0.0320513  0.470085  0.160256  0.160256  0.106838 -0.0320513
0.0801282  0.106838 -0.0320513  0.160256  0.470085  0.160256  0.0320513 -0.213675
0.0320513  0.0320513 -0.213675  0.160256  0.160256  0.470085  0.0801282 -0.0320513
-0.0106838  0.0160256 -0.0160256  0.106838  0.0320513  0.0801282  0.470085 -0.160256
-0.0160256 -0.17094  0.160256 -0.0320513 -0.213675 -0.0320513 -0.160256  0.470085
0.0160256  0.160256 -0.17094  0.0801282  0.0320513  0.106838  0.160256 -0.160256
0.106838  0.0320513 -0.0801282 -0.0106838  0.0160256  0.0160256  0.106838 -0.0801282
-0.0320513 -0.213675  0.0320513 -0.0160256 -0.17094 -0.160256 -0.0801282  0.106838
-0.0801282 -0.0320513  0.106838 -0.0160256 -0.160256 -0.17094 -0.0320513  0.0320513
-0.213675 -0.0320513  0.0320513 -0.17094 -0.0160256 -0.160256 -0.117521  0.0801282
0.0320513  0.106838 -0.0801282  0.0160256 -0.0106838  0.0160256  0.0801282 -0.117521
-0.0320513 -0.0801282  0.106838 -0.160256 -0.0160256 -0.17094 -0.0801282  0.0801282
-0.17094 -0.0160256  0.160256 -0.213675 -0.0320513 -0.0320513 -0.17094  0.160256
0.0160256 -0.0106838 -0.0160256  0.0320513  0.106838  0.0801282  0.160256 -0.17094
0.160256  0.0160256 -0.17094  0.0320513  0.0801282  0.106838  0.0160256 -0.0160256
-0.117521 -0.0801282  0.0801282 -0.17094 -0.160256 -0.0160256 -0.213675  0.0320513
-0.0801282 -0.117521  0.0801282 -0.160256 -0.17094 -0.0160256 -0.0320513  0.106838
0.0801282  0.0801282 -0.117521  0.0160256  0.0160256 -0.0106838  0.0320513 -0.0801282
-0.17094 -0.160256  0.0160256 -0.117521 -0.0801282 -0.0801282 -0.17094  0.0160256
-0.160256 -0.17094  0.0160256 -0.0801282 -0.117521 -0.0801282 -0.0160256 -0.0106838
-0.0160256 -0.0160256 -0.0106838 -0.0801282 -0.0801282 -0.117521 -0.160256  0.0160256

```

Appendix C

Drying Model Programs

1 Dimensional Drying Model in Matlab®

```

% gelcast drying model applied to our system
%Greg Hayes
%for loop to change temperature and RH
%Conditions:
T=273+20; % + drying temperature in Kjust add the C
RH = .64; % relative humidity
P = 101325; % standard pressure in Pa
L = 400E-6; % layer thickness in meters
rs = 50 *10^(-9);% particle radius
gamma = 1.1; %ro/rs
f = .40;%solids loading
%Constants#####
psat = (3.08 * (T^2)) - (1829.5*T) + 277257; %saturation pressure of
liquid
D = (2.527/P) *(T/292.86)^2.334; %diffusivity of liquid through gel
Z = .001;%drying oven constant and is approximated
ysat = psat/P;
Mw = 18; %kg/mol
rhoH2o = 1000;%density of water
Ro = 8314;
Kd = 1 - exp(-269.29*L);%Kd = 1-1.62*exp(-269.29*L) is the old eqn
De = Kd*D;
A = .0078; % 10 cm diameter area in square meters
V = A*L; %volume
C = P/(Ro *T);
mo = rhoH2o *(f* A* L);
Dp = 5*10^(-17)* (T/300)^2;
RHprime = (1 + RH)/2;
%logiccode#####
X1 = 0.7; X2 = 0.2; y1 = 0.0;
% L logic
if L <= 0.0045
X1=0.6;
elseif L <= 0.0055
X1 = 0.6 - 0.1*(L-0.0045)/0.001;
end
%RH logic
if RH < 0.31
X1 = 0.95;

```

```

elseif RH < 0.4
X1=0.95 - 0.25*(RH-0.31)/0.09;
end
%L logic
if L <= 0.003
X2 = 0.05;
elseif L <= 0.01
X2 = 0.05 + 0.25*(L-0.003)/0.012;
elseif L > 0.015
X2 = 0.3;
end
%T logic
if T > 342
y1 = 0.1;
elseif T > 323
y1 = 0.1 + 0.1*(342-T)/19;
end
%y1 logic
if y1 < X2 && y1 < 0
X2 = y1;
end
% #####
X1;
X2;
y1;
% TIME#####
t1 = (-X1+1)*rhoh2o*L*Ro*T*Z/(D*Mw*psat*(1-RH));
stageltime = t1/3600;
%t1 is solving stage 1 equation for t when stagel1m = X1
t2 = 1/2*(2*rhoh2o*L^2*X1-rhoh2o*L^2*X1^2+2*De*C*Mw*log((-1+ysat*RH)/(-
1+ysat))
*t1+rhoh2o*L^2*X2^2-2*rhoh2o*L^2*X2)/(De*C*Mw*log((-1+ysat*RH)/(-
1+ysat)));
stage2time = t2/3600;
%t2 is solving stage 2 equation for t when stage2m = X2
t3 = 1/3*(X2^2*mo*rs^2*gamma-X2^2*mo*rs^2+3*V*C*ysat*Mw*gamma^2*Dp*t2-
3*V*C*ysat*Mw*gamma^2*Dp*RHprime*t2-
3*V*C*ysat*Mw*gamma^2*Dp*f*t2+3*V*C*ysat*Mw*gamma^2*Dp*f*RHprime*t2)/
(V*C*ysat*Mw*gamma^2*Dp*(1-RHprime-f+f*RHprime));
stage3time = t3/3600;
% t3 is solving stage 3 equation for t when stage3m = 0.
%stage 1#####
stagelt = 0:t1;
stagel1m = 1 - stagelt *(D * Mw *psat *(1 - RH)/(rhoh2o * L * Ro * T *
Z));
plot(stagelt/3600,stagel1m) % divide to get hours
xlabel('time (hours)','FontSize',16)
ylabel('Normalized Moisture Mass m(t)','FontSize',16)
title('Moisture Mass vs Time during drying','FontSize',16)
hold on;
% stage 2 #####
stage2t = t1:t2;
stage2m = 1 - ( (1 - X1)^2 + (2* De* C* Mw / (rhoh2o * L ^ 2) * log((1
- ysat* RH)/(1 -
ysat))) * (stage2t - t1)).^(1/2);

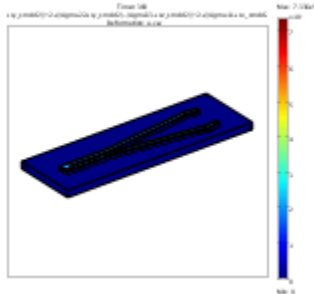
```

```
plot(stage2t/3600,stage2m) % divide to get hours
hold on;
% pause;
% stage 3 #####
stage3t = t2:t3;
stage3m = X2-(3* (1 - f) *(1 - RHprime)* V* C* ysat* Mw /(X2 *mo)
*(gamma^2/(gamma - 1)*
(Dp/rs^2)))*(stage3t-t2);
plot(stage3t/3600,stage3m)
```

3 Dimensional Constrained Drying Model in Comsol Multiphysics® v3.5a



Constrained Drying Stress



1. Table of Contents

Title - Constrained Drying Stress

Table of Contents

Model Properties

Constants

Geometry

Geom1

Solver Settings

Postprocessing

Variables

2. Model Properties

Property	Value
Model name	Constrained Drying Stress
Author	Greg Hayes
Company	PSU
Department	MATSE
Reference	
URL	
Saved date	Jan 15, 2011 6:10:14 PM
Creation date	Jul 8, 2010 2:26:12 PM
COMSOL version	COMSOL 3.5.0.608

File name: /gpf/home/grh144/3D comsol modeling/Final Forceps ar40 straight/ar40 straight final.mph

Application modes and modules used in this model:

Geom1 (3D)

PDE, Coefficient Form
Solid, Stress-Strain (Structural Mechanics Module)

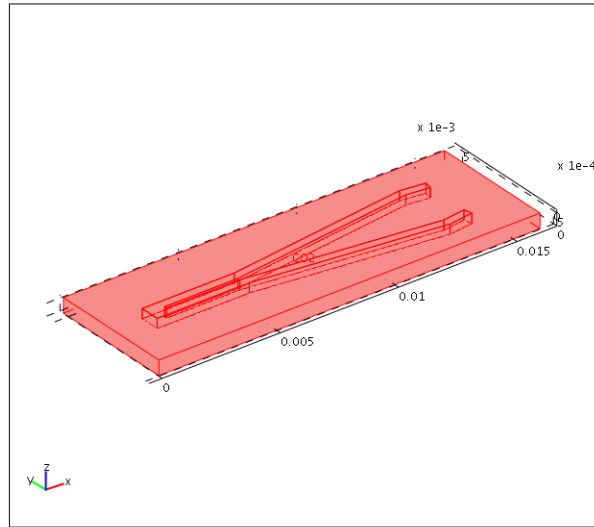
3. Constants

Name	Expression	Value	Description
C1	$2 * M + A_{star}$	1.59699e10	
C2	M	4e9	
C3	$M + A_{star}$	1.19699e10	
C4	γ / Clx	21250	
C5	γ / ρ	1416.666667	
C6	$A_{mu} * Clx / \rho * change$	4.026667e-10	
gamma	17e5	1.7e6	
rho	1200	1200	
Clx	80	80	
A _{mu}	6.04e-8	6.04e-8	
lv	8.64e-5	8.64e-5	
L	A _{star}	7.969896e9	
G	M	4e9	
E _{new}	$G * (3 * L + 2 * G) / (L + G)$	1.066331e10	
n _{new}	$L / 2 / (L + G)$	0.332914	
M _{un}	160	160	
M _{ua}	30	30	
M	4e9	4e9	
A	8e9	8e9	
change	.1	0.1	
test	$C6 * lv / A_{mu}$	5.76e-7	
A _{star}	$A - \gamma^2 / (Clx * \rho)$	7.969896e9	

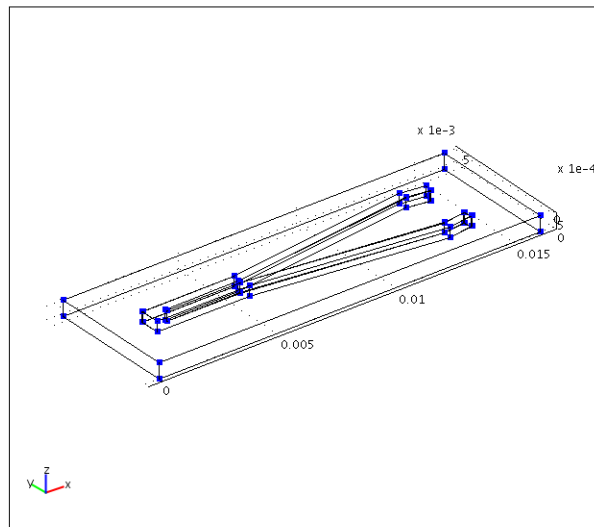
4. Geometry

Number of geometries: 1

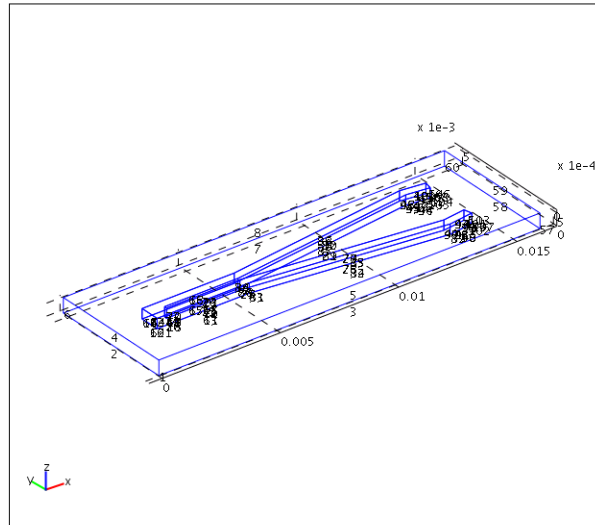
4.1. Geom1



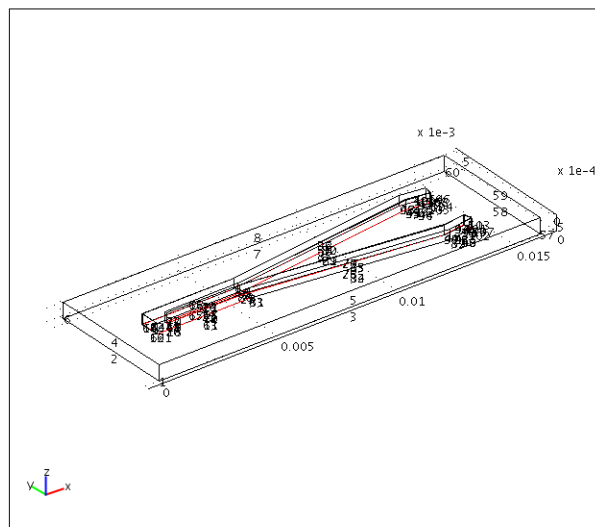
4.1.1. Point mode



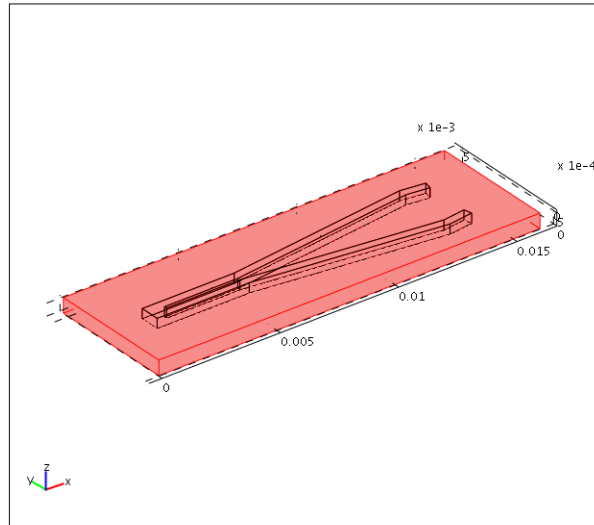
4.1.2. Edge mode



4.1.3. Boundary mode



4.1.4. Subdomain mode



5. Geom1

Space dimensions: 3D

Independent variables: x, y, z

5.1. Scalar Expressions

Name	Expression	Unit	Description
sigmax	$M*(u_x+u_x)+(A-\gamma^2/(\rho*Cl_x))*u_x-\gamma/Cl_x*m$		
sigmay	$M*(u_y+u_y)+(A-\gamma^2/(\rho*Cl_x))*u_y-\gamma/Cl_x*m$		
sigmaz	$M*(u_z+u_z)+(A-\gamma^2/(\rho*Cl_x))*u_z-\gamma/Cl_x*m$		
total	$\sqrt{\text{sigmax}^2+\text{sigmay}^2+\text{sigmaz}^2}$		
sigma11	$M*(u_x+v_x+w_x)+A*u_x-C4*m$		
sigma22	$M*(u_y+v_y+w_y)+A*(v_y)-C4*m$		
sigma33	$M*(u_z+v_z+w_z)+A*(w_z)-C4*m$		
sigmadry	$\sqrt{\text{sigma11}^2+\text{sigma22}^2+\text{sigma33}^2}$		

5.2. Contact Pairs

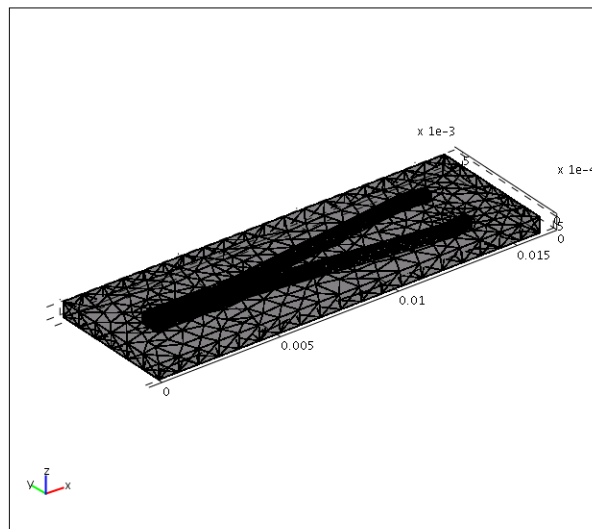
Contact pair	Source boundaries	Destination boundaries	Suffix	Contact variable
Pair 1	6-7, 9-17, 20	24-25, 28-36, 39-41	_cp1	contact_cp1
Pair 2	18-19	37-38	_cp2	contact_cp2

5.3. Mesh

5.3.1. Mesh Statistics

Number of degrees of freedom	59102
Number of mesh points	2415
Number of elements	7045
Tetrahedral	7045

Prism	0
Hexahedral	0
Number of boundary elements	4362
Triangular	4362
Quadrilateral	0
Number of edge elements	879
Number of vertex elements	72
Minimum element quality	0.262
Element volume ratio	0.001



5.4. Application Mode: PDE, Coefficient Form (c)

Application mode type: PDE, Coefficient Form

Application mode name: c

5.4.1. Application Mode Properties

Property	Value
Default element type	Lagrange - Quadratic
Wave extension	Off
Frame	Frame (ref)
Weak constraints	Off

5.4.2. Variables

Dependent variables: u, v, w, m, u_t, v_t, w_t, m_t

Shape functions: shlag(2,'u'), shlag(2,'v'), shlag(2,'w'), shlag(2,'m')

Interior boundaries active

5.4.3. Boundary Settings

Boundary	1-25, 28-41	26	27
y			

Type	Neumann boundary condition	Neumann boundary condition	Neumann boundary condition
(h)	{1,0,0,0;0,1,0,0;0,0,1,0;0,0,0,1}	{0,0,0,0;0,0,0,0;0,0,0,0;0,0,0,0}	{0,0,0,0;0,0,0,0;0,0,0,0;0,0,0,0}
(g)	{0;0;0;0}	{0;0;0;0}	{0;0;0;-C6*(m-Mua)*lv/Amu}

Pair	Pair 1, Pair 2
Type	Neumann boundary condition

5.4.4. Subdomain Settings

Subdomain	1-2
Time-dependent weak term (dweak)	{0;0;0;C5*(uxt+vyt+wzt)*test(m)}
Diffusion coefficient (c)	{{C1,0,0;0,C2,0,0;0,C2},{0,C3,0;0,0;0,0},{0,0,C3;0,0;0,0},0;{0,0,0;C3,0,0;0,0,0},{C2,0,0;0,C1,0;0,0,C2},{0,0,0;0,0,C3;0,0,0},0;{0,0,0;0,0,0;C3,0,0},{0,0,0;0,0,0;0,C3,0},{C2,0,0;0,C2,0;0,0,C1},0;0,0,0,{C6,0,0;0,C6,0,0,C6}}
Source term (f)	{0;0;0;0}
Damping/Mass coefficient (da)	{0,0,0,0;0,0,0,0;0,0,0,0;0,0,0,1}
Convection coefficient (be)	{{0;0;0},{0;0;0},{0;0;0},{C4;0;0};{0;0;0},{0;0;0},{0;0;0},{0;C4;0};{0;0;0},{0;0;0},{0;0;0},{0;0;0};{0;0;0},{0;0;0},{0;0;0},{0;0;0}}

Subdomain initial value	1-2
m	Mun

5.5. Application Mode: Solid, Stress-Strain (smsld2)

Application mode type: Solid, Stress-Strain (Structural Mechanics Module)

Application mode name: smsld2

5.5.1. Scalar Variables

Name	Variable	Value	Unit	Description
t_old_ini	t_old_ini_smsld2	-1	s	Initial condition previous time step (contact with dynamic friction)

refpntx	refpntx_smsld2	0	m	Reference point moment computation x coord.
refpnty	refpnty_smsld2	0	m	Reference point moment computation y coord.
refpntz	refpntz_smsld2	0	m	Reference point moment computation z coord.

5.5.2. Application Mode Properties

Property	Value
Default element type	Lagrange - Quadratic
Analysis type	Quasi-static transient
Large deformation	On
Specify eigenvalues using	Eigenfrequency
Create frame	On
Deform frame	Frame (deform)
Frame	Frame (ref)
Weak constraints	Off
Constraint type	Ideal

5.5.3. Variables

Dependent variables: u, v, w, p3

Shape functions: shlag(2,'u'), shlag(2,'v'), shlag(2,'w')

Interior boundaries active

5.5.4. Boundary Settings

Boundary		1-25, 27-28, 30-41	29	26
constrcond		Free	Fixed	Roller
Pair		Pair 1	Pair 2	
pn	Pa/m	E_smsld2/hmin_cp1_smsld2	E_smsld2/hmin_cp2_smsld2	
pt	Pa/m	E_smsld2/hmin_cp1_smsld2	E_smsld2/hmin_cp2_smsld2	
searchdist		Manual	Manual	
mandist	m	5e-5	5e-5	
contacttol		Manual	Manual	
mantol	m	1e-9	1e-9	
mustat	1	.1	.1	
Tni	Pa	10	10	

5.5.5. Subdomain Settings

Subdomain		1	2
Young's modulus (E)	Pa	2.0e11	10e9
Density (rho)	kg/m ³	7850	3000
Isotropic tangent modulus (ETiso)	Pa	2.0e10	2.0e11
Yield stress level (Sys)	Pa	2.0e8	1e5
Poisson's ratio (nu)	1	0.33	.3
constrcond		Fixed	Free

6. Solver Settings

Solve using a script: off

Auto select solver	On
Solver	Time dependent
Solution form	Automatic
Symmetric	auto
Adaptive mesh refinement	Off
Optimization/Sensitivity	Off
Plot while solving	On

6.1. Direct (UMFPACK)

Solver type: Linear system solver

Parameter	Value
Pivot threshold	0.1
Memory allocation factor	0.7

6.2. Time Stepping

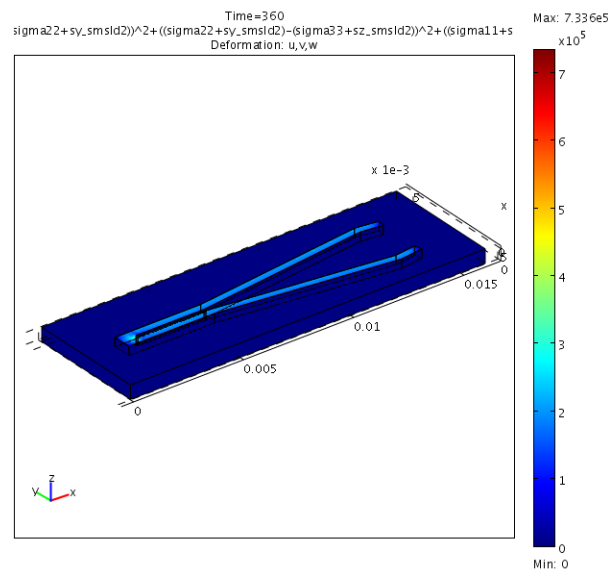
Parameter	Value
Times	range(0,500,3600)
Relative tolerance	0.01
Absolute tolerance	0.0010
Times to store in output	Time steps from solver
Time steps taken by solver	Free
Maximum BDF order	5
Singular mass matrix	Maybe
Consistent initialization of DAE systems	Backward Euler
Error estimation strategy	Include algebraic
Allow complex numbers	Off

6.3. Advanced

Parameter	Value
Constraint handling method	Elimination
Null-space function	Automatic
Automatic assembly block size	On
Assembly block size	1000
Use Hermitian transpose of constraint matrix and in symmetry detection	Off
Use complex functions with real input	Off
Stop if error due to undefined operation	On
Store solution on file	Off
Type of scaling	Automatic

Manual scaling	
Row equilibration	On
Manual control of reassembly	Off
Load constant	On
Constraint constant	On
Mass constant	On
Damping (mass) constant	On
Jacobian constant	On
Constraint Jacobian constant	On

7. Postprocessing



8. Variables

8.1. Point

Name	Description	Unit	Expression
RFx_smsld2	Reaction force x-dir.	N	reactf(u)
RFy_smsld2	Reaction force y-dir.	N	reactf(v)
RFz_smsld2	Reaction force z-dir.	N	reactf(w)
RMxpnt_smsld2	Reaction moment x-dir.	N*m	$(y+v-\text{refpnty_smsld2}) * \text{RFz_smsld2} - (z+w-\text{refpntz_smsld2}) * \text{RFy_smsld2}$
RMypnt_smsld2	Reaction moment y-dir.	N*m	$(z+w-\text{refpntz_smsld2}) * \text{RFx_smsld2} - (x+u-\text{refpntx_smsld2}) * \text{RFz_smsld2}$
RMzpnt_smsld2	Reaction moment z-dir.	N*m	$(x+u-\text{refpntx_smsld2}) * \text{RFy_smsld2} - (y+v-\text{refpnty_smsld2}) * \text{RFx_smsld2}$
Fxg_smsld2	Point load in global x dir.	N	0

Fyg_smsld2	Point load in global y dir.	N	0
Fzg_smsld2	Point load in global z dir.	N	0
disp_smsld2	Total displacement	m	$\sqrt{\text{real}(u)^2+\text{real}(v)^2+\text{real}(w)^2}$

8.2. Edge

Name	Description	Unit	Expression
RFx_smsld2	Reaction force x-dir.	N	reactf(u)
RFy_smsld2	Reaction force y-dir.	N	reactf(v)
RFz_smsld2	Reaction force z-dir.	N	reactf(w)
RMx_smsld2	Reaction moment x-dir.	N*m	$(y+v-\text{refpnty_smsld2}) * \text{RFz_smsld2} - (z+w-\text{refpntz_smsld2}) * \text{RFy_smsld2}$
RMy_smsld2	Reaction moment y-dir.	N*m	$(z+w-\text{refpntz_smsld2}) * \text{RFx_smsld2} - (x+u-\text{refpntx_smsld2}) * \text{RFz_smsld2}$
RMz_smsld2	Reaction moment z-dir.	N*m	$(x+u-\text{refpntx_smsld2}) * \text{RFy_smsld2} - (y+v-\text{refpnty_smsld2}) * \text{RFx_smsld2}$
Fxg_smsld2	Edge load in global x-dir.	N/m	0
Fyg_smsld2	Edge load in global y-dir.	N/m	0
Fzg_smsld2	Edge load in global z-dir.	N/m	0
disp_smsld2	Total displacement	m	$\sqrt{\text{real}(u)^2+\text{real}(v)^2+\text{real}(w)^2}$

8.3. Boundary

8.3.1. Boundary 1-5, 8, 21-23, 26-27

Name	Description	Unit	Expression
RFx_smsld2	Reaction force x-dir.	N	reactf(u)
RFy_smsld2	Reaction force y-dir.	N	reactf(v)
RFz_smsld2	Reaction force z-dir.	N	reactf(w)
RMx_smsld2	Reaction moment x-dir.	N*m	$(y+v-\text{refpnty_smsld2}) * \text{RFz_smsld2} - (z+w-\text{refpntz_smsld2}) * \text{RFy_smsld2}$
RMy_smsld2	Reaction moment y-dir.	N*m	$(z+w-\text{refpntz_smsld2}) * \text{RFx_smsld2} - (x+u-\text{refpntx_smsld2}) * \text{RFz_smsld2}$
RMz_smsld2	Reaction moment z-dir.	N*m	$(x+u-\text{refpntx_smsld2}) * \text{RFy_smsld2} - (y+v-\text{refpnty_smsld2}) * \text{RFx_smsld2}$
Fxg_smsld2	Face load in global x-dir.	N/m ²	0
Fyg_smsld2	Face load in global y-dir.	N/m ²	0

Fzg_smsld2	Face load in global z-dir.	N/m ²	0
disp_smsld2	Total displacement	m	$\sqrt{\text{real}(u)^2+\text{real}(v)^2+\text{real}(w)^2}$
Tax_smsld2	Surface traction (force/area) in x dir.	Pa	$(F11_smsld2 * Sx_smsld2+F12_smsld2 * Sxy_smsld2+F13_smsld2 * Sxz_smsld2) * nx_smsld2+(F11_smsld2 * Sxy_smsld2+F12_smsld2 * Sy_smsld2+F13_smsld2 * Syz_smsld2) * ny_smsld2+(F11_smsld2 * Sxz_smsld2+F12_smsld2 * Syz_smsld2+F13_smsld2 * Sz_smsld2) * nz_smsld2$
Tay_smsld2	Surface traction (force/area) in y dir.	Pa	$(F21_smsld2 * Sx_smsld2+F22_smsld2 * Sxy_smsld2+F23_smsld2 * Sxz_smsld2) * nx_smsld2+(F21_smsld2 * Sxy_smsld2+F22_smsld2 * Sy_smsld2+F23_smsld2 * Syz_smsld2) * ny_smsld2+(F21_smsld2 * Sxz_smsld2+F22_smsld2 * Syz_smsld2+F23_smsld2 * Sz_smsld2) * nz_smsld2$
Taz_smsld2	Surface traction (force/area) in z dir.	Pa	$(F31_smsld2 * Sx_smsld2+F32_smsld2 * Sxy_smsld2+F33_smsld2 * Sxz_smsld2) * nx_smsld2+(F31_smsld2 * Sxy_smsld2+F32_smsld2 * Sy_smsld2+F33_smsld2 * Syz_smsld2) * ny_smsld2+(F31_smsld2 * Sxz_smsld2+F32_smsld2 * Syz_smsld2+F33_smsld2 * Sz_smsld2) * nz_smsld2$

8.3.2. Boundary 6-7, 9-17, 20

Name	Description	Unit	Expression
RFx_smsld2	Reaction force x-dir.	N	reactf(u)
RFy_smsld2	Reaction force y-dir.	N	reactf(v)
RFz_smsld2	Reaction force z-dir.	N	reactf(w)
RMx_smsld2	Reaction moment x-dir.	N*m	$(y+v-\text{refpnty_smsld2}) * RFz_smsld2-(z+w-\text{refpntz_smsld2}) * RFy_smsld2$
RMy_smsld2	Reaction moment y-dir.	N*m	$(z+w-\text{refpntz_smsld2}) * RFx_smsld2-(x+u-\text{refpntx_smsld2}) * RFz_smsld2$
RMz_smsld2	Reaction moment z-dir.	N*m	$(x+u-\text{refpntx_smsld2}) * RFy_smsld2-(y+v-\text{refpnty_smsld2}) * RFx_smsld2$
Fxg_smsld2	Face load in global x-dir.	N/m ²	0
Fyg_smsld2	Face load in global y-dir.	N/m ²	0
Fzg_smsld2	Face load in global z-dir.	N/m ²	0
disp_smsld2	Total displacement	m	$\sqrt{\text{real}(u)^2+\text{real}(v)^2+\text{real}(w)^2}$
gap_cp1_smsld2	Gap distance, contact Pair 1	m	geomgap_mst_cp1

Tnp_cp1_smsld2	Penalized contact pressure, contact Pair 1	Pa	0
Ttcrit_cp1_smsld2	Critical friction force, contact Pair 1	Pa	0
friction_cp1_smsld2	Enabling friction variable, contact Pair 1	1	0
contact_cp1	Contact variable, contact Pair 1	1	(geomgap_mst_cp1
wcn_cp1_smsld2	Contact help variable, contact Pair 1	Pa	0
slip_cp1_smsld2	Slip vector ref. frame, contact Pair 1	m	0
slipd_cp1_smsld2	Slip vector deform frame, contact Pair 1	m	0
vslip_cp1_smsld2	Slip velocity vector deform frame, contact Pair 1	m/s	0
Tttrial_cp1_smsld2	Trial friction force, contact Pair 1	Pa	0
mu_cp1_smsld2	Frictional coefficient, contact Pair 1	1	0
Tttrialx_cp1_smsld2	Trial friction force x dir., contact Pair 1	Pa	0
Ttpx_cp1_smsld2	Penalized friction force x dir., contact Pair 1	Pa	0
wctx_cp1_smsld2	Friction help variable x dir., contact Pair 1	Pa	0
slipx_cp1_smsld2	Slip vector ref. frame x dir., contact Pair 1	m	0
slipdx2_cp1_smsld2	Slip vector deform frame x2 dir., contact Pair 1	m	0
vslipx2_cp1_smsld2	Slip velocity	m/s	0

	vector deform frame x dir., contact Pair 1		
Ttrialy_cp1_smsld2	Trial friction force y dir., contact Pair 1	Pa	0
Ttpy_cp1_smsld2	Penalized friction force y dir., contact Pair 1	Pa	0
wcty_cp1_smsld2	Friction help variable y dir., contact Pair 1	Pa	0
slipy_cp1_smsld2	Slip vector ref. frame y dir., contact Pair 1	m	0
slipy2_cp1_smsld2	Slip vector deform frame y2 dir., contact Pair 1	m	0
vslipy2_cp1_smsld2	Slip velocity vector deform frame x dir., contact Pair 1	m/s	0
Ttrialz_cp1_smsld2	Trial friction force z dir., contact Pair 1	Pa	0
Ttpz_cp1_smsld2	Penalized friction force z dir., contact Pair 1	Pa	0
wctz_cp1_smsld2	Friction help variable z dir., contact Pair 1	Pa	0
slipz_cp1_smsld2	Slip vector ref. frame z dir., contact Pair 1	m	0
slipdz2_cp1_smsld2	Slip vector deform frame z2 dir., contact Pair 1	m	0
vslipz2_cp1_smsld2	Slip velocity vector deform frame x dir., contact Pair 1	m/s	0
offset_cp1_smsld2	Contact surface offset, contact Pair 1	m	0

pn_cp1_smsld2	Contact normal penalty factor, contact Pair 1	Pa	E_smsld2/hmin_cp1_smsld2
pt_cp1_smsld2	Contact tangential penalty factor, contact Pair 1	Pa	0
mustat_cp1_smsld2	Static friction coefficient, contact Pair 1	1	0
cohe_cp1_smsld2	Cohesion sliding resistance, contact Pair 1	Pa	0
Ttmax_cp1_smsld2	Maximum tangential traction, contact Pair 1	Pa	0
mudyn_cp1_smsld2	Dynamic friction coefficient, contact Pair 1	1	0
dcfric_cp1_smsld2	Exponential decay coefficient, contact Pair 1	s/m	0
mantol_cp1_smsld2	Absolute tolerance, contact Pair 1	m	1e-09
mandist_cp1_smsld2	Absolute search distance, contact Pair 1	m	5e-05
gap_cp2_smsld2	Gap distance, contact Pair 2	m	0
Tnp_cp2_smsld2	Penalized contact pressure, contact Pair 2	Pa	0
Tcrit_cp2_smsld2	Critical friction force, contact Pair 2	Pa	0
friction_cp2_smsld2	Enabling friction variable, contact Pair 2	1	0
contact_cp2	Contact variable, contact Pair 2	1	0
wcn_cp2_smsld2	Contact help variable, contact Pair 2	Pa	0
slip_cp2_smsld2	Slip vector ref. frame, contact	m	0

	Pair 2		
slipd_cp2_smsld2	Slip vector deform frame, contact Pair 2	m	0
vslip_cp2_smsld2	Slip velocity vector deform frame, contact Pair 2	m/s	0
Ttrial_cp2_smsld2	Trial friction force, contact Pair 2	Pa	0
mu_cp2_smsld2	Frictional coefficient, contact Pair 2	1	0
Ttrialx_cp2_smsld2	Trial friction force x dir., contact Pair 2	Pa	0
Ttpx_cp2_smsld2	Penalized friction force x dir., contact Pair 2	Pa	0
wctx_cp2_smsld2	Friction help variable x dir., contact Pair 2	Pa	0
slipx_cp2_smsld2	Slip vector ref. frame x dir., contact Pair 2	m	0
slipdx2_cp2_smsld2	Slip vector deform frame x2 dir., contact Pair 2	m	0
vslipx2_cp2_smsld2	Slip velocity vector deform frame x dir., contact Pair 2	m/s	0
Ttrialy_cp2_smsld2	Trial friction force y dir., contact Pair 2	Pa	0
Ttpy_cp2_smsld2	Penalized friction force y dir., contact Pair 2	Pa	0
wcty_cp2_smsld2	Friction help variable y dir., contact Pair 2	Pa	0
slipy_cp2_smsld2	Slip vector ref. frame y dir., contact Pair 2	m	0

slipdy2_cp2_smsld2	Slip vector deform frame y2 dir., contact Pair 2	m	0
vslipy2_cp2_smsld2	Slip velocity vector deform frame x dir., contact Pair 2	m/s	0
Tttrialz_cp2_smsld2	Trial friction force z dir., contact Pair 2	Pa	0
Ttpz_cp2_smsld2	Penalized friction force z dir., contact Pair 2	Pa	0
wctz_cp2_smsld2	Friction help variable z dir., contact Pair 2	Pa	0
slipz_cp2_smsld2	Slip vector ref. frame z dir., contact Pair 2	m	0
slipdz2_cp2_smsld2	Slip vector deform frame z2 dir., contact Pair 2	m	0
vslipz2_cp2_smsld2	Slip velocity vector deform frame x dir., contact Pair 2	m/s	0
offset_cp2_smsld2	Contact surface offset, contact Pair 2	m	0
pn_cp2_smsld2	Contact normal penalty factor, contact Pair 2	Pa	0
pt_cp2_smsld2	Contact tangential penalty factor, contact Pair 2	Pa	0
mustat_cp2_smsld2	Static friction coefficient, contact Pair 2	1	0
cohe_cp2_smsld2	Cohesion sliding resistance, contact Pair 2	Pa	0
Ttmax_cp2_smsld2	Maximum tangential traction, contact	Pa	0

	Pair 2		
mudyn_cp2_smsld2	Dynamic friction coefficient, contact Pair 2	1	0
dcfric_cp2_smsld2	Exponential decay coefficient, contact Pair 2	s/m	0
mantol_cp2_smsld2	Absolute tolerance, contact Pair 2	m	0
mandist_cp2_smsld2	Absolute search distance, contact Pair 2	m	0
Ft11_smsld2	Deformation gradient projected on tangent plane 11 comp.	1	1+uTx
Ft12_smsld2	Deformation gradient projected on tangent plane 12 comp.	1	uTy
Ft13_smsld2	Deformation gradient projected on tangent plane 13 comp.	1	uTz
Ft21_smsld2	Deformation gradient projected on tangent plane 21 comp.	1	vTx
Ft22_smsld2	Deformation gradient projected on tangent plane 22 comp.	1	1+vTy
Ft23_smsld2	Deformation gradient projected on tangent plane 23 comp.	1	vTz
Ft31_smsld2	Deformation gradient projected on tangent plane 31 comp.	1	wTx

Ft32_smsld2	Deformation gradient projected on tangent plane 32 comp.	1	wTy
Ft33_smsld2	Deformation gradient projected on tangent plane 33 comp.	1	1+wTz
Tax_smsld2	Surface traction (force/area) in x dir.	Pa	$(F11_smsld2 * Sx_smsld2 + F12_smsld2 * Sxy_smsld2 + F13_smsld2 * Sxz_smsld2) * nx_smsld2 + (F11_smsld2 * Sxy_smsld2 + F12_smsld2 * Sy_smsld2 + F13_smsld2 * Syz_smsld2) * ny_smsld2 + (F11_smsld2 * Sxz_smsld2 + F12_smsld2 * Syz_smsld2 + F13_smsld2 * Sz_smsld2) * nz_smsld2$
Tay_smsld2	Surface traction (force/area) in y dir.	Pa	$(F21_smsld2 * Sx_smsld2 + F22_smsld2 * Sxy_smsld2 + F23_smsld2 * Sxz_smsld2) * nx_smsld2 + (F21_smsld2 * Sxy_smsld2 + F22_smsld2 * Sy_smsld2 + F23_smsld2 * Syz_smsld2) * ny_smsld2 + (F21_smsld2 * Sxz_smsld2 + F22_smsld2 * Syz_smsld2 + F23_smsld2 * Sz_smsld2) * nz_smsld2$
Taz_smsld2	Surface traction (force/area) in z dir.	Pa	$(F31_smsld2 * Sx_smsld2 + F32_smsld2 * Sxy_smsld2 + F33_smsld2 * Sxz_smsld2) * nx_smsld2 + (F31_smsld2 * Sxy_smsld2 + F32_smsld2 * Sy_smsld2 + F33_smsld2 * Syz_smsld2) * ny_smsld2 + (F31_smsld2 * Sxz_smsld2 + F32_smsld2 * Syz_smsld2 + F33_smsld2 * Sz_smsld2) * nz_smsld2$

8.3.3. Boundary 18-19

Name	Description	Unit	Expression
RFx_smsld2	Reaction force x-dir.	N	reactf(u)
RFy_smsld2	Reaction force y-dir.	N	reactf(v)
RFz_smsld2	Reaction force z-dir.	N	reactf(w)
RMx_smsld2	Reaction moment x-dir.	N*m	$(y+v-refpnty_smsld2) * RFz_smsld2 - (z+w-refpntz_smsld2) * RFy_smsld2$
RMy_smsld2	Reaction moment y-dir.	N*m	$(z+w-refpntz_smsld2) * RFx_smsld2 - (x+u-refpntx_smsld2) * RFz_smsld2$
RMz_smsld2	Reaction moment z-dir.	N*m	$(x+u-refpntx_smsld2) * RFy_smsld2 - (y+v-refpnty_smsld2) * RFx_smsld2$
Fxg_smsld2	Face load in global x-dir.	N/m ²	0
Fyg_smsld2	Face load in global y-dir.	N/m ²	0
Fzg_smsld2	Face load in	N/m ²	0

	global z-dir.		
disp_smsld2	Total displacement	m	$\sqrt{\text{real}(u)^2 + \text{real}(v)^2 + \text{real}(w)^2}$
gap_cp1_smsld2	Gap distance, contact Pair 1	m	0
Tnp_cp1_smsld2	Penalized contact pressure, contact Pair 1	Pa	0
Ttcrit_cp1_smsld2	Critical friction force, contact Pair 1	Pa	0
friction_cp1_smsld2	Enabling friction variable, contact Pair 1	1	0
contact_cp1	Contact variable, contact Pair 1	1	0
wcn_cp1_smsld2	Contact help variable, contact Pair 1	Pa	0
slip_cp1_smsld2	Slip vector ref. frame, contact Pair 1	m	0
slipd_cp1_smsld2	Slip vector deform frame, contact Pair 1	m	0
vslip_cp1_smsld2	Slip velocity vector deform frame, contact Pair 1	m/s	0
Tttrial_cp1_smsld2	Trial friction force, contact Pair 1	Pa	0
mu_cp1_smsld2	Frictional coefficient, contact Pair 1	1	0
Tttrialx_cp1_smsld2	Trial friction force x dir., contact Pair 1	Pa	0
Ttpx_cp1_smsld2	Penalized friction force x dir., contact Pair 1	Pa	0
wctx_cp1_smsld2	Friction help variable x dir., contact Pair 1	Pa	0
slipx_cp1_smsld2	Slip vector ref. frame x dir.,	m	0

	contact Pair 1		
slipdx2_cp1_smsld2	Slip vector deform frame x2 dir., contact Pair 1	m	0
vslipx2_cp1_smsld2	Slip velocity vector deform frame x dir., contact Pair 1	m/s	0
Tttrialy_cp1_smsld2	Trial friction force y dir., contact Pair 1	Pa	0
Ttpy_cp1_smsld2	Penalized friction force y dir., contact Pair 1	Pa	0
wcty_cp1_smsld2	Friction help variable y dir., contact Pair 1	Pa	0
slipy_cp1_smsld2	Slip vector ref. frame y dir., contact Pair 1	m	0
slipdy2_cp1_smsld2	Slip vector deform frame y2 dir., contact Pair 1	m	0
vslipy2_cp1_smsld2	Slip velocity vector deform frame x dir., contact Pair 1	m/s	0
Tttrialz_cp1_smsld2	Trial friction force z dir., contact Pair 1	Pa	0
Ttpz_cp1_smsld2	Penalized friction force z dir., contact Pair 1	Pa	0
wctz_cp1_smsld2	Friction help variable z dir., contact Pair 1	Pa	0
slipz_cp1_smsld2	Slip vector ref. frame z dir., contact Pair 1	m	0
slipdz2_cp1_smsld2	Slip vector deform frame z2 dir., contact Pair 1	m	0
vslipz2_cp1_smsld2	Slip velocity	m/s	0

	vector deform frame x dir., contact Pair 1		
offset_cp1_smsld2	Contact surface offset, contact Pair 1	m	0
pn_cp1_smsld2	Contact normal penalty factor, contact Pair 1	Pa	0
pt_cp1_smsld2	Contact tangential penalty factor, contact Pair 1	Pa	0
mustat_cp1_smsld2	Static friction coefficient, contact Pair 1	1	0
cohe_cp1_smsld2	Cohesion sliding resistance, contact Pair 1	Pa	0
Ttmax_cp1_smsld2	Maximum tangential traction, contact Pair 1	Pa	0
mudyn_cp1_smsld2	Dynamic friction coefficient, contact Pair 1	1	0
dcfric_cp1_smsld2	Exponential decay coefficient, contact Pair 1	s/m	0
mantol_cp1_smsld2	Absolute tolerance, contact Pair 1	m	0
mandist_cp1_smsld2	Absolute search distance, contact Pair 1	m	0
gap_cp2_smsld2	Gap distance, contact Pair 2	m	geomgap_mst_cp2
Tnp_cp2_smsld2	Penalized contact pressure, contact Pair 2	Pa	0
Tcrit_cp2_smsld2	Critical friction force, contact Pair 2	Pa	0
friction_cp2_smsld2	Enabling friction variable, contact Pair 2	1	0
contact_cp2	Contact variable,	1	(geomgap_mst_cp2

	contact Pair 2		
wcn_cp2_smsld2	Contact help variable, contact Pair 2	Pa	0
slip_cp2_smsld2	Slip vector ref. frame, contact Pair 2	m	0
slipd_cp2_smsld2	Slip vector deform frame, contact Pair 2	m	0
vslip_cp2_smsld2	Slip velocity vector deform frame, contact Pair 2	m/s	0
Tttrial_cp2_smsld2	Trial friction force, contact Pair 2	Pa	0
mu_cp2_smsld2	Frictional coefficient, contact Pair 2	1	0
Tttrialx_cp2_smsld2	Trial friction force x dir., contact Pair 2	Pa	0
Ttpx_cp2_smsld2	Penalized friction force x dir., contact Pair 2	Pa	0
wctx_cp2_smsld2	Friction help variable x dir., contact Pair 2	Pa	0
slipx_cp2_smsld2	Slip vector ref. frame x dir., contact Pair 2	m	0
slipdx2_cp2_smsld2	Slip vector deform frame x2 dir., contact Pair 2	m	0
vslipx2_cp2_smsld2	Slip velocity vector deform frame x dir., contact Pair 2	m/s	0
Tttrialy_cp2_smsld2	Trial friction force y dir., contact Pair 2	Pa	0
Ttpy_cp2_smsld2	Penalized friction force y dir., contact Pair 2	Pa	0

wcty_cp2_smsld2	Friction help variable y dir., contact Pair 2	Pa	0
slipy_cp2_smsld2	Slip vector ref. frame y dir., contact Pair 2	m	0
slipdy2_cp2_smsld2	Slip vector deform frame y2 dir., contact Pair 2	m	0
vslipy2_cp2_smsld2	Slip velocity vector deform frame x dir., contact Pair 2	m/s	0
Tttrialz_cp2_smsld2	Trial friction force z dir., contact Pair 2	Pa	0
Ttpz_cp2_smsld2	Penalized friction force z dir., contact Pair 2	Pa	0
wctz_cp2_smsld2	Friction help variable z dir., contact Pair 2	Pa	0
slipz_cp2_smsld2	Slip vector ref. frame z dir., contact Pair 2	m	0
slipdz2_cp2_smsld2	Slip vector deform frame z2 dir., contact Pair 2	m	0
vslipz2_cp2_smsld2	Slip velocity vector deform frame x dir., contact Pair 2	m/s	0
offset_cp2_smsld2	Contact surface offset, contact Pair 2	m	0
pn_cp2_smsld2	Contact normal penalty factor, contact Pair 2	Pa	$E_smsld2/hmin_cp2_smsld2$
pt_cp2_smsld2	Contact tangential penalty factor, contact Pair 2	Pa	0
mustat_cp2_smsld2	Static friction coefficient, contact Pair 2	1	0

cohe_cp2_smsld2	Cohesion sliding resistance, contact Pair 2	Pa	0
Ttmax_cp2_smsld2	Maximum tangential traction, contact Pair 2	Pa	0
mudyn_cp2_smsld2	Dynamic friction coefficient, contact Pair 2	1	0
dcfric_cp2_smsld2	Exponential decay coefficient, contact Pair 2	s/m	0
mantol_cp2_smsld2	Absolute tolerance, contact Pair 2	m	1e-09
mandist_cp2_smsld2	Absolute search distance, contact Pair 2	m	5e-05
Ft11_smsld2	Deformation gradient projected on tangent plane 11 comp.	1	1+uTx
Ft12_smsld2	Deformation gradient projected on tangent plane 12 comp.	1	uTy
Ft13_smsld2	Deformation gradient projected on tangent plane 13 comp.	1	uTz
Ft21_smsld2	Deformation gradient projected on tangent plane 21 comp.	1	vTx
Ft22_smsld2	Deformation gradient projected on tangent plane 22 comp.	1	1+vTy
Ft23_smsld2	Deformation gradient projected on tangent plane 23	1	vTz

	comp.		
Ft31_smsld2	Deformation gradient projected on tangent plane 31 comp.	1	wTx
Ft32_smsld2	Deformation gradient projected on tangent plane 32 comp.	1	wTy
Ft33_smsld2	Deformation gradient projected on tangent plane 33 comp.	1	1+wTz
Tax_smsld2	Surface traction (force/area) in x dir.	Pa	$(F11_smsld2 * Sx_smsld2 + F12_smsld2 * Sxy_smsld2 + F13_smsld2 * Sxz_smsld2) * nx_smsld2 + (F11_smsld2 * Sxy_smsld2 + F12_smsld2 * Sy_smsld2 + F13_smsld2 * Syz_smsld2) * ny_smsld2 + (F11_smsld2 * Sxz_smsld2 + F12_smsld2 * Syz_smsld2 + F13_smsld2 * Sz_smsld2) * nz_smsld2$
Tay_smsld2	Surface traction (force/area) in y dir.	Pa	$(F21_smsld2 * Sx_smsld2 + F22_smsld2 * Sxy_smsld2 + F23_smsld2 * Sxz_smsld2) * nx_smsld2 + (F21_smsld2 * Sxy_smsld2 + F22_smsld2 * Sy_smsld2 + F23_smsld2 * Syz_smsld2) * ny_smsld2 + (F21_smsld2 * Sxz_smsld2 + F22_smsld2 * Syz_smsld2 + F23_smsld2 * Sz_smsld2) * nz_smsld2$
Taz_smsld2	Surface traction (force/area) in z dir.	Pa	$(F31_smsld2 * Sx_smsld2 + F32_smsld2 * Sxy_smsld2 + F33_smsld2 * Sxz_smsld2) * nx_smsld2 + (F31_smsld2 * Sxy_smsld2 + F32_smsld2 * Sy_smsld2 + F33_smsld2 * Syz_smsld2) * ny_smsld2 + (F31_smsld2 * Sxz_smsld2 + F32_smsld2 * Syz_smsld2 + F33_smsld2 * Sz_smsld2) * nz_smsld2$

8.3.4. Boundary 24-25, 28-36, 39-41

Name	Description	Unit	Expression
RFx_smsld2	Reaction force x-dir.	N	reacf(u)
RFy_smsld2	Reaction force y-dir.	N	reacf(v)
RFz_smsld2	Reaction force z-dir.	N	reacf(w)
RMx_smsld2	Reaction moment x-dir.	N*m	$(y+v-refpnty_smsld2) * RFz_smsld2 - (z+w-refpntz_smsld2) * RFy_smsld2$
RMy_smsld2	Reaction moment y-dir.	N*m	$(z+w-refpntz_smsld2) * RFx_smsld2 - (x+u-refpntx_smsld2) * RFz_smsld2$
RMz_smsld2	Reaction moment z-dir.	N*m	$(x+u-refpntx_smsld2) * RFy_smsld2 - (y+v-refpnty_smsld2) * RFx_smsld2$

Fxg_smsld2	Face load in global x-dir.	N/m ²	0
Fyg_smsld2	Face load in global y-dir.	N/m ²	0
Fzg_smsld2	Face load in global z-dir.	N/m ²	0
disp_smsld2	Total displacement	m	$\sqrt{\text{real}(u)^2 + \text{real}(v)^2 + \text{real}(w)^2}$
gap_cp1_smsld2	Gap distance, contact Pair 1	m	geomgap_slv_cp1
Tnp_cp1_smsld2	Penalized contact pressure, contact Pair 1	Pa	$\max(\text{if}(\text{gap_cp1_smsld2} \leq 0, \text{Tn_cp1_smsld2} - \text{pn_cp1_smsld2} * \text{gap_cp1_smsld2}, \text{Tn_cp1_smsld2} * \exp(-\text{pn_cp1_smsld2} * \text{gap_cp1_smsld2} / \max(\text{Tn_cp1_smsld2}, 1e-10))), 0)$
Ttcrit_cp1_smsld2	Critical friction force, contact Pair 1	Pa	0
friction_cp1_smsld2	Enabling friction variable, contact Pair 1	1	0
contact_cp1	Contact variable, contact Pair 1	1	(geomgap_slv_cp1
wcn_cp1_smsld2	Contact help variable, contact Pair 1	Pa	$\text{nojac}(\text{Tnp_cp1_smsld2}) - \text{Tn_cp1_smsld2}$
slip_cp1_smsld2	Slip vector ref. frame, contact Pair 1	m	0
slipd_cp1_smsld2	Slip vector deform frame, contact Pair 1	m	0
vslip_cp1_smsld2	Slip velocity vector deform frame, contact Pair 1	m/s	0
Tttrial_cp1_smsld2	Trial friction force, contact Pair 1	Pa	0
mu_cp1_smsld2	Frictional coefficient, contact Pair 1	1	mustat_cp1_smsld2
Tttrialx_cp1_smsld2	Trial friction force x dir., contact Pair 1	Pa	0
Ttpx_cp1_smsld2	Penalized	Pa	0

	friction force x dir., contact Pair 1		
wctx_cp1_smsld2	Friction help variable x dir., contact Pair 1	Pa	0
slipx_cp1_smsld2	Slip vector ref. frame x dir., contact Pair 1	m	0
slipdx2_cp1_smsld2	Slip vector deform frame x2 dir., contact Pair 1	m	0
vslipx2_cp1_smsld2	Slip velocity vector deform frame x dir., contact Pair 1	m/s	0
Tttrialy_cp1_smsld2	Trial friction force y dir., contact Pair 1	Pa	0
Ttpy_cp1_smsld2	Penalized friction force y dir., contact Pair 1	Pa	0
wcty_cp1_smsld2	Friction help variable y dir., contact Pair 1	Pa	0
slipy_cp1_smsld2	Slip vector ref. frame y dir., contact Pair 1	m	0
slipy2_cp1_smsld2	Slip vector deform frame y2 dir., contact Pair 1	m	0
vslipy2_cp1_smsld2	Slip velocity vector deform frame x dir., contact Pair 1	m/s	0
Tttrialz_cp1_smsld2	Trial friction force z dir., contact Pair 1	Pa	0
Ttpz_cp1_smsld2	Penalized friction force z dir., contact Pair 1	Pa	0
wctz_cp1_smsld2	Friction help variable z dir., contact Pair 1	Pa	0

slipz_cp1_smsld2	Slip vector ref. frame z dir., contact Pair 1	m	0
slipdz2_cp1_smsld2	Slip vector deform frame z2 dir., contact Pair 1	m	0
vslipz2_cp1_smsld2	Slip velocity vector deform frame x dir., contact Pair 1	m/s	0
offset_cp1_smsld2	Contact surface offset, contact Pair 1	m	0
pn_cp1_smsld2	Contact normal penalty factor, contact Pair 1	Pa	$E_smsld2/hmin_cp1_smsld2$
pt_cp1_smsld2	Contact tangential penalty factor, contact Pair 1	Pa	0
mustat_cp1_smsld2	Static friction coefficient, contact Pair 1	1	0
cohe_cp1_smsld2	Cohesion sliding resistance, contact Pair 1	Pa	0
Ttmax_cp1_smsld2	Maximum tangential traction, contact Pair 1	Pa	0
mudyn_cp1_smsld2	Dynamic friction coefficient, contact Pair 1	1	0
dcfric_cp1_smsld2	Exponential decay coefficient, contact Pair 1	s/m	0
mantol_cp1_smsld2	Absolute tolerance, contact Pair 1	m	1e-09
mandist_cp1_smsld2	Absolute search distance, contact Pair 1	m	5e-05
gap_cp2_smsld2	Gap distance, contact Pair 2	m	0

Tnp_cp2_smsld2	Penalized contact pressure, contact Pair 2	Pa	0
Ttcrit_cp2_smsld2	Critical friction force, contact Pair 2	Pa	0
friction_cp2_smsld2	Enabling friction variable, contact Pair 2	1	0
contact_cp2	Contact variable, contact Pair 2	1	0
wcn_cp2_smsld2	Contact help variable, contact Pair 2	Pa	0
slip_cp2_smsld2	Slip vector ref. frame, contact Pair 2	m	0
slipd_cp2_smsld2	Slip vector deform frame, contact Pair 2	m	0
vslip_cp2_smsld2	Slip velocity vector deform frame, contact Pair 2	m/s	0
Tttrial_cp2_smsld2	Trial friction force, contact Pair 2	Pa	0
mu_cp2_smsld2	Frictional coefficient, contact Pair 2	1	0
Tttrialx_cp2_smsld2	Trial friction force x dir., contact Pair 2	Pa	0
Ttpx_cp2_smsld2	Penalized friction force x dir., contact Pair 2	Pa	0
wctx_cp2_smsld2	Friction help variable x dir., contact Pair 2	Pa	0
slipx_cp2_smsld2	Slip vector ref. frame x dir., contact Pair 2	m	0
slipdx2_cp2_smsld2	Slip vector deform frame	m	0

	x2 dir., contact Pair 2		
vslipx2_cp2_smsld2	Slip velocity vector deform frame x dir., contact Pair 2	m/s	0
Tttrialy_cp2_smsld2	Trial friction force y dir., contact Pair 2	Pa	0
Ttpy_cp2_smsld2	Penalized friction force y dir., contact Pair 2	Pa	0
wcty_cp2_smsld2	Friction help variable y dir., contact Pair 2	Pa	0
slipy_cp2_smsld2	Slip vector ref. frame y dir., contact Pair 2	m	0
slipdy2_cp2_smsld2	Slip vector deform frame y2 dir., contact Pair 2	m	0
vslipy2_cp2_smsld2	Slip velocity vector deform frame x dir., contact Pair 2	m/s	0
Tttrialz_cp2_smsld2	Trial friction force z dir., contact Pair 2	Pa	0
Ttpz_cp2_smsld2	Penalized friction force z dir., contact Pair 2	Pa	0
wctz_cp2_smsld2	Friction help variable z dir., contact Pair 2	Pa	0
slipz_cp2_smsld2	Slip vector ref. frame z dir., contact Pair 2	m	0
slipdz2_cp2_smsld2	Slip vector deform frame z2 dir., contact Pair 2	m	0
vslipz2_cp2_smsld2	Slip velocity vector deform frame x dir., contact Pair 2	m/s	0

offset_cp2_smsld2	Contact surface offset, contact Pair 2	m	0
pn_cp2_smsld2	Contact normal penalty factor, contact Pair 2	Pa	0
pt_cp2_smsld2	Contact tangential penalty factor, contact Pair 2	Pa	0
mustat_cp2_smsld2	Static friction coefficient, contact Pair 2	1	0
cohe_cp2_smsld2	Cohesion sliding resistance, contact Pair 2	Pa	0
Ttmax_cp2_smsld2	Maximum tangential traction, contact Pair 2	Pa	0
mudyn_cp2_smsld2	Dynamic friction coefficient, contact Pair 2	1	0
defric_cp2_smsld2	Exponential decay coefficient, contact Pair 2	s/m	0
mantol_cp2_smsld2	Absolute tolerance, contact Pair 2	m	0
mandist_cp2_smsld2	Absolute search distance, contact Pair 2	m	0
Ft11_smsld2	Deformation gradient projected on tangent plane 11 comp.	1	1+uTx
Ft12_smsld2	Deformation gradient projected on tangent plane 12 comp.	1	uTy
Ft13_smsld2	Deformation gradient projected on tangent plane	1	uTz

	13 comp.		
Ft21_smsld2	Deformation gradient projected on tangent plane 21 comp.	1	vTx
Ft22_smsld2	Deformation gradient projected on tangent plane 22 comp.	1	1+vTy
Ft23_smsld2	Deformation gradient projected on tangent plane 23 comp.	1	vTz
Ft31_smsld2	Deformation gradient projected on tangent plane 31 comp.	1	wTx
Ft32_smsld2	Deformation gradient projected on tangent plane 32 comp.	1	wTy
Ft33_smsld2	Deformation gradient projected on tangent plane 33 comp.	1	1+wTz
Tax_smsld2	Surface traction (force/area) in x dir.	Pa	$(F11_smsld2 * Sx_smsld2 + F12_smsld2 * Sxy_smsld2 + F13_smsld2 * Sxz_smsld2) * nx_smsld2 + (F11_smsld2 * Sxy_smsld2 + F12_smsld2 * Sy_smsld2 + F13_smsld2 * Syz_smsld2) * ny_smsld2 + (F11_smsld2 * Sxz_smsld2 + F12_smsld2 * Syz_smsld2 + F13_smsld2 * Sz_smsld2) * nz_smsld2$
Tay_smsld2	Surface traction (force/area) in y dir.	Pa	$(F21_smsld2 * Sx_smsld2 + F22_smsld2 * Sxy_smsld2 + F23_smsld2 * Sxz_smsld2) * nx_smsld2 + (F21_smsld2 * Sxy_smsld2 + F22_smsld2 * Sy_smsld2 + F23_smsld2 * Syz_smsld2) * ny_smsld2 + (F21_smsld2 * Sxz_smsld2 + F22_smsld2 * Syz_smsld2 + F23_smsld2 * Sz_smsld2) * nz_smsld2$
Taz_smsld2	Surface traction (force/area) in z dir.	Pa	$(F31_smsld2 * Sx_smsld2 + F32_smsld2 * Sxy_smsld2 + F33_smsld2 * Sxz_smsld2) * nx_smsld2 + (F31_smsld2 * Sxy_smsld2 + F32_smsld2 * Sy_smsld2 + F33_smsld2 * Syz_smsld2) * ny_smsld2 + (F31_smsld2 * Sxz_smsld2 + F32_smsld2 * Syz_smsld2 + F33_smsld2 * Sz_smsld2) * nz_smsld2$

8.3.5. Boundary 37-38

Name	Description	Unit	Expression
RFx_smsld2	Reaction force x-dir.	N	reactf(u)
RFy_smsld2	Reaction force y-dir.	N	reactf(v)
RFz_smsld2	Reaction force z-dir.	N	reactf(w)
RMx_smsld2	Reaction moment x-dir.	N*m	(y+v-refpnty_smsld2) * RFz_smsld2-(z+w-refpntz_smsld2) * RFy_smsld2
RMy_smsld2	Reaction moment y-dir.	N*m	(z+w-refpntz_smsld2) * RFx_smsld2-(x+u-refpntx_smsld2) * RFz_smsld2
RMz_smsld2	Reaction moment z-dir.	N*m	(x+u-refpntx_smsld2) * RFy_smsld2-(y+v-refpnty_smsld2) * RFx_smsld2
Fxg_smsld2	Face load in global x-dir.	N/m ²	0
Fyg_smsld2	Face load in global y-dir.	N/m ²	0
Fzg_smsld2	Face load in global z-dir.	N/m ²	0
disp_smsld2	Total displacement	m	sqrt(real(u)^2+real(v)^2+real(w)^2)
gap_cp1_smsld2	Gap distance, contact Pair 1	m	0
Tnp_cp1_smsld2	Penalized contact pressure, contact Pair 1	Pa	0
Ttcrit_cp1_smsld2	Critical friction force, contact Pair 1	Pa	0
friction_cp1_smsld2	Enabling friction variable, contact Pair 1	1	0
contact_cp1	Contact variable, contact Pair 1	1	0
wcn_cp1_smsld2	Contact help variable, contact Pair 1	Pa	0
slip_cp1_smsld2	Slip vector ref. frame, contact Pair 1	m	0
slipd_cp1_smsld2	Slip vector deform frame, contact Pair 1	m	0

vslip_cp1_smsld2	Slip velocity vector deform frame, contact Pair 1	m/s	0
Ttrial_cp1_smsld2	Trial friction force, contact Pair 1	Pa	0
mu_cp1_smsld2	Frictional coefficient, contact Pair 1	1	0
Ttrialx_cp1_smsld2	Trial friction force x dir., contact Pair 1	Pa	0
Ttpx_cp1_smsld2	Penalized friction force x dir., contact Pair 1	Pa	0
wctx_cp1_smsld2	Friction help variable x dir., contact Pair 1	Pa	0
slipx_cp1_smsld2	Slip vector ref. frame x dir., contact Pair 1	m	0
slipdx2_cp1_smsld2	Slip vector deform frame x2 dir., contact Pair 1	m	0
vslipx2_cp1_smsld2	Slip velocity vector deform frame x dir., contact Pair 1	m/s	0
Ttrialy_cp1_smsld2	Trial friction force y dir., contact Pair 1	Pa	0
Ttpy_cp1_smsld2	Penalized friction force y dir., contact Pair 1	Pa	0
wcty_cp1_smsld2	Friction help variable y dir., contact Pair 1	Pa	0
slipy_cp1_smsld2	Slip vector ref. frame y dir., contact Pair 1	m	0
slipy2_cp1_smsld2	Slip vector deform frame y2 dir., contact Pair 1	m	0

vslipy2_cp1_smsld2	Slip velocity vector deform frame x dir., contact Pair 1	m/s	0
Ttrialz_cp1_smsld2	Trial friction force z dir., contact Pair 1	Pa	0
Ttpz_cp1_smsld2	Penalized friction force z dir., contact Pair 1	Pa	0
wctz_cp1_smsld2	Friction help variable z dir., contact Pair 1	Pa	0
slipz_cp1_smsld2	Slip vector ref. frame z dir., contact Pair 1	m	0
slipdz2_cp1_smsld2	Slip vector deform frame z2 dir., contact Pair 1	m	0
vslipz2_cp1_smsld2	Slip velocity vector deform frame x dir., contact Pair 1	m/s	0
offset_cp1_smsld2	Contact surface offset, contact Pair 1	m	0
pn_cp1_smsld2	Contact normal penalty factor, contact Pair 1	Pa	0
pt_cp1_smsld2	Contact tangential penalty factor, contact Pair 1	Pa	0
mustat_cp1_smsld2	Static friction coefficient, contact Pair 1	1	0
cohe_cp1_smsld2	Cohesion sliding resistance, contact Pair 1	Pa	0
Ttmax_cp1_smsld2	Maximum tangential traction, contact Pair 1	Pa	0
mudyn_cp1_smsld2	Dynamic friction	1	0

	coefficient, contact Pair 1		
dcfric_cp1_smsld2	Exponential decay coefficient, contact Pair 1	s/m	0
mantol_cp1_smsld2	Absolute tolerance, contact Pair 1	m	0
mandist_cp1_smsld2	Absolute search distance, contact Pair 1	m	0
gap_cp2_smsld2	Gap distance, contact Pair 2	m	geomgap_slv_cp2
Tnp_cp2_smsld2	Penalized contact pressure, contact Pair 2	Pa	$\max(\text{if}(\text{gap_cp2_smsld2} \leq 0, \text{Tn_cp2_smsld2} - \text{pn_cp2_smsld2} * \text{gap_cp2_smsld2}, \text{Tn_cp2_smsld2} * \exp(-\text{pn_cp2_smsld2} * \text{gap_cp2_smsld2} / \max(\text{Tn_cp2_smsld2}, 1e-10))), 0)$
Ttcrit_cp2_smsld2	Critical friction force, contact Pair 2	Pa	0
friction_cp2_smsld2	Enabling friction variable, contact Pair 2	1	0
contact_cp2	Contact variable, contact Pair 2	1	(geomgap_slv_cp2
wcn_cp2_smsld2	Contact help variable, contact Pair 2	Pa	nojac(Tnp_cp2_smsld2)-Tn_cp2_smsld2
slip_cp2_smsld2	Slip vector ref. frame, contact Pair 2	m	0
slipd_cp2_smsld2	Slip vector deform frame, contact Pair 2	m	0
vslip_cp2_smsld2	Slip velocity vector deform frame, contact Pair 2	m/s	0
Tttrial_cp2_smsld2	Trial friction force, contact Pair 2	Pa	0
mu_cp2_smsld2	Frictional coefficient, contact Pair 2	1	mustat_cp2_smsld2
Tttrialx_cp2_smsld2	Trial friction	Pa	0

	force x dir., contact Pair 2		
Ttpx_cp2_smsld2	Penalized friction force x dir., contact Pair 2	Pa	0
wctx_cp2_smsld2	Friction help variable x dir., contact Pair 2	Pa	0
slipx_cp2_smsld2	Slip vector ref. frame x dir., contact Pair 2	m	0
slipdx2_cp2_smsld2	Slip vector deform frame x2 dir., contact Pair 2	m	0
vslipx2_cp2_smsld2	Slip velocity vector deform frame x dir., contact Pair 2	m/s	0
Tttrialy_cp2_smsld2	Trial friction force y dir., contact Pair 2	Pa	0
Ttpy_cp2_smsld2	Penalized friction force y dir., contact Pair 2	Pa	0
wcty_cp2_smsld2	Friction help variable y dir., contact Pair 2	Pa	0
slipy_cp2_smsld2	Slip vector ref. frame y dir., contact Pair 2	m	0
slipdy2_cp2_smsld2	Slip vector deform frame y2 dir., contact Pair 2	m	0
vslipy2_cp2_smsld2	Slip velocity vector deform frame x dir., contact Pair 2	m/s	0
Tttrialz_cp2_smsld2	Trial friction force z dir., contact Pair 2	Pa	0
Ttpz_cp2_smsld2	Penalized friction force z dir., contact Pair 2	Pa	0

wctz_cp2_smsld2	Friction help variable z dir., contact Pair 2	Pa	0
slipz_cp2_smsld2	Slip vector ref. frame z dir., contact Pair 2	m	0
slipdz2_cp2_smsld2	Slip vector deform frame z2 dir., contact Pair 2	m	0
vslipz2_cp2_smsld2	Slip velocity vector deform frame x dir., contact Pair 2	m/s	0
offset_cp2_smsld2	Contact surface offset, contact Pair 2	m	0
pn_cp2_smsld2	Contact normal penalty factor, contact Pair 2	Pa	E_smsld2/hmin_cp2_smsld2
pt_cp2_smsld2	Contact tangential penalty factor, contact Pair 2	Pa	0
mustat_cp2_smsld2	Static friction coefficient, contact Pair 2	1	0
cohe_cp2_smsld2	Cohesion sliding resistance, contact Pair 2	Pa	0
Ttmax_cp2_smsld2	Maximum tangential traction, contact Pair 2	Pa	0
mudyn_cp2_smsld2	Dynamic friction coefficient, contact Pair 2	1	0
dftric_cp2_smsld2	Exponential decay coefficient, contact Pair 2	s/m	0
mantol_cp2_smsld2	Absolute tolerance, contact Pair 2	m	1e-09
mandist_cp2_smsld2	Absolute search distance,	m	5e-05

	contact Pair 2		
Ft11_smsld2	Deformation gradient projected on tangent plane 11 comp.	1	1+uTx
Ft12_smsld2	Deformation gradient projected on tangent plane 12 comp.	1	uTy
Ft13_smsld2	Deformation gradient projected on tangent plane 13 comp.	1	uTz
Ft21_smsld2	Deformation gradient projected on tangent plane 21 comp.	1	vTx
Ft22_smsld2	Deformation gradient projected on tangent plane 22 comp.	1	1+vTy
Ft23_smsld2	Deformation gradient projected on tangent plane 23 comp.	1	vTz
Ft31_smsld2	Deformation gradient projected on tangent plane 31 comp.	1	wTx
Ft32_smsld2	Deformation gradient projected on tangent plane 32 comp.	1	wTy
Ft33_smsld2	Deformation gradient projected on tangent plane 33 comp.	1	1+wTz
Tax_smsld2	Surface traction (force/area) in x dir.	Pa	$(F11_smsld2 * Sx_smsld2 + F12_smsld2 * Sxy_smsld2 + F13_smsld2 * Sxz_smsld2) * nx_smsld2 + (F11_smsld2 * Sxy_smsld2 + F12_smsld2 * Sy_smsld2 + F13_smsld2 * Syz_smsld2) *$

			$ny_smsld2+(F11_smsld2 * Sxz_smsld2+F12_smsld2 * Syz_smsld2+F13_smsld2 * Sz_smsld2) * nz_smsld2$
Tay_smsld2	Surface traction (force/area) in y dir.	Pa	$(F21_smsld2 * Sx_smsld2+F22_smsld2 * Sxy_smsld2+F23_smsld2 * Sxz_smsld2) * nx_smsld2+(F21_smsld2 * Sxy_smsld2+F22_smsld2 * Sy_smsld2+F23_smsld2 * Syz_smsld2) * ny_smsld2+(F21_smsld2 * Sxz_smsld2+F22_smsld2 * Syz_smsld2+F23_smsld2 * Sz_smsld2) * nz_smsld2$
Taz_smsld2	Surface traction (force/area) in z dir.	Pa	$(F31_smsld2 * Sx_smsld2+F32_smsld2 * Sxy_smsld2+F33_smsld2 * Sxz_smsld2) * nx_smsld2+(F31_smsld2 * Sxy_smsld2+F32_smsld2 * Sy_smsld2+F33_smsld2 * Syz_smsld2) * ny_smsld2+(F31_smsld2 * Sxz_smsld2+F32_smsld2 * Syz_smsld2+F33_smsld2 * Sz_smsld2) * nz_smsld2$

8.4. Subdomain

Name	Description	Unit	Expression
absux_c	$ \text{grad}(u) $	1	$\text{sqrt}(ux^2+uy^2+uz^2)$
absvx_c	$ \text{grad}(v) $	1	$\text{sqrt}(vx^2+vy^2+vz^2)$
abswx_c	$ \text{grad}(w) $	1	$\text{sqrt}(wx^2+wy^2+wz^2)$
absmx_c	$ \text{grad}(m) $		$\text{sqrt}(mx^2+my^2+mz^2)$
RFx_smsld2	Reaction force x-dir.	N	reactf(u)
RFy_smsld2	Reaction force y-dir.	N	reactf(v)
RFz_smsld2	Reaction force z-dir.	N	reactf(w)
RMx_smsld2	Reaction moment x-dir.	N*m	$(y+v-\text{refpnty_smsld2}) * RFz_smsld2-(z+w-\text{refpntz_smsld2}) * RFy_smsld2$
RMy_smsld2	Reaction moment y-dir.	N*m	$(z+w-\text{refpntz_smsld2}) * RFx_smsld2-(x+u-\text{refpntx_smsld2}) * RFz_smsld2$
RMz_smsld2	Reaction moment z-dir.	N*m	$(x+u-\text{refpntx_smsld2}) * RFy_smsld2-(y+v-\text{refpnty_smsld2}) * RFx_smsld2$
Fxg_smsld2	Body load in global x-dir.	N/m ³	0
Fyg_smsld2	Body load in global y-dir.	N/m ³	0
Fzg_smsld2	Body load in global z-dir.	N/m ³	0
disp_smsld2	Total displacement	m	$\text{sqrt}(\text{real}(u)^2+\text{real}(v)^2+\text{real}(w)^2)$
sx_smsld2	sx normal stress global sys.	Pa	$(F11_smsld2 * (Sx_smsld2 * F11_smsld2+Sxy_smsld2 * F12_smsld2+Sxz_smsld2 * F13_smsld2)+F12_smsld2 * (Sxy_smsld2 * F11_smsld2+Sy_smsld2 * F12_smsld2+Syz_smsld2 * F13_smsld2)+F13_smsld2 * (Sxz_smsld2 * F11_smsld2+Syz_smsld2 * F13_smsld2) * F13_smsld2)$

			$(F12_smsld2+Sz_smsld2 * F13_smsld2))/J_smsld2$
sy_smsld2	sy normal stress global sys.	Pa	$(F21_smsld2 * (Sx_smsld2 * F21_smsld2+Sxy_smsld2 * F22_smsld2+Sxz_smsld2 * F23_smsld2)+F22_smsld2 * (Sxy_smsld2 * F21_smsld2+Sy_smsld2 * F22_smsld2+Syz_smsld2 * F23_smsld2)+F23_smsld2 * (Sxz_smsld2 * F21_smsld2+Syz_smsld2 * F22_smsld2+Sz_smsld2 * F23_smsld2))/J_smsld2$
sz_smsld2	sz normal stress global sys.	Pa	$(F31_smsld2 * (Sx_smsld2 * F31_smsld2+Sxy_smsld2 * F32_smsld2+Sxz_smsld2 * F33_smsld2)+F32_smsld2 * (Sxy_smsld2 * F31_smsld2+Sy_smsld2 * F32_smsld2+Syz_smsld2 * F33_smsld2)+F33_smsld2 * (Sxz_smsld2 * F31_smsld2+Syz_smsld2 * F32_smsld2+Sz_smsld2 * F33_smsld2))/J_smsld2$
sxy_smsld2	sxy shear stress global sys.	Pa	$(F11_smsld2 * (Sx_smsld2 * F21_smsld2+Sxy_smsld2 * F22_smsld2+Sxz_smsld2 * F23_smsld2)+F12_smsld2 * (Sxy_smsld2 * F21_smsld2+Sy_smsld2 * F22_smsld2+Syz_smsld2 * F23_smsld2)+F13_smsld2 * (Sxz_smsld2 * F21_smsld2+Syz_smsld2 * F22_smsld2+Sz_smsld2 * F23_smsld2))/J_smsld2$
syz_smsld2	syz shear stress global sys.	Pa	$(F21_smsld2 * (Sx_smsld2 * F31_smsld2+Sxy_smsld2 * F32_smsld2+Sxz_smsld2 * F33_smsld2)+F22_smsld2 * (Sxy_smsld2 * F31_smsld2+Sy_smsld2 * F32_smsld2+Syz_smsld2 * F33_smsld2)+F23_smsld2 * (Sxz_smsld2 * F31_smsld2+Syz_smsld2 * F32_smsld2+Sz_smsld2 * F33_smsld2))/J_smsld2$
sxz_smsld2	sxz shear stress global sys.	Pa	$(F11_smsld2 * (Sx_smsld2 * F31_smsld2+Sxy_smsld2 * F32_smsld2+Sxz_smsld2 * F33_smsld2)+F12_smsld2 * (Sxy_smsld2 * F31_smsld2+Sy_smsld2 * F32_smsld2+Syz_smsld2 * F33_smsld2)+F13_smsld2 * (Sxz_smsld2 * F31_smsld2+Syz_smsld2 * F32_smsld2+Sz_smsld2 * F33_smsld2))/J_smsld2$
ex_smsld2	ex normal strain global sys.	1	$ux+0.5 * (ux^2+vx^2+wx^2)$
ey_smsld2	ey normal strain global sys.	1	$vy+0.5 * (uy^2+vy^2+wy^2)$
ez_smsld2	ez normal strain global sys.	1	$wz+0.5 * (uz^2+vz^2+wz^2)$
exy_smsld2	exy shear strain global sys.	1	$0.5 * (uy+vx+ux * uy+vx * vy+wx * wy)$
eyz_smsld2	eyz shear strain global sys.	1	$0.5 * (vz+wy+uy * uz+vy * vz+wy * wz)$
exz_smsld2	exz shear strain global sys.	1	$0.5 * (uz+wx+ux * uz+vx * vz+wx * wz)$
Sx_smsld2	Sx Second Piola-Kirchhoff global sys.	Pa	$E_smsld2 * ((1-nu_smsld2) * ex_smsld2+nu_smsld2 * ey_smsld2+nu_smsld2 * ez_smsld2)/((1+nu_smsld2) * (1-2 * nu_smsld2))$

Sy_smsld2	Sy Second Piola-Kirchhoff global sys.	Pa	$E_smsld2 * (nu_smsld2 * ex_smsld2 + (1 - nu_smsld2) * ey_smsld2 + nu_smsld2 * ez_smsld2) / ((1 + nu_smsld2) * (1 - 2 * nu_smsld2))$
Sz_smsld2	Sz Second Piola-Kirchhoff global sys.	Pa	$E_smsld2 * (nu_smsld2 * ex_smsld2 + nu_smsld2 * ey_smsld2 + (1 - nu_smsld2) * ez_smsld2) / ((1 + nu_smsld2) * (1 - 2 * nu_smsld2))$
Sxy_smsld2	Sxy Second Piola-Kirchhoff global sys.	Pa	$E_smsld2 * exy_smsld2 / (1 + nu_smsld2)$
Syz_smsld2	Syz Second Piola-Kirchhoff global sys.	Pa	$E_smsld2 * eyz_smsld2 / (1 + nu_smsld2)$
Sxz_smsld2	Sxz Second Piola-Kirchhoff global sys.	Pa	$E_smsld2 * exz_smsld2 / (1 + nu_smsld2)$
p3	Pressure	Pa	$-K_smsld2 * evol_smsld2$
cp_smsld2	Pressure wave velocity	m/s	$\sqrt{(K_smsld2 + 4 * G_smsld2 / 3) / rho_smsld2}$
cs_smsld2	Shear wave velocity	m/s	$\sqrt{G_smsld2 / rho_smsld2}$
mises_smsld2	von Mises stress	Pa	$\sqrt{(sx_smsld2^2 + sy_smsld2^2 + sz_smsld2^2 - sx_smsld2 * sy_smsld2 - sy_smsld2 * sz_smsld2 - sx_smsld2 * sz_smsld2 + 3 * sxy_smsld2^2 + 3 * syz_smsld2^2 + 3 * sxz_smsld2^2)}$
Ws_smsld2	Strain energy density	J/m ³	$0.5 * (sx_smsld2 * ex_smsld2 + sy_smsld2 * ey_smsld2 + sz_smsld2 * ez_smsld2 + 2 * sxy_smsld2 * exy_smsld2 + 2 * syz_smsld2 * eyz_smsld2 + 2 * sxz_smsld2 * exz_smsld2)$
evol_smsld2	Volumetric strain	1	$-1 + Jel_smsld2$
F11_smsld2	Deformation gradient 11 comp.	1	$1 + ux$
F12_smsld2	Deformation gradient 12 comp.	1	uy
F13_smsld2	Deformation gradient 13 comp.	1	uz
F21_smsld2	Deformation gradient 21 comp.	1	vx
F22_smsld2	Deformation gradient 22 comp.	1	$1 + vy$
F23_smsld2	Deformation gradient 23 comp.	1	vz

F31_smsld2	Deformation gradient 31 comp.	1	wx
F32_smsld2	Deformation gradient 32 comp.	1	wy
F33_smsld2	Deformation gradient 33 comp.	1	1+wz
detF_smsld2	Determinant of deformation gradient	1	$F11_smsld2 * F22_smsld2 * F33_smsld2 + F12_smsld2 * F23_smsld2 * F31_smsld2 + F13_smsld2 * F21_smsld2 * F32_smsld2 - F11_smsld2 * F23_smsld2 * F32_smsld2 - F12_smsld2 * F21_smsld2 * F33_smsld2 - F13_smsld2 * F22_smsld2 * F31_smsld2$
J_smsld2	Volume ratio	1	detF_smsld2
Jel_smsld2	Elastic volume ratio	1	J_smsld2
invF11_smsld2	Inverse of deformation gradient 11 comp.	1	$(F22_smsld2 * F33_smsld2 - F23_smsld2 * F32_smsld2) / \text{detF_smsld2}$
invF12_smsld2	Inverse of deformation gradient 12 comp.	1	$(F13_smsld2 * F32_smsld2 - F12_smsld2 * F33_smsld2) / \text{detF_smsld2}$
invF13_smsld2	Inverse of deformation gradient 13 comp.	1	$(F12_smsld2 * F23_smsld2 - F13_smsld2 * F22_smsld2) / \text{detF_smsld2}$
invF21_smsld2	Inverse of deformation gradient 21 comp.	1	$(F31_smsld2 * F23_smsld2 - F21_smsld2 * F33_smsld2) / \text{detF_smsld2}$
invF22_smsld2	Inverse of deformation gradient 22 comp.	1	$(F11_smsld2 * F33_smsld2 - F31_smsld2 * F13_smsld2) / \text{detF_smsld2}$
invF23_smsld2	Inverse of deformation gradient 23 comp.	1	$(F21_smsld2 * F13_smsld2 - F11_smsld2 * F23_smsld2) / \text{detF_smsld2}$
invF31_smsld2	Inverse of deformation gradient 31 comp.	1	$(F21_smsld2 * F32_smsld2 - F31_smsld2 * F22_smsld2) / \text{detF_smsld2}$
invF32_smsld2	Inverse of deformation gradient 32 comp.	1	$(F31_smsld2 * F12_smsld2 - F11_smsld2 * F32_smsld2) / \text{detF_smsld2}$

	comp.		
invF33_smsld2	Inverse of deformation gradient 33 comp.	1	$(F11_smsld2 * F22_smsld2 - F21_smsld2 * F12_smsld2) / \det F_smsld2$
tresca_smsld2	Tresca stress	Pa	$\max(\max(\text{abs}(s1_smsld2 - s2_smsld2), \text{abs}(s2_smsld2 - s3_smsld2)), \text{abs}(s1_smsld2 - s3_smsld2))$

Appendix D

Non-aqueous Zirconia and Stainless Steel Composite Colloidal Suspensions

Introduction

Composite materials can combine the properties of the component materials [1]. By mixing the stainless steel and zirconia particulates, material properties combine the strength, hardness, and high elastic modulus from the ceramic, but will not fail catastrophically like the ceramic. It is also important, for biological applications, that the material remains inert and biocompatible without oxidizing or reacting to anything in the physiological environment of the human body. Functionally graded composites of 300 series stainless steel and 3Y-TZP have been previously studied [2, 3], but there have been only a few studies of homogenous composite microstructure [4, 5]. In this work, a 300 series stainless steel and 3 mol% yttria-stabilized zirconia (3Y-TZP) composite was formulated and incorporated into the LM-RIF process. The composite suspension's rheological properties and mechanical strength are reported and discussed.

The objective in preparing non-aqueous suspensions of 300 series stainless steel and 3Y-TZP was to prepare metal matrix, with 3Y-TZP as a dispersed phase, composite materials. The composite materials, which may exhibit a higher hardness, would be useful in new meso-scale device design. A prerequisite to combining suspensions of two particulate materials is that the solvent systems be miscible. To this end, the same solvent system, a 50:50 ratio of 200 proof ethanol:xylenes (a mixture of meta, ortho and para-isomers) was utilized. Metal matrix composite particulate suspensions composed of 300 series stainless steel and 3Y-TZP were

formulated in non-aqueous environments to work with the LM-RIF process. Micro-Melt® -22 μm 300 series stainless steel microparticles (Carpenter Powder Products, Wyomissing, PA) with average radius of $5.5 \mu\text{m}$ (from the size distribution shown in the 300 series stainless steel study) and density of 8.0 g/cm^3 served as the metallic colloidal species. The ceramic particles were 3 mol% yttria-stabilized zirconia (3Y-TZP) (Tosoh Corp., Tokyo, Japan). The zirconia had an average radius of 65 nm [6] and density of 6.05 g/cm^3 .

Preliminary experiments were conducted to determine the optimized formulation for the 300 series stainless steel for optimal dispersion and rheological properties. As shown in Figure D., the optimal 300 series stainless steel colloidal suspension was formulated using a mixture of 90.7 wt% (50 vol%) stainless steel, 4.77 wt% (24.5 vol%) oleic acid (J. T. Baker, Phillipsburg, NJ), 2.26 wt% (12.3 vol%) 200 proof ethanol (VWR International, West Chester, PA), and 2.26 wt% (12.3 vol%) ACS reagent grade xylenes (Sigma-Aldrich®, St. Louis, MO). The suspensions were milled using a Szegvari 01-HDDM attrition mill equipped with a stainless steel spindle and vessel (Union Process, Inc., Akron, OH). After the dispersant was added to the ethanol and xylenes, the solvent and dispersant solution was added to the attrition mill pre-loaded with 2mm stainless steel media. Powder addition took place at a rate of 20g per minute at 430 rpm at 10°C . Once all of the powder was added, the mill speed was increased to 800 rpm and maintained at this rpm for 20 hours. To prevent evaporation of the ethanol and xylenes solvents, the mill vessel was held at 10°C for the duration of the milling time, while the mill vessel is equipped with a sealed lid to minimize solvent evaporation.

The optimal zirconia suspension, also described in Figure D., consists of 82.4 wt% (40 vol%) powder, 9.1 wt% (28.9 vol%) Menhaden fish oil (Richard E. Mistler, Inc., Yardley, PA), 4.2 wt% (15.5 vol%) ethanol, and 4.2 wt% (15.5 vol%) xylenes. The xylenes added to the suspension were shown experimentally to help dissolve the menhaden fish oil and produce more uniform green parts in studies by Mistler [7]. The suspensions were milled using a Szegvari 01-

HDDM attrition mill equipped with a polyurethane-coated spindle and vessel (Union Process, Inc., Akron, OH). After the dispersant was added to the ethanol and xylenes, the solvent and dispersant solution were added to the attrition mill loaded with 2mm zirconia media. Powder was added at a rate of 1g per minute at 430 rpm at 10°C. Once all of the powder was added, the mill speed was increased to 800 rpm and maintained at this rpm for 5 hours. To prevent evaporation of the ethanol and xylenes, the mill was held at 10°C for the duration of the milling time, while the mill vessel was equipped with a sealed lid.

Composite suspensions were formulated by mixing various volumes of both the stainless steel and zirconia suspensions. The composite suspensions were then mixed in the attrition mill loaded with 1/8" zirconia media for 1 hour at 800 rpm. The exact composition of the composite suspension was adjusted by altering the ratio of 300 series stainless steel to 3Y-TZP that was combined.

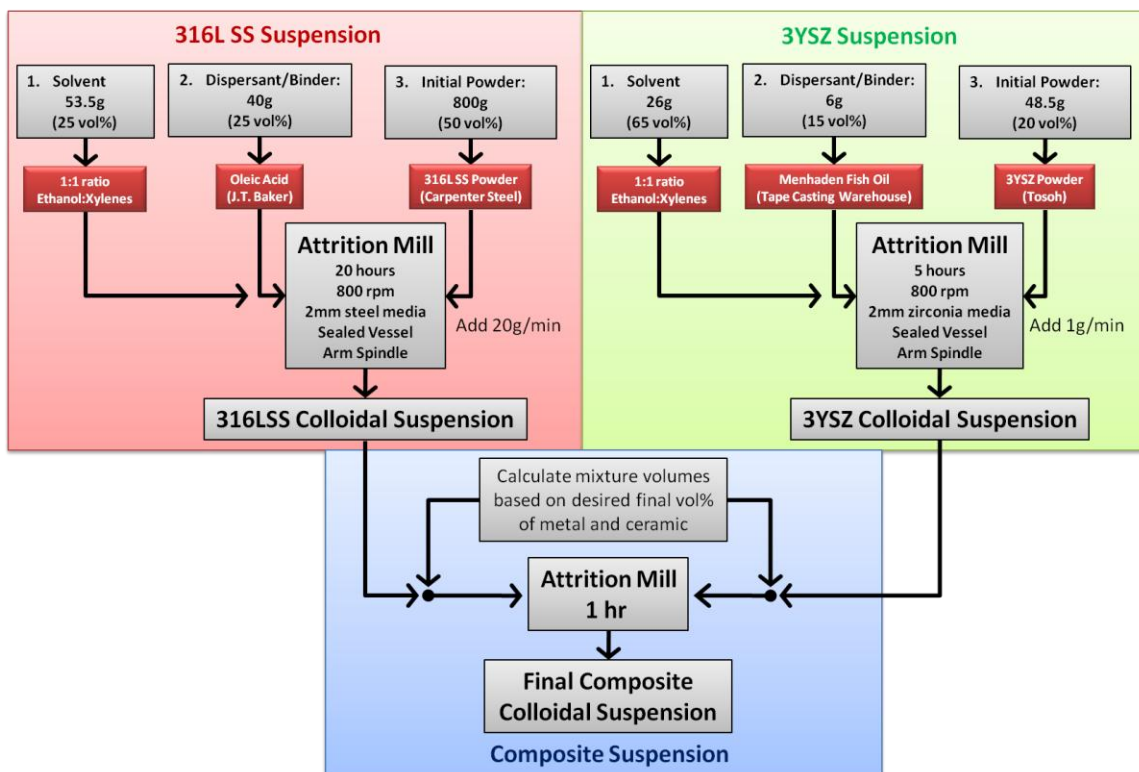


Figure D.1. The formulation process for homogeneous composites of 300 series stainless steel and 3Y-TZP is shown. Both material systems are in the same solvent, while having different dispersants present. The final composition of the composite suspension can be tailored through controlling the volume of 3Y-TZP suspension added to the 300 series stainless steel suspension. The order of addition of components is labeled in the upper left corner of each component.

Rheological Properties of Composite Suspensions

Striking effects were observed in the rheological behavior of the platelet stainless steel and equiaxed, nanoscale 3Y-TZP. When particles of different sizes and compositions are mixed together in a complex suspension, there are several phenomena that occur. van der Waals forces, as well as other attractive and repulsive interactions such as steric interactions among particles can influence the rheological behavior of the system. In addition to particle interaction forces, other factors influence the viscosity of a composite suspension, including particle sizes as well as volume fraction of solids in the system. Furthermore, the particle shape can have a considerable

role because of orientation of anisotropic particles as shear rate increases resulting in decreased interparticle interactions with the alignment of platelet or rod-like particulates. In the case of particulate mixtures, Zsigmondy [8] and more recently, Lewis et al. [9] have observed a ‘halo’ effect with the finer, well dispersed particulates leading to better dispersion of the larger particulate phase. In the current work, we look at the effect of shape as well as halo effects.

In this study, the effects of the volume percent of the composite suspension for the microparticles of 300 series stainless steel and nanoparticles of yttria-stabilized zirconia at varying ratios were examined to determine the effects on rheological behavior.

The rheological behavior of the prepared suspensions was determined with a Malvern Instruments Bohlin Visco88 with a 14 mm concentric cylinder system. Initially, the high shear, or apparent viscosity, of composite suspensions was determined as a function of solids content (vol%) with constant ratio of 300 series stainless steel to 3Y-TZP of 1:1. Secondly, these values were fit to the Dougherty-Krieger relationship given in Equation (D.1), where η is viscosity, ϕ is the packing fraction in vol%, and n is the intrinsic viscosity parameter [10].

$$\frac{\eta_{suspension}}{\eta_{solvent}} = \left(1 - \frac{\phi}{\phi_{max}} \right)^{-n} \quad (D.1)$$

As the volume fraction of particles in the suspension increases, so does the apparent viscosity. In Figure D.2 Top, the best fit approach of Equation (5.5) results in maximum packing fraction of 0.72, a number almost not physically possible, at least for spherical particles, as the maximum packing of spheres possible in FCC configuration is 0.74. The platelet like nature of the 300 series stainless steel particulates in the suspension facilitates the higher packing density. As shown in Figure 5.21 (Bottom), the platelet particles can pack much more efficiently than spheres. Furthermore, the addition of smaller 3Y-TZP particulates to the suspension can roll between larger 300 series stainless steel particles, effectively lubricating the system at high solids

loading. For comparison, in Figure D.2 Bottom, the maximum packing fraction is fixed at 0.65, a reasonable value after which, spherical particles systems would normally experience an infinitely large increase in apparent viscosity.

The volume ratio of stainless steel to zirconia particles in a composite suspension influences the average apparent viscosity of the composite. This phenomenon has been studied previously by Farris et al. based on spherical particulate mixing [11]. In Figure D.3, at a constant composite suspension volume percent of 40 vol% the ratio of 300 series stainless steel to 3Y-TZP was varied. As the stainless steel content increases, the viscosity of the suspension decreases. This is expected, but there is a specific ratio of large particles to small particles that results in the lowest composite suspension viscosity, theoretically between 60 and 70 vol% [11]. This composite ratio of 60 vol% large particles is the ideal initial composite suspension to incorporate into the LM-RIF process.

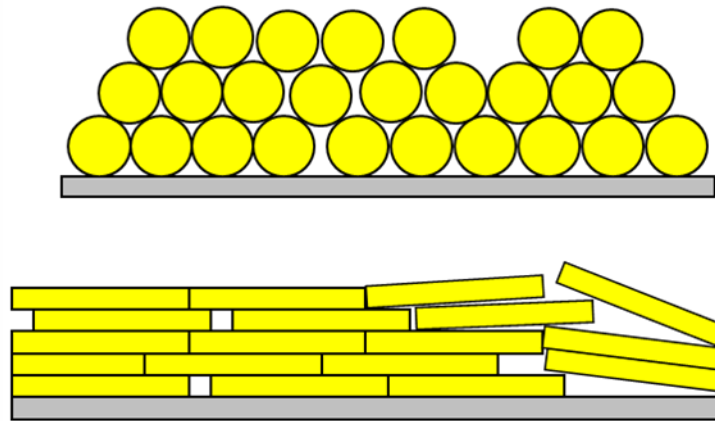
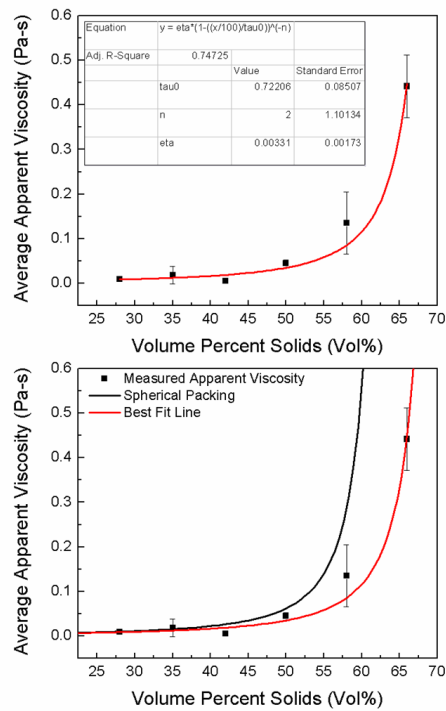


Figure D.2. Left: Top: Composite mixtures of 1:1 volume ratio of stainless steel to zirconia in a suspension of ethanol and xylenes, at a ratio of 1:1, show an exponential increase in the average apparent viscosity as a function of volume % solid, and fit by the Dougherty-Krieger relationship. The maximum packing vol% is 0.72, almost the theoretical limit of hard sphere packing. The platelet like shape of the 300 series stainless steel particles in the system, as well as the addition of smaller 3Y-TZP particles is the reason for this high maximum packing fraction. Bottom: A spherical comparison was carried out by fixing the maximum packing fraction at 0.65 and plotting in comparison to the Top best fit curve, the deviation of the measured viscosity increase from the spherical Dougherty-Krieger model can be seen as the shift between the red black curves. Error bars given are for 95% confidence interval, while standard error is used for the parameters in the best fit line. Right. The relative orientation of the platelet particles leads to a higher packing density than that possible with spherical particles [12].

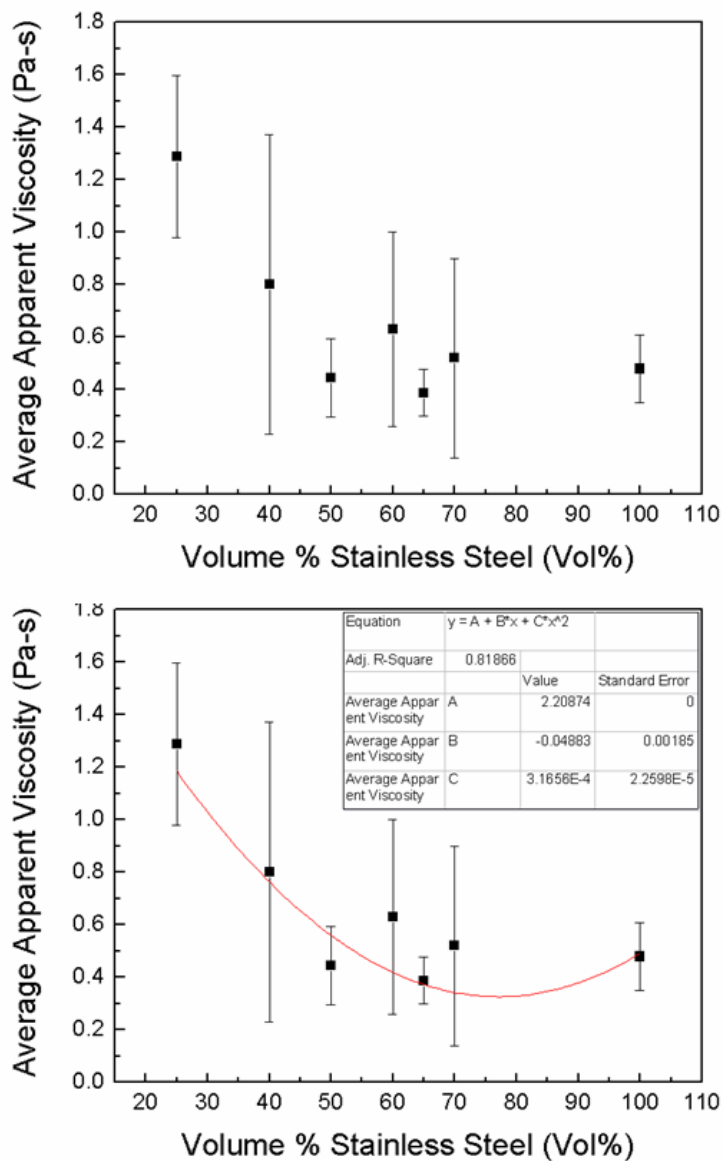


Figure D.3. Top: The apparent viscosity of a composite suspension with 40 volume % solids loading and varying volume ratios of stainless steel to zirconia particles is shown. As the zirconia content increases (moving from right to left in the figure) in the composite suspension, the average apparent viscosity also increases. It is expected that viscosity will decrease with the addition of a second particle size distribution in the system, as smaller particles are seen as an additional “fluid” to the larger particles [11], with a minimum occurring around 65vol% large particles, and constant total solids loading [11]. Error bars given are for 95% confidence interval. Bottom: the data is fit with a trend line that highlights the affects of adding large particles to the small particle suspension. Further rheological experimentation can provide the information needed to model the system, as described by Farris et al. [11].

State of Dispersion of Composite Suspensions

The state of dispersion of a composite can be described through consideration of the three possible interactions of particulates in the suspension, calculated from the attractive energies and steric barriers, with Equations (5.1 to 5.3), as previously discussed for the 300 series stainless steel system. In the composite system, the low dielectric constant of ethanol and xylenes provides no electrostatic repulsion among the particles. Therefore, $V_{electrostatic}$ in the current material system is zero due to a zero ζ -potential value in the non-aqueous environment. However, steric repulsion forces are present with the thickness of the steric barrier used in the system at 1.4 nm, assuming a 45° bonding angle of oleic acid with the surface of the particle for 300 series stainless steel particles (see earlier discussion). Furthermore, there are steric interaction forces among 3Y-TZP particles, and between 3Y-TZP particles and 300 series stainless steel particles. For this reason, three interaction curves are calculated, for the three cases of attraction, SS-SS, 3Y-TZP-3Y-TZP, and SS-3Y-TZP particulates. Furthermore, the nature of the interaction curve is the same as that in Chapter 5, for the 300 series stainless steel to 300 series stainless steel interaction in the composite slurry. It is assumed that one nanoscale 3Y-TZP particle is between the two metal particles, providing, in effect, an additional steric barrier to agglomeration. This is a reasonable assumption due to the fact that this is a composite, and is also consistent with the experimental observation that the viscosity decreases as 300 series stainless steel is added to the 3Y-TZP suspension. Finally, the particle surface roughness is assumed to be 25 nm for the 300 series stainless steel and 5 nm for the 3Y-TZP particles. Thus, the distance of closest approach for the 300 series stainless steel particles is 25 μm plus 65 μm for a total distance of closest approach equal to 90 μm to accommodate the nanoscale 3Y-TZP between the stainless steel particles. The volume fraction of organic in the steric layer is assumed to be 0.5 in both particulate systems, and the solvent adsorbent interaction parameter is assumed to be 0.3. The

parameters used to calculate the interaction energy curves, as a function of particle to particle separation distance and given in Table D.6.2.

Table D.6.2. The parameters used to calculate the interactions energy as a function particle to particle separation distance are listed. The three cases of particle interaction are metal to metal, ceramic to ceramic, and metal to ceramic are listed.

<i>Parameter</i>	<i>300 series stainless steel:300 series stainless steel</i>	<i>3Y-TZP:3Y-TZP</i>	<i>300 series stainless steel:3Y-TZP</i>
ζ -potential	0 mV	0 mV	0 mV
Thickness of adsorbed polymer layer	2 nm	2 nm	2 nm
Hamaker constant [13, 14]	2.12×10^{-19} J	7.2×10^{-20} J	Used appropriate A_{ham} for each particle
Particle diameter	11 μm	114 nm	Used appropriate d_{particle} for each particle
Solvent Dielectric Constant assumed	24.3	24.3	24.3
Temperature (T)	300°K	300°K	300°K
Volume Fraction of polymer in steric barrier(ϕ)	0.5	0.5	0.5
Solvent absorbent interaction parameter(χ)	0.3	0.3	0.3
Boltzmann's Constant (k)	$1.3806503 \times 10^{-23}$	$1.3806503 \times 10^{-23}$	$1.3806503 \times 10^{-23}$

The large distance of closest approach truncates the strong van der Waals attraction energies at small interparticle separation distances. In Figure D.4, all interactions result in an

secondary energy well, with the interaction between 3Y-TZP and 3Y-TZP having the deepest energy well. Therefore, it is the particle-particle interaction that is of most concern. However, rheological measurements, given in the previously discussed, show that these suspensions are still exhibit viscosities low enough to be easily cast during LM-RIF processing. The interaction energy curves as a function of particle separation distance are given for the three possible interactions in the composite system. In green, the 300 series stainless steel:300 series stainless steel particle interaction, the separation distance is large due to the surface roughness of the 300 series stainless steel powder, as well as the fact that there is an assumed 3Y-TZP powder between the attracting particles. In red, a 3Y-TZP:3Y-TZP interaction, the smallest separation distance is observed, as well as the deepest secondary minimum energy well. In blue, a 300 series stainless steel:3Y-TZP interaction, the large separation distance comes from the assumed roughness of the 300 series stainless steel particle, as well as a smallest secondary minimum energy well.

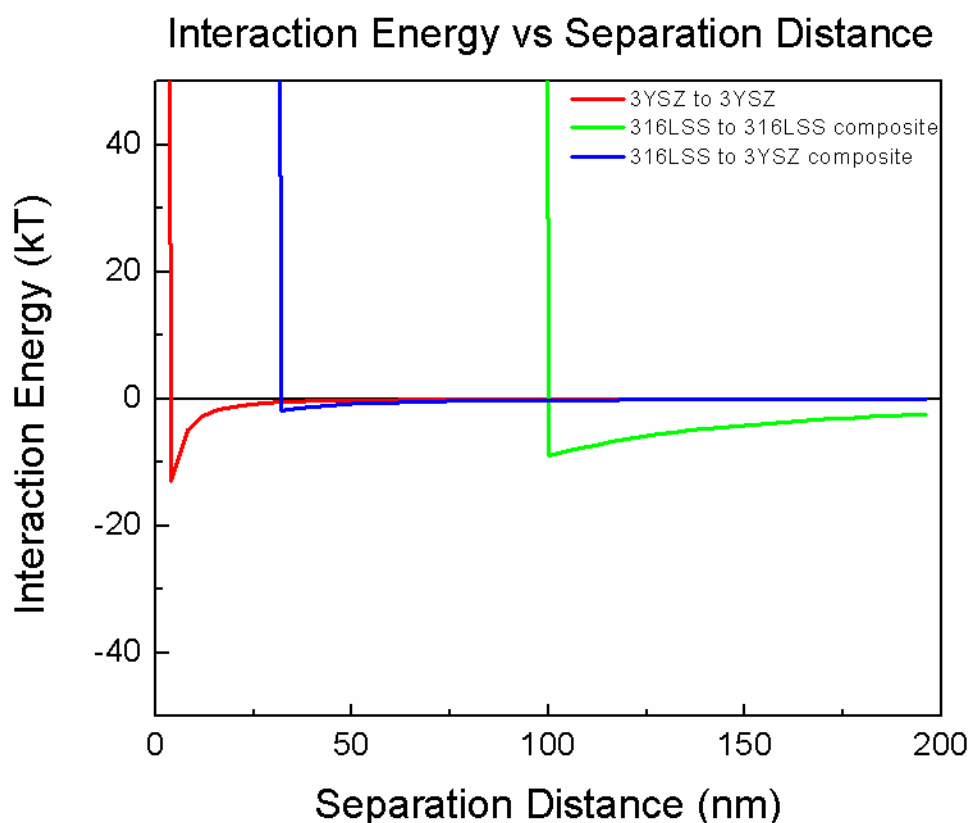


Figure D.4. The interaction energy curves as a function of particle separation distance are given for the three possible interactions in the composite system. Green: a 300 series stainless steel particle interaction with another stainless steel particle. In this case, the separation distance is large due to the surface roughness of the 300 series stainless steel powder, as well as the fact that there is an assumed 3Y-TZP powder between the attracting particles, due to the fact that this is a composite. If not such particle were there, then the curve would look like the interaction energy curve in Chapter 5. Red: a 3Y-TZP to 3Y-TZP interaction shows the smallest separation distance, as well as the deepest secondary minimum energy well. Blue: a 300 series stainless steel particle interaction with a 3Y-TZP particle. The large separation distance comes from the assumed roughness of the 300 series stainless steel particle, as well as a smallest secondary minimum energy well.

Sintering of composite suspensions was carried out in a two step process, similar to the binder combustion and sintering process previously used for the 300 series stainless steel suspension. Combustion of the dispersant of the composite suspension takes place at 600°C for 2 hours in ambient atmosphere conditions, followed by sintering in a dissociated ammonia reducing

atmosphere at 1300°C for 2 hours. In order to determine the grain morphology of the fabricated parts, optical cross sectional images were taken. Cross sectional samples were prepared by mounting the parts in a two part epoxy (Allied High Tech Products, Inc.) and polishing with the steps outlined in Chapter 5.

In Figure D.5, an increase in the vol% of 300 series stainless steel in the composite shows an increase in the connectivity on the metallic phase. In addition, using ImageJ [15] software, the area fraction of the stainless steel phase is compared to the area fraction of the zirconia phase. The area fraction is assumed to directly correlate to volume fraction with uniform phase dispersion throughout three-dimensions [16]. In this way, the calculated ratios of 300 series stainless steel to 3Y-TZP in the composites can be compared to the actual values, as shown Table D.6.3.

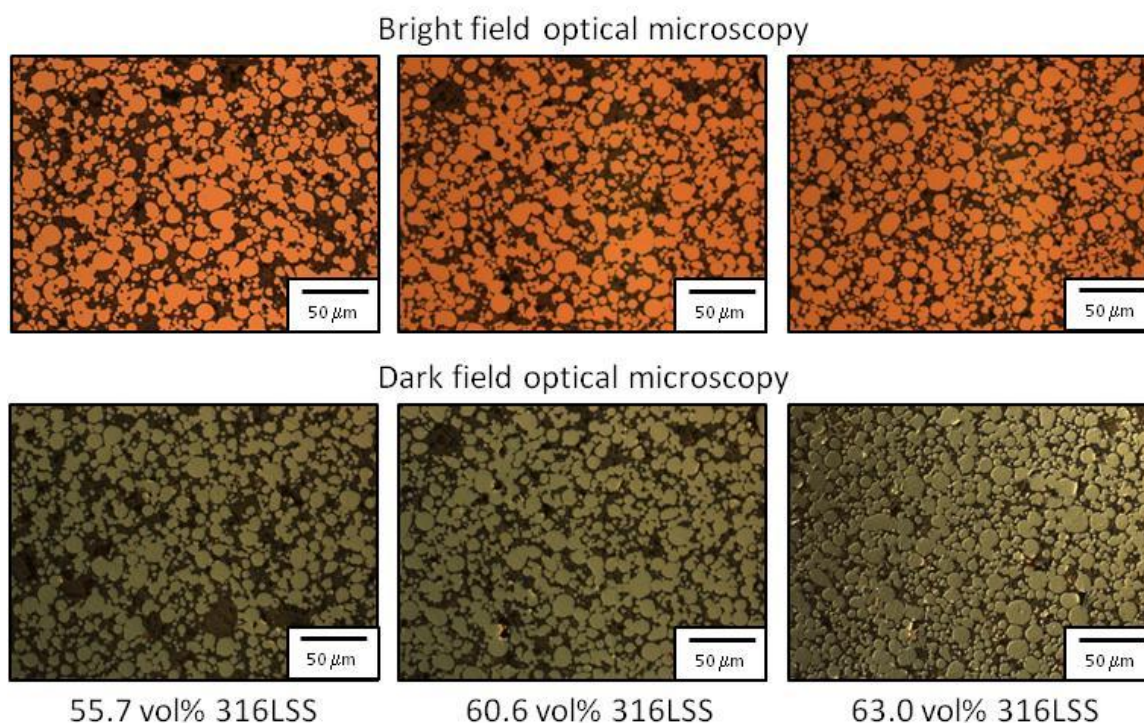


Figure D.5. Cross sectional optical microscopy images are shown for sintered composites ranging from 55.7 to 63 vol% 300 series stainless steel. As the vol% of 300 series stainless steel increases, the composite changes from having almost no interconnected metallic phase, to almost completely interconnected metallic phase. The image analysis of volume percent 300 series stainless steel measured versus calculated is shown in Table 3.8.

Table D.6.3. The theoretically calculated volume fraction of 300 series stainless steel in the composites is compared with the measured volume percent using ImageJ [15] software. Measured volume percent of 300 series stainless steel is consistently less than the calculated target goals. One reason for this may be inherent porosity, not accounted for in the calculated vol%.

<i>Composite Sample</i>	<i>Calculated Vol% 300 series stainless steel</i>	<i>Measured Vol% 300 series stainless steel</i>
1	60.0	55.7
2	65.0	60.6
3	70.0	63.0

The final density of the sintered composite was also determined using ImageJ cross sectional analysis. In Figure D.6 A, the polished optical cross sectional image of 60.6 vol% 300 series stainless steel is shown. Using ImageJ software [15], the pore area, and thus porosity, can be calculated. In Figure D.6 B, the pores are highlighted in black, showing a porosity of 4.5%.

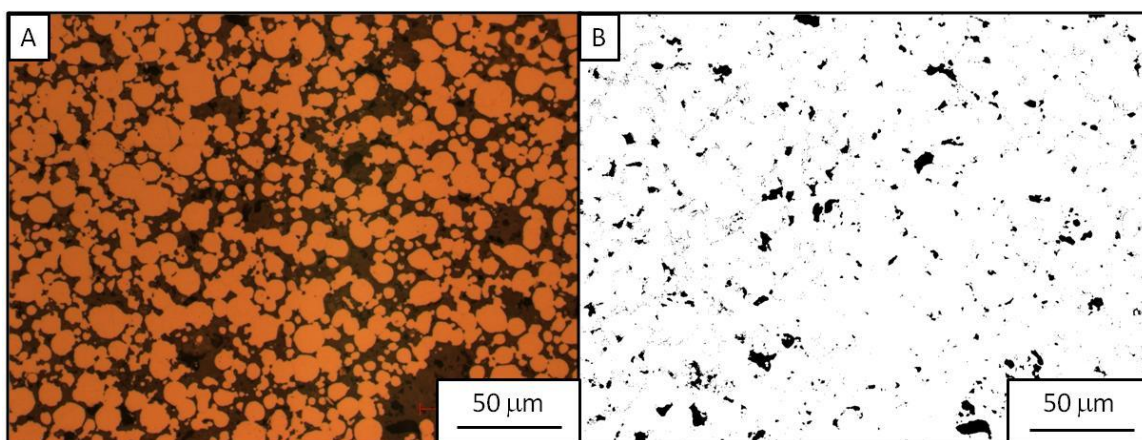


Figure D.6. A polished cross sectional image of a sintered composite material with 60.6 vol% 300 series stainless steel is shown in A. In B, ImageJ software was used to identify the porosity in the sample, and quantify it at 4.5%.

Mechanical property evaluation of the composite formulations was carried out using Vickers hardness testing [17], (Leco Model V1-100-C1). With a constant load of 300gf, the hardness was evaluated for the three composite compositions listed in Table D.6.3, as well as a sample of 300 series stainless steel, with no 3Y-TZP present, sintered to 94.5 % theoretical density by cross sectional image analysis. The hardness testing results are shown in Figure D.7, with composite 1, 2, and 3 having average hardness numbers of 324, 306, and 344 HV respectively, and pure 300 series stainless steel have an average hardness of 209 HV. With the addition of 3Y-TZP powder to the metal matrix, an increase in the value of HV for the composite is expected. Therefore, by the addition of 3Y-TZP to the 300 series stainless steel, a decrease in

viscosity, allowing easier mold infiltration, as well as an increase in hardness, expanding the design materials design area was observed.

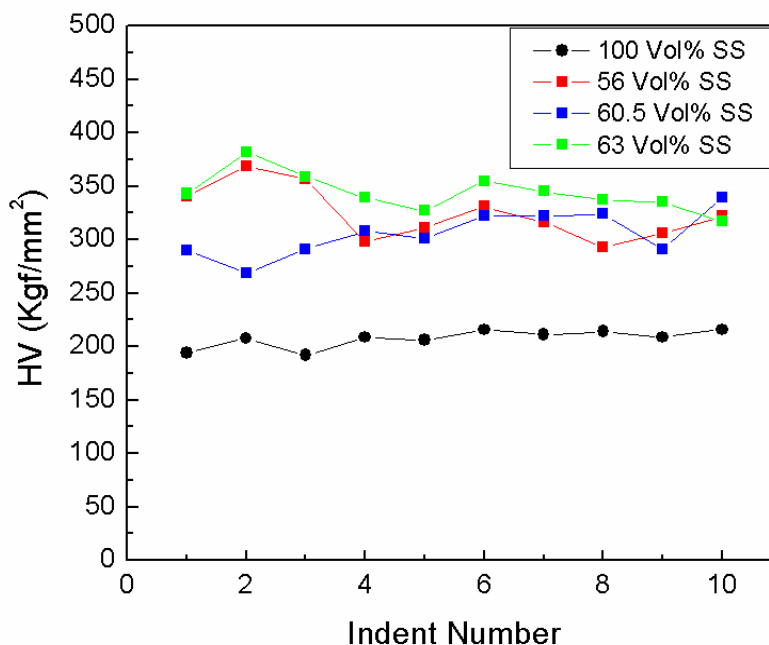


Figure D.7. Vickers hardness results numbers are shown as a function of indentation number for composite suspensions of 100, 63, 60.5, and 56 vol% 300 series stainless steel. The composite parts have HV values very close together, at 324 ± 18 , 306 ± 15 , and 344 ± 13 HV for 56 vol%, 60.5vol%, and 63vol% 300 series stainless steel, however, the 100vol% 300 series stainless steel has significantly lower hardness of 208 ± 6 . An increase in hardness performance could lead to new device designs. The \pm values given are for the 95% confidence interval.

Conclusion

Composite suspensions of 3Y-TZP and 300 series stainless steel were also successfully formulated and incorporated into the LM-RIF process. While these particles also rely on steric forces as a barrier to agglomeration while in suspension, it was found that the addition of the 300 series stainless steel particles to the 3Y-TZP suspension decreased the apparent viscosity of the composite suspension. The interaction energy curve with the deepest secondary minimum, have

the strongest affinity for agglomeration was a 3Y-TZP particle interaction with another 3Y-TZP particle. Also, the theoretical maximum packing fraction of particles is 0.72, as fit with the Dougherty-Krieger relationship. Furthermore, Vickers hardness testing showed an increase from 209HV for pure metal, to 344HV with the addition of the 3Y-TZP particles into microstructure of the final parts.

References

1. Green, D.J., *An introduction to the mechanical properties of ceramics*. 1998: Cambridge University Press.
2. Zhang, W.Q., J.X. Xie, and C.Z. Wang, *Properties of 300 series/PSZ composites fabricated by means of extrusion forming and gas-pressure sintering*. Materials Science and Engineering a-Structural Materials Properties Microstructure and Processing, 2004. 382(1-2): p. 387-394.
3. Mishina, H., Y. Inumaru, and K. KaitokU, *Fabrication of ZrO₂/AISI300 series functionally graded materials for joint prostheses*. Materials Science and Engineering a-Structural Materials Properties Microstructure and Processing, 2008. 475(1-2): p. 141-147.
4. Yoshida, K., H. Mishina, S. Sasaki, M. Morita, and K. Mabuchi, *Development of 3Y-PSZ/AISI 300 series composites for joint prostheses*. Materials Transactions, 2004. 45(11): p. 3209-3215.
5. Wildan, M., H.J. Edrees, and A. Hendry, *Ceramic matrix composites of zirconia reinforced with metal particles*. Materials Chemistry and Physics, 2002. 75(1-3): p. 276-283.
6. Antolino, N., G. Hayes, R. Kirkpatrick, C.L. Muhlstein, M. Frecker, and J. Adair, *Lost Mold Rapid Infiltration Forming of Mesoscale Ceramics: Part 1, Fabrication*. Journal of the American Ceramic Society, 2009. 92(s1): p. S63-S69.
7. Mistler, R.E. and E.R. Twiname, *Tape casting: theory and practice*. 2000: American Ceramic Society.
8. Zsigmondy, R., E.B. Spear, and J.F. Norton, *The Chemistry of colloids: Kolloidchemie*. 1917: John Wiley & Sons, Inc.
9. Tohver, V., J.E. Smay, A. Braem, P.V. Braun, and J.A. Lewis, *Nanoparticle halos: A new colloid stabilization mechanism*. Proceedings of the National Academy of Sciences of the United States of America, 2001. 98(16): p. 8950-8954.

10. Krieger, I.M. and T.J. Dougherty, *A MECHANISM FOR NON-NEWTONIAN FLOW IN SUSPENSIONS OF RIGID SPHERES*. Transactions of the Society of Rheology, 1959. 3: p. 137-152.
11. Farris, R.J., *Prediction of the viscosity of multimodal suspensions form unimodal viscosity data*. Transactions of the Society of Rheology, 1968. 12(2): p. 281-301.
12. Adair, J.H., *Private communication and unpublished publication*.
13. Visser, J., *On Hamaker constants: A comparison between Hamaker constants and Lifshitz-van der Waals constants*. Advances in Colloid and Interface Science, 1972. 3(4): p. 331-363.
14. Bergstrom, L., *Hamaker constants of inorganic materials*. Advances in Colloid and Interface Science, 1997. 70: p. 125-169.
15. Rasband, W.S., *ImageJ*, B. National Institutes of Health, MD, USA, Editor. 1997-2009.
16. Konstowicz, K.J. and J. Boutin, *Study of Porosity in Corroded Refractories*. Journal of the American Ceramic Society, 1993. 76(5): p. 1169-1176.
17. ASTM Standard E384 - 10e2, 2002, *Standard Test Method for Knoop and Vickers Hardness of Materials*, ASTM International, West Conshohoken, PA, 2003, 10.1520/E0384-10E02 www.astm.org

Appendix E

Nomenclature

Table E.6.4. The parameters and variables utilized throughout this dissertation are defined in terms of units, and the value assigned.

<i>Parameters and initial conditions</i>	<i>Definition</i>	<i>Units</i>	<i>Value</i>
θ^l	Moisture content %	NA	Variable
$\gamma^{(x)}$	Modulus of humid expansion [†] [1]	Pa	17×10^5
M	Shear elastic modulus [‡]	Pa	4×10^9
A^*	$A - \frac{\gamma^{(x)2}}{\rho^s C^{l(x)}}$	NA	NA
A	Bulk elastic modulus [‡]	Pa	8×10^9
ρ^s	Density of solid particles	kg/m ³	6050
K^μ	$\frac{\Lambda^\mu C^{l(x)}}{\rho^s}$	NA	NA
ε	Total strain	NA	Variable
$C^{l(x)}$	Moisture content coefficient [†] [1]	J/kg	80
t	Time	seconds	0 to 3600
μ^l	Liquid moisture potential	J/kg	Variable
μ_n	Saturated sample moisture potential	J/kg	Fit experimentally to 160

μ_a	Atmospheric moisture potential	J/kg	Fit experimentally to 15
Λ^μ	Coefficient of moisture mass [†] transfer[1]	kg.s/m ³	6x10 ⁻⁸
λ^v	Coefficient of convective [†] exchange of vapor [1]	kg.s/m ⁴	9x10 ⁻⁵
σ	Stress	Pa	Variable
u	Displacement	m	Variable
Subscripts (x,y,z)	Vector direction of displacement	NA	Unit vector direction
B_{\min}	Minimum feature size resolution	m	Variable
λ	UV light wavelength	m	0.4x10 ⁻⁶
g	Contact gap	m	5x10 ⁻⁶
t	Photoresist thickness	m	Variable
P^{cap}	Capillary pressure	Pa	Variable
γ	Surface tension	mN/m	Variable
r_c	Characteristic radius of curvature for surface tension	m	Variable
V_{total}	Total interaction energy	kT	Variable
V_{vdW}	van der Walls interaction energy also written as V_{gre}	kT	variable
$V_{\text{electrostatic}}$	Electrostatic interaction energy	kT	Variable
V_{steric}	Steric barrier interaction energy also written as	kT	variable

	$V_{bergstrom}$		
ζ -potential	Surface charge of particle in solution at shear plane.	mV	Variable
d	Interparticle separation distance	m	Variable
d_a	Thickness of adsorbed polymer layer	m	Variable
A_H	Hamaker constant [2]	Joule	Variable
a_1 and a_2	Particle diameter, for particle 1 and particle 2, respectively	m	Variable
T	Temperature	Kelvin	Variable
ϕ	Volume Fraction of polymer in steric barrier	NA	0.5
χ	Solvent absorbent interaction parameter	NA	0.3
k	Boltzmann's Constant	$m^2.kg.s^{-2}.K^{-1}$	1.38065×10^{-23}
K	Temperature	Kelvin	Variable

[†] Values are good approximations taken from the literature.

[‡] Values obtained from diametral compression testing in Appendix A.

References

1. Kowalski, S.J., *Thermomechanics of Drying Processes*. Lecture Notes in Applied and Computational Mechanics, ed. W. Pfeiffer. Vol. 8. 2003, New York: Springer.
2. Visser, J., *On Hamaker constants: A comparison between Hamaker constants and Lifshitz-van der Waals constants*. *Advances in Colloid and Interface Science*, 1972. 3(4): p. 331-363.

Appendix F

Design of Experiments

Due to the complexity of many nanomanufacturing processes that consist of several stages, experimenters do not readily employ traditional design of experiment (DOE) techniques. The underlying assumption behind traditional DOE techniques is based on the randomization principle. The randomization principle refers to the concept that both the allocation of the experimental material and the order in which the individual runs or trials of the experiment are performed are randomly determined.

However, as with many manufacturing applications it is impossible to execute a fully randomized design across the whole system. This is because the system is actually a multiple-stage process where factors across stages are not independent. It is difficult to change the levels of some of the factors and there are physical restrictions on the process and instrument. In such cases, the design can be treated as having a split-plot structure. In a concurrent study by Yuangyai et al. [1], a multistage fractional factorial (FF) split plot (MSFFSP) design was developed and primarily used for factor screening and for process optimization. The design is applied to improve the manufacturability of the lost mold rapid infiltration forming (LM-RIF) process while minimizing the number of experimental trials required. Yuangyai et al. shows that with a split plot plus split block structured experiment, the number of experimental runs can be reduced from 32 to 8 [1]. Furthermore, the reduction of experimental trials can be carefully tailored to include specific parameters deemed important by manufacturing engineers.

As discussed in Appendix A, well dispersed, high solids loading slurries are required to fabricate dense ceramic parts. Ytria tetragonal stabilized zirconia (Tosoh Corp. TZ-3Y) is

dispersed and concentrated by chemically-aided attrition milling (CAAM). The initial aqueous dispersion scheme has been developed in previous work by Antolino et al. [2, 3].

After well dispersed, high solids suspensions are obtained, gel-casting monomers and crosslinker, as well as binder and plasticizer are added to the system. In an effort to optimize the yield of parts obtained from this slurry, varying amounts of gel-casting precursors, and binder/plasticizer were added to the system. Design of Experiments was utilized to optimize the process, and investigate the effects of part yield by mold fabrication, slurry formulation, mold filling, drying, and sintering. This work is part of an overall goal to develop a DOE model of the LM-RIF process in order to predict part yield as a function of the input factors in each process step. The design space investigated is shown below in Figure F.1.

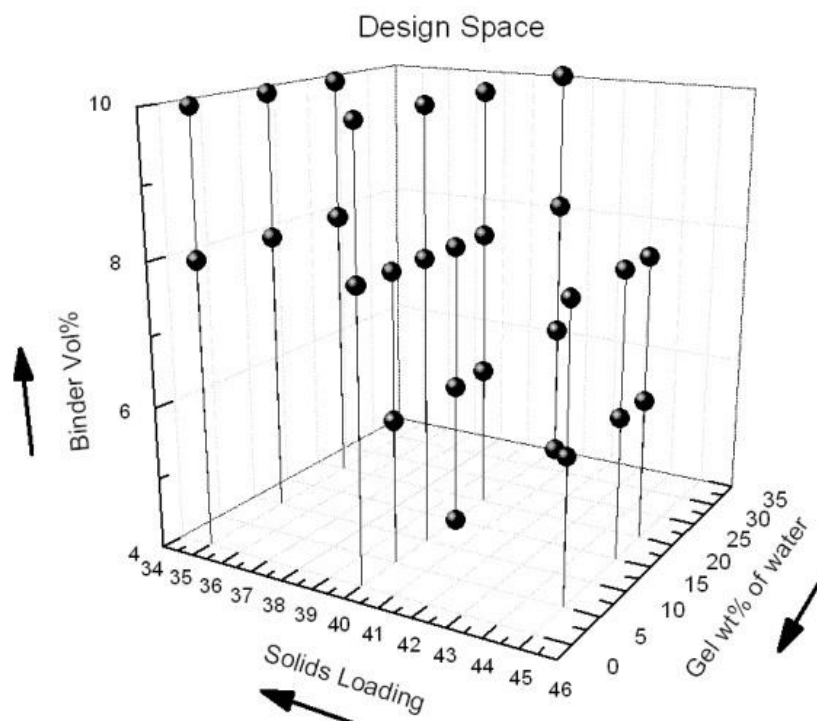


Figure F.1. The design space of interest in the DOE study is shown as a function of binder vol% gel wt% and solids loading. Each point in the design space represents an executed experimental trial with green part yield as the output metric. The arrows indicate the initial results of the DOE trials with increasing green part yield following the directions indicated by the arrows.

Initial determinations using DOE with green part yield (intact parts in the green state) as the output metric show trends indicated by the arrows in Figure F.1. A low gel wt% as well as a low solids loading with a high binder vol% show the best yield improvements. However, significant, practical, limitations exist that must be followed including, the solids loading needs to be higher than 35 vol% in order to obtain dense parts after sintering, the gel wt% needs to be at least 5% otherwise yield significantly decreases, and the binder vol% is limited to 10 vol% due to solubility restrictions.

Table F.1. The results of MSFFSP are given in terms of green part yield for two replications. The largest impact on part yield is seen in the additional experimental replication. Replication 1 and 2 were completed by two different experimentalists, showing that human variation is still present within the LM-RIF.

<i>Experimental</i>	<i>Binder</i>	<i>Solids</i>	<i>Binder</i>	<i>Mold</i>	<i>Solvent</i>	<i>Yield</i>	<i>Yield</i>
<i>Run</i>	<i>Vol%</i>	<i>Content</i>	<i>Ratio</i>	<i>Surface</i>	<i>Exchange</i>	<i>Percentage</i>	<i>Percentage</i>
		<i>Vol%</i>		<i>Treatment</i>	<i>Emersion</i>	<i>Rep 1</i>	<i>Rep 2</i>
					<i>Chemical</i>		
1	8	35	1:1.5	No	Toluene	16.7	72.2
2	8	35	1:1.5	Yes	Ethanol	87.5	100
3	8	40	1:1	No	Ethanol	37.5	98.6
4	8	40	1:1	Yes	Toluene	16.7	80.0
5	10	35	1:1	No	Toluene	0.0	59.7
6	10	35	1:1	Yes	Ethanol	75.0	94.4
7	10	40	1:1.5	No	Ethanol	52.8	97.2
8	10	40	1:1.5	Yes	Toluene	31.9	76.4

Further DOE include the effect of a silicone mold surface coating, immersion drying scheme, and human variation in the LM-RIF process. The yield results of this study are shown in Table F.1. The immersing solution is used in the process because a solvent exchange drying process is employed to minimize drying stress and improve yield. Water saturated, gelled, green parts are placed into an ethanol bath for four hours, during which solvent exchange takes place. After four hours, the parts are dried in ambient atmosphere. Ethanol was chosen because of its miscibility with water as well as a low surface tension. The lower surface tension reduces the capillary drying stresses in the porous parts and minimizes cracking.

The silicone mold surface coating was selected for this process to ensure a non-wetting surface for the aqueous based slurries, as well as provide lubrication between the green parts and the mold walls. As the parts dry, they shrink away from the mold walls. If green parts adhere to the mold walls, the part experiences increased stress during drying and cracking can occur. The main effect plots of the immersing solution, coating effect and block factors are shown in Figure F.2. In addition, from the experimental analysis, we know which factors are significant. This knowledge will be used to further optimize the process.

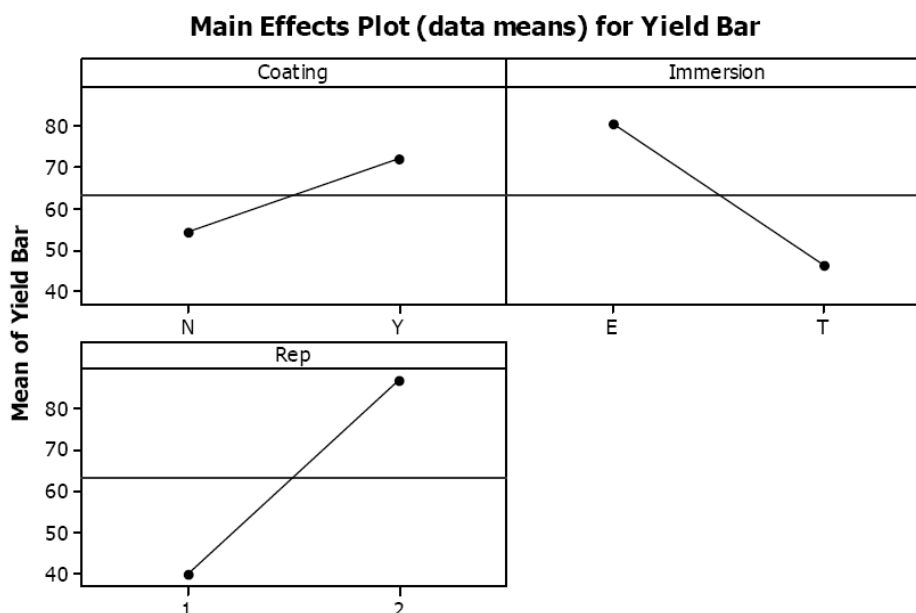


Figure F.2. The main effects of mold surface coating, immersion chemical and experimental replication are given. Results indicate that a non wetting surface treatment should be utilized, along with an ethanol immersion drying scheme. Furthermore, operator influence on part yield is notably high with the difference between operator 1 and 2 shown in the experiment replication [1].

References

1. Yuangyai, C., Hayes, G., Antolino, N., Nembhard, H. B., and Adair, J. H. , *Yield Improvement for Lost Mold Rapid Infiltration Forming Process by a Multi-Stage Fractional Factorial Split Plot Design*. International Journal of Nanomanufacturing, 2009. 3(4): p. 351-367.
2. Antolino, N.E., G. Hayes, R. Kirkpatrick, C.L. Muhlstein, M.I. Frecker, E.M. Mockensturm, and J.H. Adair, *Lost Mold Rapid Infiltration Forming of Mesoscale Ceramics: Part 1, Fabrication*. Journal of the American Ceramic Society, 2009. 92(1): p. S63-S69.
3. Antolino, N.E., G. Hayes, R. Kirkpatrick, C.L. Muhlstein, M.I. Frecker, E.M. Mockensturm, and J.H. Adair, *Lost Mold-Rapid Infiltration Forming of Mesoscale Ceramics: Part 2, Geometry and Strength Improvements*. Journal of the American Ceramic Society, 2009. 92(1): p. S70-S78.

VITA
Gregory R. Hayes

Greg was born and raised in Pipersville, PA, USA. Throughout his High School years, he worked with his father, a carpenter, on various home improvement jobs throughout the northeast Philadelphia area. Greg chose to go to the University of Delaware in 2001, where he would take up Mechanical Engineering. As an undergraduate, he worked as a researcher in Dr. Ismat Shah's materials science laboratory, on synthesizing and characterization of transition metal doped TiO₂ nanoparticles for catalysis applications. He was a teaching assistant and program assistant for study abroad trips to both Germany and Italy during the winter sessions at UD. Outside of school he worked as a civil engineer for Pennoni Engineering in Doylestown, PA. He graduated UD with distinction in 2005, and was awarded the engineering department wide Sigma Xi undergraduate thesis award for his work with Dr. Shah. Following graduation he applied to work for Dr. James H. Adair in the Materials Science Department at The Pennsylvania State University, under the co-advising of Dr. Mary I. Frecker in Mechanical Engineering. Prior to attending PSU in the fall of 2005, Greg worked at the University of Freiburg, Germany, on the synthesis of carbon nanotubes using quantum dots as catalysts. Since 2005, Greg has been involved in research at PSU that spans both mechanical engineering and materials science, working on the processing of nanoparticles for surgical instrument applications, and morphing airplane skins. He has also been involved in the Iron Lion design challenge, resulting in a patent for a surgical instrument design, as well as had collaborations with the Hershey Hospital Endoscopic Surgery Staff, and Departments of Mechanical, Aerospace, Industrial, and Materials Science Engineering.